High Field Superconductors for Fusion Energy Applications

RAINE, MARK,JOHN

High Field Superconductors for Fusion Energy Applications

Mark John Raine

A thesis submitted in partial fulfilment
of the requirements for the degree of
Doctor of Philosophy

Department of Physics,
Durham University
2015

High Field Superconductors for Fusion Energy Applications

Mark John Raine

Abstract

The fabrication and processing by solid-state heat-treatment, mechanical ball milling and hot isostatic pressing of *microcrystalline* and *nanocrystalline* niobium carbonitride is reported. This material is subjected to a number of characterisation measurements including x-ray diffraction, resistivity, ac-susceptibility, dc-extraction and heat capacity. The resultant measurement data are used to assess the adequacy of the material's processing and quality with respect to the fundamental superconducting characteristics, transition temperature, T_c, upper critical magnetic field, B_{c2}, and critical current density, J_c. It is shown that a substantial increase in B_{c2} from ~ 11 T (in the microcrystalline material) to ~ 21 T (in the nanocrystalline material) has been produced. A *fortyfold* increase in J_c from 1.8 x 10^7 Am^{-2} (in microcrystalline material measured at 3 T and 6 K) to 7.4 x 10^8 Am^{-2} (in nanocrystalline material measured at 3 T and 5.9 K) has also been produced. These substantial increases have been made with only a 32 % reduction in T_c from ~17.6 K to ~ 11.9 K, well above the temperature of liquid helium.

The accurate large quantity metrology of 10,000 Nb_3Sn samples for the International Thermonuclear Experimental Reactor toroidal field coils is also reported and an overview analysis of the data provided. In particular, all *seven* measurement types; critical current, hysteresis loss, residual resistivity ratio, diameter, chromium plating thickness, twist pitch and copper to non-copper volume ratio are discussed in relation to the accuracy with which they were performed. The methodology in performing the heat-treatments and measurements is discussed and the detail of the necessary equipment set up is given. The results from some additional experiments that deal with the effect of heat-treatment cleanliness and sample geometry on various measurement types is provided.

Publications

M. J. Raine and D. P. Hampshire, "Characterization of the Low Temperature Superconductor Niobium Carbonitride," *IEEE Transactions on Applied Superconductivity*, vol. 21, pp. 3138-3141, 2011.

P. Sunwong, J. S. Higgins, Y. Tsui, M. J. Raine, and D. P. Hampshire, "The critical current density of grain boundary channels in polycrystalline HTS and LTS superconductors in magnetic fields," *Superconductivity Science and Technology*, vol. 26, pp. 095006, 2013.

D. Hu, M. D. Ainslie, J. P. Rush, J. H. Durrell, J. Zou, M. J. Raine, and D. P. Hampshire, "DC characterization and 3D modelling of a triangular, epoxy-impregnated high temperature superconducting coil," *Superconductor Science & Technology*, vol. 28, pp. 8, 2015.

M. J. Raine and D. P. Hampshire, "Improved Critical Magnetic Field and Critical Current Density of the Low Temperature Superconductor Niobium Carbonitride by making it Nanocrystalline," to be published.

M. J. Raine and D. P. Hampshire, "Large Quantity Characterisation of Nb_3Sn Strands for ITER," to be published.

Table of Contents

Declaration and copyright

I confirm that no part of the material offered in this thesis has previously been submitted by me for a degree in this or any other University. If material has been generated through joint work, my independent contribution has been clearly indicated. In all other cases material from the work of others has been acknowledged and quotations and paraphrases suitably indicated.

Mark J. Raine

February 2015

Acknowledgements

There have been many people who have provided me with guidance, advice, their services and their motivating attitude throughout my Ph.D. One person in particular who has consistently made available all of the above, and who I owe substantial thanks, is my supervisor, Professor Damian Hampshire. I must also thank everyone who is or has been in the Superconductivity Group because they have all helped me in one form or another. These people are Helen Cramman, Steve Pragnell, Joshua Higgins, Jian-Yong, Xi-Feng, Elisabetta Pusceddu, Peter Byrne, Prapaiwan Sunwong, James Ore, YeKin Tsui, Paul Branch and Guanmei Wang. I have completed a lot of engineering work during my Ph.D. that would not have been possible without the practical skills and experience available within the departmental workshops. In this respect thanks must go to Stephen Lishman and the rest of his team in the Mechanical Workshop and to John Scott and his team in the Electronics Workshop. The level of sarcasm offered to me during my Mechanical Workshop visits has always made me feel warm inside and especially wanted. I must also thank Norman Thompson, David Pattinson and Duncan McCallum for their help; especially to David for his SEM expertise. Special thanks must also go to what became known as the ITER team; Andrea Dawson, Emily Roe, Michael McBreen and Matthew Plumb who all came together to help make a success of the Reference Laboratory. In this respect I must also thank Frederic Hatanian who helped me with a substantial amount of sample preparation and measurement work at the very beginning of the laboratory before the ITER team was formed. There has also been a number of summer students who have worked to improve various aspects of the laboratory. These were Thomas Jubb, Guanmei Wang, Callum Murray, Thomas Whittles, Paul Branch, David Stobbs, Simon Zieleniewski, James Keye, Megan Leoni, Aleksander Lasek, Simon Cunningham, Kit Gallagher, Stephen Webster, Simone Smith, Alexander Blair, Tom Hudson, Victoria Grigson and Robin Linten. I especially thank those summer students who returned annually to the laboratory and provided some additional consistency; these are quite obviously people with a strong constitution. With regard to the ITER work I thank Thierry Boutboul and Peter Readman for their advice in the early days and for always being reasonable and realistic. I also thank the Engineering Laboratory at Cambridge University for providing some magnetisation measurements that helped to confirm the calibration of our equipment.

On a more personal level a deep hearted thank you must go to my wife, Gill. Not only for the support she has given me during my Ph.D. but also for all the previous years' support in getting me to where I am (where *we* are) today. Through incredibly difficult and stressful times she has always done her very best to ensure my studies have remained uncompromised. I also thank my children, Daniel and Calum, for helping, in their own very different ways, to motivate me into doing my best. Finally, I must thank my parents who have always looked after and supported me in everything I have ever done in life… even those things they did not agree with. This attitude instilled within me an aspiration never to be a disappointment to them; I therefore leave it to them to be the judge of my success in this regard.

I dedicate this thesis to my late father, John Raine, whose level-headedness, intelligence, physical skill, foresight and good humour, coupled with his bravery and selflessness when faced with death, have all made me the person I am today… I only hope that I might equal him tomorrow.

PART I: Basic and Applied Superconductivity

Chapter 1

Introduction

If you were asked to describe the entire universe, based on your own experience within it, in just one word, what would it be? For me, that word would have to be “change”. Without change there would be no way in which time could be measured, no means by which measurement could be performed and no way in which the universe could be viewed or assessed. Change is something that people understand, that people are not confused by. Change is something that we expect. And yet, change is purely a symptom of a more fundamental underlying driving influence, a less well understood influence… energy. Energy is Nature’s currency and change is just an outcome of Nature’s transactions in energy. These transactions are merely the transformations of energy from one form to another, say, from chemical energy (stored within fossil fuels) to electrical energy (that lights our homes). Our sources of stored energy are, however, dwindling and our transformation of that energy has been detrimental to the health of our planet. This has prompted our community to make more careful energy choices and has generated a collective effort to seek more efficient ways of dealing with our energy needs.

Electrical energy is transported to our homes through copper wires. Copper is a very good and economical conductor of electricity, which is why it is the most widely used conductor, and this means that most of the electrical energy it transports successfully reaches our homes. However, some is lost. In 2012 as much as 8 % of the electrical energy generated in the UK was wasted due to inefficiencies in the National Grid [1]; inefficiencies largely inherent to the means by which the energy was delivered. In copper the inefficiency is generated by its *resistance* to the flow of electricity. As electrons that constitute electricity move along a copper wire they encounter imperfections and impurities that remove some of their motive energy causing them to slow down. In order to maintain the flow, the lost energy must be replaced by applying a voltage to the wire. We can do very little about this electrical *resistance* or the wasted energy but fortunately, there is a class of conducting materials called *superconductors* in which resistance does not have this undesirable outcome.

Superconductors and superconductivity have been known about since their discovery in 1911 but have failed to sustain public attention. This might be a consequence of the never ending promise of room temperature superconductivity that established too high an expectation far too early. All technologies develop over time but few are actually as exciting or have similar potential as

superconductivity. There are approximately *sixty million* magnetic resonance image (MRI) scans performed worldwide each year to help with medical diagnosis and yet the vast majority of the people scanned do not realise that they have laid within the bore of a *superconducting* magnet cooled to a temperature almost as cold as the coldest outer reaches of the universe. Likewise, the public, influenced by politicians and the contemporary media, have not been sufficiently introduced to what just might become a real and viable sustainable energy solution, not only to our energy crisis, but also to the consequences felt by our planet due to our current methods of energy extraction. This possible solution is *fusion* energy. Furthermore, rather than having to wait for the advent of room temperature superconductivity to harness fusion energy, today's superconducting materials and technologies are being implemented now, in what might become, the world's most important experiment… the International Thermonuclear Experimental reactor (ITER) currently being built in Cadarache, southern France.

The work described in this thesis is entirely concerned with superconductivity and in part one of the workhorses of superconducting applications, niobium tin. Niobium tin is a low temperature superconductor that is able to carry very large electrical currents without resistive losses and because flowing currents generate their own magnetic fields this means we can use niobium tin (and other similar superconductors) to produce very strong magnets, similar to those found in the MRI scanners discussed above. Additionally, niobium tin is one of the superconducting materials being used to build very large magnets (~ 14 m high by ~ 9 m wide) for the ITER project to trap a hot plasma with a temperature *ten* times that at the core of our sun. The importance of this project is such that most of the niobium tin wires must have a number of physical and superconducting characteristics carefully measured – some measurements performed at extremely cold temperatures (- 269 ℃) – before they can be used to build the magnets. The metrology of these wires is, in part, the subject of this thesis.

Applications that rely on strong magnetic fields are, however, not limited to MRI scanners and ITER alone but the message here is that a lot can be achieved with strong magnetic fields and superconducting materials are not only good at producing them but are also the most efficient way of doing so. Unfortunately, although superconductors are not hindered by electrical resistance, they are limited by temperature, current and magnetic field strength. Superconductivity only occurs if a superconductor is sufficiently cooled below a particular temperature, characteristic of that particular type of superconductor. This does not present an insurmountable problem for applications because we have a very good understanding of cooling technologies. Additionally though, the superconducting state is destroyed by electrical currents that exceed a critical value and/or if the superconductor is placed within a sufficiently strong magnetic field; even if that field is generated by the current flowing through the superconductor itself. This presents a maximum upper limit on the current that can be carried, and the magnetic field strength a superconductor can be subjected to. This, unfortunately, puts limits on the use of superconductors in real-world applications. It is therefore important to try and overcome these limits so that technologies can be improved and enhanced. One such effort to overcome the

upper critical magnetic field limit of the low temperature superconductor *niobium carbonitride* is the other main focus of this thesis' work.

There are a number of ways in which the ability of a superconductor, not only to carry current, but also to withstand strong magnetic fields, can be manipulated and improved. One way is to make the material *nanocrystalline*. Most solid materials, to some degree, have a crystalline structure. This means that the atoms they are comprised of are held together in a regular pattern or configuration that is repeated throughout the material. Sometimes the orientations of these small atomic configurations - let's call them grains - are so perfectly aligned that we deem the material to be a *single* crystal. The crystal looks the same everywhere. In reality such perfect crystals are rarely very big because it is so unlikely for such perfection to occur without disruption of one form or another. It just so happens, however, that the closer a superconductor gets to having a perfect crystalline structure, the less useful it becomes. These very clean and ordered superconductors are not able to carry useful electrical currents (for reasons that won't be addressed in this introduction) and are therefore unable to generate useful magnetic fields. The way around this is to produce some level of crystalline *disorder*. In other words, randomly *change* the orientation of all the constituent grains that form the superconductor's structure. This disordering enables a superconductor to carry current and can improve the maximum magnetic field it can withstand before losing the superconducting state. As with most things, however, there is a limit beyond which these abilities are reduced. The secret is to find the optimum. Another thing that can be done that might improve the maximum magnetic field is to reduce the size of the grains that form the crystal structure. This is where the term *nanocrystalline* comes from. It refers to *nano*-sized *crystals* i.e. crystalline grains that have a length scale of a billionth of a metre. In fact, on the face of it, reducing grain size and randomising grain orientation is usually considered to be undesirable because it increases electrical resistance. Fortunately, this only effects non-superconductors, such as copper, and if done carefully, can be a desirable outcome of the kinds of material processing applied to niobium carbonitride discussed in this work.

This thesis is divided into three parts: PART I: *Basic and Applied Superconductivity* deals with the theoretical background to the phenomenon and our microscopic understanding and provides an introduction to one of the most important projects in the world that will use superconductivity to harness a star's energy for the good of humankind, namely, the ITER project; PART II: *NbCN – A Possible New Material for Fusion Applications* deals with the fabrication and processing of the low temperature superconductor niobium carbonitride that has led to a substantial increase in its ability to withstand strong magnetic fields by making it nanocrystalline; PART III: *The Metrology of Nb_3Sn for ITER* deals with the measurement of 10,000 samples of Nb_3Sn as part of the verification and acceptance testing of the superconducting strands earmarked for inclusion in the ITER fusion tokamak reactor.

Chapter 2

Basic and applied superconductivity

2.1 Introduction

In the one hundred years or so since the discovery of superconductivity the field has witnessed a number of seminal theoretical and experimental developments, such as a complete understanding of low temperature superconductivity, the understanding and application of the Josephson effect, the discovery of high temperature superconductivity and the discovery of novel iron based superconductors, to name but a few. In parallel with this work we have seen a plethora of new materials, ranging from very low to very high temperature superconductors. Some have been of no particular applicable interest and others have enabled technologies once considered to be in the realm of science fiction, such as magnetic resonance imaging scanners and fusion tokamaks.

In today's world where global domestic energy usage has become a major "green" issue, the prospects for the future that superconductivity offers will only intensify the search for better superconductors. While the field of superconductivity has been an active one for over a century, it seems that it has not yet fully matured.

In this chapter the major fundamental theories of Ginzburg-Landau and Bardeen-Cooper-Schrieffer will be reviewed. Bean's critical state model of magnetic hysteresis will also be discussed before moving onto the properties of microcrystalline and nanocrystalline materials. The chapter ends by discussing the exciting, fundamental and essential role superconductors are playing in the International Thermonuclear Experimental Reactor.

2.2 Phenomenological and microscopic theories of superconductivity

2.2.1 London equations

The discovery of superconductivity in 1911 and its unusual zero-resistance state led to the premature conclusion that superconductors were simply *perfect* conductors. The *exclusion* of an applied magnetic field from the interior of a pre-cooled superconductor was explained by Lenz's law, in which the applied field induces currents within the superconductor that generate opposing

fields that maintain a field-free interior. This explanation of magnetic screening was, however, found to be in error when in 1933 Walther Meissner and Robert Ochsenfeld discovered that a superconductor *expels* magnetic fields from its interior when cooled to below its transition temperature in a non-zero static magnetic field. This Meissner effect was in stark contrast to the behaviour expected of a *perfect* conductor. A perfect conductor would actually resist any change in the applied field (again, according to Lenz's law) and in so doing would maintain the original field - even in the extreme case in which the applied field was completely removed. So whilst superconductors did indeed display behaviour in accordance with perfect conductivity (*zero* resistance and field exclusion), this alone could not fully account for their behaviour; a full account had also to include the *expulsion* of applied fields.

Prior to 1935 the two main characteristics of superconductivity, namely, zero resistance and perfect diamagnetism, were not explicit within electromagnetic theory. This situation was remedied, however, by Fritz and Heinz London. The London brothers proposed two equations that in conjunction with Maxwell's equations describe zero resistance and perfect diamagnetism. The first of these two equations is

$$\mathbf{E} = \mu_0 \lambda_L^2 \frac{d}{dt}\mathbf{J} \qquad \text{with} \qquad \lambda_L^2 = \frac{m}{\mu_0 n_s e^2}, \tag{2.1}$$

where μ_0 is the permeability of free space, λ_L is the London penetration depth, m is the electron mass, n_s is the superelectron density and e is the electron charge. If an electric field $\mathbf{E}$, permeates a superconductor then the charge density, $\mathbf{J}$, continuously increases, since there is an uninterrupted acceleration of the superelectrons. Furthermore, this equation shows that if a steady current is maintained then the electric field is *zero* - no resistance, no potential difference.

The second of the London equations is

$$\mathbf{B} = -\mu_0 \lambda_L^2 \mathrm{curl}(\mathbf{J}). \tag{2.2}$$

This describes *perfect* diamagnetism. This can be seen as follows.

Maxwell's fourth equation

$$\mathrm{curl}(\mathbf{H}) = \mathbf{J} + \frac{\delta \mathbf{D}}{\delta t}, \tag{2.3}$$

where $\mathbf{H}$ is the magnetic field strength and $\mathbf{D}$ is the electric displacement, becomes, in the absence of magnetisation and displacement currents, Ampere's law [2],

$$\mathrm{curl}(\mathbf{B}) = \mu_0 \mathbf{J} \tag{2.4}$$

Substitution of (2.4) into (2.2) gives

$$\mathbf{B} = -\lambda_L^2 \mathrm{curl}\big(\mathrm{curl}(\mathbf{B})\big), \tag{2.5}$$

and on use of the vector identity

$$\mathrm{curl}\big(\mathrm{curl}(\mathbf{B})\big) \equiv \mathrm{grad}\big(\mathrm{div}(\mathbf{B})\big) - \nabla^2\mathbf{B}, \tag{2.6}$$

where Maxwell's second equation

$$\mathrm{div}(\mathbf{B}) = 0 \tag{2.7}$$

is used to reduce (2.6) to

$$\mathrm{curl}\big(\mathrm{curl}(\mathbf{B})\big) = -\nabla^2\mathbf{B},$$

and equation (2.5) becomes

$$\mathbf{B} = \lambda_L^2\nabla^2\mathbf{B} \quad \Longrightarrow \quad \nabla^2\mathbf{B} = \frac{\mathbf{B}}{\lambda_L^2}, \tag{2.8}$$

which is a second order differential equation with solution,

$$B(x) = B_0 \exp\left(-\frac{x}{\lambda_L}\right). \tag{2.9}$$

Assuming the magnetic field is applied along the *z*-axis. This solution shows that the applied field exponentially decreases from its maximum at the surface of a superconductor to $B_0\exp(-1)$ over the characteristic London penetration depth λ_L.

2.2.2 Ginzburg and Landau theory of superconductivity

Introduction

In 1950 Vitaly Ginzburg and Lev Landau published a paper entitled "On the Theory of Superconductivity" [3] in which they presented an extension to the London brothers' phenomenological approach [4]. This paper provided an extension to Landau's previous, unsuccessful, attempt at applying the theory of phase transitions to superconductivity. However, the success of the 1950 paper was nevertheless primarily due to Landau's perseverance with the transition approach [5].

The Ginzburg-Landau equations

During a structural phase transition a change occurs within a material in which the structure's order is either increased or decreased. Ginzburg and Landau (GL) proposed a complex order parameter, ϕ, whose squared modulus is proportional to the density of superconducting electrons. Their reason for this was simple. The number of superconducting electrons above the transition temperature, $T > T_c$, is *zero*, and below that temperature they increase in number until $T = 0$ is reached [6], and so they are also related to the *order* of the superconducting material.

In formulating their theory they focussed on temperatures very close to the transition temperature, T_c, since the order parameter, ϕ, would be sufficiently small at these temperatures to be conducive to mathematical formulation. In particular, the theory's foundation is concerned with minimising the Helmholtz free energy (in zero field) because when the order parameter is small the free energy can be expanded as a power series in ϕ. Fortunately, although this treatment is not generally applicable, it is applicable to superconductivity. In order to increase the applicability to superconductivity in magnetic fields, it was necessary to minimise the Gibbs free energy density

$$g(\mathbf{r}) = f_n + \alpha|\phi(\mathbf{r})|^2 + \frac{1}{2}\beta|\phi(\mathbf{r})|^4 + \frac{1}{2m}|(-i\hbar\boldsymbol{\nabla} - 2e\mathbf{A})\phi|^2 + \frac{\mathrm{B}^2}{2\mu_0} - \mathbf{H}_0 \cdot \mathbf{B} + \frac{1}{2}\mu_0\mathbf{H}_0^2, \qquad (2.10)$$

where f_n is the free energy density in the *normal* state, α and β are functions of temperature and $\mathbf{A}$ is the magnetic vector potential [7].

The minimisation of equation (2.10) with respect to ϕ, using variational methods, yields the *first* GL equation

$$\frac{1}{2m}(-i\hbar\boldsymbol{\nabla} - 2e\mathbf{A})^2\phi + \alpha\phi + \beta|\phi|^2\phi = 0, \qquad (2.11)$$

which is similar to the Schrodinger equation (and includes a non-linear term) [8]. This also means that the complex order parameter can be regarded as quantum mechanical wavefunction.

The associated boundary condition for (2.11) is given by

$$\mathbf{n} \cdot (-i\hbar\boldsymbol{\nabla} - 2e\mathbf{A})\phi = 0, \qquad (2.12)$$

where $\mathbf{n}$ is a unit vector *normal* to the surface boundary.

Minimising equation (2.10) with respect to the vector potential, $\mathbf{A}$, yields the *second* GL equation

$$\mathbf{J} = -\frac{ie\hbar}{m}(\phi^*\boldsymbol{\nabla}\phi - \phi\boldsymbol{\nabla}\phi^*) - \frac{4e^2}{m}|\phi|^2\mathbf{A}. \qquad (2.13)$$

So, the *first* (2.11) and *second* (2.13) GL equations form a set of simultaneous equations from which the order parameter, the current density, and the vector potential can be determined and then used to obtain the major characteristic parameters of superconductivity.

The penetration depth

The GL theory is an extension to the London brothers' previous work that generalises Maxwell's electromagnetic equations to take account of the fundamental superconducting phenomena - perfect conductivity and perfect diamagnetism. It is therefore reasonable that the GL theory includes within it some of the superconducting characteristics predicted by the Londons' work. One such prediction is the *penetration depth*.

Deep inside a Type I superconducting material the magnetic field is *zero* and the order parameter must remain constant if the free energy is to be at a *minimum* [7]. Hence, equation (2.13) reduces to

$$\mathbf{J} = -\frac{4e^2}{m}|\phi|^2\mathbf{A}. \tag{2.14}$$

Taking the *curl* of (2.14), applying $\mathbf{B} = \mathrm{curl}(\mathbf{A})$ and rearranging yields

$$\mathbf{B} + \frac{m}{4e^2}\frac{1}{|\phi|^2}\mathrm{curl}(\mathbf{J}) = \mathbf{0} \tag{2.15}$$

and on use of Maxwell equations (2.4) and (2.7) and the identity (2.6), equation (2.15) becomes

$$\nabla^2\mathbf{B} = \frac{e^2\mu_0 n_s}{m}\mathbf{B} \tag{2.16}$$

where n_s is the superelectron density.

Equation (2.16) can be written in the more standard form

$$\nabla^2\mathbf{B} = \frac{\mathbf{B}}{\lambda_{GL}^2} \quad \text{with} \quad \lambda_{GL}^2 = \frac{m}{e^2\mu_0 n_s}.$$

The coherence length

The order parameter ϕ is a locally defined parameter i.e. its value is position dependent, and therefore it changes from place-to-place within a superconductor depending upon the local conditions. However, the variation in the change of ϕ is not without restriction; the restriction being the *coherence length* ξ. This is the characteristic length over which ϕ can vary appreciably [9]. It can also be interpreted as the average *maximum* spacing between Cooper pairs [10], though this does not form part of the GL theory.

The expression for the coherence length can be determined as follows [9]. Considering the zero field case and therefore setting $\mathbf{A} = \mathbf{0}$ in equation (2.13) shows that

$$\phi^* \boldsymbol{\nabla} \phi = \phi \boldsymbol{\nabla} \phi^*, \tag{2.17}$$

which forces the phase of the order parameter to be independent of position, otherwise (2.17) would not be satisfied. Further, the phase is constant and can be *real* valued. Considering the one-dimensional case, and employing the above constraints on equation (2.11) yields

$$-\frac{\hbar^2}{2m}\frac{d^2\phi}{dx^2} + \alpha\phi + \beta|\phi|^2\phi = 0, \tag{2.18}$$

which is a one-dimensional (non-linear) Schrodinger equation. A change in variables leads to the solution

$$\phi = \phi_\infty \tanh\left(\frac{x}{\sqrt{2}\xi_{GL}}\right), \tag{2.19}$$

where

$$\xi_{GL} = \left(\frac{\hbar^2}{2m|\alpha|}\right)^{\frac{1}{2}} \tag{2.20}$$

is the GL coherence length.

The Ginzburg-Landau parameter

Type I and Type II superconductors can be characterised by the ratio of the penetration depth, λ_{GL}, to the coherence length ξ_{GL}. This ratio, κ, known as the Ginzburg-Landau parameter, determines the superconducting *type* as follows,

$$\kappa = \frac{\lambda_{GL}}{\xi_{GL}} \leq \frac{1}{\sqrt{2}} \qquad \text{then Type I behaviour follows}$$

$$\kappa = \frac{\lambda_{GL}}{\xi_{GL}} > \frac{1}{\sqrt{2}} \qquad \text{then Type II behaviour follows.}$$

Type I critical fields

The critical magnetic field, B_c, is the demarcation point between *superconducting* and *normal* behaviour in Type I superconductors. When the applied field equals or exceeds the critical field the superconducting state is destroyed and the material is forced into the *normal* state.

Considering a superconducting bulk material with dimensions far greater than the penetration depth that is in the superconducting state, the internal magnetic field $\mathbf{B} = \mathbf{0}$ and the order parameter, are constant [7]. Applying these conditions to equation (2.11) yields

$$\alpha\phi + \beta|\phi|^2\phi = 0 \quad \Longrightarrow \quad |\phi|^2 = -\frac{\alpha}{\beta} = \frac{|\alpha|}{\beta}. \tag{2.21}$$

Applying the above conditions to equation (2.10), substituting for (2.21) and integrating over the volume of the material yields the Gibbs free energy density as a function of applied field strength H_0 for the superconducting state,

$$g_s = f_n - \frac{|\alpha|^2}{2\beta} + \frac{1}{2}\mu_0 H_0^2. \tag{2.22}$$

Further, in the normal state the order parameter $\phi = 0$. Applying the same method with the conditions for normal state behaviour yields

$$g_s = f_n \tag{2.23}$$

the Gibbs free energy density for the *normal* state. Therefore, since the critical field occurs at the boundary between the superconducting state and the normal state, the Gibbs free energy densities of both states are the same at this point. Equating (2.22) and (2.23) and rearranging gives

$$H_c^2 = \frac{|\alpha|^2}{\mu_0\beta}, \tag{2.24}$$

where $\alpha = -A(T_c - T)$ and β is a constant. Note that T_c is the critical temperature and can be empirically measured. Likewise, the critical field strength, H_c, can be experimentally determined.

Type II critical fields

In contrast to Type I superconductors, Type II superconductors do not remain free of magnetic flux until the critical field is reached. Instead, a Type II superconductor remains flux free up to a *lower* critical field, beyond which flux vortices begin to penetrate the bulk material forming a *mixed state*. This penetration increasingly continues until the *upper* critical field is reached, at which point the material enters the *normal* state.

The lower critical field

The lower critical field strength H_{c1} is the demarcation point between total flux exclusion and the mixed state. As such, the Gibbs free energy densities in both states must be equal at this point

whether a single flux vortex has penetrated the material or not. Equating the Gibbs free energy equations for both states at this point and noting that the Gibbs free energy is equal to the Helmholtz free energy, F_s, at H_{c1}, yields [11]

$$F_s = F_s + \varepsilon_1 L - H_{c1}\Phi_0 L, \tag{2.25}$$

where ε_1 is the free energy per unit length, L is the length of a vortex line and Φ_0 is a flux quantum.

Solving (2.25) for H_{c1} gives

$$H_{c1} = \frac{\varepsilon_1}{\Phi_0}. \tag{2.26}$$

The free energy per unit length and the flux quantum are given by

$$\varepsilon_1 = 2\pi\mu_0 H_c^2 \xi^2 \ln(\kappa) \approx \frac{\Phi_0^2}{4\pi\mu_0\lambda_L^2}\ln(\kappa) \tag{2.27}$$

and

$$\Phi_0 = 2\sqrt{2}\pi\lambda_L\xi\mu_0 H_c, \tag{2.28}$$

where H_c is the thermodynamic critical field strength. Substituting for the approximation (2.27) and expression (2.28) into (2.26) yields

$$H_{c1} = \frac{H_c}{\sqrt{2}\kappa}\ln(\kappa),$$

which can be seen to be dependent on the Ginzburg-Landau parameter.

The upper critical field

Close to the upper critical field strength, H_{c2}, the value of the order parameter, ϕ, is small. Therefore, equation (2.11) can be linearised to be

$$-\frac{\hbar^2}{2m}\frac{\partial^2\phi}{\partial x^2} + \frac{1}{2m}\left(-i\hbar\frac{\partial}{\partial y} - 2e\mu_0 H_0 x\right)^2 \phi - \frac{\hbar^2}{2m}\frac{\partial^2\phi}{\partial z^2} = |\alpha|\phi, \tag{2.29}$$

where (2.29) has also had the vector potential $\mathbf{A}$ expanded in the component form $\mathbf{A} = (0, \mu_0 H_0 x, 0)$.

Equation (2.29) is the Schrodinger equation for a particle of mass m and charge $2e$ moving in a uniform magnetic field directed along the *z*-axis [12].

The eigenvalues of (2.29) are given by

$$|\alpha| = \frac{H_0}{m}(2n+1)\hbar e\mu_0 + \frac{\hbar^2 k_z^2}{2m}, \tag{2.30}$$

where k_z is the *z*-component of the wavevector.

Solving (2.30) for H_0 gives

$$H_0 = \frac{m}{(2n+1)\hbar e\mu_0}\left(|\alpha| - \frac{\hbar^2 k_z^2}{2m}\right) \tag{2.31}$$

and the upper critical field strength occurs at the point this expression takes its highest value i.e. when $n = 0$ and $k_z = 0$, leading to

$$H_{c2} = \frac{m|\alpha|}{\hbar e\mu_0}, \tag{2.32}$$

which can be written in terms of the coherence length (2.20)

$$B_{c2} = \mu_0 H_{c2} = \frac{\hbar}{2e\xi^2} = \frac{\Phi_0}{2\pi\xi^2}. \tag{2.33}$$

Magnetic response

Type I and Type II superconducting materials behave very differently in response to an externally applied magnetic field $\mathbf{B}_{app}$.

Type I magnetic response

For an applied magnetic field, $\mathbf{B}_{app}$, less than the critical magnetic field, $\mathbf{B}_c$, a bulk Type I superconductor will prevent $\mathbf{B}_{app}$ from remaining within (expulsion) or entering (exclusion) the bulk of the superconducting material. Once in the superconducting state the presence of $\mathbf{B}_{app}$ forces superconducting surface currents to flow. These currents act to create an additional magnetic field that opposes $\mathbf{B}_{app}$ and ensures that the total internal magnetic field $\mathbf{B}_{in} = \mathbf{0}$. These surface currents can be thought of as being generated by magnetisation, $\mathbf{M}$, created by Copper pair supercurrents flowing within the penetration depth. For an applied magnetic field equal to or greater than the critical magnetic field, the superconducting state is destroyed and *normal* behaviour ensues (see Figure 2.1a).

Type II magnetic response

For a Type II superconducting material, the lower critical field, $\mathbf{B}_{c1}$, is less than the thermodynamic critical field, $\mathbf{B}_c$, (which is the same as the Type I critical field). Below $\mathbf{B}_{c1}$ the Type II superconductor acts in the same manner as a Type I superconductor. However, once $\mathbf{B}_{c1}$ is reached, the superconductor enters the *mixed* state and an increasing number of flux vortices penetrate the material until the upper critical field, $\mathbf{B}_{c2}$, is reached. It is not until this point that the material is forced into *normal state* behaviour (see Figure 2.1b).

Flux quantisation

When flux begins to penetrate into the bulk of a superconductor it does so in discrete threads of quantised flux. By writing the order parameter as a product of a modulus and a phase factor and then taking the line integral of equation (2.13) around a closed path and ensuring that the order parameter remains single-valued, the following equation can be derived [13]

$$\frac{m}{e^2}\oint \frac{\mu_0 \mathbf{J}}{|\phi|^2}\cdot d\mathbf{l} + \Phi = n\Phi_0. \tag{2.34}$$

This shows that the line integral of the current density, $\mathbf{J}$, that encloses the flux, Φ, added to the enclosed flux, Φ, is quantised i.e. only a whole number, n, of flux quanta, Φ_0, can exist.

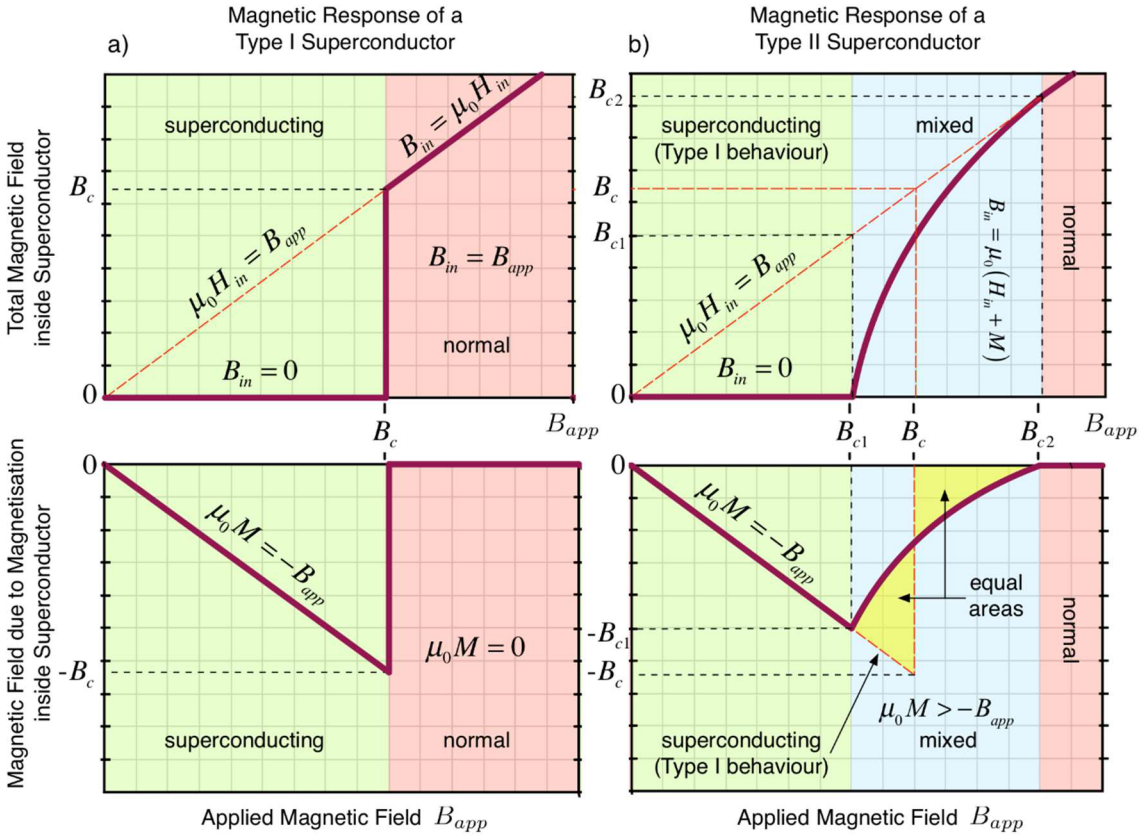

Figure 2.1: The reversible magnetic response of a) Type I and b) Type II superconductors. Adapted from [13].

The vortex lattice

The mixed state of Type II superconductors involves a progressive change in the number of penetrating (quantised) vortices within the bulk of the material. However, the two GL equations (2.11) and (2.13) can be used to reveal more of the behaviour of these vortices.

For an applied field strength, H_0, close to the upper critical field strength, H_{c2}, the solution to (2.11) will be very close to that of the linearised equation (2.29), and therefore the solution can be expanded as the linear combination [14]

$$\phi = \phi_L + \phi_1, \tag{2.35}$$

where ϕ_L is the solution to the linear equation (2.29).

Taking ϕ_L and ϕ_1 in (2.35) to be orthogonal, a general solution for ϕ_L is given by

$$\phi_L(x,y) = \sum_n C_n \exp(inky) \exp\left[\frac{-(x-x_n)^2}{2\xi^2(T)}\right] \tag{2.36}$$

with

$$x_n = \frac{n\hbar k}{2e\mu_0 H_{c2}} = nk\xi^2(T) \tag{2.37}$$

in which only linear combinations in (2.16) with periodic x and y are considered. This can be achieved by ensuring the constant C_n is periodic i.e.

$$C_{n+N} = C_n. \tag{2.38}$$

Substituting (2.16) into the second GL equation (2.13) yields

$$J_{Lw} = -\frac{e\hbar}{m}\frac{\partial}{\partial w}|\phi_L|^2, \tag{2.39}$$

where (2.39) represents two equations, one for $w = x$ and one for $w = y$. Further, the magnitude of the magnetic field generated by the supercurrent, $\mathbf{J}_L$, is given by

$$B_{\mathrm{J}_L} = -\frac{\mu_0 e\hbar|\phi_L|^2}{m}; \tag{2.40}$$

the significance of which is that the lines of constant $\mathbf{B}$ coincide with the lines of constant $|\phi_L|^2$, and that these lines are also the lines of current flow, $\mathbf{J}_L$ [14].

Equation (2.11) can be rewritten in terms of the correction term ϕ_1 in (2.35) and further consideration of the normalisation of the linear term ϕ_L leads to the equation,

$$\int \left(\frac{1}{2m}\phi_L^*(-i\hbar\nabla - 2e\mathbf{A}_{c2} - 2e\mathbf{A}_1)^2\phi_L + \alpha|\phi_L|^2 + \beta|\phi_L|^4\right) d^2\mathbf{r} = 0, \tag{2.41}$$

where $\mathbf{A}_{c2}$ is the vector potential of H_{c2} and $\mathbf{A}_1$ is a small correction vector potential.

Further manipulation of (2.41) leads to the equations

$$\langle|\phi_L|^2\rangle = \frac{m}{e\hbar}\frac{H_{c2} - H_0}{(2\kappa^2 - 1)\beta_A} \tag{2.42}$$

with

$$\beta_A = -\frac{\langle|\phi_L|^4\rangle}{(\langle|\phi_L|^2\rangle)^2} \tag{2.43}$$

and

$$\langle B\rangle = \mu_0 H_0 - \frac{\mu_0(H_{c2} - H_0)}{(2\kappa^2 - 1)\beta_A} \quad \Longrightarrow \quad M = -\frac{\mu_0(H_{c2} - H_0)}{(2\kappa^2 - 1)\beta_A} \tag{2.44}$$

The Gibbs free energy is proportional to β_A and therefore, low free energies are achieved with low β_A, which can be reduced to a minimum by letting $N = 2$ in (2.38) and setting $C_1 = \pm C_0$. The significance of this result is that the vortices that penetrate the mixed state form a triangular lattice (see Figure 2.2).

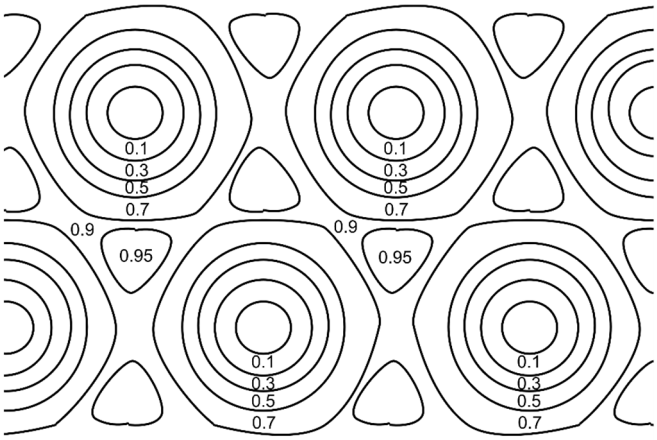

Figure 2.2: Level surface of $|\phi_L|^2$ showing the triangular flux line lattice [14].

Anisotropies

Some type II superconductors are anisotropic i.e. their critical field values are dependent upon the direction in which they are measured. It is therefore necessary to account for this within the Ginzburg-Landau theory. To achieve this it is necessary to consider each of the crystallographic axes separately by replacing the mass by an effective-mass tensor [15]. The principle axes of the tensor have elements m_i with $i = 1$ representing the *a*-axis, $i = 2$ representing the *b*-axis and $i = 3$ the *c*-axis. The elements are normalised so that $\mathrm{m}_1\mathrm{m}_2\mathrm{m}_3 = 1$ and the penetration depths and coherence lengths are written in terms of these normalised masses,

$$\lambda_i = \lambda(\mathrm{m}_i)^{\frac{1}{2}} \quad \Longrightarrow \quad \lambda = (\lambda_1\lambda_2\lambda_3)^{\frac{1}{3}}$$

$$\xi_i = \xi(\mathrm{m}_i)^{\frac{1}{2}} \quad \Longrightarrow \quad \xi = (\xi_1\xi_2\xi_3)^{\frac{1}{3}}$$

The relationship between the coherence length and the upper critical field is,

$$H_{c2} \approx \frac{\Phi_0}{2\pi\xi^2}$$

where Φ_0 is the flux quantum, and the relationship between the upper critical field and the coherence length along each of the crystallographic axes can be written,

$$H_{c2a} = \frac{\Phi_0}{2\pi\xi_b\xi_c} \quad H_{c2b} = \frac{\Phi_0}{2\pi\xi_a\xi_c} \quad H_{c2c} = \frac{\Phi_0}{2\pi\xi_a\xi_b}$$

In the case of tetragonal symmetry the lower critical fields along the *c*-axis and parallel to the ab-plane are then given by,

$$H_{c1}^{ab} = \left(\frac{\Phi_0}{4\pi\lambda_c\lambda_{ab}}\right)\left(\ln\left(\frac{\lambda_c\lambda_{ab}}{\xi_c\xi_{ab}}\right)^{\frac{1}{2}} + 0.5\right)$$

$$H_{c1}^{c} = \left(\frac{\Phi_0}{4\pi\lambda_c^2}\right)\left(\ln\left(\frac{\lambda_c^2}{\xi_c^2}\right) + 0.5\right).$$

Concluding comments

The Ginzburg-Landau theory describes a number of characteristics of superconductivity, such as the penetration depth, the coherence length, Type I field expulsion (and exclusion) as well as the Type II upper and lower critical fields, which are themselves separated by the mixed state.

2.2.3 The Bardeen-Cooper-Schrieffer theory of superconductivity

Introduction

In 1957 John Bardeen, Leon Cooper and Robert Schrieffer (BCS) published a microscopic theory of superconductivity that explained the mechanism responsible for the onset of the phenomenon [16]. Considering it took 46 years to get from the discovery of superconductivity to this microscopic explanation, it is easy to regard the BCS paper as a breakthrough, which has also been described by Tinkham as an "epoch-making" moment [17]. Furthermore, the Ginzburg-Landau phenomenological theory, so far largely ignored by the west due to the cold war and anti-communist feelings within Europe and the USA [18], was finally recognised and was eventually shown to be derivable from the BCS theory by Lev Gorkov [10].

BCS set out to explain five main superconducting characteristics, namely, the second-order phase transition at the critical temperature, the energy gap of individual particle-like excitations, the Meissner effect, infinite conductivity and the isotope effect. In the process, their theory predicted a penetration depth - in agreement with the London brothers' - and a coherence length - in broad agreement with the Ginzburg-Landau theory.

The isotope effect

The electric current flowing through a conductor is comprised of streams of electrons whose motions act against physical resistances that dissipate energy from the flow. This is the reason why a constant potential difference must be maintained across the ends of a normal conductor if the energy lost to the resistance is to be replenished and the current kept constant. The resistance in question is caused by the electrons inelastically bombarding the crystal lattice ions due to their own thermal agitation, the thermal agitation of the crystal lattice itself, and lattice imperfections and impurities. Good conductors are those materials in which these electron-ion bombardments are kept to an absolute minimum. However, good conductors do not necessarily make good superconductors. The best (conventional) superconductors are generally poor conductors in the *normal* state. This counterintuitive situation suggests that the physical structure of a superconductor must in some way be conducive to electron-ion interactions and that these interactions are a necessary feature of superconductivity.

The emphasis here is that electron-ion interactions must be involved in the onset of the superconducting state. If this is so, then a change in the mass of the crystal lattice ions should produce a change in the electron-ion interaction and likewise, a change in the onset of the superconducting state. This *isotope effect* has been observed experimentally and it has been shown that an increase in the nuclear mass corresponds to a decrease in the transition temperature, T_c, [19], according to the proportionality

$$T_c \propto \frac{1}{M^{\alpha}} \quad \text{with} \quad \alpha \approx \frac{1}{2}. \tag{2.45}$$

It should be noted that α varies depending upon the material in question.

Lattice vibrations, the formation of Cooper pairs and infinite conductivity

The characteristics of the vibrations of the crystal lattice ions depend on the nuclear mass of the ions themselves. Therefore, the isotope effect is related to the change in the crystal lattice vibrations. Also, as the temperature of a superconducting material is reduced towards the transition temperature, the thermal excitation of the crystal lattice is reduced, and consequently, the lattice ion vibrations are reduced. This decreased thermal agitation (of the electrons as well as the lattice) gives rise to a situation in which the electron-ion interaction suffers less disturbance because of the reduced number of scattering phonons (quantised packets of vibrational energy). In classical terms, some of the electrons at the Fermi surface slightly attract nearby lattice ions, through mutual Coulomb interaction, as they pass them by. This local deformation of the crystal lattice serves to surround an electron with positive charge and effectively screens its repulsion from other, more distant, electrons. Further, these distant electrons are then attracted to the same screening ions. Overall, the screening of one electron by the lattice ions, which then also attracts a more distant electron, is equivalent to the electrons being attracted to each other. As long as the temperature of the material is kept low enough to keep the lattice vibrations from disrupting this *virtual* attraction, the pair of electrons in question remain coupled together in what is called a Cooper pair.

This electron-electron attraction can also be regarded as being mediated by the exchange of virtual phonons between the participating electrons [10]. Further, the bond between the Cooper pair electrons is strongest when the electrons have equal and opposite momentum and opposite spin. This particular situation also ensures that the pair expresses boson behaviour i.e. their coupling does not adhere to the Pauli Exclusion Principle, and therefore, all Cooper pairs can occupy the same quantum state. It is this situation that ensures the Cooper pair state is a stable state below the transition temperature (and below critical applied fields). On a quantum mechanical basis, the uncertainty principle reveals that since the momentum of the Cooper pair electrons is well defined, their spatial positions are uncertain, and can lie within an extended region. The extended regions of all the Cooper pair electrons tend to overlap, and hence, the superconducting Cooper pairs act in unison in the same quantum state. This coherence makes it even more difficult for the superconducting state to be destroyed below critical fields and temperatures, and it is this that is responsible for the infinite conducting (zero resistance) behaviour; it also demonstrates microscopic quantum mechanical effects on a macroscopic scale.

Since the interaction between the Cooper pair electrons can be thought of as being a direct exchange of virtual phonons, the interaction can be modelled by [20]

$$V(\mathbf{k},\mathbf{k}',\mathbf{q}) = \frac{g^2\hbar\omega_{\mathrm{q}}}{\left(\varepsilon_{\mathrm{k+q}} - \varepsilon_{\mathrm{k}}\right)^2 - \left(\hbar\omega_{\mathrm{q}}\right)^2}, \tag{2.46}$$

where g is the interaction (phonon) coupling constant, ε_{k} is the energy of the electron state with wavenumber $\mathbf{k}$, and $\hbar\omega_{\mathrm{q}}$ is the phonon energy. Equation (2.46) shows that for $\left|\varepsilon_{\mathrm{k+q}} - \varepsilon_{\mathrm{k}}\right| < \hbar\omega_{\mathrm{q}}$ the interaction potential is negative i.e. the electrons *attract* each other.

In formulating their theory, BCS simplified equation (2.46) to

$$V_{\mathrm{kk'}} = \begin{cases} -V & for\ |\varepsilon_{\mathrm{k}}| < \hbar\omega_{\mathrm{D}} \\ 0 & \text{otherwise} \end{cases}, \tag{2.47}$$

where $\hbar\omega_{\mathrm{D}}$ is the Debye energy of lattice phonons. They then proceeded to solve the Schrodinger equation for two electrons that are subject to the potential (2.47).

The energy gap, the isotope effect and the transition temperature

The presence of an energy gap is what gives superconductivity stability below the transition temperature and in applied fields below their critical magnetic fields. Initially, in the *normal* state, all the energy levels below (and including) the Fermi level are occupied by electrons adhering to the exclusion principle. However, the onset of superconductivity gives rise to the formation of Cooper pairs with combined energies that lie below the Fermi surface energy; hence, their formation is energetically favourable and the normal electrons are said to be unstable to Cooper pair formation. Further, the minimum energy required to destroy a Cooper pair by separating the constituent electrons is equal to twice the difference between the Fermi surface and the Cooper pair energies (2Δ). This means that the total energy gap is centred at the Fermi surface.

BCS solved the Schrodinger equation (for the potential (2.47)) for the energy eigenvalues and derived two expressions

$$|\Delta| = 2\hbar\omega_D \exp\left[-\frac{1}{N(0)V}\right] \tag{2.48}$$

$$k_B T_c = 1.14\hbar\omega_D \exp\left[-\frac{1}{N(0)V}\right], \tag{2.49}$$

where Δ is the energy gap from the Fermi surface, $\hbar\omega_D$ is the Debye energy of lattice phonons, $N(0)$ is the density of energy states at the Fermi surface and V is the interaction potential in accord with (2.47). Dividing equation (2.48) by (2.49), rearranging and multiplying by two yields

$$2\Delta(0) = 3.52 k_B T_c. \tag{2.50}$$

This is in good agreement with experiment [20].

Equation (2.48) is interesting for another reason. It reveals a proportionality between the energy gap Δ and the phonon energy $\hbar\omega_D$. Further, ω_D is related to the atomic mass of different isotopes,

and therefore, through equation (2.50), we see that Δ is related to the transition temperature T_c. The significance of this is that the transition temperature is related to the isotopic mass, and hence, the isotope effect (2.45) is predicted by the BCS model. Likewise, equation (2.49) also predicts the transition temperature, T_c.

Specific heat

The BCS theory also predicts the specific heat of a superconductor in accord with the following equation

$$C = 2\beta k \sum_k -\frac{\partial f_k}{\partial E_k}\left(E_k^2 + \frac{1}{2}\beta\frac{d\Delta^2}{d\beta}\right), \tag{2.51}$$

where,

$$\beta = \frac{1}{kT}, \tag{2.52}$$

$$f_k = \frac{1}{1 + exp(\beta E_k)}, \tag{2.53}$$

$$E_k = \sqrt{\xi_k^2 + \Delta(T)^2}, \tag{2.54}$$

E_k is the temperature dependent set of fermion excitation energies [21].

The Meissner effect

BCS formulated a Hamiltonian based on the Cooper pairing mechanism. This Hamiltonian can be made complex to give

$$H_{BCS} = \frac{1}{2}\int d^3r \times \int d^3r' \Psi_\alpha^\dagger(\mathbf{r}') H_{\alpha\beta}(\mathbf{r}', \mathbf{r}) \Psi_\beta(\mathbf{r}) \tag{2.55}$$

in which case Bogoliubov amplitudes are the components of the eigenvectors of $H_{\alpha\beta}(\mathbf{r}', \mathbf{r})$ [22]. These Bogoliubov amplitudes satisfy a coupled set of equations which can be used in conjunction with the initial condition that the vector potential $\mathbf{A} = \mathbf{0}$ (where $\mathbf{B} = \mathrm{curl}(\mathbf{A})$). The outcome, after some manipulation, is that the average current density induced by the applied field is [22]

$$\langle \mathbf{J}(\mathbf{r}) \rangle = -\frac{e^2 n_s}{m}\mathbf{A}(\mathbf{r}), \tag{2.56}$$

where n_s is the super electron density.

Taking the curl of (2.56) gives

$$\text{curl}(\mathbf{J}) = -\frac{e^2 n_s}{m}\text{curl}(\mathbf{A}) \quad \Longrightarrow \quad \text{curl}(\mathbf{J}) = -\frac{e^2 n_s}{m}\mathbf{B} \quad \Longrightarrow \quad \text{B} = -\mu_0 \lambda_L^2 \text{curl}(\mathbf{J}) \qquad (2.57)$$

i.e. Londons' equation (2.2) complete with the penetration depth λ_L.

The BCS model therefore correctly predicts the current density that flows in an applied field, which in turn explains the Meissner effect.

Concluding comments

The BCS model gives a detailed account of the mechanism responsible for the onset of superconductivity and has explained why some materials are superconducting while others are not. It has also provided experimentalists with predictions that can be tested, namely, the transition temperature, the energy gap, the isotope effect, the specific heat and the current density induced by applied fields. In the process it explains the Meissner effect and perfect conductivity.

2.3 High temperature superconducting materials

High temperature superconductivity was first discovered by Bednorz and Muller in a lanthanum-barium-copper oxide superconductor in 1986. Their material had a transition temperature of 30 K [23]. This discovery was, however, quickly followed by Wu *et al*. in 1987 who produced an yttrium-barium-copper oxide (YBCO) superconductor with a transition temperature close to 93 K [24]. Not only was this the warmest superconductor by a substantial margin but more importantly, it was the first superconductor to have a transition temperature above the temperature of liquid nitrogen (77 K). In 2005 thallium-barium-calcium-copper oxide was found to have a transition temperature of 138 K by Dai *et al* [25]. As of February, 2015, this still stands as the highest transition temperature at atmospheric pressure [26].

The two most widely investigated high temperature superconductors, with a view to real world applications, are YBCO and bismuth-strontium-calcium-copper oxide (BSCCO). These belong to a group of superconductors called cuprates that signifies their copper oxide content. It is the electrons (or holes) within these copper oxide planes that are thought to be paired by a non-phonon mediated pairing mechanism that has so far eluded discovery [27].

2.4 Critical current density – Bean's model and losses

2.4.1 Introduction

In 1964 Charles P. Bean published a very simple model that successfully describes hysteretic behaviour in inhomogeneous Type II superconductors [28] i.e. Type II superconductors with granular/polycrystalline microstructures. The model's greatest utility is its ability to reveal the critical current density, J_c, of these types of superconductor from magnetisation measurement

data. The main benefit of this is that magnetisation data are collected in a contactless way; not only removing the need to make four-terminal contacts to the sample but also removing the need to drive transport current through the sample (which could introduce Joule heating at the contact points). This facility, in conjunction with the model's simplicity, makes it the most widely used model of its kind.

2.4.2 Bean's model

The low-field case

In understanding Bean's model it is first helpful to describe the way in which magnetic flux moves into a Type II superconductor. In this description we set the initial conditions so that the superconductor has been cooled to below its transition temperature, T_c, in *zero* applied magnetic field, providing certainty of its history and that internally it is field-free throughout. We now apply a small external magnetic field that causes magnetic flux to begin to enter the bulk of the sample. The inhomogeneity of the sample provides pinning centres that are energetically favourable sites for flux vortices to occupy. These pinning sites stop flux from moving freely and therefore cause flux flow to be *viscous* with stronger pinning leading to greater viscosity. This pinning means flux vortices only enter the material up to a limited depth, dependent upon the physical size of the sample, the applied field, the nature of the pinning and the characteristics of the superconductor. In this condition there remains a central field-free region.

As the applied magnetic field is increased further, an increased density of flux vortices push their way into the superconductor from the outside surface. This causes the existing lower density flux vortices, which are already within the sample, to be pushed deeper into the bulk, further reducing the size of the central field-free region. For sub-millimetre sized samples only very small applied fields (mT) are necessary to cause flux to reach the sample's centre, which means no field-free region remains. This state is called the *upper limit of the low-field case* or more helpfully, the *intermediate field*, B^*, which is shown in Figure 2.3.

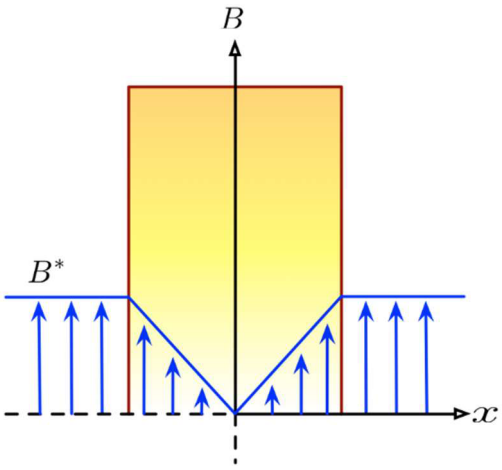

Figure 2.3: The *intermediate* field, B^*. This is the value of the applied field when magnetic flux just reaches the centre of a superconducting sample.

The description so far has explained that flux pinning is the mechanism responsible for producing a flux gradient within the superconductor. We now pause this description to look at Bean's assumptions.

Bean's assumptions and the relationship between the internal field and the critical current density

In Figure 2.4a, a strong magnetic field (well above the intermediate field) has been applied to a small sample (the cross-section of which is depicted in the figure). We have seen that flux pinning is responsible for the depth dependent decreasing flux density and we will now see that the *linear* magnetic field gradient (shown in the figure) is a consequence of the assumptions made by Bean in devising his model. These assumptions are;

(1) wherever screening currents flow, they do so at the critical current density $\pm J_c$,

(2) the critical current density, J_c, is independent of magnetic field,

(3) the lower critical magnetic field, B_{c1}, can be set to *zero* with no loss to the validity of the model i.e. B_{c1} is ignored,

(4) the penetration depth, λ, can be set to *zero* with no loss to the validity of the model i.e. λ is ignored.

Bean also set the simplifying condition that there is only a *z*-component of magnetic field and he ignored currents travelling in the *x*-direction.

On use of Ampere's law (equation (2.4)) and Bean's assumptions, a general magnetic field profile is given by

$$B_z(x) = \pm\mu_0 J_c x + C. \tag{2.58}$$

This says that there is a *linear relationship* between the field, B_z, and position, x, within the superconductor and that the critical current density, J_c, determines the *gradient* of the relationship. Figure 2.5 exemplifies this relationship for the field profiles shown in Figure 2.4.

The high-field case, flux shielding/trapping, and the cause of hysteresis

We now continue to describe the internal field profile as further, small, increases in the applied field are made. In this scenario the magnetic field gradient within the material remains unchanged. This is depicted in Figure 2.4a to Figure 2.4b, for example. Qualitatively it can also be seen in these figures that the average magnetic field within the material is less than the applied field. This means that the bulk is being *shielded* from magnetic flux. The figures also show that once flux has reached the sample's centre, increasing the external field increases the internal field by the

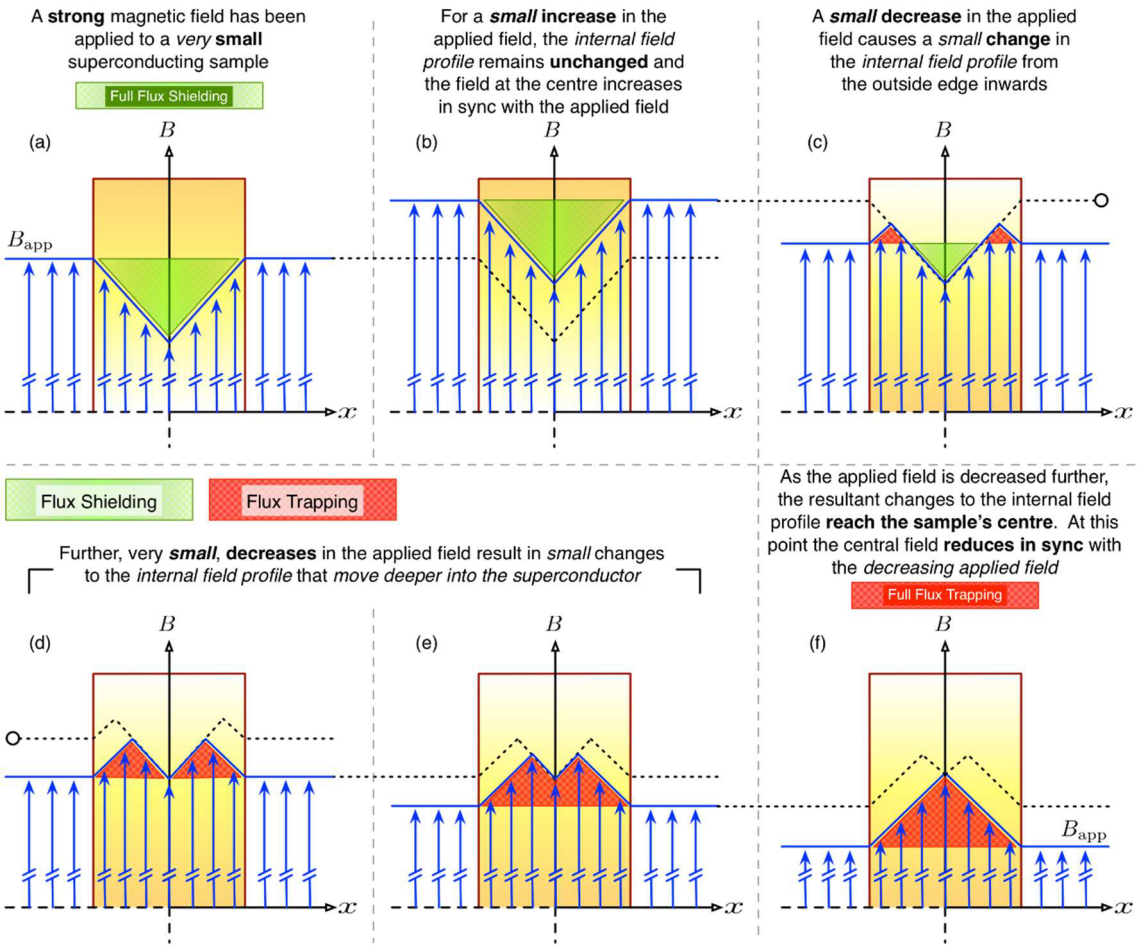

Figure 2.4: Effect of a strong applied magnetic field on a Type II superconductor as the field strength is changed; (a) full flux shielding, (b) small increase in the applied field, (c) a small decrease in the applied field (causes flux trapping to begin), (d) to (f) further decreases in the applied field increase the amount of trapped flux and decreases the amount of shielded flux.

same amount, all the way to the centre (Figure 2.4b) i.e. the intercept in (2.58) increases. In reality, increases to the applied field will noticeably change the shape of the internal field profile, since J_c is actually field dependent, with the effect being more pronounced in larger samples and/or with larger steps in applied field. However, Bean's simplifying assumptions remove this greater detail without reducing the validity of the model.

So far only increasing fields have been discussed. We now turn our attention to small reductions in the applied field (see Figure 2.4c). The influence of this change acts from the superconductor's outside surface inwards – as has been the case so far. This is an important point – all field changes are generated at the material's outer surface. If the field is held constant at any intermediate stage then the field profile will remain steady (ignoring flux creep and jumping). Figure 2.4c also reveals another consequence of changing from increasing to decreasing applied field, namely, *flux trapping*. On inspection of Figure 2.4c it can be seen that, not only is there less *shielded* flux than that in Figure 2.4b, but the change to the internal field profile has caused flux to be *trapped* in a region that begins at the inside surface of the sample. This *flux trapping* coincides with a change in sign of the field gradient in accordance with equation (2.58). It is also

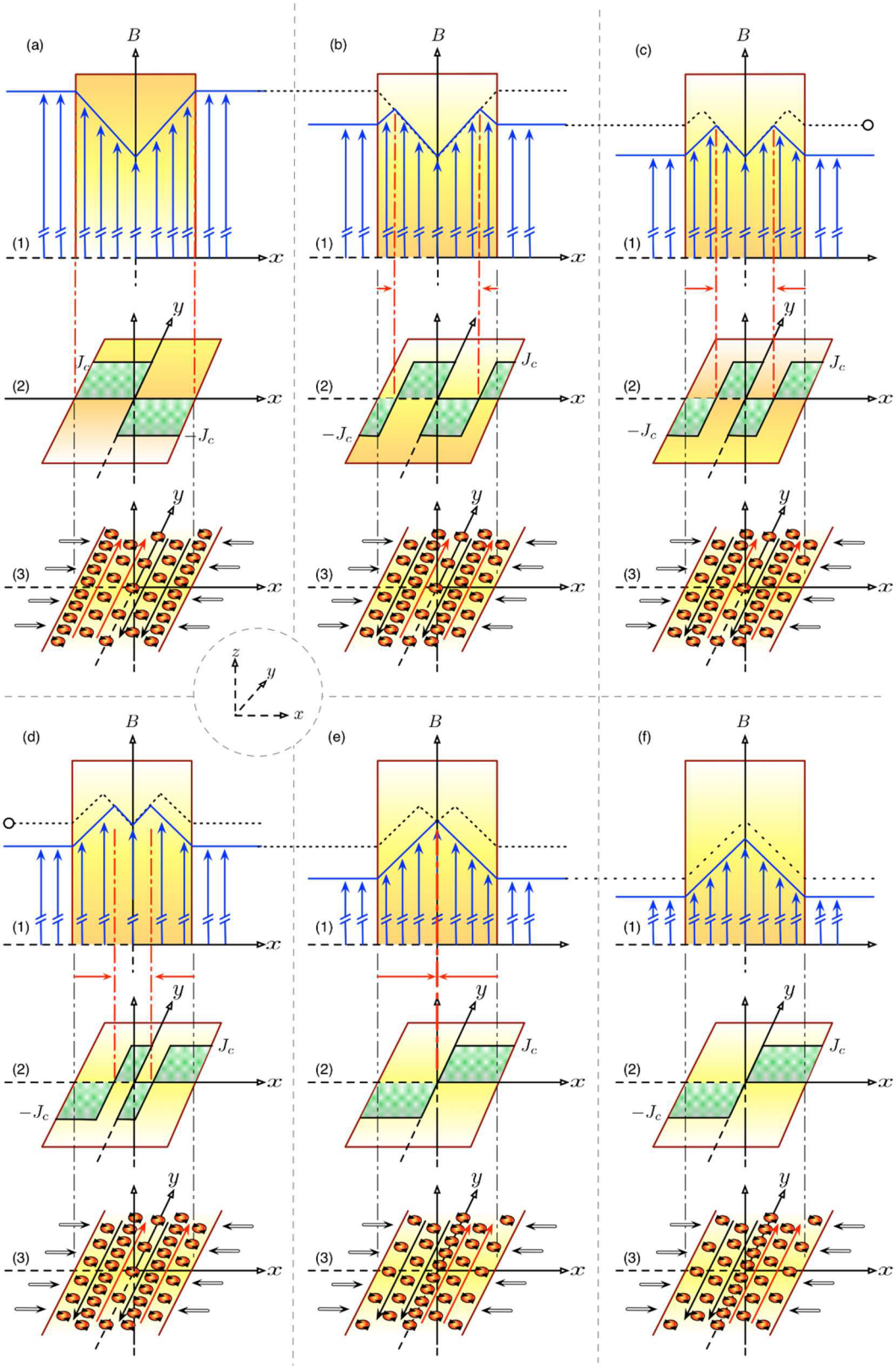

Figure 2.5: Relationship between the magnetic field profiles from Figure 2.4 ((a1) to (f1)) and the critical current density ((a2) to (f2)). It can be seen in (b2) to (e2) that flux trapping and shielding is accompanied by alternately opposing screening currents in each half of the infinitely long slab, which is determined by the sign of the flux density gradients in (b1) to (e1). (a3) to (f3) are a simplified illustration of flux vortices entering the slab from the outside surface and moving inwards.

evident that the total amount of *trapped flux* is less than the *shielded flux* and so the average internal field is still less than the applied field at this stage in the description.

As further reductions to the applied field are made, the total amount of trapped flux increases as the total amount of shielded flux decreases. In Figure 2.4d there is no shielded flux and it is easy to see that the average internal field is now greater than the applied field. Eventually, further reductions in applied field result in a *maximum* amount of trapped flux (see Figure 2.4f), which can be seen to occupy the same area as the maximum amount of shielded flux in Figure 2.4a.

So, a basic answer to what causes hysteresis in Type II inhomogeneous superconductors is that flux pinning stops the motion of flux vortices, with all causal changes originating at the outside surface of the sample. Also, the internal average magnetic field differs from the applied field as the applied field is changed and this explains why the magnetisation of a superconducting sample depends on its previous magnetic state i.e. its history. However, the major point to remember from this section is that, no matter what the actual shape of the trapped (or shielded) flux profile happens to be, as long as the applied field is cycled through fields that are larger than the intermediate field, then we can be certain that *maximum* trapping and shielding has occurred. Bean's major insight was in realising that this maximum trapping and shielding, in conjunction with knowledge about the sample's geometry, is all that is required to find the sample's critical current density.

Obtaining the critical current density – the model's greatest utility

We have seen that flux *shielding* and *trapping* ensure that the average internal magnetic field, $\langle B_{\mathrm{int}} \rangle$, differs from the applied field, B_{app}, throughout most of a field-swept cycle. The magnetisation of the sample at any point throughout this cycle is given by

$$\mu_0 M = \langle B_{\mathrm{int}} \rangle - B_{\mathrm{app}}. \tag{2.59}$$

As is shown in Figure 2.3 the value of the applied field necessary to make magnetic flux just reach the centre of the sample is B^* (the *intermediate* field). Therefore, for maximum internal shielding the average internal field is related to the intermediate field by

$$\langle B_{\mathrm{int}} \rangle = B_{\mathrm{app}} - \frac{1}{2} B^*, \tag{2.60}$$

where B_{app} is some large (in comparison to B^*) applied field. In the case of *maximum* flux *trapping* it is related to the intermediate field by

$$\langle B_{\mathrm{int}} \rangle = B_{\mathrm{app}} + \frac{1}{2} B^*. \tag{2.61}$$

Substitution of (2.60) into (2.59) yields

$$\mu_0 M_- = -\frac{1}{2}B^* \tag{2.62}$$

and substitution of (2.61) into (2.59) yields

$$\mu_0 M_+ = \frac{1}{2}B^*, \tag{2.63}$$

which suggests that

$$M_+ - M_- = \frac{B^*}{\mu_0}. \tag{2.64}$$

Comparison of Figure 2.5 (a3) to (f3) highlights that the greatest density flux lines move into the centre of the slab as the applied field is reduced.

The magnetic moment, $|\mathbf{m}| = m$, of an arbitrarily shaped sample can be found through the volume integral

$$\mathbf{m} = \frac{1}{2}\int_V \mathbf{r} \times \mathbf{J}(\mathbf{r}) d^3\mathbf{r}, \tag{2.65}$$

which for the slab shaped sample in Figure 2.6 yields the magnitude

$$m = \frac{1}{2}Ja_2\left(1 - \frac{a_2}{3a_1}\right)V, \tag{2.66}$$

where V is the slab's volume.

Substituting for $J = J_c$ in (2.66) and taking into account the relationship between magnetisation and magnetic moment, $M = m/V$, (2.66) becomes

$$M = \frac{1}{2}Ja_2\left(1 - \frac{a_2}{3a_1}\right) \tag{2.67}$$

and substitution of this into (2.64) yields

$$M_+ - M_- = \Delta M = J_c a_2\left(1 - \frac{a_2}{3a_1}\right) \quad \Longrightarrow \quad J_c = \frac{\Delta M}{a_2\left(1 - \frac{a_2}{3a_1}\right)}. \tag{2.68}$$

Therefore, the critical current density, at any particular applied field within a sample's hysteresis loop, can be calculated from a measurement of the change in magnetisation at that applied field. Equation (2.68) is good for a slab shaped sample but other geometries are calculable on application of equation (2.65) to the specific case in question.

The beauty of Bean's model is that it cuts through the complexities of hysteretic behaviour to reveal a very simple relationship between the change in magnetisation at a particular field and the critical current density at that field. Only knowledge of a sample's geometry, in conjunction with a set of hysteresis data, are required to obtain J_c.

Other critical state models

Bean's model is just one of a collection of so called *critical state* models. However, whereas Bean's model makes no attempt to fit to hysteresis data (its sole purpose being to determine J_c), the motivation for these other models is in their ability to model the field dependence of whole datasets. The commonality between all of the models is the equality between the pinning force density $\mathbf{F}_p$, that holds the magnetic flux lines in place, and the Lorentz force density $\mathbf{J} \times \mathbf{B}$, that is generated through the interaction between the supercurrent and the magnetic flux lines.

2.4.3 Concluding comments

While Bean's model does not provide a microscopic understanding of hysteresis in superconductors or is able to reproduce the shape of magnetisation data for a sample cycled through large magnetic fields, its power is in its ability to simply obtain critical current density, at any particular field, from a sample's magnetisation data.

Bean's assumptions are clearly very simple and are extremely successful at satisfying their purpose but other researchers, such as Kim, have added greater degrees of complexity to fit whole experimental datasets. However, in regard to the determination of J_c specifically, these other models do not offer anything that Bean's more simple model does not provide and this has ensured it still remains the most widely used model of its kind.

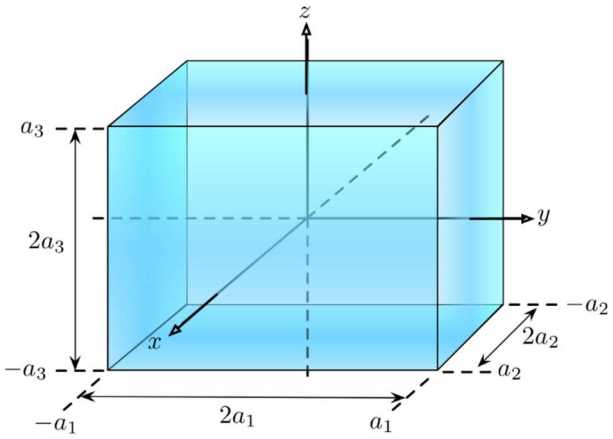

Figure 2.6: The geometry of a slab shaped sample.

2.5 Microcrystalline and nanocrystalline superconductors – important length scales

2.5.1 A review of the important superconductors

There are *two* main classes of superconductors; Type I and Type II. The elemental superconductors are mostly of Type I but those materials important for applications are all of Type II. The conventional superconductors are mostly low temperature i.e. superconductors with a transition temperature below ~ 30 K, with the possible exception of MgB_2, which has a transition temperature of ~ 37 K. Conventional superconductors provide the vast majority of materials used in modern day applications, such as MRI scanners, fusion tokamaks (ITER) and particle accelerators, for example. The major workhorse materials are Nb_3Sn and NbTi, which have respectable upper critical fields and critical current densities (see Table 2.1).

The unconventional superconductors are those with high critical temperatures and are not explained by BCS theory. They are mostly Type II in nature but have so far evaded major utilisation in applications because of the engineering difficulties involved in forming high-field magnetic coils with them. However, the benefits of high-temperature superconductivity in applications are too high to simply remain with the conventional workhorses discussed above, and therefore, there is a huge amount of research work going into the unconventional materials. The National High Magnetic Field Laboratory in Tallahassee, Florida, are experts in the manufacture and operation of very high field magnets using low temperature and high temperature superconducting materials as well as conventional resistive materials. They currently hold a number of world records including one for the highest sustained magnetic field of 45 T using a hybrid superconducting/resistive design [29].

2.5.2 A review of Taylor and Byrne work

A new paradigm for fabricating bulk high-field superconductors

In 2008 David Taylor of the Superconductivity Group in Durham, UK, published a paper entitled “A new paradigm for fabricating bulk high-field superconductors” in which he presented a record value of the upper critical field of elemental niobium (~ 3 T) [30]. Taylor used mechanical ball milling to reduce the niobium powder grain size from ~ 100 nm to between 6 and 15 nm in four independently milled samples using niobium milling media to reduce foreign contamination. He then exposed *three* of these samples to a pressure of 2000 bar and a temperature of 450, 600 and 750 °C respectively for up to 5 h using a hot isostatic press (HIP). This materials processing was employed to manipulate and control the degree of crystalline disorder, which resulted in each sample having a substantially increased *normal* state resistivity, ρ_n, in comparison to the as-supplied material. The sample milled for 69 h and HIPed at 450 °C showed the largest increase in $B_{c2}(0)$ from 0.57 T to 3.00 T with a depression in T_c from 9.14 to 7.11 K.

Table 2.1: Some of the best high-field superconducting materials.

Material	T_c (K)	B_{c2} (T)
---------- Low Temperature ----------		
Nb_3Sn [31]	18	25
Nb_3Ge [32]	23.2	37
Nb_3AlGe [33]	~21	~44
Nb3Al [33]	~ 18.5	~33
Nb_3Ga [33]	~20	~35
Nb-Ti [32]	9.5	13
Nb-N [32]	16	15
$NbC_{0.3}N_{0.7}$ [34]	17.6	11
Nb-C	11.1[35]	16.9 [36]
V_3Ga [32]	15	23
V_3Si [32]	16	23
$Gd_{02}PbMo_6S_8$ [33]	~14	~61
MgB_2 [31]	36.7	14
---------- High Temperature ----------		
$YBa_2Cu_3O_{7-\delta}$ [37]	92.4	34 (along *c*-axis)
$Bi_2Sr_2Ca_2Cu_3O_{10+\delta}$ [38-40]	110	39 (along *c*-axis)
$Tl_2Ba_2Ca_2Cu_3O_{10}$ [38, 41, 42]	120	28 (along *c*-axis)

Taylor went on to propose a model that delivers the "ultimate limit to the increase in $B_{c2}(0)$" that a conventional superconducting material could be made to have in order to aid the selection of likely high-field nanocrystalline superconductors for applications. This model is based on established microscopic theory and Taylor's proposition that there is a proportionality between the electron-phonon coupling parameter, λ (which describes the strength of the attractive electron-phonon interaction), and the unrenormalised density of states at the Fermi surface, $N(E_F)$. The relationship between $B_{c2}(0)$ and ρ_n is provided by Ginzburg-Landau-Abrikosov-Gorkov (GLAG) theory

$$B_{c2}(0) = 0.973\sqrt{\mu_0}\kappa^* R^{-1}\left[7.3\times10^{37}\eta_{\text{clean}}\left(\frac{\gamma T_c}{S}\right)^2 + 2.78\times10^{6}\eta_{\text{dirty}}\gamma T_c\rho_n\right], \quad (2.69)$$

where κ^* is the ratio of the Ginzburg-Landau parameter at 0 K to that at T_c, γ is the Sommerfeld constant, S is the Fermi surface area, R is the Gorkov function

$$R(\lambda_{\text{tr}}) = \left[\frac{\left(\frac{\pi^2}{8.414}\right)-1}{2}\right](\tanh(-0.04\log(\lambda_{\text{tr}})^2 + 1.07\log(\lambda_{\text{tr}}) - 0.83) + 1) + 1 \quad (2.70)$$

with

$$\lambda_{\text{tr}} = 3.81\times10^{-32}\frac{S^2\rho_n}{\gamma T_c} \quad (2.71)$$

and

$$\eta_{\text{clean}} = 1 - 2.7\left(\frac{T_c}{\omega_{\ln}}\right)^2 \ln\left[\frac{1}{20\left(\frac{T_c}{\omega_{\ln}}\right)}\right] \quad (2.72)$$

$$\eta_{\text{dirty}} = 1 - 1.5\left(\frac{T_c}{\omega_{\ln}}\right) + 2\left(\frac{T_c}{\omega_{\ln}}\right)^2 \ln\left[\frac{1}{0.08\left(\frac{T_c}{\omega_{\ln}}\right)}\right] \quad (2.73)$$

are necessarily included to modify the original GLAG theory for superconductors with strong electron-phonon coupling. $\omega_{\ln}$ is a phonon moment i.e. a particular expectation value of the electron-phonon spectrum function. The broadening of the unrenormalised density of states, $N(E_F)$, by increases in normal state resistivity, ρ_n, is incorporated into the model by fitting a Lorentzian with half-width E_0 to the normal state density of states at the Fermi surface, $N_0(E_F)$, and then using another Lorentzian function of half-width dependent on ρ_n to model the actual broadening, which lead to

$$N(E_F) = N_0(E_F)\left(\frac{\left(4/\pi\right)\left(\hbar/\tau E_0\right)\tan^{-1}\left(\hbar/\tau E_0\right) - 1}{\left(\hbar/\tau E_0\right)^2 - 1}\right) \quad (2.74)$$

with

$$N_0(E_F) = \frac{3\gamma}{2\pi^2 k_B^2(1+\lambda)} \quad (2.75)$$

and

$$\tau = \frac{1.65 \times 10^{19}\gamma}{S^2\rho_n}, \tag{2.76}$$

where τ is the mean scattering time. The link between equation (2.69) and (2.74) is provided by the Allen and Dynes equation relating the transition temperature to the electron-phonon coupling parameter, λ

$$T_c = \frac{\hbar\bar{\omega}_1}{1.20k_B}\exp\left(-\frac{1.04(1+\lambda)}{\lambda-\mu^*[1+0.62\lambda]}\right), \tag{2.77}$$

where μ^* is the Coulomb pseudopotential, which accounts for the Coulomb repulsion that exists between electrons, and $\bar{\omega}_1$ is another characteristic phonon moment of the spectrum function. Equation (2.77) is related to $N(E_F)$ through the Sommerfeld constant γ, which is itself related to $N(E_F)$ through

$$\gamma = \frac{2}{3}\pi^2 k_B^2 N(E_F)(1+\lambda), \tag{2.78}$$

which is a rearrangement of (2.75) followed by a substitution of $N_0(E_F)$ for $N(E_F)$ and is the essence of Taylor's assumption. Equation (2.75) essentially represents a scattering-free state.

In Taylor's model, provided by equations (2.69) to (2.78), increases in disorder produce increases in electron scattering that lead to increases in ρ_n. These increases in ρ_n cause direct increases in $B_{c2}(0)$ (eq. (2.69)) but also cause decreases in $N(E_F)$ due to the broadening caused by scattering events (eq. (2.74)). This broadening then decreases γ (eq. (2.78)) and T_c (eq. (2.77)), which both then act to directly influence $B_{c2}(0)$ (eq. (2.69)). This competition between the *lowering* influences of T_c and γ on equation (2.69), against the *heightening* influence of ρ_n on (2.69) produces a *maximum* in $B_{c2}(0)$ as a function of T_c.

Taylor applied this model to niobium and to Nb_3Sn using parameter values readily obtainable from the literature and compared it against his experimental data for niobium and Orlando's for Nb_3Sn. These plots are shown in Figure 2.7. Taylor points out that the maximum $B_{c2}(0)$ predicted by the model for both materials is reasonable and close to experiment. However, the curves shown in Figure 2.7 are not closely matched by the data points for either material. The model's applicability is restricted by Taylor's reliance on the broadening of the density of states at the Fermi energy, which requires that the materials being modelled must have a peak in the normal state density of states at the Fermi Energy. If this peak exists off centre, then the broadening could actually result in an increase in the density of states at the Fermi energy, which would reverse the relationship that T_c and γ has with ρ_n, possibly leading to unphysical results. Nevertheless, for those materials that do have a peak at the Fermi energy in the density of states, the model is a promising development with real practical advantages.

Ab-initio calculations of the thermal and electronic properties of superconductors and their grain boundaries

An understanding of grain boundaries in superconducting materials is of great importance since increases in $B_{c2}(0)$, caused by reductions in grain size, inevitably lead to an increase in the concentration of boundaries. It is these boundaries that are overwhelmingly responsible for trapping flux vortices, which allows the flow of supercurrents in Type II superconducting materials. So, not only is the presence of boundaries *indirectly* responsible for a superconductor's ability to accommodate transport currents, but those currents are *directly* affected by the barriers that these boundaries present. The Superconductivity Group in Durham is using density functional theory (DFT) in conjunction with a specialist software package called CASTEP to model the electronic and thermal properties of grain boundaries in superconductors. This research is currently being done by Peter Byrne.

Applying the time independent many body Schrodinger equation (TI-MBSE) to a system of electrons and nuclei in a crystal lattice results in an equation whose solutions are obtainable, at least in theory. In practice, however, the computational resources required are not obtainable. It is therefore necessary to make some simplifying assumptions that approximate the solutions being sought. For instance, because of the difference in the mass of an electron and a nucleus, the electrons can be regarded as moving within a fixed *nuclear* potential. This is called the Born-Oppenheimer approximation. Further reductions in complexity are made on use of the Hohenberg Kohn Theorems that allow the minimum energy of the system to be found by varying the ground

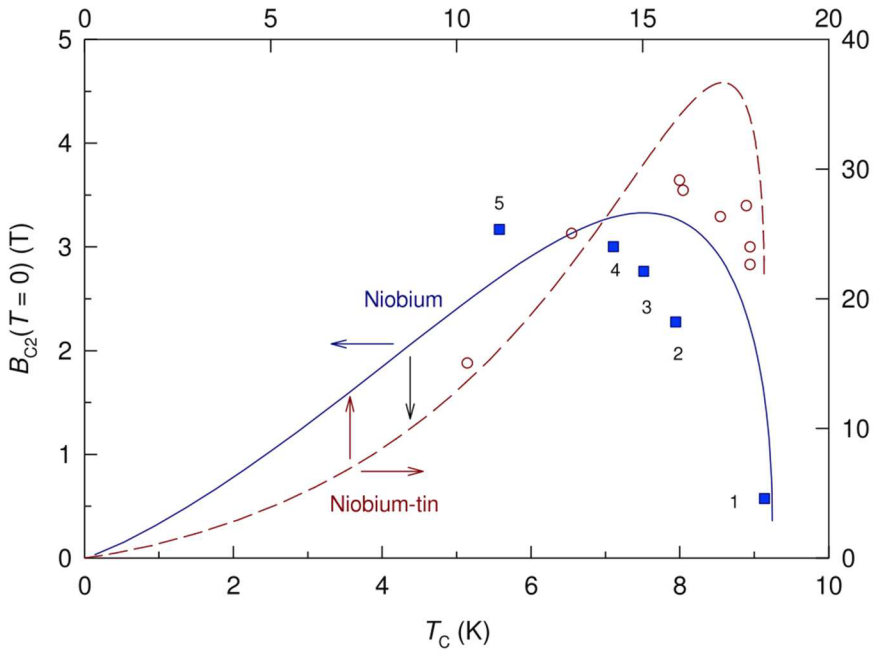

Figure 2.7: Theoretical upper critical field of nanocrystalline niobium and niobium–tin. Upper critical field as a function of critical temperature for niobium and niobium–tin with different levels of disorder. The lines show the theoretical values obtained by increasing the resistivity. The symbols show the experimental data of the five samples prepared by Taylor [30].

state density. However, it is the Kohn-Sham equations that fully allow the one *n*-body TI-MBSE to be satisfactorily transformed into a set of *n* one-body equations, which not only can be solved using available computing resources, but on application of Bloch's Theorem, can be dramatically decreased in quantity, further reducing the computational overhead.

DFT is being used in conjunction with the Coincidence Site Lattice model, to model low energy grain boundaries between unit cells of Au and Nb_3Sn. Gold is a very well researched material and therefore it serves as a quality test for similar calculations performed on less researched materials. The density of states over a range of energies about the Fermi energy for boundaries of varying angle are being generated and compared against similar calculations done on the same materials doped with various impurity atoms.

Calculations on bulk materials are also being performed to calculate electron-phonon constants and Eliashberg spectral functions. These calculations can then be used to obtain transition temperatures, heat capacities, resistivities and thermal conductivities. Furthermore, from the calculated electron-phonon constant λ, a value of transition temperature T_c, (acquired from calculation or susceptibility data) and a value of the phonon moment $\bar{\omega}_1$ (calculated from heat capacity data), equation (2.77) can be used to obtain a value for the Coulomb pseudopotential μ^*, for any of the superconductors studied. Initially, this work has been restricted to copper, aluminium, silver, lead and niobium with a view to extending it to binary Nb_3Sn (and possibly MgB_2) and ternary NbC_xN_{1-x} in the near future.

2.5.3 Concluding comments

If the applicability of Taylor's model can be extended to a greater number of materials, it would exceptionally enhance our ability to select those materials worthy of further investigation, which could lead to new "workhorse" materials.

Byrne's use of DFT to determine *normal* and *superconducting* state properties of superconductors could be used to provide the necessary parameter values required of Taylor's model so that the prospects of other materials for applications could be investigated. Furthermore, if Byrne can successfully model the grain boundaries in superconductors, and determine their electrical and thermal properties, then, in a similar fashion to Taylor's work, grain boundaries could be engineered to improve critical current densities, for example.

2.6 The road to ITER

On November the 19th and 20th of 1985 Ronald Reagan and Mikhail Gorbachev, both leaders of their respective superpower nations, met face-to-face for talks that signified the beginning of the end of the "cold war". This meeting, now widely known as the "Geneva Summit", mainly concentrated on diplomatic relations and the nuclear arms race but in a summary speech to the American people on the 21st of November, 1985, Ronald Reagan reported that,

> "*as a potential way of dealing with the energy needs of the world of the future, we have also advocated international cooperation to explore the feasibility of developing fusion energy*"[43].

Although this statement, and in particular the term "*developing fusion energy*", was by no means the highlight outcome of the summit, history might just judge this to be the Summit's greatest success. The foresight expressed by the two leaders that "*dealing with the energy needs of the world of the future*" was important enough to merit their cooperation, not only at such an early stage in their defrosted relationship, but also much before the term "green energy" had become the media soundbite it is today, is astounding… and fortunate. The Geneva Summit therefore channelled the disparate nuclear fusion efforts of both superpowers towards what would become the International Thermonuclear Experimental Reactor (ITER), an international project currently being built in Cadarache, southern France.

2.6.1 ITER and sustained nuclear fusion

The ITER project is an immensely complicated and expensive undertaking that requires the cooperative organisation, funding, expertise, design and building effort of an international community including China, the European Union, India, Japan, South Korea, Russia and the United States of America. It will be the first experimental attempt at producing a *net* energy gain from sustained fusion reactions between deuterium and tritium [44]. Although the primary aim of the project is to achieve a Q (ratio of output energy to input energy) equal to or greater than a factor ten (50 MW *in*, 500 MW *out*), nuclear fusion has never been used as an energy source before and the ITER project is no different in this respect. The surplus energy gained will actually be wasted to the atmosphere through cooling towers that will remove the heat from the blanket walls of the tokomak. However, the information and skills developed during the experiment will facilitate the next step fusion technology, namely, DEMO; a larger fusion reactor (and power plant) that will prove the feasibility of transforming the extracted *fusion* energy into useful *commercial* energy by using the heat from the blanket walls to produce steam, which in turn will drive turbines attached to electric generators. This more advanced project is currently only in the conceptual/design stage but will mature at an accelerated rate as ITER progresses.

For ITER to produce nuclear fusion it is first necessary to confine, through strong magnetic fields, a charged plasma within which tritium and deuterium are energetically excited to cause mutual collision. This is achieved by employing a combination of ohmic heating, neutral beam injection and electromagnetic radiation [45]. Ohmic heating is an internal heating mechanism (internal to the tokamak) and induces large currents into the plasma by changing magnetic fields generated by a central solenoid coil. As the temperature of the plasma increases - as a consequence of the energy transferred from the induced currents - the effectiveness of this heating method decreases. However, external heating mechanisms that work at the same time begin to dominate and raise the plasma temperature even further. Neutral beam injection involves externally accelerating deuterium nuclei to large energies before neutralising their electric charge prior to

firing them into the plasma. The other external heating process transfers energy to the plasma by *irradiating* it with high-energy electromagnetic waves. The combination of these heating methods produces a plasma temperature of 150,000,000 ℃, which is hot enough to cause deuterium-tritium collisions. The result of this fusion process is the release of helium nuclei, excess energy and neutrons. The helium produced is a waste by-product that is harmless to the environment and the excess energy is carried in the form of photons, but it is the released neutrons that actually contain *eighty percent* of the reaction energy and it is these neutrons from which the net useful energy gain is obtained. By their very nature, neutrons lack electric charge. This means that they are not influenced by the magnetic fields used to contain the plasma and so they leave the plasma and bombard the blanket walls of the tokomak (see Figure 2.8). These bombardments cause the blanket wall modules to heat up (due to the reactions contained within) and this heat is eventually extracted and used to provide useful power. However, the blanket wall modules contain lithium, of which there is at least one thousand years' supply within the Earth's crust [46]. The bombarding neutrons collide and react with the lithium and produce helium and tritium. The helium, as already mentioned, is a harmless by-product but the tritium is a vital consequence of the process. The half-life of tritium is ~ 12.3 years [47], making it an exceptionally rare radioisotope. There is only approximately twenty kilograms of tritium in the entire world [46] and it is therefore absolutely necessary to extract the generated tritium from the blanket walls and use it to refuel the plasma reactions. This is called tritium breading and is an example of the almost total self-sufficiency of the process. The other major constituent, deuterium, has an almost limitless abundance in the Earth's oceans.

If sustained nuclear fusion can be harnessed on earth as an energy source, it has the potential to counter the public's distrust and fear of nuclear power by being a safe and clean process that does not create a hazardous legacy in the form of nuclear waste or as a possible route to nuclear weapons proliferation. It could provide an almost limitless supply of pollution-free commercial energy, which has to be its greatest driving motivator.

2.6.2 The use of superconducting magnets for plasma containment

Nuclear fusion requires the containment of a charged plasma within a tokamak but due to its exceptionally high temperature (approximately ten times that of the Sun) it needs to be held in place without physical contact. As described, this is achieved by using large magnetic fields that influence the motions of the charged particles within the plasma. Iron core electromagnets are only able to produce relatively modest magnetic fields up to ~ 2 T before the iron saturates and ceases to be advantageous. For much higher fields Bitter magnets that contain water cooled resistive plates, able to withstand large Lorentz forces, are available and can be used in conjunction with superconducting magnets to form "hybrid" systems capable of producing magnetic fields as strong as 45 T [48]. These *resistive* based magnets, however, come with a substantial energy burden. For instance, the 45 T hybrid magnet at the High Magnetic Field Laboratory in Tallahassee, Florida, contains a 33.5 T resistive insert that needs a 56 MW DC power supply to drive it – as well as 15,000 sq. ft. of cooling equipment; though this is for the

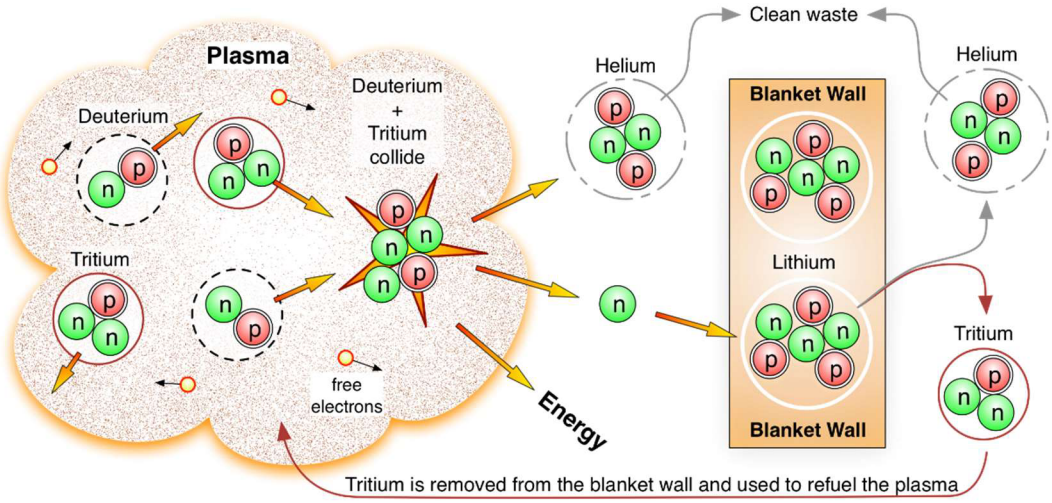

Figure 2.8: Schematic diagram of the sustained fusion process. Collisions between deuterium and tritium nuclei within a confined plasma result in the release of helium, neutrons and energy. The neutrons then collide with the lithium containing blanket wall and react with the lithium atoms to produce helium and tritium. The tritium is removed used to refuel the plasma. Image is loosely based on http://www.iter.org/sci/whatisfusion.

complete magnet system, including the superconducting coil [49]. Although this magnetic field strength is exceptionally large and is much larger than that needed by ITER, this example serves to highlight an issue that cannot be ignored. The energy required to power resistive electromagnets is substantial and continual, and actually disqualifies their use in fusion tokamak reactors designed for the sole purpose of high efficiency energy extraction – a process which requires energy to release energy. With resistive magnets the energy required has always been greater than the energy released, which is just not a viable option for ITER. The intended tenfold gain in energy to be generated by ITER is therefore only made possible by using highly efficient *superconducting* magnets. These magnets are designed to produce a peak magnetic field of 13 T from the central solenoid coil [50] but a field of 11.8 T is also generated from the toroidal field coils and leads to a central toroidal field of 5.3 T [51]. 41 GJ of energy will be needed to energise the magnets, but, unlike resistive based magnets, the electrical losses are exceptionally low (< 5 % [52]), and are only this severe during charging and discharging. Furthermore, the cooling power needed for the superconducting magnets is ~ 20 MW, approximately 100 times less than that required for a resistive system [53]. It is therefore easy to recognise the fundamental importance of the superconducting magnet system.

The ITER magnet system is comprised of *four* major subsystems (see Figure 2.9): a toroidal field (TF) system that provides primary plasma containment and is made of *eighteen* Nb_3Sn magnets (plus one spare) – these TF coils are the second largest component of the entire project weighing a total of 6540 tons and containing 150,000 km of superconducting strand; a poloidal field (PF) system that augments the plasma containment by providing shape control and is comprised of *six* NbTi magnets; a central solenoid (CS) system used for plasma heating that contains *six* (plus one spare) Nb_3Sn magnets and finally a correction coil (CC) system that contains *nine* pairs of

NbTi coils used to smooth the fields generated from the other magnets due to their physically separated locations. This superconducting magnet system is the *enabling* technology without which the tenfold output to input power ratio just cannot be achieved.

2.6.3 ITER in the context of other magnetic confinement projects

ITER will not be the first time superconducting magnets have been used for plasma containment. Many other tokamaks have utilised them, either partially - in conjunction with resistive magnets - or completely. In early 1980 Tore Supra was developed and built in France on a similar timescale to T-15 that was built in the Soviet Union. Both of these fusion devices produced containment fields up to ~ 9 T and utilised NbTi alongside resistive materials [53]. In 2006 the Experimental Advanced Superconducting Tokamak (EAST - built in China) became the first tokamak to exclusively use superconducting magnets, also made from NbTi. India built a tokamak called SST-1 (Steady State Superconducting Tokamak) around the same time and employed NbTi in conjunction with resistive magnets. A similar sized tokamak was built in Korea in 2008 called KSTAR (Korea Superconducting Tokamak Advanced Research) that used both NbTi and Nb_3Sn materials and also adopted a cooling system similar to the one intended for use in ITER. Additionally, Japan began construction of JT-60SA in 2013; a NbTi based tokamak intended to compliment the ITER project. These various tokamaks are only an example of a great number of various machines that have been built since the early work on fusion containment by the Soviet Union in the 1930s, but, whereas their roles were mainly intended to probe the nature of plasma control, ITER's role is additionally concerned with energy extraction. Furthermore, ITER is a much larger machine (6.2 m major radius) in order to generate a sufficient energy density to meet the stated goal of $Q \geq 10$; a goal that distinctly sets ITER apart from all previous efforts.

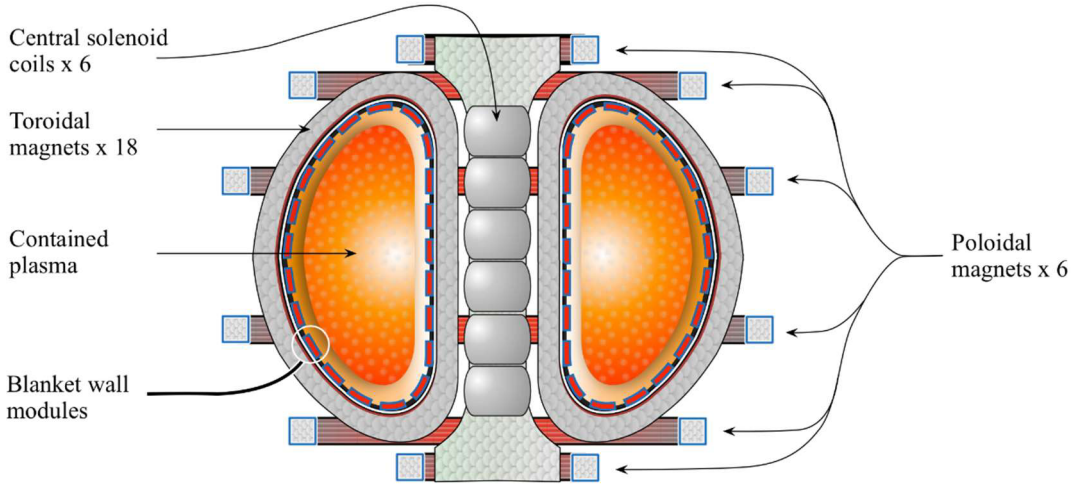

Figure 2.9: Schematic diagram depicting a cross-section through the ITER tokomak reactor showing the relative positions of the toroidal field magnets, poloidal field magnets, central solenoid, the blanket wall modules and the contained plasma.

2.6.4 Concluding comments

In today's energy obsessed climate the importance of the ITER project (and eventually DEMO) cannot be overstated. As mentioned on the ITER website its tokamak is "one of the most complicated machines ever engineered". It is tasked with not only accommodating a star on earth but also with persuading that star to work for humankind in a way never achieved before. The magnet system is responsible for the star's containment, a task difficult in itself, but it must do it in the least energetic way. This demands the use of superconducting materials and technologies that could be regarded as the machine's Achilles heel. If these components underperform or fail to meet the design criteria the machine could possibly fail or at the very least not reach its intended goal; a scenario that could have severe consequences for the hopes of our long term energy future. Prior to the commencement of the manufacturing stage of the ITER magnets the world's annual production of Nb_3Sn superconducting strand was around 15 tons [54]. This has seen a *sevenfold* increase to 100 tons per year in order to meet ITER's needs. This substantial increase in production, however, has not been accepted at the expense of strand quality. All the major components of the tokamak have to meet very high standards and in this respect the superconducting strands are no different.

PART II: NbCN – A Possible New Material for Fusion Applications

Chapter 3

Niobium carbonitride (NbC_xN_{1-x}) - Review

3.1 Introduction

The wisest place to begin the hard job of improving any characteristic of any material is to study similar, preceding, work often conducted by those highly respected members of the scientific community whose successes you wish to emulate and build upon. In light of this, it is the purpose of this review to establish which materials have the best superconducting properties and what the best methods for their fabrication are.

The material of interest is niobium carbonitride (NbC_xN_{1-x}). The review begins with a brief look at the structural properties of the precursor materials niobium nitride and niobium carbide, followed by an overview of some of their normal state properties. A detailed account of the major fabrication techniques is then given in which bulk fabrication, thin film fabrication and wire fabrication are given separate treatments. This is followed by a section on the use of mechanical alloying (milling), which is the route used in this thesis.

3.2 Structural properties and phase diagram

There are a great many common features between niobium nitride and niobium carbide and it is therefore very difficult to completely separate discussions of these materials without repeating the same or similar information. For example, both materials are very rarely found in a completely stoichiometric form since they have a propensity for defects [55]. Also, because the elements nitrogen and carbon are so much smaller than niobium, these are often found to be interstitially located between the niobium atoms as opposed to substituting in place of niobium [55].

3.2.1 Niobium nitride

Niobium nitride (NbN) is a refractory material. It has a B1 rocksalt structure with a high hardness, high wear resistance, high melting point ($\sim 2050\,^{\circ}C$ [56]), good temperature stability and good chemical stability at high temperatures [57]. In bulk form it is porous and brittle [58]; features that are not conducive to the production of thin, coiled wires, for example. It is therefore not surprising to find that the literature mostly deals with the fabrication of thin films, which provide greater physical flexibility. Further, thin films of NbN are used in Josephson junction electronic devices

[59], which increases the demand for the thin film form over bulk or wire form. Another beneficial characteristic of this material is that it is effected less by irradiation than typical A15 compounds - such as Nb_3Sn, for example - extending its usefulness to radioactive environments [60]. Figure 3.1 shows the various phases of niobium nitride and Figure 3.2 the face centred cubic structure of its δ-phase (which shows the most promising superconducting properties).

3.2.2 Niobium carbide

Niobium carbide has a B1 rocksalt structure and has a high hardness, excellent chemical stability and good wear resistance [61]. It also has an extremely high melting point of 3610 ℃. These properties make niobium carbide an excellent material for increasing the hardness and longevity of industrial tooling, for example. There are five solid single-phase regions in the bulk material, these are depicted in Figure 3.3 [62].

3.3 Electronic structure and normal state properties

3.3.1 Niobium nitride

Niobium nitride is a transition-metal compound in which the niobium and nitrogen atoms are strongly bonded together [70]. The conduction bands depend critically on nearest-neighbour niobium-nitrogen interactions and the conduction electrons are primarily 4d-like in character [70].

The band structure and density of states of niobium nitride are depicted in Figure 3.4 in which the 4d bands are those that begin at the centre of the Brillouin zone (at Γ_{25}). Table 3.1 contains other

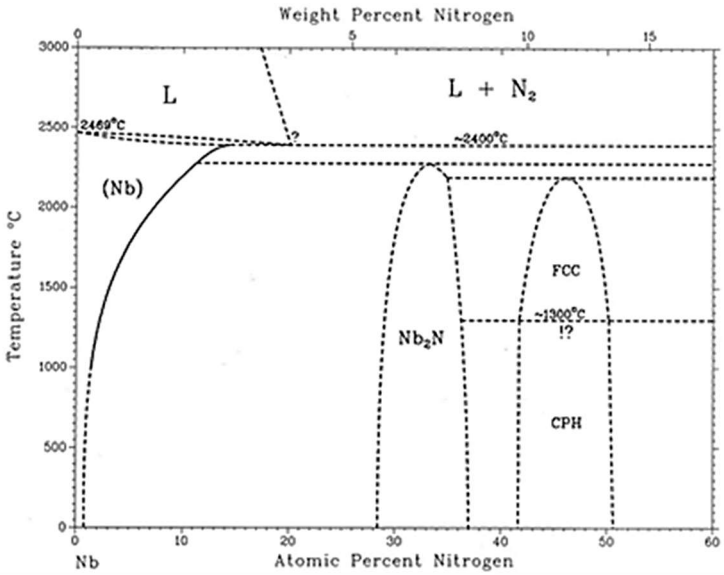

Phases

$\beta - Nb_2N$

$\gamma - Nb_4N_3$

$\delta - NbN$

$\delta' - NbN$

$\varepsilon - NbN$

δ'-phase is a transient phase during the δ to ε transformation [63]

Figure 3.1: Phase diagram of niobium nitride [64], supplemented from [56, 65-69]. The δ-phase structure is the one of interest in this review.

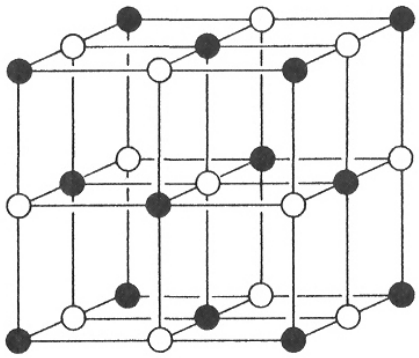

Figure 3.2: Crystal structure of δ-phase niobium nitride and niobium carbide.

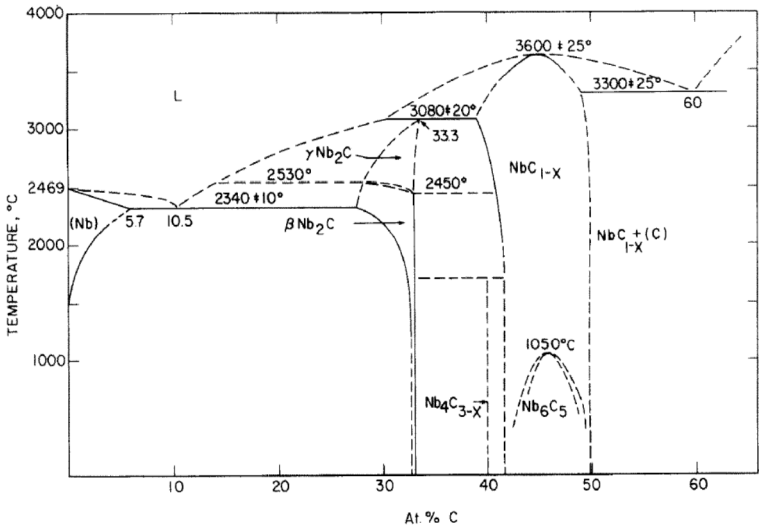

Phases

Solid solution of C in Nb (bcc)

Nb_2C (hcp)

NbC (fcc)

$\zeta - Nb_4C_{3-x}$

$\zeta - NbC_{1-x}$

Figure 3.3: Phase diagram of niobium carbide [71], supplemented from [62]. The cubic (fcc) structure is the one of interest in this review.

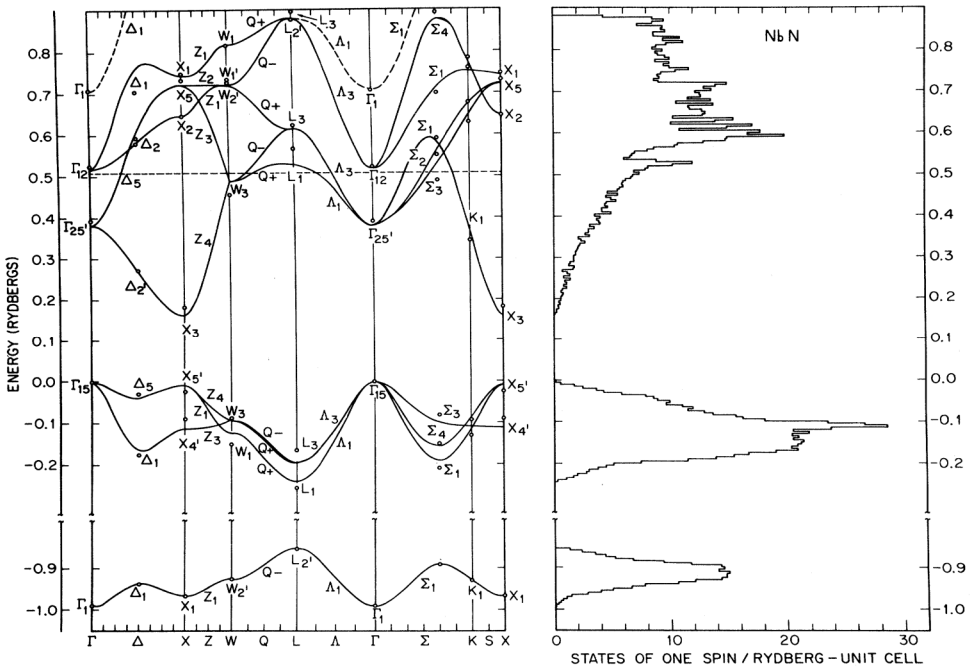

Figure 3.4: Band structure and density of states of niobium nitride [70]. The dashed horizontal line represents the Fermi energy for stoichiometric niobium nitride.

Table 3.1: Other normal state properties of bulk niobium nitride and carbide

Material	Thermal Conductivity $\left(\frac{W}{mK}\right)$	Coefficient of Thermal Expansion (K^{-1})	Resistivity $(\mu\Omega cm)$ (at 300 K)	Microhardness $\left(\frac{kg}{mm^2}\right)$
NbN	3.77 [55]	1.01 x 10^{-5} [55]	~ 57 [72]	1400 [55]
$NbC_{0.99}$	14.23 [55]	6.6 x 10^{-6} [55]	35-51.1 [73]	2400 [55]
Cu	397 [74]	1.67 x 10^{-5} [74]	1.70 (295 K) [74]	

normal state properties of the bulk form of this material. The thermal conductivity of niobium nitride is more than one-hundred times less than that of copper and its electrical resistivity at room temperature is approximately thirty times greater.

3.3.2 Niobium carbide

The band structure of niobium carbide is shown in Figure 3.5. The valence bands are comprised of niobium 4d and carbon 2s and 2p bands [75]. So, as is the case for niobium nitride, the 4d band is in part responsible for the supply of conduction electrons.

Table 3.1 contains other normal state properties of the bulk form of this material. Niobium carbide's thermal conductivity is approximately twenty-eight times less than copper while its resistivity at room temperature is approximately twenty-five times greater.

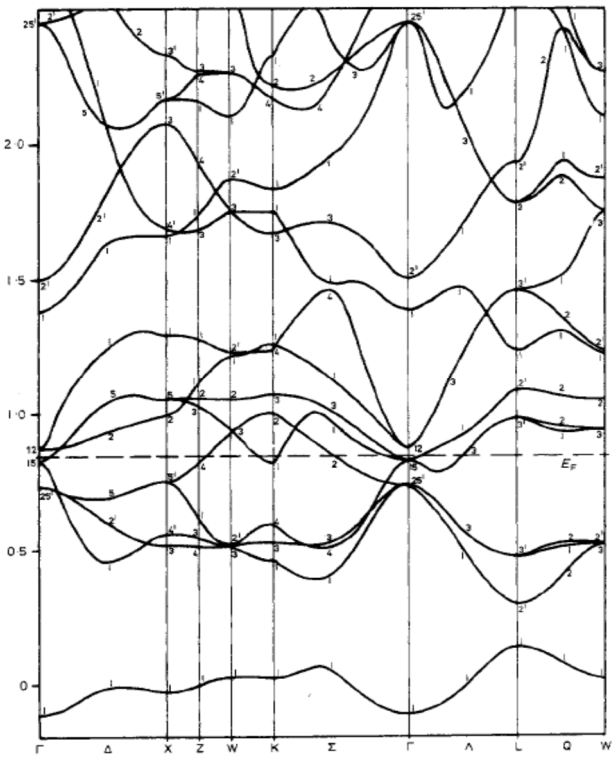

Figure 3.5: Band structure of niobium carbide [75]. Energy is in units of Rydbergs with the dashed line representing the Fermi energy.

3.4 Review of fabrication techniques

There are three primary forms of material considered here; bulk, film and wire, with various fabrication techniques associated with each one. This section discusses some of the most prevalent of these techniques by way of specific examples, which include the work of some of the most active experimentalists in the field.

3.4.1 Bulk fabrication

While there are a number of different fabrication techniques for the production of bulk form niobium containing compounds, there are broadly four distinct approaches that are of particular interest here. These are; the reaction of powders (or gases) of the constituent elements at *high temperatures*, the reaction of compounds (or gases) that contain the required elements at *lower temperatures*, the use of *combustion synthesis* of the elements at varying pressures and finally mechanical alloying. What follows is a broad discussion of these approaches, beginning with those that require the highest *reaction* temperatures and ending with those that require the lowest.

Niobium nitride

A very high reaction temperature was used by Buscaglia *et al*. in 1998 to fabricate δ-phase and γ-phase niobium nitride by a process called combustion synthesis [76]. The method uses forced heating within elevated pressures to raise the temperature of the reactants to a point at which they ignite. Once the ignition has occurred the temperature due to combustion increases and drives further self-sustaining reactions. Buscaglia *et al*. estimate their temperature to have been in the range 2400 to 2500 ℃. Their process began with a niobium powder of average grain size ~ 55 *μ*m (with a broad size distribution) that was first pressed and then subjected to varying nitrogen pressures in the range 3.5 to 700 bar within a stainless steel autoclave. Induction heating was employed to ignite the samples. Buscaglia *et al*. suggest that the nitrogen gas diffused through the outer nitride layer to further react with the solid phase. Above a nitrogen pressure of 100 bar, only δ-phase niobium nitride was formed. Below 100 bar and above 10 bar both γ-phase and δ-phase were formed. At 70 bar, the largest lattice parameter was 0.439 nm, which is the lattice constant for stoichiometric δ-NbN. The success of Buscaglia's combustion synthesis is in the production of stoichiometric material. Figure 3.6 shows their results.

A more traditional method of material fabrication that did not require elevated pressure was adopted by Pessall *et al*. in 1965 [77]. They reacted niobium hydride powder and high purity nitrogen gas at 1800 ℃ to obtain near stoichiometric niobium nitride with a lattice parameter of 0.438 nm. In 1952 a cruder form of bulk fabrication, that used a lower reaction temperature, was employed by Brauer *et al*. [65]. They produced a batch of niobium filings by filing off the edge of a niobium sheet prior to reacting the filings in a nitrogen atmosphere at 1300 ℃ for between 4 and 5 hours. Although this method produced niobium nitride at a lower temperature, the material had a varying stoichiometry that was not as good as Pessall's material.

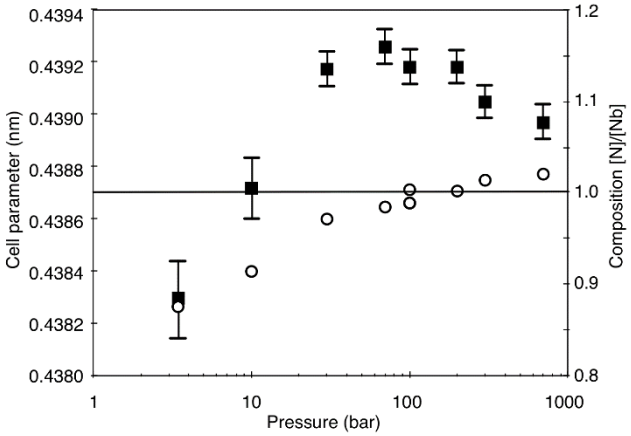

Figure 3.6: Unit cell parameter (squares) and composition (circles) of δ-phase niobium nitride fabricated as a function of pressure at a temperature of 2400 to 2500 ℃. Results of Buscaglia *et al*. (Reproduced from [76].)

Watari *et al*. used more moderate reaction temperatures in 1984 to fabricate niobium nitride *powder* [78]. They generated a vapour phase reaction in a horizontal alumina reactor, as shown in Figure 3.7, given by

$$\mathrm{NbCl_4(g) + NH_3(g) + \frac{1}{2}H_2(g) \longrightarrow NbN(s) + 4HCl(g).}$$

They found that the temperature at which the $\mathrm{NbCl_4}$ was mixed with the $\mathrm{NH_3 + \frac{1}{2}H_2}$ strongly affected the properties of their niobium nitride [78]. The optimal mixing temperature that produced the purest δ-phase niobium nitride was 800 ℃ , while the optimal *reaction* temperature was between 800 and 1200 ℃ with a gas composition ratio $\mathrm{NH_3/NbCl_4}$ of 1 to 12. Point A in Figure 3.7 represents the point at which the mixing took place and the actual mixing temperature was controlled by sliding the inner quartz tube 7 in and out of the outer alumina tube 3. A method developed by Li *et al*. in 2003 also employed moderate reaction temperatures to react different niobium oxides in nitrogen containing gases. It consisted of flowing NH_3 (ammonia) gas over amorphous Nb_2O_5 powder (of 5 nm particle size) at a flow rate of 1000 mL/min within a tube

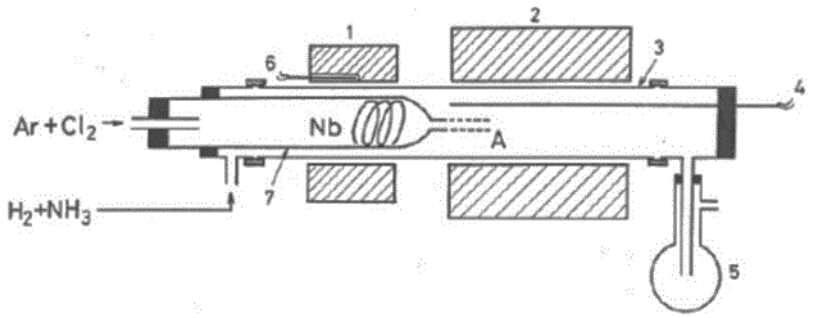

Figure 3.7: Apparatus used by Watari *et al*. to produce NbN powder. 1-Kenthal heater, 2-SiC resistance furnace, 3-alumina tube,4-Pt/Pt thermocouple, 5-collecting flask, 6-chrome-alumina thermocouple, 7-quartz tube [78].

furnace over the temperature range 650 to 800 ℃ for 3 to 8 hours (these were found to be the optimum condition ranges) [79]. The niobium nitride was then allowed to cool within the NH_3 gas flow prior to removing it from the furnace tube. Their results, for different temperatures and reaction times, are shown in Figure 3.8. Li *et al*. determined that as the reaction time increased so did the particle size. Likewise, there was a similar relationship between reaction temperature and particle size. Their method produced niobium nitride powder with particle sizes in the range 15-40 nm. The significance of Li's method, apart from relatively moderate reaction temperatures and times, is the production of *nanocrystalline* material. Li *et al*. call their method a direct nitridation method for the synthesis of nanocrystalline cubic-phase NbN powders [79] and this is the first report of such a method and is the preferred method in much of the literature. Another use of a moderate reaction temperature was adopted by Powell *et al*. to react a niobium-bearing spray-dried powder (which they prepared themselves) in an ammonia atmosphere at 700 ℃ [80]. Their powder was then hand pressed at a pressure of 4000 psi and repeatedly sintered and then quenched. The resultant bulk material consisted of crystallites and voids of between 1-5 μm as well as δ-phase stoichiometric niobium nitride. Powell's method is similar to Pessall's but produced better stoichiometry at a vastly reduced reaction temperature (700 ℃ instead of 1800 ℃), which has obvious practical advantages.

The lowest temperature treatment was used by Ma *et al*. to produce nanocrystalline niobium nitride through a benzene-thermal route vapour phase reaction [57]. Ma's method included the reaction of $NbCl_5$ and NaN_3 in an autoclave at 380 ℃ for 10 hours in accord with the following formula

$$NbCl_5 + 5NaN_3 \longrightarrow NbN + 5NaCl + 7N_2.$$

These were found to be the optimum conditions that led to particle sizes in the range 10 to 20 nm. The benzene was used to control the reaction speed, which in turn affected particle size.

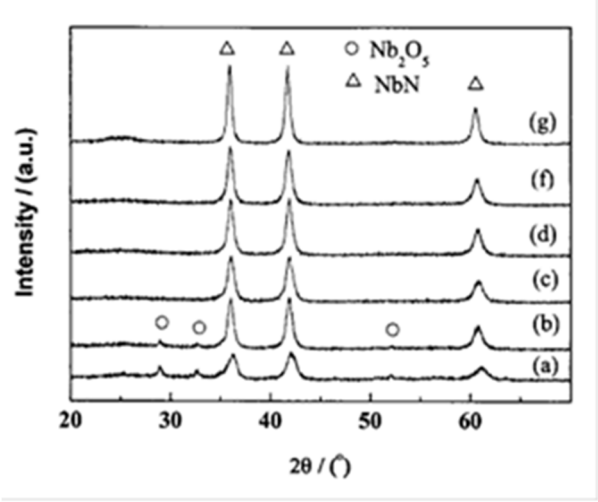

Figure 3.8: X-ray diffraction pattern of the formation of NbN over the temperature ranges and times (a) 600℃, 5h (b) 650℃, 5h (c) 650℃, 8h (d) 700℃, 3h (f) 750℃, 3h (g) 800℃, 3h [79].

A gradual improvement in bulk fabrication methods employed by different specialists in the field occurred over a period of *seven* decades. During this time stoichiometric material was formed at decreasing reaction temperatures, facilitated by reacting niobium containing compounds with nitrogen containing gases. The least popular method is the direct reaction between niobium and nitrogen, and yet, as far as the constituent reactants are concerned, this method requires the least preparation. However, the method also requires a very high reaction temperature and the longest reaction time.

Niobium carbide (and Nitride)

The literature concerning the fabrication of niobium carbide is a little scarcer than that of niobium nitride and is sometimes not presented in isolation of that material. It is for this reason that this section does not deal with niobium carbide *exclusively*, however, niobium nitride is only paid minimal attention.

The majority of the work fabricating niobium carbide began in the mid-1950s; though non-stoichiometric niobium carbide was first prepared by Joly as far back as 1877 [82]. The methodologies used in the 1950s and 60s to fabricate bulk material were very similar and relied on mixing niobium and carbon (graphite) powders together prior to reacting at high temperatures. In 1959 Storms *et al*. [81] mixed niobium and graphite powders and formed pellets by cold pressing. They then used induction heating to heat their pellets (within high vacuum conditions) to different temperatures (1800 ℃ to 3000 ℃) and over different periods of time (0.5 hours to 38 hours). The result of Storm's investigation into the lattice parameter as a function of composition of this material is shown in Figure 3.9. This figure shows that the inclusion of carbon increases the lattice parameter. In 1960 Storms (in collaboration with Krikorian and Kempter [83]) repeated this work. This time, after heating the mixture to 2300 ℃ for 3 hours, they reground the pellet into

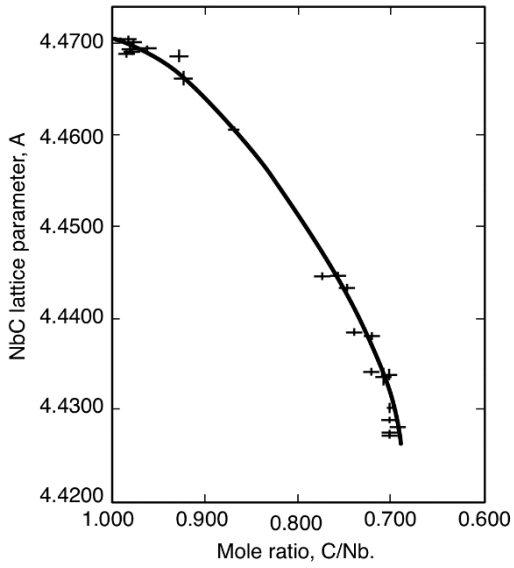

Figure 3.9: Niobium carbide lattice parameter as a function of composition according to Storms *at al*. (Reproduced from [81].)

a fine powder (325 mesh), reheated it to 2200 ℃ for 3 hours and then repeated the process again at 1860 ℃ for 65 hours. This treatment led to the formation of *near* stoichiometric $NbC_{0.993}$. A similar reaction temperature was used by Tsuchida *et al*. to produce niobium carbide from mixtures of the constituent elements themselves. However, they did this without actually needing to generate the high reaction temperatures directly [84]. This was achieved through spontaneous combustion synthesis. The process consisted of mechanically milling graphite and niobium powders in a Fritsch planetary ball mill for between 80 and 135 minutes at 2700 rpm. The ball to powder ratio used by Tsuchida *et al*. ranged from 1:19 to 1:4 with 5 to 24g of mixed powders. The inside wall of the milling pot was scraped every 15 minutes to increase the yield and, once the milling was completed, the powders were placed into a graphite crucible to avoid contamination. The milled powders were then exposed to air, at which point they spontaneously reacted, beginning with independent red glowing regions that were followed by a violent exothermic reaction which engulfed the entire mixture. The reaction temperature was estimated to have peaked at approximately 2200 ℃. The fabrication was then repeated for different proportions of graphite and, as had been discovered by other groups, an increased carbon content coincided with an increase in lattice constant. This can be seen in Figure 3.10 while Table 3.2 lists the morphology of the products and the phases identified according to the graphite content and milling time. It is apparent that the reaction temperatures required to form niobium carbide are far in excess of those needed to form niobium nitride. However, Giorgi *et al*. in 1962 (in collaboration with Storms) managed to produce niobium carbide at 2000 ℃ over time periods between 2 and 24 hours [35].

2000 ℃ is by no means the lowest reaction temperature used. In 1988 Oyama *et al*. applied his previously developed *temperature-programmed method* to the production of transition-metal carbides [85]. The main purpose of this process was to produce large grain size refractory materials. The method consisted of reducing Nb_2O_5 to Nb_2O_3 at around 790 ℃ followed by

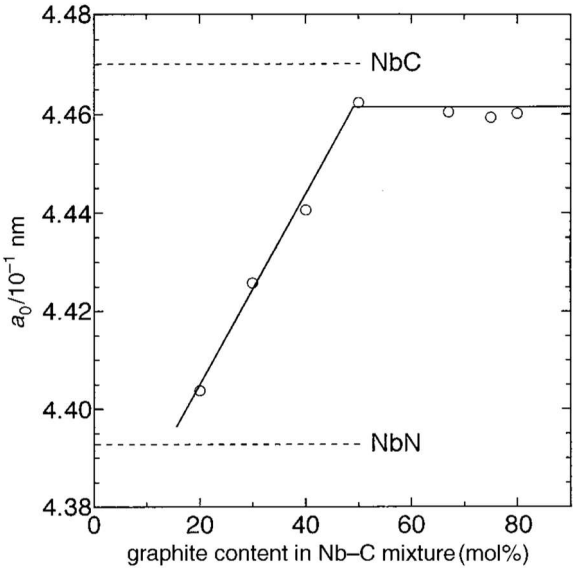

Figure 3.10: Lattice constant as a function of graphite content according to Tsuchida *et al*. [84]. The dashed lines represent the lattice constants reported elsewhere in the literature.

Table 3.2: The niobium carbide morphology and phases produced by Tsuchida *et al*. according to graphite content and milling time. (Reproduced from [84].)

graphite content (mol%)	grinding time/min	products		
		morphology	color	Phase identified by XRD
80	120	powdery	black	NbC>Nb>NbO, NbO_2, Nb_2C
75	90			NbC>Nb>NbO, NbO_2, Nb_2C
67	90			NbC>Nb>NbO, NbO_2, Nb_2C
50	80			NbC>>Nb>NbO, NbO_2, Nb_2C
40	80	highly swelled, scale-like	light grey	NbC>>NbO, NbO_2, Nb_2C
30	80	very brittle		NbC, Nb_2C>>Nb, NbO, NbO_2
20	90	slightly swelled, stratified; brittle	dark grey	NbC, Nb_2C, Nb>>NbO, NbO_2
10	135	Non-swelled; brittle		Nb_2N>>Nb_2C, Nb, NbC, MbO, NbO2, Nb_2O_5

changing Nb_2O_3 to NbC at around 1060 ℃. To achieve this, a gas flow consisting of 4% CH_4 (methane) and 96% H_2 was flowed over the Nb_2O_3 precursor at a pressure of 200 kPa and a flow rate of 2700 μmol s^{-1}. The temperature was initially raised rapidly to a level just below that at which the main solid-state transformation began to occur. This can be seen in Figure 3.11, which shows that the process time exceeded 16 hours. From then on it was heated at a slow rate of 0.0023 ℃ s^{-1}. Figure 3.12 shows the thermal analysis results on Oyama's material. The particle size of the niobium carbide was found to be 69 nm using XRD measurement techniques. The significance of Oyama's method, in light of this discussion, is the relatively low reaction temperature and process time in comparison to the methods employed by Storms *et al*. and Giorgi *et al*. It should be noted that Oyama *et el*. did not restrict their material production to niobium carbide alone, but applied the same method to the production of niobium nitride as well as other

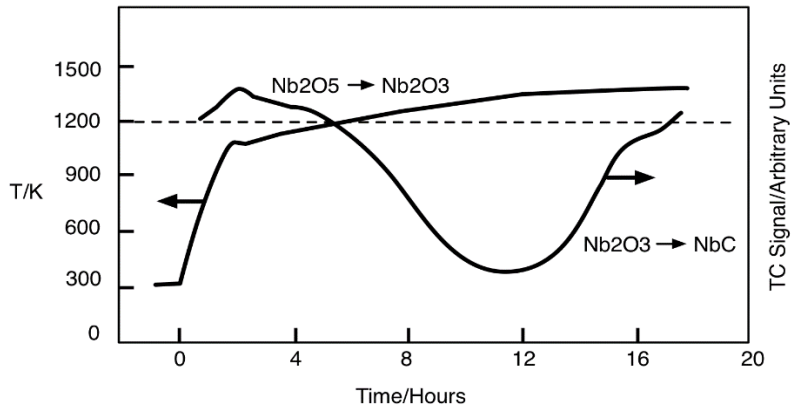

Figure 3.11: Temperature program and the thermal conductivity response of Oyama's method. The initial rapid temperature rise is clearly visible and the figure shows that the process time exceeded 16 hours. (Reproduced from [85].)

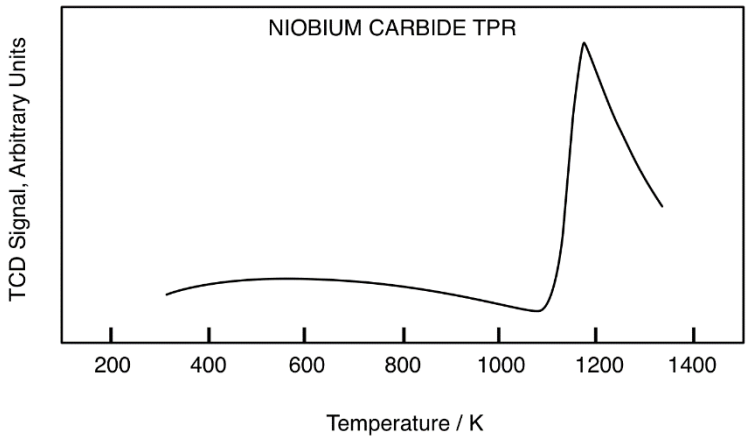

Figure 3.12: Thermal analysis of the niobium carbide produced by Oyama's Temperature-programmed method. The figure shows the temperature range over which the NbC was formed. (TCD, thermal conductivity detector.) (TPR, temperature-programmed reaction.) (Reproduced from [85].)

nitrides and carbides. In the case of niobium nitride, they used a gas flow containing 100% NH_3 at a pressure of 180 kPa and at a rate of 1300 μmol s^{-1}. The temperature was again increased rapidly to start with and was then slowly ramped at a rate of 0.065 ℃ s^{-1}. The particle size of the niobium nitride was measured to be 62 nm. This work has since been repeated by da Silva *et al*. in 1996 and it was established that different gas flow rates and lower reaction temperatures have very little effect on the grain size of the products [62].

In conclusion, the fabrication techniques discussed here have mostly relied on reactions occurring between different niobium containing and carbon containing compounds and on the direct reaction of niobium and carbon elements themselves. Very high reaction temperatures and many hours are required to form homogeneous material; in the spirit of Storm's efforts. However, Oyama's temperature programmed method required the lowest reaction temperature (~ 1030 ℃) to produce powders with nanometer sized grains but also required more demanding preparation.

Niobium carbonitride

In comparison to niobium nitride and carbide, the available literature concerning the fabrication of niobium carbonitride is extremely sparse. Of that which is available, the most detailed account is provided by Williams *et al*. in 1967 [86]. They fabricated samples of niobium carbonitride with varying stoichiometries ($NbN_{0.8}C_{0.2}$, $NbN_{0.7}C_{0.3}$, $NbN_{0.5}C_{0.5}$). They mixed commercially available niobium and niobium carbide powders (both 99.9% purity, -325 mesh) to prepare $NbC_{0.2}$, $NbC_{0.3}$ and $NbC_{0.5}$ by dry mixing. These powders were then extruded into rods which were then sintered to form a porous mixture of Nb and Nb_2C. Different samples of this mixture were then nitrided at 1280 ℃, 1360 ℃ and 1470 ℃, under different pressures (1 to 7600 torr) and reaction times (4 or 8 h). To prevent nitrogen loss they avoided vacuum sintering of the nitrided specimens. Table 3.3 lists the compositions of the various niobium carbonitride samples they produced.

Table 3.3: Measured compositions of the various niobium carbonitride samples fabricated by Williams. (Reproduced from [86].)

Nominal composition	NbN	$NbN_{0.8}C_{0.2}$	$NbN_{0.7}C_{0.3}$	$NbN_{0.5}C_{0.5}$
C (wt. %)	0.266	2.28	3.26	5.78
N (wt. %)	12.76	9.67	7.76	5.10
O (wt. %)	0.031	<0.005	<0.005	<0.005
Formula based on analysis	$NbN_{0.969}C_{0.023}$	$NbN_{0.726}C_{0.200}$	$NbN_{0.576}C_{0.281}$	$NbN_{0.379}C_{0.511}$
Formula based on carbon analysis and weight gain	$NbN_{0.918}C_{0.026}$	$NbN_{0.745}C_{0.183}$	$NbN_{0.657}C_{0.280}$	$NbN_{0.466}C_{0.466}$

Williams *et al*. found that the nitrogen content increased with nitriding pressure but was not appreciably affected by the nitriding time. Furthermore, the greatest nitrogen content occurred at 1280 ℃ and the smallest at 1470 ℃, which indicates that nitrogen content (or stoichiometry) is important in this temperature range. Williams' method shows that niobium carbonitride can be formed at moderate temperatures using a direct nitriding technique.

A technique similar to Oyama's temperature programmed method was adopted by Kim *et al*. in 1999 to produce niobium carbonitride [87]. The process consisted of reacting niobium pentoxide (Nb_2O_5) in a flow of ammonia gas (NH_3) at a rate of 175 mole h^{-1} to produce niobium oxynitride (NbN_xO_y). The niobium oxynitride was then subjected to a methane-hydrogen gas flowing at 80 to 120 mole h^{-1} at a temperature that was increasingly elevated at a rate of 0.5 to 2.5 ℃ min^{-1}. The temperature was stabilised at 850 ℃, which is relatively low in comparison to Williams's process. The reaction was allowed to continue until methane consumption had been achieved, at which point the system was cooled rapidly prior to being flushed with pure helium. Table 3.4 lists the various properties of the niobium carbonitride and their specific reaction conditions. Kim *et al*. conclude that this process leads to the formation of non-stoichiometric niobium carbonitride. Comparison of Kim's niobium carbonitride particle size to that of Oyama's niobium *carbide* particle size reveals that the niobium cabonitride particles are less than a third that of the niobium carbide. This may well help to enhance the superconducting properties of the material without the need for further grinding.

Table 3.4: Properties of niobium carbonitride fabricated by Kim *et al*. [87].

	Synthesis conditions[a]		Cell parameter,	Crystallite size	C amount	N amount	Surface area	Particule size
Precursor	T_f	x_{CH_4}	a_0 (Å)	D_c (Å)	(%wt)	(%wt)	Sg ($m^2 g^{-1}$)	D_p (Å)
$Nb N_x O_y$	1123 K	0.1	4.3971 (2)	192	4.64	10.72	27	284
$Nb N_x O_y$	1177 K	0.25	4.3781 (12)	145	4.53	11.59	35	219
$Nb N_x O_y$	1151 K	0.5	4.3556 (6)	133	4.41	11.99	49	156

[a] T_f is the final temperature of carburization process; x_{CH_4} the molar fraction of methane. The other synthesis conditions are: heating rate = 2.5 K min^{-1}; molar space veloticiy = 120 h^{-1}.

3.4.2 Thin film fabrication

Many of the important thin film fabrication techniques, including sputtering, diffusion and sintering methods, have been used to produce niobium carbonitride [89]. In sputtering, typically a target cathode (made from the same material that a substrate is to be coated) is bombarded by positively charged argon atoms within an ionised argon atmosphere. These bombardments chip the cathode surface away. Over extended periods of time these chippings, which form a vapour, condense onto a substrate to form the required film. The production of clean superconducting films using the sputtering technique was initially very difficult due to the impurities that condense onto (or are gettered by) the film during the process. The need for clean superconducting films led Rudolf Frerichs in 1962 to propose a modification to the process based on the observation that the cathode always stays "bright and shiny" due to the continuous bombardment of Ar+ ions which drives out the impurities [90]. He therefore reasoned that no gettering by the films would take place if, in addition, they could also be bombarded by Ar+ ions during the sputtering process. The main feature of Frerichs's method is that an asymmetric alternating current, set up between a vertically separated cathode and anode, first sputters the cathode prior to a polarity change after which the substrate, which is placed on top of the anode, is then sputtered with a vastly decreased current density. In this way any impurities in the newly formed thin film layer are driven out by a current density that will not damage the film itself. In 1963 Frerichs, in collaboration with Kircher, improved the ac sputtering technique further [88]. In order to improve the superconducting properties of the sputtered films, and in response to observations made by other researchers that the edges of rectangular shaped films might affect the superconducting properties, Frerichs *et al*. formed cylindrical films by changing the shape of the substrate and the anode and cathode. Figure 3.13 is a diagram of their apparatus. A further enhancement was achieved by allowing the inside surface of the bell-jar to become coated with the cathode material

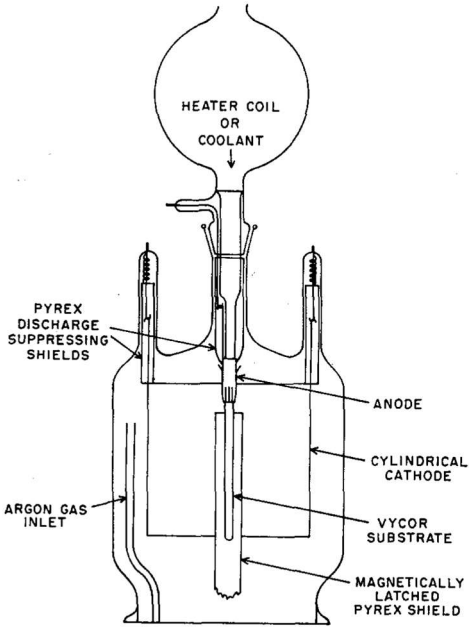

Figure 3.13: AC sputtering apparatus used by Frerichs and Kircher to produce cylindrical superconducting films [88].

to act as a getter to pick up traces of residual reactive gas. Further, Frerichs *et al*. established that the optimum sputtering conditions were a substrate temperature of 500 ℃ and an alternating current density ratio of 4:1. The improvements made to the thin film fabrication techniques have therefore led to the production of very clean superconducting films.

Niobium nitride

Gerstenberg and Hall were the first to reactively sputter niobium in an argon-nitrogen atmosphere to obtain niobium nitride thin films [91]. During their process they maintained a background pressure of ~10^{-6} Torr, whereas Bell *et al*. who also produced niobium nitride films in 1968, maintained a background pressure of 10^{-9} Torr [91-93]. This preparatory work paved the way for further improvements to be made. For instance, Cukauskas *et al*. investigated the fabrication of niobium nitride films using radio frequency magnetron sputtering, with the addition of methane into the argon-nitrogen atmosphere [93]. They established that the optimum conditions were an elevated substrate temperature and approximately 2% methane added to the sputter gas. They also determined that films fabricated without the addition of sputter methane were found to be two-phase δ and ε NbN, whereas those fabricated with the additional methane were single-phase δ only. Figure 3.14 shows the lattice parameter as a function of methane partial pressure for the films in question. Cukauskas suggested that the increased lattice parameter with increased methane partial pressure may well be due to the formation of NbC or interstitial carbon at higher partial pressures.

The fabrication of niobium nitride thin films using dc magnetron sputtering onto an ambient temperature substrate has been investigated by Bacon *et al*. [94]; though the process itself resulted in some heating of the substrate, this was estimated to be less than 900 ℃. They established that films of thickness 100 nm or less were granular with grain size 5 nm and a lattice parameter of 4.46 Å, which is significantly higher than the bulk value for cubic NbN (4.39 Å [76]). They also established that the N/Nb ratio increased as the N_2/Ar ratio increased up to 30% N_2.

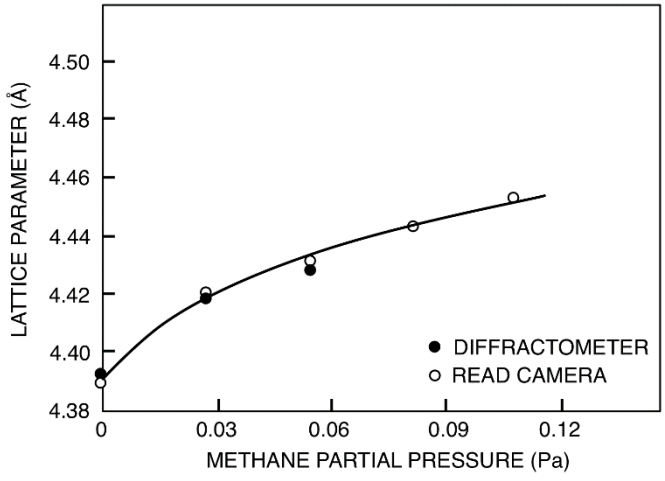

Figure 3.14: Lattice parameter as a function of methane partial pressure for the niobium nitride films fabricated by Cukauskas *et al*. (Reproduced from [93].)

Further increases in N_2 up to 50% did not affect the N/Nb ratio. Figure 3.15 shows the resistivity of the niobium nitride films produced by Bacon *et al*. as a function of N_2 gas in the argon atmosphere. Figure 3.16 shows how the nitrogen content in the argon-nitrogen atmosphere affected the phases of the material.

Niobium carbonitride (and Carbide)

The literature on the fabrication of niobium carbonitride thin films is extremely scarce. Furthermore, the fabrication processes used to produce niobium carbide and carbonitride thin films are identical in most respects to those used to produce niobium nitride thin films, and therefore, only a brief overview of carbide and carbonitride films is given here.

DC diode sputtering was used by Gavaler *et al*. in 1971 to fabricate niobium carbonitride thin films for the purposes of investigating their superconducting properties [95]. The films were fabricated by sputtering a niobium-carbon target in an atmosphere of pure nitrogen or a mixture of nitrogen and argon with elevated substrate temperatures in the range 500 to 800 ℃. The target was made

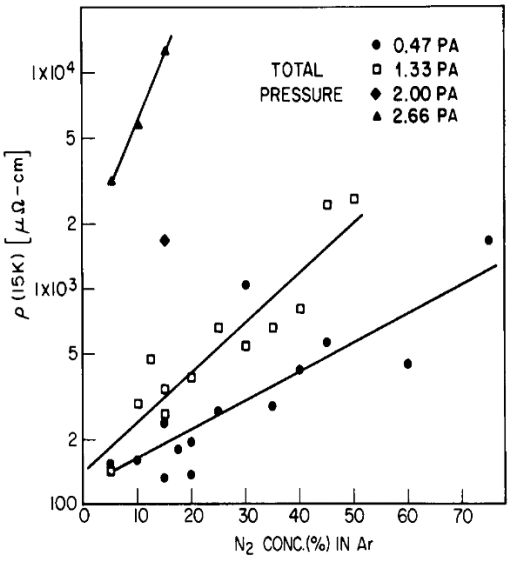

Figure 3.15: The resistivity "as a function of the mole fraction of N2 in the Ar-N2 sputter gas mix for various values of the total Ar-N2 pressure" [94].

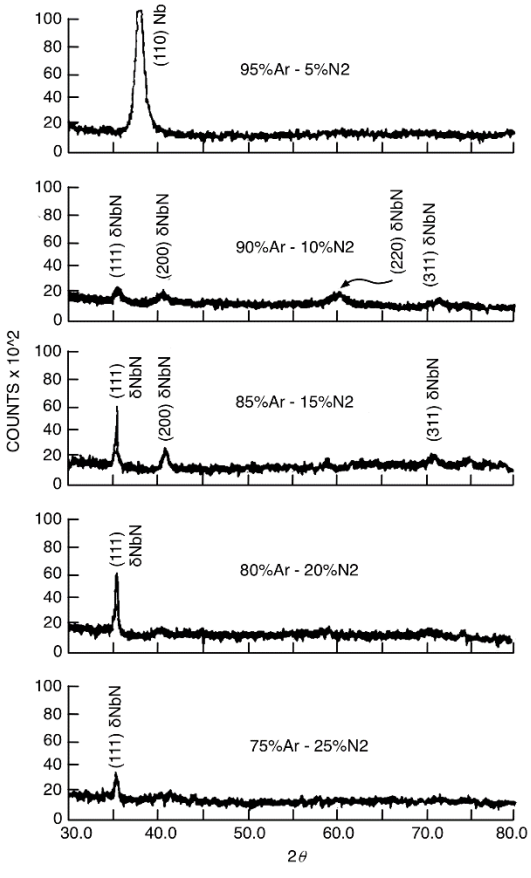

Figure 3.16: X-ray diffraction results of measurements on NbN films of thickness 250-400 nm. The traces show the transition from Nb to a δ-phase NbN as the nitrogen content was changed. (Reproduced from [94].)

by hot pressing niobium and carbon powders at approximately 1000 ℃ in the ratio 3.33/1. Similar methods of film production were employed by Hermann Spitzer in 1972 to fabricate niobium carbide films [96]. He used a substrate temperature of 700 ℃ and added methane to the sputtering atmosphere. The deposition rate was approximately 2 Å/sec, which is very similar to the 3 Å/sec deposition rate used by Aubert *et al*. in 1982 to produce niobium carbonitride films. The average thickness of the films fabricated by Spitzer was 300 nm.

Radio frequency sputtering techniques have been used by Moodera *et al*. in 1987 to fabricate thin niobium carbonitride films using heated sapphire substrates. The sputtering atmosphere consisted of an argon, nitrogen and a cyanogen gas mixture (C_2N_2), which was varied to control the carbon content. The resulting film samples ranged in thickness from 112 μm to 370 μm and had lattice parameters between 4.420 and 4.428 Å. Moodera *et al*. conclude that the addition of C in NbN seems to improve the quality of the intergrain regions or grain boundaries, thereby reducing resistivity.

3.4.3 Wire fabrication

The literature concerning the fabrication of niobium nitride, carbide and carbonitride *wires* is the least available of the three types of material discussed in this review. It is assumed that this situation reflects the difficulties involved in producing long thin wires of these refractory compounds.

Niobium nitride

A technique utilised in the production of thin films, namely, reactive sputtering, has also been utilised by Morita *et al*. to produce a long thin wire of superconducting niobium nitride [97]. To achieve this they fed a tungsten wire substrate through the centre of a niobium hollow cylindrical tube of dimensions 50 mm long by 50 mm outside diameter and 42 mm inside diameter. The feeding rate was 7.5 mm per minute. They then proceeded to reactively sputter the niobium in an argon partial pressure of $2x10^{-2}$ Torr and a nitrogen partial pressure of $2x10^{-4}$ to $4x10^{-3}$ Torr. These partial pressures were important parameters that helped control the superconducting properties of the wire.

Nanometre sized niobium nitride superconducting wires used in the production of sensitive measuring devices have been fabricated by Patel *et al*. [98]. Their method involved two stages; they first produced one-dimensional nanostructures of $NbSe_3$ and then converted $NbSe_3$ nanostructures into niobium nitrides by adjusting their composition while maintaining their 1D nanostructure shapes [98]. They annealed the $NbSe_3$ nanostructures in flowing ammonia gas at 700-1000 ℃ to produce a superconducting material. Figure 3.17 shows scanning electron micrographs of the niobium nitride nanowires (and nanoribbons).

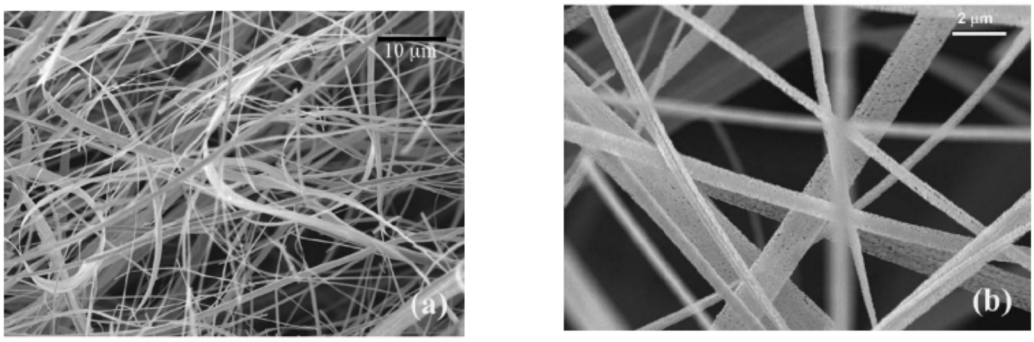

Figure 3.17: Scanning electron micrographs of the nanowires and nanoribbons produced by Patel *et al*. Image (a) is low magnification and image (b) is high magnification [98].

Niobium carbonitride

Pike *et al*. in 1975 used chemical vapour deposition to fabricate niobium carbonitride wires. A carbon filament was used as a substrate that was deposited with a niobium carbonitride layer ranging in thickness from 30 to 300 nm [99]. The lattice constant ranged from approximately 4.45 Å to 4.46 Å. Pike's primary motivation for producing these wires was to study their superconducting properties. In this respect it was desirable to produce wires with the optimum superconducting composition of $NbC_{0.3}N_{0.7}$, however, Pike failed to achieve this.

3.4.4 Mechanical alloying

Mechanical alloying consists of delivering high energy impacts to powdered materials to cause the constituent elements (or compounds) to form various (other) compounds. It is the impact energies that drive the necessary reactions between the constituents. One of the main benefits of using this method is that the high temperatures usually associated with such compound formations do not have to be produced. Hence, expensive furnaces and the practical difficulties involved in protecting the precursor materials from the atmosphere, prior to, during, and after baking, are alleviated, for example. Further, the method also produces extremely fine powder products that can facilitate further processing using different complimentary techniques.

The use of mechanical alloying as a technique for fabricating the particular materials under review here, is not widespread. This is primarily due to the materials themselves and not indicative of the unpopularity of the technique, since mechanical alloying is regularly used in the production of tough tooling materials, for example.

Niobium nitride

The production of nanocrystalline niobium nitride by mechanical alloying of niobium in a nitrogen atmosphere has been conducted by Miki *et al*. in 1992 [63]. This method is of particular interest here due to the equipment they used being readily available in Durham and the similarities with the thesis work presented here.

A Spex 8000 milling machine with stainless steel (304) vial and balls of diameter 12.7 mm were used. A ball-to-powder ratio of 13:2, which is close to the more common 10:1 ratio used by some other groups, was adopted. The vial had to be connected to a nitrogen gas chamber in order to provide a continuous supply of nitrogen during the milling process, both of which were evacuated prior to releasing nitrogen into the system. Milling for thirty hours resulted in the niobium absorbing 50 at% nitrogen gas (see Figure 3.18). As expected, particle size reduced as the milling time increased. After thirty hours δ-phase niobium nitride (lattice parameter *a*=0.4392) and δ'-phase niobium nitride were formed.

Niobium carbonitride

The process of mechanical alloying has also been applied to the formation of niobium carbonitride by Cordoba *et al*. in 2007 [100]. In mechanically alloying the material Cordoba *et al*. took advantage of mechanically induced self-propagating reactions in which a self-sustaining exothermic reaction propagates through the powder charge as a combustion process. Cordoba emphasises that these reactions are difficult to create due to heat loss to the milling media i.e. the balls and vial themselves. However, they produce a high yield of product in a short time with high purity and are therefore advantageous. Further, Cordoba *et al*. show that these reactions result in good stoichiometry control. Tempered steel balls (7 in total, diameter 15 mm with weight 12.39 g each) and a tempered steel vial were used. A Fritsch planetary ball mill had been modified to allow a continuous gas connection to the vial through which a continuous supply of high-purity nitrogen gas, pressurised to between 6 and 11 bar, was fed to the contents of the vial. The permanent gas connection was made by a rotary valve and a flexible polyamide tube. Two ball-to-powder ratios were used, 1:14 and 1:7, with either 6 or 12 g of powder (Nb-C). The Fritsch was set to rotate between 600 and 800 rpm for both the rotation of the supporting disc and the rotation of the vial. Table 3.5 summarises the milling conditions for 11 different samples and Figure 3.19 shows their XRD patterns. It should be noted that for niobium carbide the temperature at which the powder mixture ignites and a self-sustaining reaction propagates is 2537 ℃; only

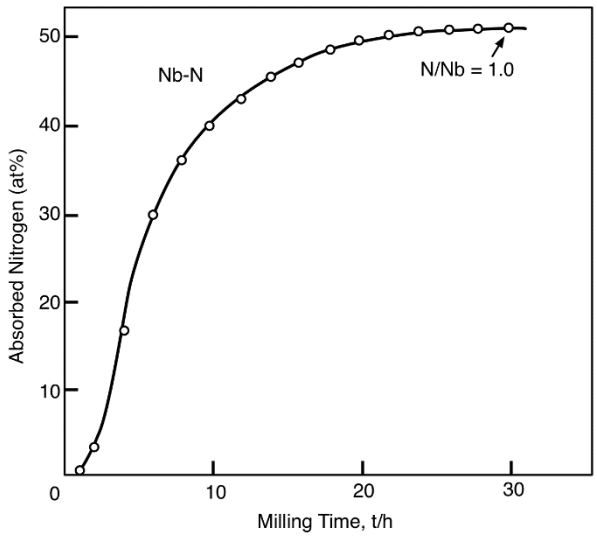

Figure 3.18: Absorbed nitrogen as a function of milling time. (Reproduced from [63].)

Table 3.5: Summary of milling conditions and ignition times for the niobium/carbon-milled samples by Cordoba *et al*. [100]. The ignition time is an activation period during which time the powders are mechanically altered. Once the activation period is complete then the mechanical energy due to impacts creates the required reaction temperature to initiate the mechanically induced self-propagating reactions (MSR).

Sample	Nb/C molar ratio	Balls (PBR)	N_2 (atm)	*v* (rpm)	Milling time (min)	Ignition time (min)
1	1:1	7 (1:14)	11	600	60	56
2	1:0.75	7 (1:14)	11	600	60	56
3	1:0.65	7 (1:14)	11	600	60	57
4	1:0.5	7 (1:14)	11	600	60	56
5	1:0.35	7 (1:14)	11	600	60	54
6	1:0.25	7 (1:14)	11	800	180	No MSR
7	1:1	7 (1:14)	6	600	69	68
8	1:0.75	7 (1:14)	6	600	60	52
9	1:0.65	7 (1:14)	6	600	60	54
10	1:0.5	7 (1:14)	6	600	60	56
11	1:0.35	7 (1:14)	6	800	120	No MSR

samples 6 and 11 did not satisfy this condition. Table 3.6 lists the various results of the fabrication process obtained by XRD. The lattice parameters are all larger than those of niobium nitride, which is to be expected due to the absorption of carbon. However, most of the particle sizes compare favourably with those obtained for bulk niobium nitride using non-mechanical processes and therefore the increased lattice parameter is not necessarily increasing the particle sizes themselves.

3.5 Superconducting properties

The superconducting properties of the materials discussed in this review are in general dependent on the specific form of the material in question. For instance, we note that thin films tend to have higher transition temperatures than bulk form; most likely due to strain. Superconducting properties including critical temperature, upper critical field and critical current density are dealt

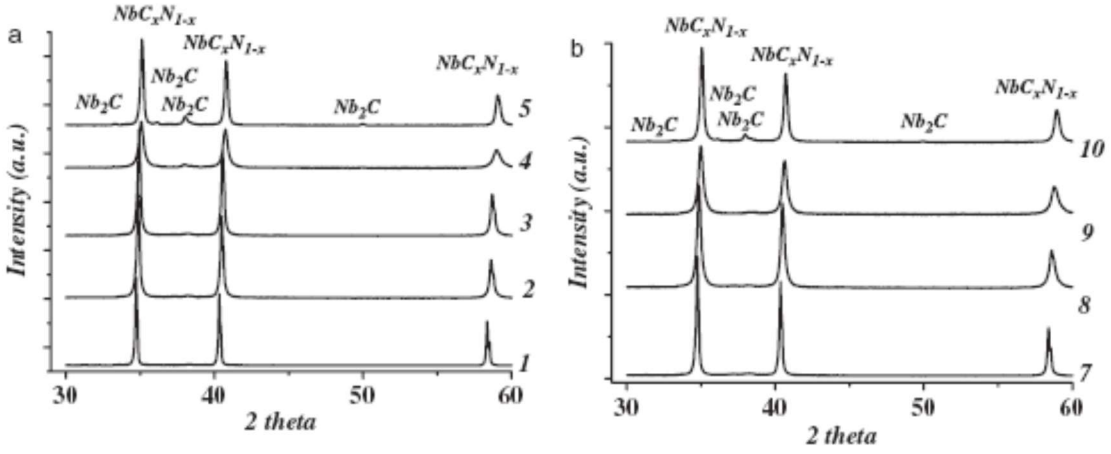

Figure 3.19: Graphs (a) and (b) show the XRD patterns of the samples listed in Table 3.5 above [100]. The samples 1 to 10 are those listed in Table 3.5 above.

Table 3.6: The results of XRD measurements conducted on the niobium carbonitride produced by Cordoba *et al*. [100]. "*e*" is the maximum strain.

Sample	*a* (Å)	Composition from XRD measurement	*D* (nm)	e ($\times 10^{-3}$)
1	4.4673	$NbC_{0.97}N_{0.03}$	94	0.19
2	4.4484	$NbC_{0.72}N_{0.28}$	52	0.95
3	4.4448	$NbC_{0.68}N_{0.32}$	45	0.66
4	4.4227	$NbC_{0.39}N_{0.61}$	44	3.99
5	4.4188	$NbC_{0.34}N_{0.66}$	52	1.36
7	4.4646	$NbC_{0.93}N_{0.07}$	63	0.17
8	4.4490	$NbC_{0.73}N_{0.27}$	30	1.39
9	4.4390	$NbC_{0.60}N_{0.40}$	24	2.56
10	4.4270	$NbC_{0.45}N_{0.55}$	46	2.05

with in the following section and care is taken to identify the materials with the best superconducting properties.

3.5.1 Critical temperature and field

Niobium nitride

When the fabrication of superconducting niobium nitride films was in its infancy, it was difficult to produce films that matched the transition temperatures of bulk material. However, in 1969 Deis *et al*. came very close at ~ 15 K [101] and Gavaler *et al*. also produced transition temperatures comparable to bulk form by employing ultra-high vacuum techniques to reduce the background residual gas contamination in the films [95, 102].

Thin films are extensively used in electronic applications but are not without their own limitations. For instance, polycrystalline niobium nitride thin films have large magnetic penetration depths, which limit their application in high-frequency circuits [103]. Further, they have small coherence lengths, which causes difficulty for fabrication of high-quality tunnel junctions [103]. In response to these limitations, single crystal thin films have been developed using reactive sputtering, chemical vapour deposition and thermal diffusion techniques [59, 103]. An example of this is provided by the work of Wang *et al*. who fabricated single crystal niobium nitride thin films in 1996 [103]. Wang's method did not include intentional substrate heating but they managed to produce a film with a transition temperature of 16.0 K. According to Cukauskas *et al*. (see Figure 3.20) the transition temperature is expected to increase with increasing substrate temperature. However, Wang *et al*. established that lower sputtering pressure was the reason for their success; this can be seen in Figure 3.21. While Wang's achievement is commendable, Keskar *et al*. used radio frequency sputtering techniques in 1971 to produce a niobium nitride film with a maximum transition temperature of 17.3 K. This still remains the highest reported niobium nitride thin film transition temperature.

In 1968 Horn *et al*. [104] produced superconducting niobium nitride bulk material and conducted measurements on its superconducting properties. Figure 3.22 shows their measurements that

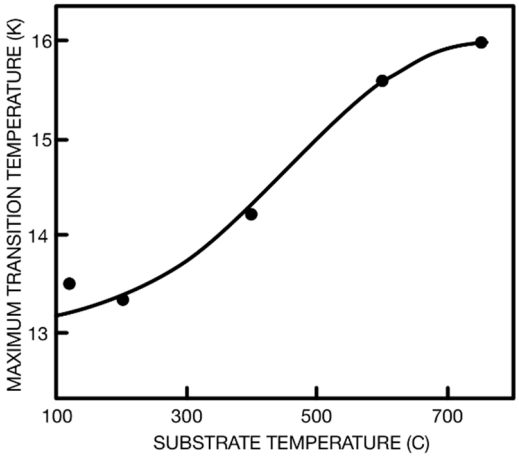

Figure 3.20: The results of Cukauskas *et el*. investigation into the effect of substrate temperature on transition temperature of r.f. sputtered NbN thin film [93].

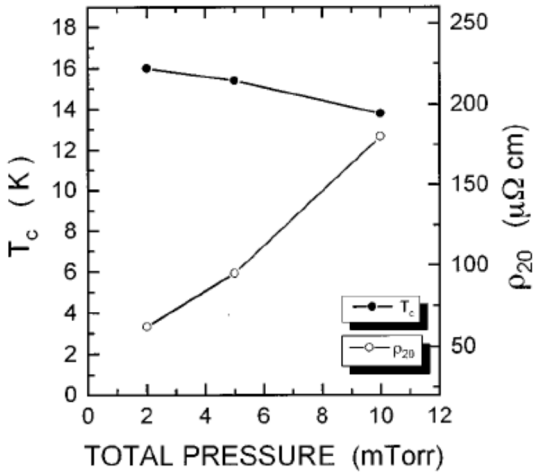

Figure 3.21: Transition temperature and resistivity as a function of total pressure in accordance with Wang *et al*. [103].

reveal that near stoichiometric niobium nitride has the greatest transition temperature (approx. 16.2 K).

Penetration depth measurements on single crystal niobium nitride films have been conducted by Komiyama *et al*. [105]. Their results are shown in Figure 3.23. At zero Kelvin the calculated penetration depth was 194 nm, which is nearly half the value reported for polycrystalline films [105].

Bulk form niobium nitride was fabricated by Watari *et al*. in 1984 (see Figure 3.24) [78]. They determined that the lattice constant and T_c of the δ-phase varies with the N/Nb ratio. The effect of the N/Nb ratio on the lattice constant was also observed by Troitskiy *et al*. [106] and Miki

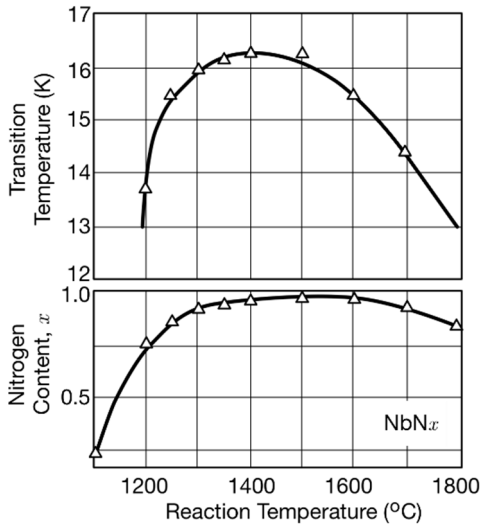

Figure 3.22: Upper graph: superconducting transition temperature as a function of nitrogen content. Lower graph: nitrogen content as a function of reaction temperature. Horn *et al*. [104]

et al. [63]. The maximum lattice constant according to Watari *et al*. occurred at a N/Nb ratio of 0.99 and a ratio of 0.95 led to the *maximum* transition temperature of 16.3 K (after annealing). This is the highest T_c reported for bulk form niobium nitride fabricated at atmospheric pressure.

The effect of particle size on transition temperature has been investigated by a number of groups including Shi *et al*. [107] who say that differences in particle size had very little effect on the transition temperature of their material (15.4 K). This is not the case with upper critical field, however. Studies conducted by Troitskiy *et al*. show that powders with mean grain sizes of ~ 35 nm have upper critical magnetic fields of about 32 T and particle sizes of less than 20 nm have B_{c2} of almost 45 T [106].

Niobium carbide and carbonitride

The emphasis in this section is given to niobium carbonitride. Although the literature is scarce, it makes clear the superior superconducting properties of the carbonitride. Producing solid solutions of niobium carbide and niobium nitride is a direct route to the formation of superconducting niobium carbonitride, so niobium nitride is also discussed in this section.

Experiments designed to determine the effect of composition on the transition temperature of niobium carbide were conducted by Giorgi *et al*. in 1962 [35]. They concluded that the highest critical temperature was reached for the stoichiometric composition, as shown in Table 3.8. These results were derived from measurements made on bulk material, however, in 2005 Shi *et al*. published results from measurements obtained on niobium carbide *nanotubes* for which the

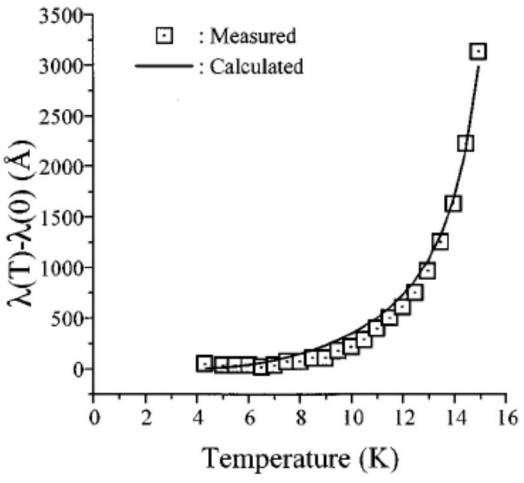

Figure 3.23: Penetration depth as a function of temperature of single crystal niobium nitride films [105].

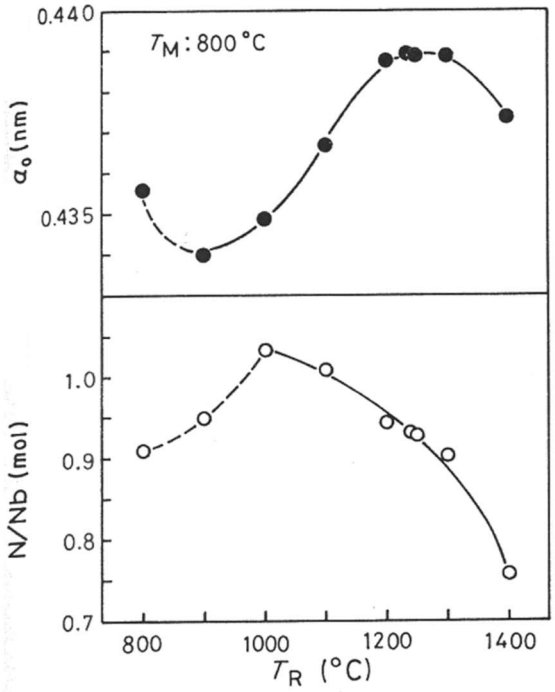

Figure 3.24: Lattice constant (a_0) and atomic ratio N/Nb as a function of reaction temperature. Watari *et al*. [78].

transition temperature was 11.2 K [61]. They also comment that T_c varies with carbon stoichiometry in NbC_x, and the T_c=11~12 K corresponds to x=0.99, which is consistent with the work of Giorgi *et al*.

As long ago as 1953 Matthias realised that a rise in unit cell volume tends to increase the transition temperature of superconducting materials [109]. It was also known that the inclusion of carbon results in such a volume increase. Consequently, Matthias *et al*. increased the lattice by forming solid solutions between NbC and NbN. This resulted in a *maximum* transition temperature of 17.8 K for a niobium carbide content of between 25 and 30 percent. These findings correlate well with those obtained by Willams *et al*. in 1967, in which a maximum transition temperature of 17.8 K was confirmed. This transition temperature actually supersedes that of niobium nitride in thin film form (which is 17.3 K). Both Matthias and Williams have produced the best bulk niobium carbonitride [86, 109].

Attempts by Gavaler *et al*. in 1971 to fabricate thin films of niobium carbonitride that matched (or even superseded) this bulk value of 17.8 K were disappointing. They used dc diode sputtering with a composition similar to the optimum reported for the bulk system i.e. $NbC_{0.3}N_{0.7}$ [95]. They achieved a transition temperature of 17.3 K. However, they also reported a corresponding decrease in other critical values such as current density and upper critical magnetic field. They attribute these poorer properties to fewer dislocations and grain boundaries, which reduced the total number of pinning centres in their films. Transition temperatures between 14.2 and 16.8 K for niobium carbonitride films have been produced by Moodera *et al*. in 1987 [110]. These films had an upper critical field of between 20 and 25 T and a penetration depth of 237 nm to 303 nm.

Table 3.7: Fundamental properties of superconducting niobium nitride (bulk) [108]. (a) This value has been increased to 17.3 K in thin film [89]. (b) This value has been decreased to 194 nm in thin film [105].

T_c (K)	ξ (nm)	λ (nm)	$\mathbf{B}_{c1}$ (mT)	$\mathbf{B}_{c2}$ (T)
16.3[a]	5	200[b]	9.3	15.0

Table 3.8: Transition temperatures of various compositions of niobium carbide by Giorgi *et al*. [35].

Composition	T_c (°K)
$NbC_{0.977\pm.002}$	11.1
$NbC_{0.975\pm0.02}$	11.1
$NbC_{0.968\pm0.02}$	10.6
$NbC_{0.918\pm0.01}$	7.3
$NbC_{0.885\pm0.01}$	3.2
$NbC_{0.881\pm0.01}$	4.2
$NbC_{0.878\pm0.01}$	3.5
$NbC_{0.829\pm0.01}$	1.05
$NbC_{0.79\pm0.01}$	a
$NbC_{0.76\pm0.01}$	a
$NbC_{0.75\pm0.01}$	a
$NbC_{0.70\pm0.01}$	a

It is clear that the structure of the material plays an essential role in determining its superconducting properties. Troitskiy *et al.*, who worked on the production of ultrafine niobium carbonitride *powders* with particle sizes in the range 20 to 60 nm [106], compared standard bulk material with their *ultrafine* material and found the lattice of these powders to be smaller; although, after annealing, the lattice parameters increased to match those of the standard bulk material. They also found that their ultrafine niobium carbonitride, with the composition $NbC_{0.2}N_{0.8}$, had an upper critical field *three* times that of the standard bulk material approaching ~42 T (this is supported by Figure 3.25). With regard to upper critical magnetic field, Troitskiy's material is undoubtedly the best. Figure 3.26 is from early work conducted by Pessall *et al.* in 1965 that also shows the same compositional trend as Troitskiy's work. It also confirms the increase in lattice parameter with increasing carbon content.

3.5.2 Critical current

Critical current measurements on superconducting niobium nitride, carbide and carbonitride are extremely rare. However, those measurements that have been conducted, which are pertinent to this review, will be discussed in this section. No attempt is made to segregate the discussion into the different materials or their differing forms in order to emphasise the critical current measurements themselves.

Suzuki *et al.* [111] have conducted the most promising and exciting critical current density measurements. The value of J_c for their sputtered niobium nitride films have been included in Figure 3.27, which shows the critical current densities for different applied magnetic fields of some Type II superconductors. Suzuki's niobium nitride films are anisotropic and Figure 3.27 shows the results for two orientations, $\mathbf{B}_{\perp}$, and $\mathbf{B}_{\parallel}$. The critical current density of these niobium nitride

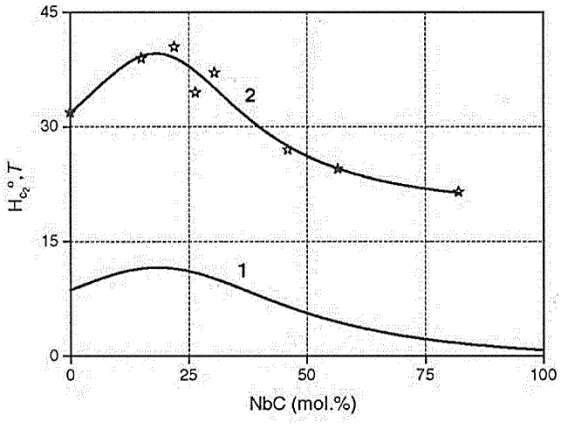

Figure 3.25: Upper critical field (T) as a function of niobium carbide composition. Curve 1 represents normal bulk material whereas curve 2 represents the ultrafine powder produced by Troitskiy *et al.* [106]

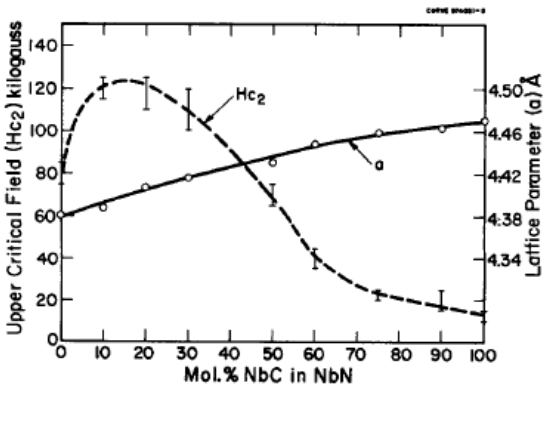

Figure 3.26: Upper critical field as a function of niobium carbide composition. Work conducted by Pessall *et al.* [77].

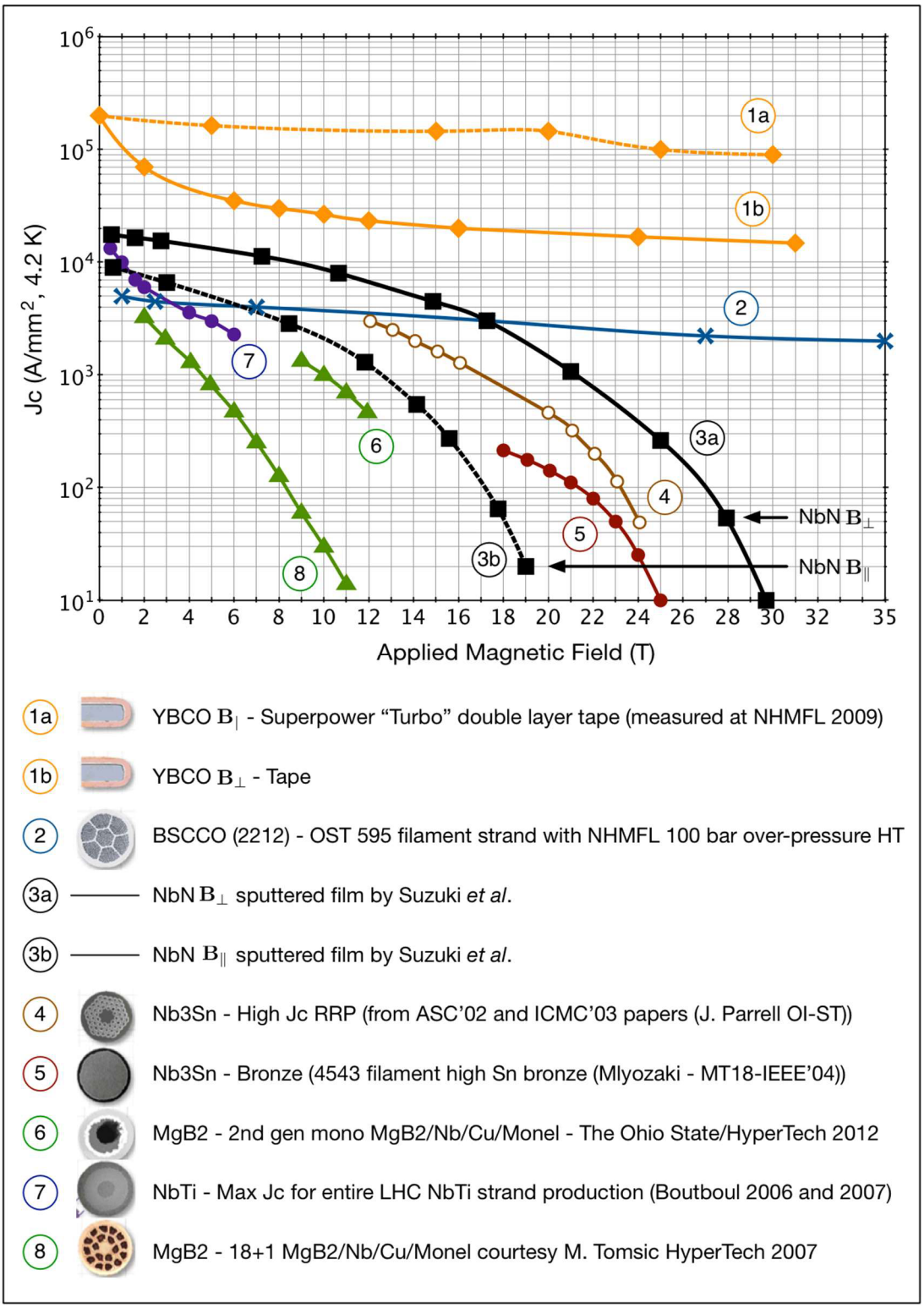

Figure 3.27: The critical current density as a function of applied magnetic field for a number of Type II superconductors. The black square symbols represent the NbN sputtered film in two orientations in accord with the findings of Suzuki *et al*. [111]. (Graph adapted from [112].)

thin films is greater than the important commercial materials NbTi and Nb_3Sn. Given the increase in the superconducting transition temperature of bulk material afforded by the inclusion of carbon, and the increase in upper critical field caused by a reduction in particle size, Suzuki's results are very encouraging. At the very least it shows that such critical currents are achievable. Unfortunately, the J_c results obtained by Pessall *et al*. on various compositions of bulk niobium carbides are much lower, particularly in high magnetic fields [77]. Figure 3.28 reveals their findings.

While Pessall's J_c results are no match for Suzuki's, they state that their samples exhibited a porosity between 25 and 50%, and that this porosity was not constant along the length of their samples, and therefore, the current density depicted in Figure 3.28 could actually be at least double those shown [77]. This reasoning is more than supported by Spitzer who later produced niobium carbide films with $J_c's$ in the range 5 to 7.5x10^5 A/cm^2 [96]. Another point to be noted about Pessall's work is that it was conducted in 1965, therefore, their concerns about the quality of their material are reinforced by the increase in the quality of the production methods that have occurred since.

Figure 3.29 shows the critical current results for two NbN-sintered compacts, one sintered in 10 atm N_2 and the other in 1 atm N_2 by Powell *et al*. [80]. Powel *et al*. also conducted critical current measurements on their niobium carbide. Their results were extremely "disappointing" with

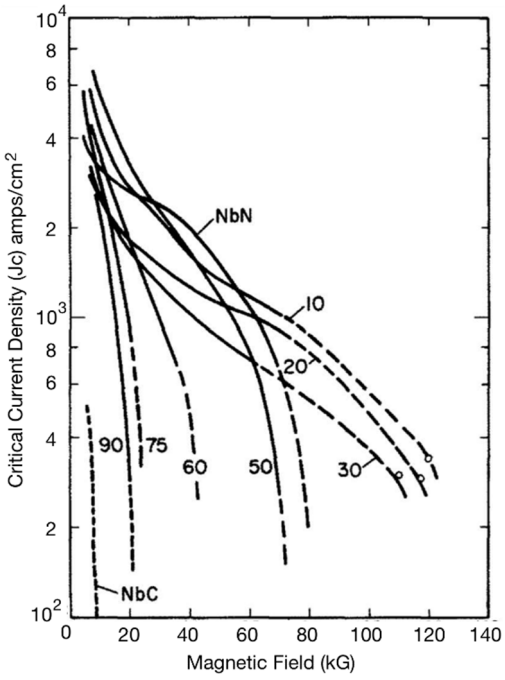

Figure 3.28: Critical current density as a function of magnetic field for niobium carbonitride. Material produced by Pessall *et al*. [77]. The numbers indicate the mole % of NbC in NbN.

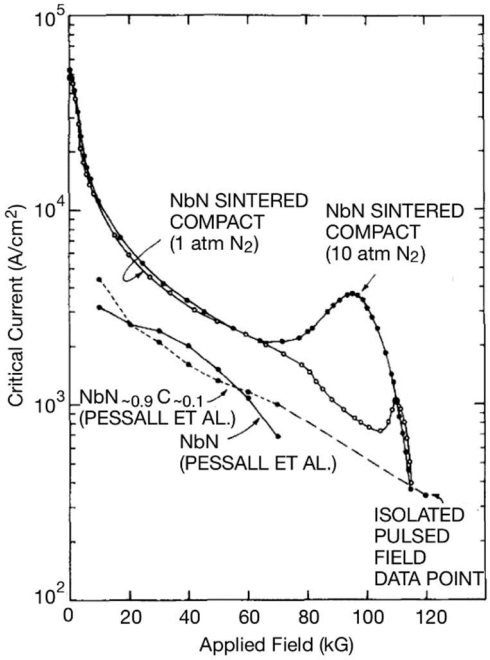

Figure 3.29: Critical current density as a function of magnetic field for two samples of niobium nitride sintered compacts. Powell *et al*. [80].

J_c less than 2x10^3 A/cm^2. However, they believe that the low J_c values were perhaps a result of excess carbon at the grain boundaries. It should be noted that Powell *et al*. paid most attention to their niobium nitride and did not pursue any improvement in their niobium carbide production technique. Therefore, their results should not be viewed as a limiting characteristic of niobium carbide itself but more as a limited attempt at its fabrication.

Work conducted by Ekin *et al*. shows that the critical current of niobium nitride thin film is not affected by uniaxial strain between magnetic fields 6 to 22 T. This can be seen in Figure 3.30. These particular films were prepared by a reactive sputtering technique developed by Gavaler *et al*. [113].

The situation regarding the reported measurements of the critical current densities of niobium nitride and carbide is a tale of two extremes. At one extreme we have the excellent results reported by Suzuki *et al*. on niobium nitride thin films, while at the other extreme we have disappointing results reported on bulk material. This impasse, rather than revealing the inadequacies of the materials in their bulk form, actually reveals the inadequacies of these previous attempts at producing the materials.

3.6 Concluding comments

There has been a number of efforts over an extended period of time to improve the superconducting properties of niobium nitride, niobium carbide and niobium carbonitride. The most utilised forms of fabrication technique have ranged from the reaction of niobium containing compounds with nitrogen containing gases (in the case of niobium nitride formation) and the direct reaction at high temperature between niobium and graphite (in the case of niobium carbide). The fabrication of bulk form niobium carbonitride has also primarily involved the direct high temperature reaction between niobium nitride and niobium carbide.

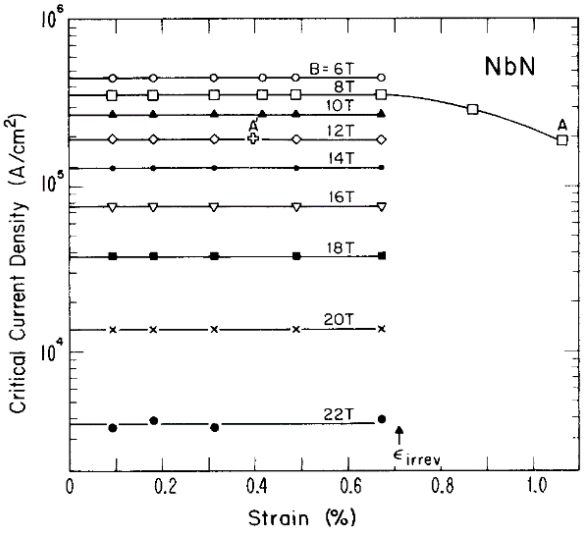

Figure 3.30: Critical current density as a function of strain applied to a sample of niobium nitride by Ekin *et al*. [113].

Of the fabrication techniques discussed in this review, no one technique can be regarded as being the *best*, since each has its own merits. It is therefore a matter of selecting the method that best matches the available facilities and expertise. For example, low temperature fabrication of all three materials is possible; unfortunately, this route is accompanied by an increase in precursor preparation and a more complicated fabrication process. These complications, however, can be avoided at the expense of increased reaction temperatures. There are therefore two major routes that can be taken; a low temperature or a high temperature route. The facilities and expertise at hand dictated that the high temperature route should be the one adopted for this thesis work.

It is apparent that all three differing forms of material i.e. bulk, film and wire, all have different superconducting limits. For instance, the current maximum transition temperature of 17.3 K in a niobium nitride thin film has been produced by Keskar *et al*. However, the current limit for niobium nitride in bulk form is only 16.3 K (produced by Watari *et al*. – other groups with T_c in this region include Horn *et al*., Troitsky *et al*, and Miki *et al*.). Giorgi *et al*. have produced niobium carbide with a transition temperature of 11.1 K in bulk form. This is extremely close to the current limit of 11.2 K, which was the result of Shi *et al*.'s production of niobium carbide nanotubes.

While it is not prudent to single out any one particular fabrication technique as being the *best*, the same cannot be said for the materials themselves. The maximum values discussed so far, as improved as they are, are deficient in comparison to that of niobium carbonitride bulk material. Both Matthias *et al*. and Williams *et al*. managed to produce niobium carbonitride with a transition temperature close to 17.8 K. This value is even superior to that of the thin film form, which is around 17.3 K. This shows that niobium carbonitride is by far the best material of the three reviewed in this chapter, as far as transition temperature is concerned.

Of course, transition temperature is not the only superconducting property of interest and this chapter has dealt with other characteristics, most notably, the upper critical magnetic field, which in the case of niobium carbonitride is approximately 11 T. This is 4 T less than bulk form niobium nitride. Fortunately, work conducted by Troitskiy *et al*. shows that this 11 T critical field can be raised to approximately 42 T by producing a *nanocrystalline* powder. Similar work by Troitskiy with niobium nitride only managed to raise its upper critical field to ~32 T. Therefore, the superiority of niobium carbonitride over niobium carbide and niobium nitride is obvious.

The highest transition temperature has been achieved by Williams *et al*. (and other groups) while the highest upper critical field has been achieved by Troitskiy *et al*. Rather than continue to treat these two properties in relative isolation of each other, the next logical step is the amalgamation of this previous work to attempt to produce bulk form niobium carbonitride with the very best transition temperature, upper critical field, and possibly critical current density. Niobium carbonitride is an obvious route to obtaining superior superconducting properties in a robust, refractory, low temperature superconductor that could possibly be included in the category of workhorse materials for future applications.

Chapter 4

Fabrication of microcrystalline and nanocrystalline niobium carbonitride

4.1 Introduction

There are many different routes that lead to the production of nanocrystalline niobium carbonitride (see Chapter 3 for details). This chapter deals specifically with the route adopted by us, which first involved the production of two batches of high quality (single phase) microcrystalline material by solid state reaction of precursor powders. This fabricated microcrystalline material was then subjected to grinding and impact mechanisms through mechanical ball milling that substantially reduced grain size and produced an amorphous powder. The milled powder was then pressed in a high heat, high pressure environment (hot isostatic press at 2000 bar) to grow larger nanocrystalline grains within a dense solid compact. The following sections detail the fabrication processes themselves, the methodologies adopted and the niobium carbonitride (NbCN) samples produced.

4.2 Fabrication of microcrystalline material

4.2.1 Preliminary experiments

There are a number of different elemental and/or compound precursor combinations that can be used to form NbCN within a number of different treatment conditions. We decided to adopt a solid-state fabrication approach, which (as Chapter 3 shows) has the advantage of requiring relatively straightforward hardware but the disadvantage of fabrication at very high temperatures. We started by performing preliminary experiments designed to determine the precursor combination and treatment conditions required to produce the very best material from the available equipment. Table 4.1 summarises the 127 samples produced using 31 independent heat-treatments using fabrication temperatures up to 1650 °C.

The early batches of sintered NbCN pellets (the first 41 in Table 4.1) were found to be encrusted in a dark multi-phase layer (~ 1 mm thick) that surrounded a distinctly lighter grey, single phase, inner volume (see Figure 4.1-a). The shape of the crust on each pellet coincided with the shape

Table 4.1: Chronological list of the 127 samples fabricated during 31 solid state sintering heat-treatments. Samples 110 to 127 are the main focus of this work. Samples marked as "rt" are previously sintered pellets that have been subsequently re-heat-treated.

samples						heat-treatments							
	composition						sintering segment		Nitriding segment				
sample pellet number	*Nb*	*C*	*Nb C*	*Nb N*	*pellet dia.* (mm)	*remarks*	*#*	*temp.* (℃)	*dwell* (h)	*temp.* (℃)	*dwell* (h)	*Nb gas guard*	*quality check* T_c	*remarks and results/conclusions*
S1			0.3	0.7	11		*1*	1650	4	1360	4		16.2	
S2			0.3	0.7	11		*2*	1650	36	1360	4		17.1	
S3-S5			0.3	0.7	11	rt. 1 & 2	*3*	1650	72	1360	4		17.6	
S6			0.3	0.7	11								17.4	
S7			0.2	0.8	11		*4*	1650	114	1360	4		17.7	*Experiments designed to find optimum sintering and nitriding conditions.*
S8			0.4	0.6	11								17.4	
S9-S15			0.3	0.7	11		*5*	1650	114			NO	17.6	Best material produced with sintering dwell time of 72 hours and above. Nitriding dwell temperature did not affect material quality.
S16						rt. 10	*6*			1280	4		17.7	
S17						rt. 11	*7*			1320	4		17.6	
S18						rt. 12	*8*			1360	4		17.6	
S19						rt. 13	*9*			1400	4		17.5	
S20						rt. 14	*10*			1440	4		17.6	
S21						rt. 15	*11*			1480	4		17.6	
S22			0.2	0.8	11								17.2	
S23			0.25	0.75	11								17.2	*Experiment investigating different carbon and nitrogen proportions.* $NbC_{0.3}N_{0.7}$ found to be optimum
S24			0.3	0.7	11		*12*	1650	114	1360	4	NO	17.4	
S25			0.35	0.65	11								17.3	
S26			0.4	0.6	11								17.3	
S27-S30			*0.3*	*0.7*	*16*		*13*	*1650*	*114*	*1360*	*4*	NO	16.5 to 17.1	*Material production intended for milling experiments.* Quality poor – low T_c and homogeneity
S31-S38			*0.3*	*0.7*	*11*		*14*	*1650*	*114*	*1360*	*4*	NO	17.0 To 17.4	*Experiment designed to investigate furnace location dependent material quality. Best location was found*

#	Nb	C	NbC	NbN	dia.	remarks	#	temp	dwell	temp	dwell	gg	T_c	remarks
S39			0.3	0.7	11		*15*	1650	114	1360	4	NO	9.5	*Ar not N_2 to investigate contaminated crust formation.* Crust still formed.
S40-S41			0.3	0.7	11		*16*	1650	114	1360	4	NO	15.2	*Furnace test after essential maintenance (aborted)*
S42			0.3	0.7	11		*17*	1650	114	1360	4	YES (1st)	17.3	*Initial test of Nb gas guard.* No crust formation but T_c still low
S43			0.3	0.7	11		*18*	1650	114	1360	4	YES (1st)	17.2	*Different pellet sizes to investigate homogeneity.* Both pellets equally low T_c
S44			0.3	0.7	3								17.1	
S45			0.3	0.7	11		*19*	1650	114			YES	17.2	*No nitriding segment.* Sample T_c still low
S46			0.3	0.7	11		*20*	1685	114			YES (1st)	17.3	*Test with increased dwell temp.* Thermocouple broke during treatment. Sample T_c still low
S47			0.3	0.7	11		*21*	1650	114	1360	4	YES (1st)	17.4	*Test of different precursor powders.* T_c better but not as high as desired
S48			0.3	NIL	3								17.5	
S49			0.3	0.7	3								17.4	
S50			0.3	0.7	11		*22*	1650	114	1360	4	YES (1st)	17.6	*Experiment to determine best precursor combination.* Sample 50 produced most solid pellet
S51	0.3	0.3		0.7	11								17.5	
S52	1	0.3			11								17.6	
S53	0.7		0.3		11								17.6	
S54-S61			0.3	0.7	11		*23*	1650	114	1360	4	YES (2nd)	15.8	*Material production intended for milling experiments.* Low T_c – problem thought to be the new gas guard.
S62			0.3	0.7	11		*24*	1650	114	1360	4	YES (1st)	17.0	*1st use of 2nd gas guard in treatment 23 resulted in poor material – this experiment was used to determine if the 2nd gas guard was at fault.*
S63	1.0	0.3												
S64						rt. 54							17.3	
S65						rt. 55								

#	Nb	C	NbC	NbN	dia.	remarks	#	temp	dwell	temp	dwell	gg	T_c	remarks
S66			0.3	0.7	11								16.4	
S67	1.0	0.3												2nd guard material lower T_c than 1st but both batches still poor.
S68						rt. 56	*24*	1650	114	1360	4	YES (2nd)	16.3	
S69						rt. 61								
S70	1.0	0.3			11								17.4	*Used open ended gas guard*.
S71			0.3	0.7	11		*25*	1650	114	1360	4	YES (1st)	17.4	Quality improved from treatment 24.
S72-S79			0.3	0.7	11								15.3	*Material production intended for milling experiments*.
S80						rt. 62	*26*	1650	114	1360	4	YES (2nd)		Furnace element breakage during treatment.
S81			0.3	0.7	11									*Post furnace repair test*.
S82-S88						rt. 74-80	*27*	1650	114	1360	4	YES (2nd)		Repair successful.
S89-S96			0.3	0.7	11							YES	16.3	
S97			0.2	0.8	11									*Experiment aborted due to furnace element breakage - the treatment was restarted after element replacement*. T_c still inferior to earlier treatments.
S98			0.25	0.75	11									
S99			0.3	0.7	11		*28*	1650	114	1360	4	YES (1st)	17.1	
S100			0.35	0.65	11									
S101			0.4	0.6	11									
S102-S108					11	rt. 89-91, 93-96							17.1	*Retest without gas guard*.
S109			0.3	0.7	11		*29*	1650	114	1360	4	NO	17.4	Moderate T_c + crust formation
S110-S119			0.3	0.7	11		*30*	1650	114	1360	8	YES	17.5	*This is sintered batch 1 material* – see Table 4.2
S120-S127			0.3	0.7	11		*31*	1650	114	1360	8	YES	17.5	*This is sintered batch 2 material* – see Table 4.2

one would expect a (gas) flow of contaminants to make as it passes over the exposed surface area. This, along with x-ray diffraction data (see Figure 4.6), strongly suggested that the sample pellets were *gettering* oxygen impurities from the nitrogen gas supply. The presence of this crust was an undesirable consequence of the continuous gas flow. It was a simple task to remove the crust by chipping it off the pellets to reveal the purer material underneath, but this resulted in a

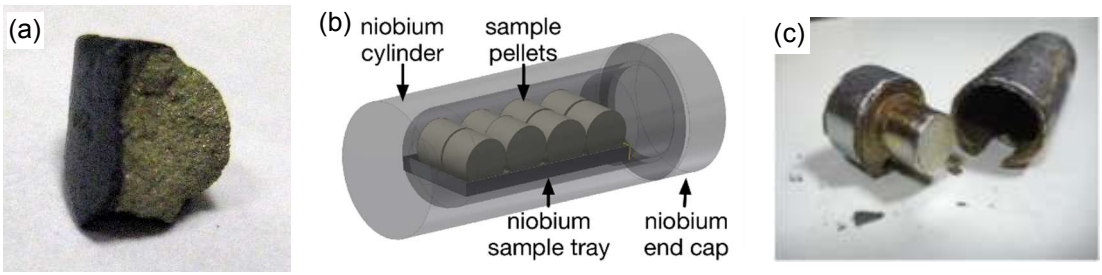

Figure 4.1: (a) Part of a heat-treated sample pellet showing the dark multi-phase crust surrounding its outer surface. (b) Diagram of the niobium gas guard used to prevent impurity crust formation. The sample pellets sit on a niobium tray inside a niobium cylinder that has its only open end loosely blocked by a niobium cap. (c) Photograph of the gas guard and end cap after a number of heat-treatment cycles.

substantial reduction in useful material. Investigations into solving the crust problem started with heat-treatment 15, which sintered sample S39 in an argon atmosphere instead of nitrogen to establish if the gas type affected the crust formation, which it did not. The contamination was either due to small amounts of impurities in the gas cylinders accumulating on the samples over the relatively long treatment time, leaks in the gas supply circuit, or a combination of both. Rather than partake in a lengthy investigation to determine the route source of the contamination, it was decided to stop the contamination from reaching the samples, as opposed to stopping it from entering the gas supply. This was achieved by replacing the alumina boat (that contained the sample pellets) with a niobium cylinder that had its only open end loosely blocked by a niobium cap (see Figure 4.1-b). This niobium cylinder - referred to as a *gas guard* from now on – was then inserted into the sintering tube (see Figure 4.2) in substitution for the alumina boat discussed earlier. The surface area of the niobium gas guard acted as a sacrificial getter that reduced the impurities in the nitrogen gas flow prior to it reaching the samples within. This solution was very successful in almost all the heat-treatments it was used. However, the niobium visibly degraded and became more brittle after each successive heat-treatment, which limited its useful lifetime to only a few heat-treatment cycles (see Figure 4.1-c).

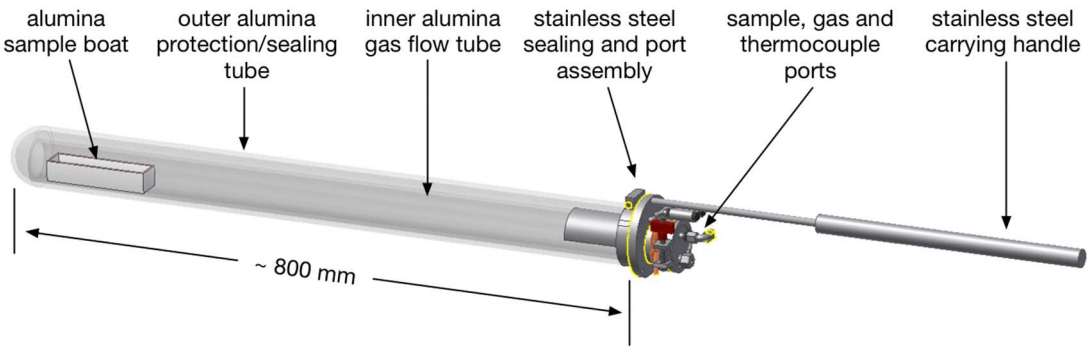

Figure 4.2: Bespoke sintering tube assembly used to transport samples between the glove box environment and the high temperature furnace for heat-treatments up to 1700 °C within a controlled atmosphere (argon or nitrogen).

Samples S42 to S49 were used to investigate gas guard use, the effect of different pellet sizes on sample homogeneity and the quality of different batches of precursor powders. Samples S50 to S53 were used to investigate the effect of different precursor combinations on the quality of the sintered material. These samples showed that the precursor compounds NbC and NbN produced the most homogeneous, solid, sintered samples of NbCN. These properties were evaluated by visual inspection, by using x-ray diffraction, by measuring the superconducting transition temperature at different locations within the sample or by some combination of them all. Samples S54 to S109 were attempts at producing batches of material for milling and HIPing experiments that were beset by equipment failures and reductions in sample quality and were accompanied by heat-treatments designed to investigate these issues. Samples S110 to S127 were successful heat-treatments that produced the microcrystalline material that became the focus of this work.

4.2.2 Preparation of powders

The NbC powder (product No. 12147) and NbN powder (product No. 12146) were purchased from Alfa Aesar (UK) and were stored within a glove box that maintained a low oxygen (≤ 1 ppm) and low moisture (≤ 5 ppm), inert argon atmosphere. All preparation work that included the use of these powders was conducted within the glove box to minimise the exposure to air. Proportions of the precursors, required to produce the composition $NbC_{0.3}N_{0.7}$, were first mixed by hand using a mortar and pestle and then mechanically mixed in a titanium vial (without balls) using a Fritsch Pulverisette 6 planetary ball miller. The mixing program was set to run for one hour at 200 rpm with a reversal in direction occurring every *fifteen* minutes. This thoroughly mixed precursor powder was then pressed into compact pellets of approximate dimensions 11 mm diameter by 10 mm high, each weighing approximately 5 g.

4.2.3 Solid-state sintering of samples

Due to the refractory nature of the precursor materials NbC and NbN - *which have very high melting points (NbC: 3610 °C [61]*, *NbN: 2050 °C [56])* - and the relatively low maximum temperature obtainable by the available equipment (Carbolite three zone 1800 °C tube furnace (TZF18/102/600)), $NbC_{0.3}N_{0.7}$ could only be fabricated using solid-state sintering, as opposed to melting. The following section provides a brief review of solid-state sintering.

Coarsening, densification and solid-state driving mechanisms

As the radius of a sphere of material increases, the surface area to volume ratio decreases. This means that larger grains have proportionately less surface areas than smaller grains and therefore, larger grains have proportionately less excess surface energies. This makes the formation of large grains, from the coalescence of small grains, energetically favourable. There are two main processes involved in reducing the excess energies associated with the surface areas of grains; they are, *coarsening* and *densification* (see Figure 4.3) [114].

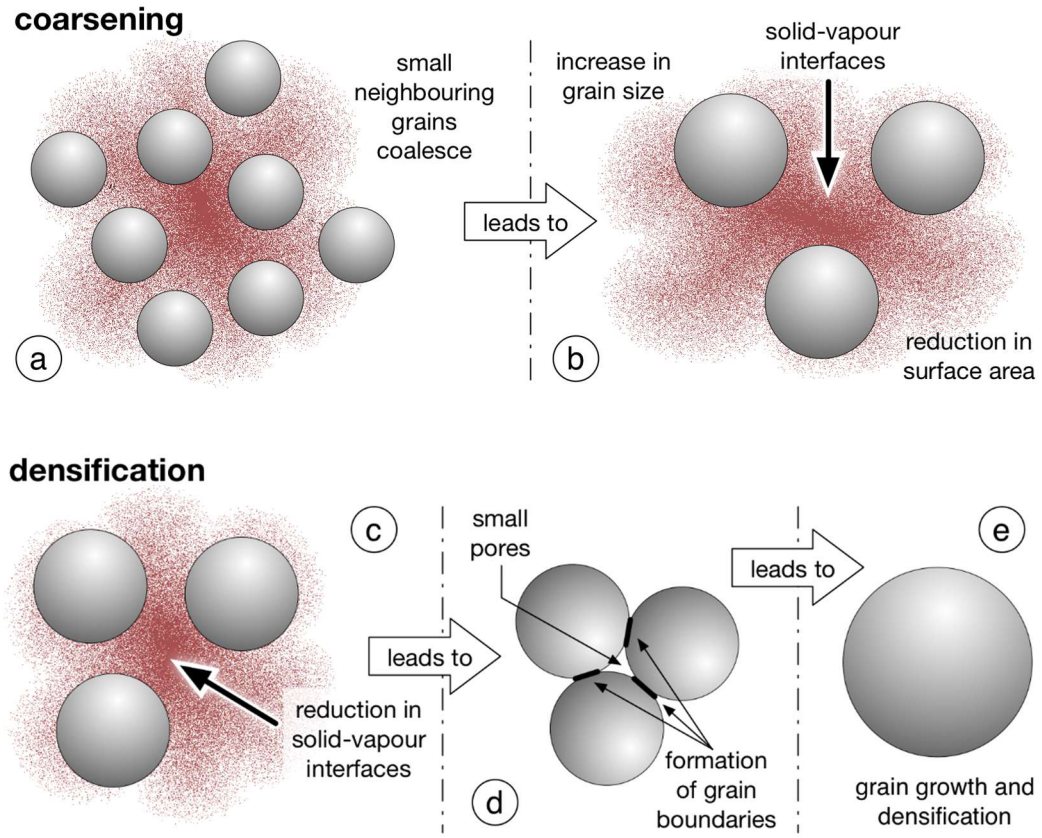

Figure 4.3: The two main processes that drive solid-state sintering are *coarsening* and *densification*. (a) The coalescence of small neighbouring grains leads to (b) increases in grain size and reductions in surface areas that produce a *coarsened*, porous bulk. (c) Reductions in solid-vapour interfaces lead to (d) grain boundary and small pore formation that produce (e) grain growth and *densification*.

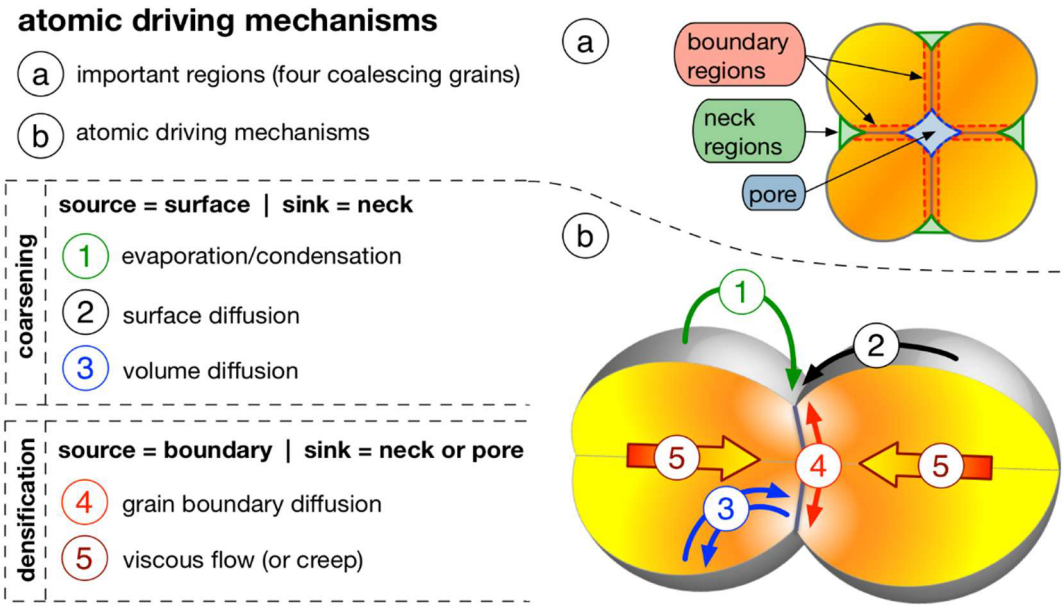

Figure 4.4: The atomic driving mechanisms that lead to coarsening and/or densification during solid state sintering. a) Some important regions within coalescing particles. b) The five atomic driving mechanisms. (Adapted from [115].)

Coarsening consists of small grains coalescing to form larger grains that remain separated from one another by vapour-solid interfaces. There are three main atomic driving mechanisms responsible for coarsening. They are;

1) *evaporation* - surface material evaporates and then re-condenses in neck and/or pore regions (see Figure 4.4-1),
1) *surface diffusion* - surface material diffuses towards neck and/or pore regions (see Figure 4.4-2),
2) *volume diffusion* - surface material diffuses through the inner volume towards boundary, neck and/or pore regions (see Figure 4.4-3).

Densification consists of grains coalescing to form grain boundaries and pore regions and is driven by two atomic mechanisms. These mechanisms are;

1) *diffusion* - grain boundary material diffuses towards neck and/or pore regions (see Figure 4.4-4),
2) *viscous flow* - volume material flows slowly towards boundaries (see Figure 4.4-5).

Coarsening and densification are often competing mechanisms in solid state sintering; which of them dominates is largely determined by the sintering temperature. Lower temperatures promote evaporation/condensation and surface diffusion, which lead to coarsening. Higher temperatures promote grain boundary and volume diffusion, which lead to densification [114]. Other factors, such as precursor density, precursor grain size distribution and vapour pressure are also parameters that can be used to discriminate between coarsening and densification providing one with an advantage over the other.

The production of sintered samples

The heat-treatment program (see Figure 4.5) consisted of a slow 264 °C/h ramp (4.4 °C/min to reduce the possibility of cracking the furnace tube) to 1650 °C, followed by a 114 hour dwell period. The furnace program then ramped the temperature down to 1360 °C where it dwelled for 8 hours. This final temperature plateau was used to control the nitrogen content of the material in accord with Williams *et al*. [86] who found that their best material was produced using a temperature of 1360 °C. Two separate heat-treatments (30 and 31 in Table 4.1) were used to produce enough material for further processing by milling and HIPing. These two batches of sample pellets – 10 in batch 1 and 8 in batch 2 - are shown in Table 4.2. The material in both batches were of similar quality. Up to 10 pressed sample pellets at a time were placed on top of a 0.25 mm thick niobium tray which was itself placed within a niobium gas guard described earlier. All work was conducted within the glove box. The gas guard (with samples) was inserted into the sintering tube (see Figure 4.2) that was then made gas tight. The sintering tube was used to transport the samples between the glove box and the high temperature furnace within a sealed environment. The samples remained within the tube throughout the heat-treatment and the tube's

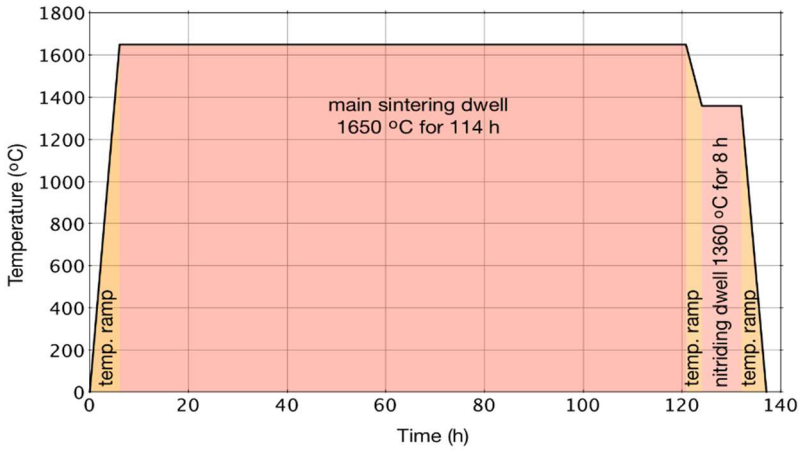

Figure 4.5: Heat-treatment profile for sintering $NbC_{0.3}N_{0.7}$ sample pellets in a flowing nitrogen atmosphere. Temperature program; ramp to 1650 °C at 264 °C/h and dwell for 114 hours, ramp to 1360 °C and dwell for 8 hours, switch off heaters.

Table 4.2: Sample pellets of $NbC_{0.3}N_{0.7}$ fabricated by solid state sintering in accordance with the heat-treatment shown in Figure 4.5. Two separate sample batches were fabricated in two separate heat-treatments (treatments 30 and 31 in Table 4.1). Only material from the central internal volume of the pellets was used for further processing to avoid the inclusion of surface contamination (this internal uncontaminated material is referred to as *recovered* mass).

	sample pellets in sintered batch 1 (*total recovered microcrystalline mass ≈ 23 g*)									
Pellet Number	$S110$	$S111$	$S112$	$S113$	$S114$	$S115$	$S116$	$S117$	$S118$	$S119$
Pre sintered mass (g)	4.91	4.93	~ 4	~ 4	4.88	3.76	5.03	5.07	4.49	3.22
	sample pellets in sintered batch 2 (*total recovered microcrystalline mass ≈ 13 g*)									
Pellet Number	$S120$	$S121$	$S122$	$S123$	$S124$	$S125$	$S126$	$S127$		
Pre sintered mass (g)	4.92	4.93	4.96	4.92	4.94	4.93	4.93	4.66		

length allowed the samples to be situated within the furnace's central heated zone. Prior to initiating the heat-treatment program the sintering tube had its stagnant argon atmosphere exchanged for flowing nitrogen through the tube's gas ports. This flowing nitrogen was maintained throughout the heat-treatment.

4.2.4 X-ray diffraction

X-ray diffraction data for these NbCN samples were obtained using a Siemens D5000 Powder Diffractometer. Two methods of data analysis were adopted. In simple cases of phase identification a visual comparison between the collected XRD data and patterns obtained from

the Chemical Database Service [116] were conducted. When more detailed knowledge was required, such as grain size and weight percent, for example, Rietveld refinement of the collected data was conducted using the TOPAS-Academic scripting software package [117].

Precursor powders

XRD data of the NbC precursor powder is shown in Figure 4.7, which confirms that it was single phase. Information available from Alfa Aesar states that the NbC had a purity of 99+%. XRD data of the NbN precursor powder (see Figure 4.8) showed that it was not single phase. A number of additional i.e. none NbN, diffraction peaks are clearly visible. A visual comparison with possible candidates, such as Nb, Nb_xN_{1-x} (of various stoichimetries) or niobium oxide, for example, did not produce an identification for the additional phase(s). A more detailed analysis was not conducted because the impurities did not affect the final fabricated material (see Figure 4.9). Alfa Aesar did not have any purity information available.

Fabricated material and impurity crust

Typical XRD data of fabricated $NbC_{0.3}N_{0.7}$ are shown in Figure 4.9. These data were obtained from material recovered from sintered batch 1 pellets (see Table 4.2) and show that this material was single phase. Figure 4.6 shows typical XRD data of the crust that forms around the surface of the fabricated $NbC_{0.3}N_{0.7}$ (see Figure 4.1-a) when a niobium gas guard is *not* used. Most of the additional diffraction peaks belong to Nb_2O.

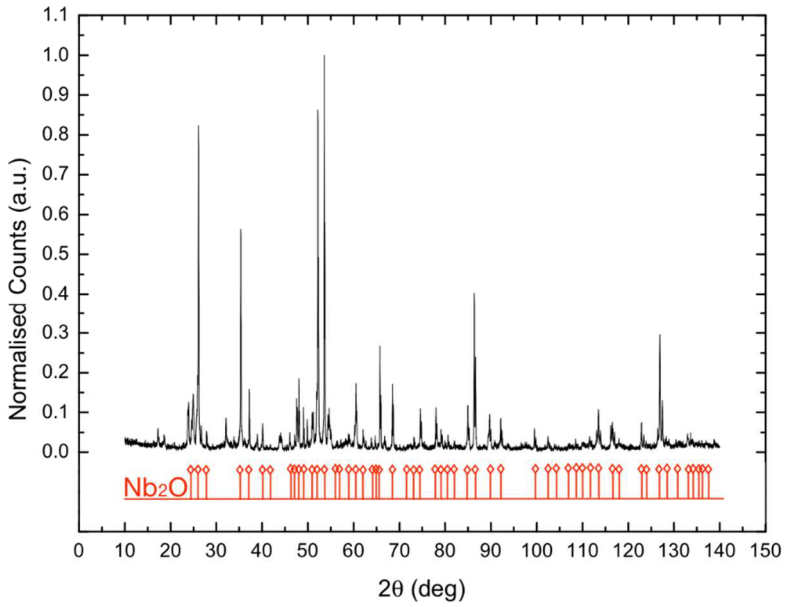

Figure 4.6: Typical XRD data of the crust that forms around the surface of the $NbC_{0.3}N_{0.7}$ sample pellets during solid state sintering (without gas guard). The red lines with open symbols indicate the expected peak positions for Nb_2O (obtained from [116]).

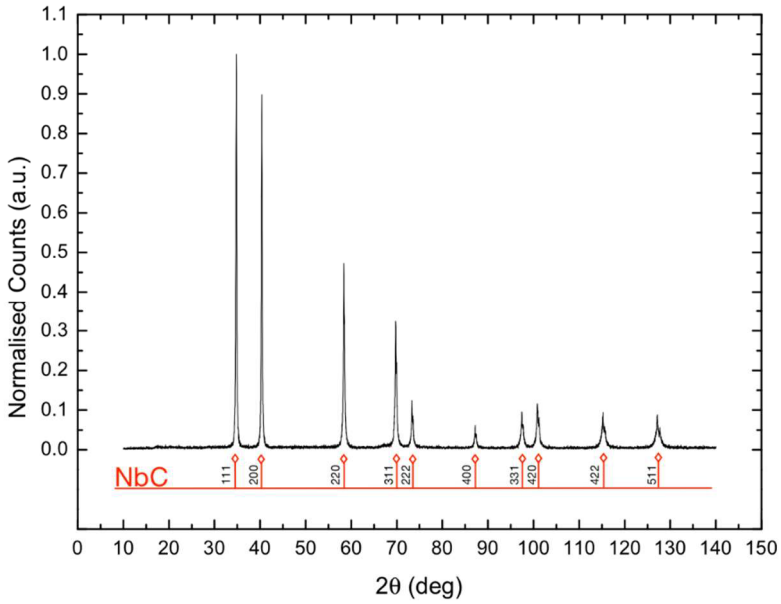

Figure 4.7 Typical XRD data of precursor NbC powder. The red lines with open symbols indicate the expected peak positions for NbC (obtained from [116]).

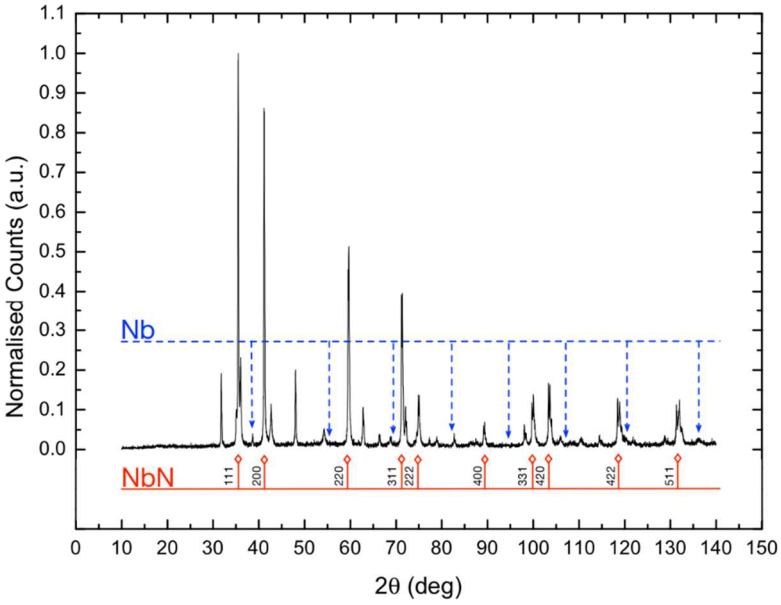

Figure 4.8: Typical XRD data of precursor NbN powder. The red lines with open symbols indicate the expected peak positions for NbN (obtained from [116]).

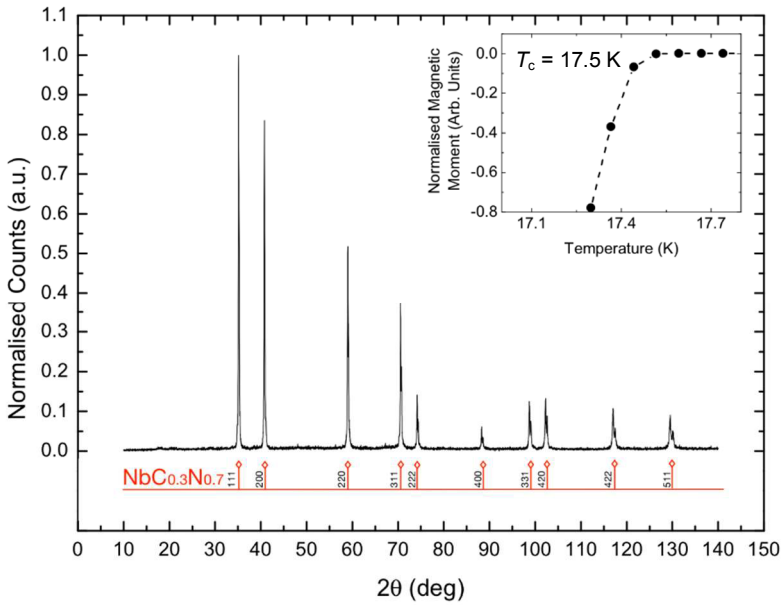

Figure 4.9: Typical XRD data of fabricated $NbC_{0.3}N_{0.7}$. These XRD data were taken from measurements conducted on pellet 6 of sintered batch 1 material, SB_6^1, (see Table 4.2). The red lines with open symbols indicate the expected peak positions for $NbC_{0.3}N_{0.7}$ [118]. The inset shows the *zero* field magnetic susceptibility data from which the onset of T_c was obtained.

4.3 Fabrication of nanocrystalline NbCN by mechanical ball milling

Mechanical ball milling is described as the delivery of a sustained sequence of high energy impacts to a powder sample (also referred to as a powder *charge*) with a view to either producing new material or changing the properties of the current one(s). The terms “disordering”, “milling”, “ball milling” and/or “mechanical milling” are used interchangeably in the literature – we shall use ball milling or milling throughout. In general, there are three main processes that lead to material changes during milling. They are: *alloying*, which is the production of material through the transfer or exchange of constituent components; *disordering*, which is the control of grain size; and *reaction milling*, which is the generation of solid-state chemical reactions [119]. These processes are selected and controlled through a number of processing parameters that in combination weight the dynamics towards a particular outcome. Some of these parameters are; miller type, container (vial) size, internal vial shape, vial material, milling speed, milling time, used vial capacity, temperature, ball-to-powder ratio (BPR) and ball size distribution. In the following sections the use of milling to reduce grain size, which is particularly important for superconducting properties (considered in Chapter 5) is discussed.

4.3.1 Milling media and preparation

A SPEX 8000D Mixer/Mill was used (see Figure 4.10-a). Its operation requires the use of a milling vial that contains the powder charge (sample material) and a number of milling balls. The working vial is clamped into the SPEX Mill and is counterbalanced by an empty vial that is clamped diametrically opposite. This set up greatly reduces the vibrations the apparatus produces. The

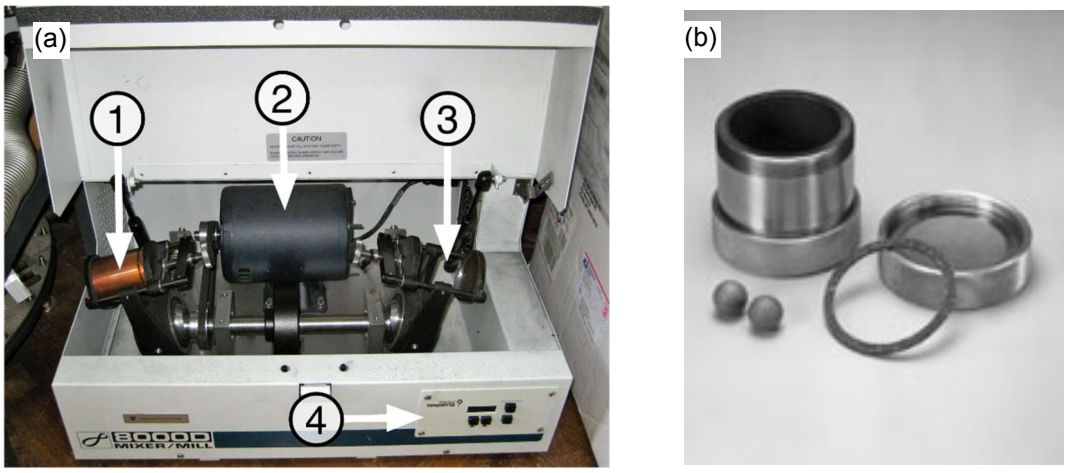

Figure 4.10: (a) SPEX 8000D mixer/mill. (a-1) Dummy vial used as a counterbalance. (a-2) Motor. (a-3) Clamp for sample vial. (a-4) Timer panel for process control. (b) Tungsten carbide milling vial and balls [121].

SPEX mechanism shakes both vials in a motion that traces out a figure eight that is approximately 60 mm high by 25 mm wide [120]. This motion controls the paths followed by the enclosed spherical milling elements causing them to scrape and impact against the sample powder 875 times per minute [120]. This scraping and impacting causes plastic deformation and particle fracture that exposes fresh surfaces. These surfaces are then able to cold weld with those from other particles, which causes some grain *growth* instead of grain size *reduction*. Careful control of the milling parameters promotes fracturing at the expense of welding and therefore leads to a particle size distribution that is strongly weighted towards reduced particle dimensions. A consequence of particle fracture, however, is the increased number of freshly exposed particle surfaces that are susceptible to collecting contamination from the vial's internal atmosphere and/or side wall. It is therefore very important to try to stop contamination from occurring and to *manage* the likely sources of contamination to reduce their influence on the desired end product.

Contamination management

The greatest source of contamination is the vial's internal walls where wall material is exchanged for sample material. There are a number of methods that can be used to reduce this type of contamination. If the sample powder is soft then hard, dense, milling media can be used. This increases the impact energy transferred to the powder charge and allows milling times to be reduced. Also, a mixture of different ball sizes randomises their motions, reducing the chances of the balls continuously moving along the same trajectory. This stops contamination arising from track formation where vial material is repeatedly gouged out of the side wall and into the powder charge. Another method of contamination control is to use milling media that is made from the same material as the powder charge. While this ensures no *foreign* material is introduced into the sample it can lead to a change in composition if the sample is comprised of more than one constituent. Low ball-to-powder ratios can also be used to promote the number of ball-to-powder impacts at the expense of ball-to-wall impacts. It is also important to ensure that the media has

an air tight seal and that the gaseous atmosphere contained within is itself contaminant-free and does not react with the powder charge (though in the case of reaction milling this might actually be a desirable outcome). This can be achieved by loading and unloading the milling media with powder charge within the confines of a glove box with a high purity inert atmosphere, such as argon. Another contamination control measure is the *conditioning* of the milling media. This is a very important process that consists of conducting a number of independent milling runs, mimicking the intended experimental procedure as closely as possible, but treating the milled product as waste. The purpose is to pre-coat the internal walls of the vial and the surface areas of the milling balls with powder charge material. The logic here is that once the coating is completed, the exchange of material between the vial's internal wall (and balls) and the powder charge is mostly comprised of powder charge material, with the powder charge coating acting as a barrier between the milling media and the sample. Of course, there is always still some contamination from the vial wall and balls but the largest contribution of contamination usually occurs during the initial coating process. The best conditioning procedure therefore requires a number of independent milling runs that are completed prior to starting the experiment proper. After each independent conditioning run the contaminated powder charge is replaced with new material, thus resetting the milling conditions back to those required. Each successive conditioning run should tend to converge towards a constant *minimum* contamination level that is the level to be expected from then on. The number of repeat conditioning runs can be empirically determined.

For this work, a preliminary investigation into the minimum number of repeated conditioning runs was undertaken using the precursors NbC and NbN. The focus of this short study was on the use of tungsten carbide (WC) milling media (for reasons discussed below) but niobium, copper and hardened steel were also considered. In the case of niobium milling media it was contamination by *niobium* that was specifically investigated. For copper milling media it was *copper* contamination, for hardened steel it was *iron* contamination and for tungsten carbide it was *tungsten* contamination. The level of contamination was measured using *inductively coupled plasma mass spectrometry* (ICP-MS). This technique ionises the sample with a hot plasma (above 5000 ℃) and then measures the charge to mass ratios of the resultant species using mass spectrometry to identify the constituents. It is a very sensitive technique that can detect concentrations down to parts per trillion [122]. Each vial was loaded with a powder mixture of niobium carbide and niobium nitride in a weight ratio consistent with the stoichiometry $NbC_{0.3}N_{0.7}$ and each milling run lasted 6 hours. The results are shown in Figure 4.11. The data for niobium contamination are interesting because they show that the niobium content of the powder charge actually reduced from its pre-milled value – at least for the first 2 milling runs (12 hours). This is due to the niobium in the powder charge being preferentially coated onto the vial wall rather than wall material being introduced into the powder charge. The data in Figure 4.11 also clearly show that, in the case of tungsten carbide, an equilibrium contamination level is reached after the third milling run from which a 3 to 4 % tungsten contamination is to be expected. The tungsten carbide media also has a cobalt content that can be as high as 6 %, which means the milled product could

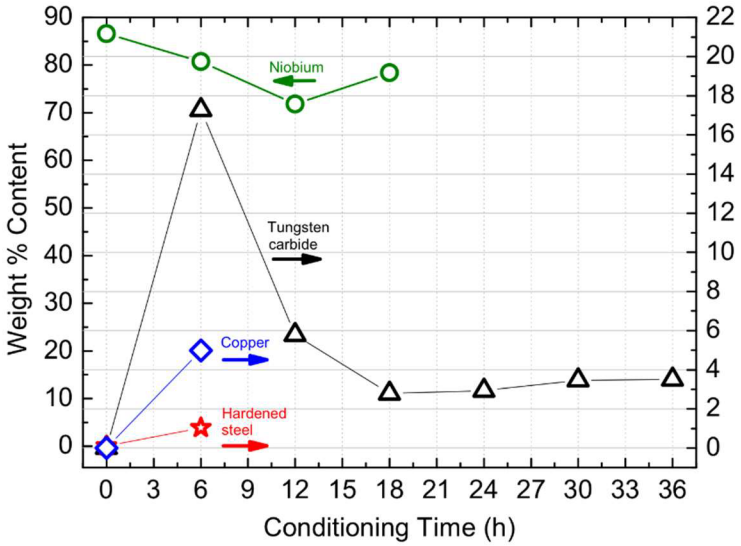

Figure 4.11: Summary of a preliminary investigation into the contamination of a niobium carbide/niobium nitride powder charge after milling for different time periods in hardened steel, copper, tungsten carbide and niobium milling media.

include a 0.24 % cobalt contamination; in the worst case scenario. Although the hardened steel media produced the least contamination, this route was not pursued due to the magnetic nature of the contaminant i.e. iron. The copper media was also discounted due to its softness in comparison to the powder charge.

Milling media and BPR selection

Niobium carbonitride is a very hard refractory material. This decreases the number of techniques available that ensure low contamination. For example, vial selection is made difficult due to the high sample hardness. Ball size is also limited to those that are commercially available since in-house fabrication of equally hard balls would require a significant investment in equipment and expertise. The control of milling speed, which affects impact energies, is also limited when using the SPEX miller because, in contrast to the Fritsch Pulverisette 6 Planetary miller, it has no speed control capabilities. With these issues acknowledged it was decided that hard, commercially available tungsten carbide (WC) milling media was the most appropriate choice - although only one size of WC milling ball was commercially available (approximately 10 mm in diameter). The size of this ball, in comparison to the internal diameter of the milling vial (~ 40 mm), was deemed to be substantial. So, although simultaneously using a quantity of balls increases the number of ball-to-powder impacts (a desirable outcome) and therefore leads to decreased milling times, the simultaneous use of only a few balls, say three, would occupy a sizeable volume of the vial. This can have undesirable affects, such as increased contamination due to ball-to-ball impacts and/or a reduced working of the material due to there being less free vial volume for the balls to move within. It was for this reason that the use of only *two* balls was chosen. It was felt that this was a sufficient compromise between decreasing the milling time (and particle size) whilst also keeping the contamination level as low as reasonably possible. This, in conjunction with the need to mill at least 4 g of fabricated NbCN (about 1 g more than was needed for a sample earmarked for hot

isostatic pressing) led to a ball-to-powder ratio (BPR) of approximately 5:1 being used (mass of two WC balls was ~ 21.6 g).

Preparation of sintered material for milling

The outer layers of each of the sample pellets from both of the sintered batches, (see Table 4.2) were manually chipped away using a niobium rod with one end shaped to a chisel-like edge. This process exposed the inner, contaminant-free, volume. This clean volume was then manually pulverised with a mortar and pestle to form a coarse powder. The powder from each pellet from the first sintered batch was then mixed together to form a precursor powder charge for the first milling campaign. Similarly, a second precursor powder charge was collected from the sample pellets of the second sintered batch for use in the second milling campaign. These two batches of materials were stored within an argon glove box and eventually used to condition the milling media and produce the nanocrystalline material.

Milling media re-conditioning

The milling vial and balls (which had been conditioned during previous experiments) was re-conditioned using 4 g of sintered $NbC_{0.3}N_{0.7}$ from the first sintered batch by milling the powder for 6 hours using the SPEX mill. At the end of this milling run, inside the glove box, the side wall was scraped clean with a niobium rod and the milled powder charge removed and disposed of. This re-conditioning procedure was then repeated with another 4 g of material from the first sintered batch. At the end of this procedure the internal surfaces of the vial and the outer surfaces of the balls were fully coated in $NbC_{0.3}N_{0.7}$.

4.3.2 Mechanical milling of microcrystalline NbCN

Two main milling campaigns were conducted. Milling campaign one, in which sintered material from Samples S110 – S119 were mixed and milled to form Batch 1 (see Table 4.2 for sintered sample details) and milling campaign two in which samples S120 –S127 were mixed and milled to form Batch 2. The general milling procedure consisted of one hour long milling sessions interleaved by half-hour rest periods for a total of twenty actual milling hours for each milling run. The rest periods are employed to stop excessive temperatures occurring. Also, the SPEX mill should not be continuously run for periods longer than 1.5 h to keep within the manufacturer's service specifications. Each campaign contained three independent milling runs. In the first milling run, of the first campaign, small quantities of material were extracted from the powder charge at 2, 6 and 12 h intervals. These extractions were carried out during rest periods. The vial was removed from the mill and put into the glove box to perform the actual extraction prior to being resealed and put back into the mill ready for the next hour long milling session. The extracted material produced milled samples, M_2, M_6 , M_{12} and a sample milled for 20 h, M_{20}. We also had a *zero* hour milled sample, M_0 obtained from sintered batch pellet sample S115. They were used for a time evolution study and will be discussed in section 4.3.3. The remaining 20 h

milled material from all the runs in both campaigns produced ≈ 23.5 g of M_{20} sample material. The details of the samples produced from these milling campaigns can be found in Table 4.3.

4.3.3 X-ray diffraction

X-ray diffraction data were obtained by measuring samples M_0 to M_{20} using the Siemens D5000 Powder Diffractometer. These data describe how the grain size changes with increased milling. The data are shown in Figure 4.12. As well as there being a visible broadening of the peak widths due to grain size reduction and strain, an additional peak clearly appears in the 6 h sample, M_6, (between angles 45 and 50 deg) and, not only increases in intensity in the 12 h, M_{12}, and 20 h, M_{20}, samples, but is also joined by another peak (near 30 deg) from 12 h onwards. These two peaks are attributed to tungsten carbide (indexes 001 and 101) contamination from the milling media. Changes in relative peak intensities are also visible in the two major peaks that reside within 35 to 42 degrees in Figure 4.12. Milling causes structural defects, such as anti-site exchange and vacancy formation that contribute to the straining of the milled grains. The repositioning of atomic species caused by this defect formation changes the relative peak intensities in XRD. This is due to the number of atoms (of a particular species), that occupy particular lattice positions, changing.

Grain size

The grain size (diameter) for each of the samples M_0 to M_{20} was obtained through an iterative Rietveld refinement of the raw XRD data using ToPas Academic software. The grain sizes are shown in Figure 4.13. The results for the grain diameter evolution show an expected trend from the microcrystalline starting material, M_0, reducing by a factor of ~ 375 from ~ 6 μm to ~ 16 nm (M_2). The reduction in diameter continues, albeit at a vastly reduced rate, to the 12 h milled material, M_{12}. We then see an increase in diameter in the 20 h milled sample, M_{20}. One explanation for this occurrence is that the small sample taken from the powder charge after 20 h is not representative of the milled sample as a whole due to the introduction of fresh tungsten carbide contamination with sufficiently large grain sizes to skew the average. This possibility is supported by the physical method used to acquire this final milled sample. Once the milling was completed, and the vial was opened within the glove box, the internal walls were scraped with a niobium rod to recover as much of the yield as possible. This recovered yield was not mixed in any way before extracting the sample for XRD. We suggest that large grain sized WC contamination, scraped off the vial walls, was introduced into the total yield and consequently the XRD sample. This process is anomalous because it was only adopted for the final milling session. All the previous milling sessions were only interrupted to extract small quantities of XRD samples directly from the milled powder charge itself, without any scraping of the side walls taking place. One possible means of checking this hypothesis would have been to thoroughly mix the recovered material to distribute the fresh contamination throughout the whole powder charge and then extract a new sample for XRD. If the grain size analysis of this new sample returned a reduced grain diameter to that of the first sample, then the hypothesis would be strengthened.

Table 4.3: Milling campaigns and samples produced. A small amount of zero hour milled material M_0 was first extracted from sample S115. Materials from samples S109 - S119 were then mixed to form batch 1 and samples S120 – S127 formed batch 2. The first campaign used batch 1 material and the second campaign used batch 2 material (see Table 4.2 for details). Each campaign was comprised of *three* independent milling runs, each of 20 h total duration. In the *first* campaign small quantities of material were extracted from the powder charge of Batch 1 at 2, 6 and 12 h intervals, producing milled samples, M_2, M_6 and M_{12} for a time evolution study. Eventually we had two batches of nominally identical material that had been milled for 20 hours: Batch 1 of ~ 11.5 g and Batch 2 of ~ 12 g.

	vial and ball conditioning		milling campaigns									
			0 h milled material	1st Batch, Samples S110 - S119						2nd Batch, Samples S120 - S127		
	run 1	*run 2*	from $S115$	*run 1*			*run 2*	*run 3*		*run 1*	*run 2*	*run 3*
Sample ID	*nil*	*nil*	M_0	M_2	M_6	M_{12}	M_{20} ≈ 11.5 g			$M_{20} \approx 12$ g		
mass (g)	4	4	N/A	0.19	0.20	0.23	3.38	4	4	4	4	4

Unfortunately, by the time this grain size analysis was completed, all the M_{20} material had been consumed by further experimentation.

Lattice parameter

The lattice parameter as a function of milling time is shown in Figure 4.14. These data were also obtained through iterative Rietveld refinement of the raw XRD data. A general reduction in lattice parameter with increased milling time is observed. This is due to strain in the unit cell caused by the repeated high energy bombardments during milling. A general reduction in lattice parameter of ultrafine powders (with grain sizes of 20 to 60 nm), in comparison to bulk material, was also found by Troitskiy *et al*. who also attribute it to lattice strain, which they say is characteristic of ultrafine particles [106].

4.3.4 Differential scanning calorimetry and thermogravimetry

Differential scanning calorimetry (DSC) data and thermogravimetric data (TGA) were collected using a Netzsch 449C/6/G simultaneous thermal analyser (STA). This equipment is able to measure mass changes as low as 0.1 μg (TGA) and heat energy transfer rates lower than 0.1 μW (DSC). The STA facilitates the simultaneous acquisition of heat flow data (between a sample and

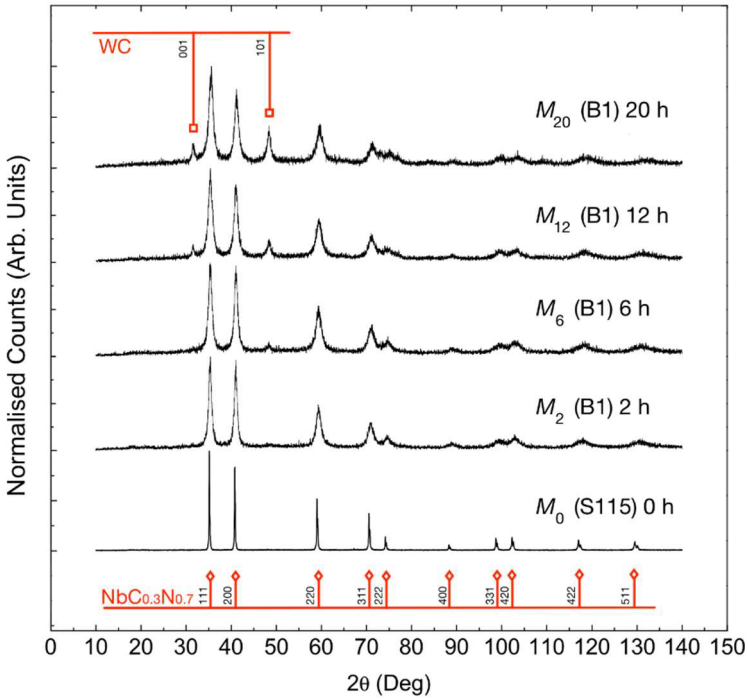

Figure 4.12: XRD data showing the time evolution of the powder charge (sintered $NbC_{0.3}N_{0.7}$ from Batch 1) for up to 20 h of mechanical ball milling. The red lines with open diamonds (bottom) indicate the expected peak positions for $NbC_{0.3}N_{0.7}$. The red lines with open squares (top) indicate two of the peak positions of tungsten carbide (indexes 001 and 101) (both data sets obtained from [118]). Peaks belonging to tungsten carbide begin to appear in the 6 h milled material i.e. peak 101 in sample M_6, and this is joined by a second peak (001) in the 12 h sample, M_{12}. The intensities of these peaks increase with milling time.

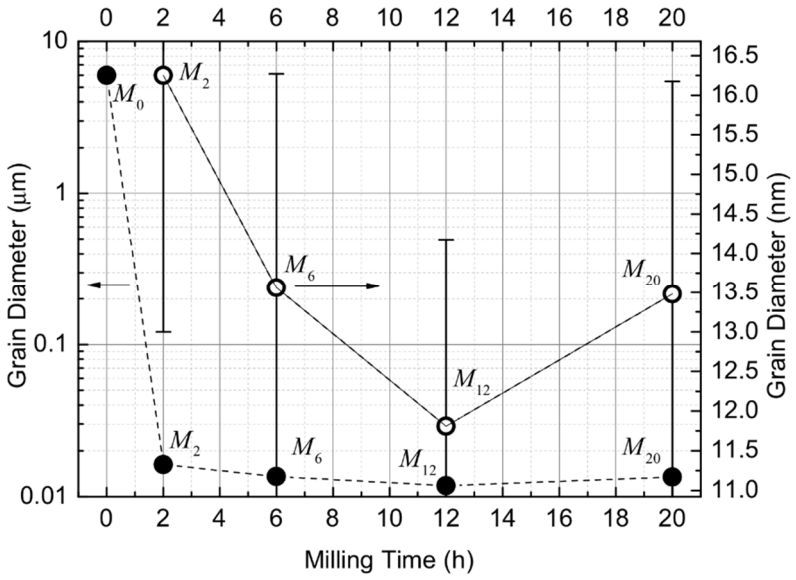

Figure 4.13: Grain diameter as a function of milling time. The open symbols show samples M_2 to M_{20} at a reduced scale (nm) in comparison to the closed symbols (µm).

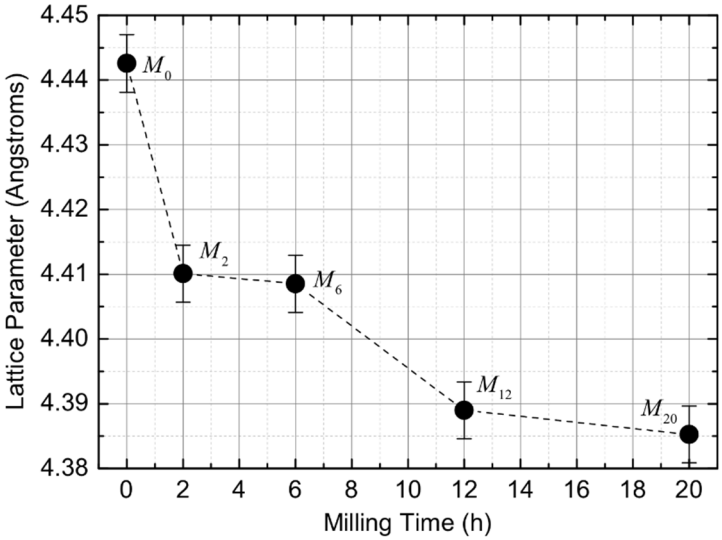

Figure 4.14: Lattice parameter as a function of milling time for all five samples.

its controlled environment) and mass data as functions of time or temperature. The simultaneous acquisition of both datasets, not only serves to increase experimental efficiency, but more importantly serves as an aid to their interpretation. The acquisition process consisted of first performing STA measurements from room temperature up to 1150 ℃ at a rate of 10 ℃/m (1st run), then cooling the sample back down to room temperature (unmeasured) prior to repeating an identical measurement programme on the same sample (2nd run). A comparison of both measurement runs reveals mass and phase changes and/or chemical reactions that have occurred during the temperature sweep by differences in the 1st and 2nd run datasets. These temperature dependent differences manifest themselves as exothermic and/or endothermic curves in the 1st run that either do not appear in the 2nd run or have a very different character in the 2nd run. Exothermic changes result in curves with downward peaks whilst endothermic changes cause upward peaks. If a structural change is occurring at some temperature, say, a crystallization of amorphous material, which is exothermic [123], then in order to maintain a steady temperature increase of the sample, the STA must reduce its heating power. This shows itself as a curve with a downward pointing peak. Figure 4.15 shows TGA and DSC data for the *zero* hour milled sample, M_0, and Figure 4.16 shows this data for the *twenty* hour milled sample, M_{20}. The reason for performing DSC and TGA measurements on these samples was to investigate the recrystallization of *amorphous* content of the nanocrystalline sample M_{20}, in comparison to the *microcrystalline*, unmilled, bulk sample M_0, with a view to using the results to help identify possible temperatures for hot isostatic pressing (to be discussed below). The 1st and 2nd run data for sample M_0 are very similar and are devoid of any interesting structure. This shows that over the temperature range measured, the sample changed little. This is an unsurprising result. The maximum temperature was 1150 ℃, which is very cool for niobium carbonitride. The data for the milled sample M_{20} are, however, more interesting. At approximately 780 ℃ the 1st and 2nd run data begin to differ. The change in curvature of the 1st run DSC data shows that the change is endothermic. This behaviour, in conjunction with the correlated decrease in mass (visible in the corresponding TGA data), is probably due to outgassing, as opposed to any physical, structural

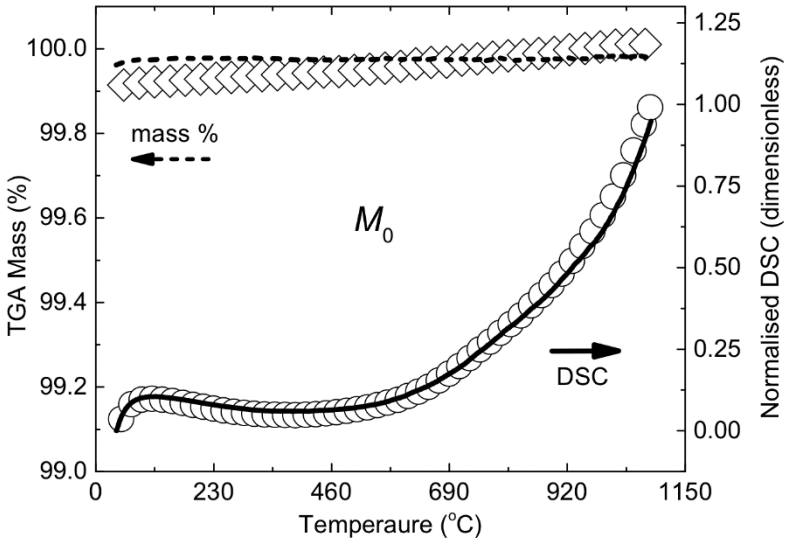

Figure 4.15: Thermogravimetric mass data (TGA) (top of plot – LH axis) and differential scanning calorimetry data (DSC) (RH axis) for the *zero* hour milled sample, M_0. The solid and dashed lines show 1st run data and the open diamonds and circles show 2nd run data.

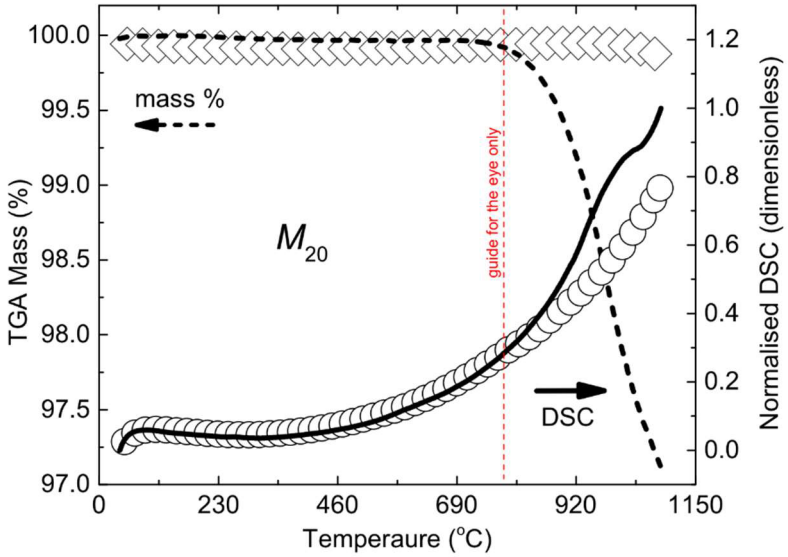

Figure 4.16: Thermogravimetric mass data (TGA) (top of plot – LH axis) and differential scanning calorimetry data (DSC) (RH axis) for the *twenty* hour milled sample, M_{20}. The solid and dashed lines show 1st run data and the open diamonds and circles show 2nd run data. The vertical red-dashed line is a guide to the eye and highlights the temperature at which the measurements in the 1st run begin to deviate from the 2nd run.

change. This nanocrystalline sample was hand pressed into a pellet in preparation for the STA measurement. Therefore, not only is the nanocrystalline sample, M_{20}, far more porous than the solid-state sintered sample, M_0, but the relatively large surface areas of its constituent grains, in conjunction with relatively large grain boundaries, provides a vastly increased surface from which nitrogen could sublimate. Furthermore, the atmosphere within the STA furnace is high purity argon, which means the nitrogen is effectively sitting within a vacuum i.e. the partial pressure of nitrogen within the STA environment is initially zero. Also, outgassing removes heat energy from the sample, which requires an increased power input from the STA to maintain the sample's current temperature rise; hence the correlated upward curvature of the DSC data. It is interesting to note that Troitskiy *et al*. found that their ultrafine powders recrystallized after annealing at temperatures above 800 ℃ i.e. their grain sizes and lattice parameters increased in size [106]. The lack of a similar recrystallization in sample M_{20}, is probably due to the short time M_{20} was above 800 ℃. Troitskiy *et al*. do not mention how long their annealing procedure lasted but it is likely to have been longer than half an hour, which is the approximate time sample M_{20} was temperature swept above 800 ℃ within the STA.

4.3.5 Other milling campaigns

In parallel to the two main milling campaigns discussed above, a further *four* experiments were conducted. The motivation for this additional work was the possibility of fabricating *nanocrystalline* $NbC_{0.3}N_{0.7}$ in just one process by mechanical *alloying* instead of first having to use solid-state sintering. These additional milling campaigns are collectively referred to as a "shortcut" route and were based on good milling practice and some work conducted by Cordoba *et. al*. [100] who used mechanical alloying to generate self-propagating reactions between Nb, C and N (see section 3.4.4 in Chapter 3). The first three of these experiments required that the milling was performed within a nitrogen atmosphere and so a Nb milling vial was modified with a bespoke valve assembly (see Figure 4.17) to allow the exchange of Ar for N_2 and to allow the replenishment of N_2 that was absorbed by the powder charge during milling. The four milling experiments are summarised in Table 4.4. The first experiment was a trial of the valve assembly, which worked well without modification. The second experiment was not based on Cordoba's work but was nevertheless a first attempt to fabricate nanocrystalline $NbC_{0.3}N_{0.7}$. Various milling times were used in the range 5 to 100 hours but none resulted in the formation of $NbC_{0.3}N_{0.7}$; though other phases were formed, such as Nb_6C_5 and Nb_2C, for example. The third experiment was in the spirit of Cordoba's work, though a greater range of milling times was employed and a permanent nitrogen supply was not used. The lack of this permanent nitrogen supply was compensated for by including NbN as a precursor. The reasoning here was that the NbN would ensure the process began with sufficient nitrogen and would therefore not require gaseous nitrogen top-ups during milling. The main outcomes of this experiment were that the contamination level from the milling media was substantial (the mass of the powder charge doubled during milling) resulting in multiphase material. XRD data showed that the product was again multi-phase with no presence of $NbC_{0.3}N_{0.7}$. The final shortcut experiment was a variation on the second. This time a Spex miller was used along with copper milling media and Ar was

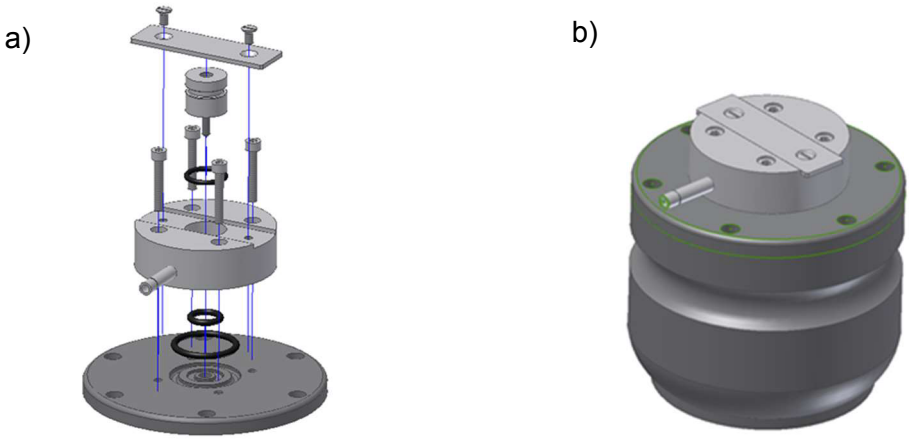

Figure 4.17: The modified Nb vial. a) Exploded view of the valve assembly – all parts were machined from stainless steel 316L. b) Fully assembled vial and valve.

used instead of N_2. The result, however, was similar to the second experiment, which was that various phases other than $NbC_{0.3}N_{0.7}$ were formed. No further shortcut routes were investigated.

4.4 Using hot isostatic pressing to control long-range order in nanocrystalline mechanically milled material

Bulk (as opposed to powder) superconductors are required for all high-field high-current applications. Powdered superconductors that have only been cold pressed into porous samples can have critical current densities that are orders of magnitude lower than their dense, bulk, counterparts due to inferior grain boundaries that reduce the presence of good quality continuous current paths. Engineering applications, such as superconducting magnets, for example, require superconducting wires made from low temperature materials that enable the highest upper critical fields and transport currents to be achieved. Furthermore, the optimisation of properties usually considered to be intrinsic, such as the upper critical magnetic field, can be obtained through an adjustment of normal state resistivity by manipulating the size of the constituent grains. So, the very best material is a polycrystalline dense bulk with an internal structure whose long-range crystalline order has been reduced and controlled. Mechanical ball milling substantially reduces long-range order and indeed produces an amorphous, unordered (or very short-range ordered), component. Hot isostatic pressing can then be used to solidify this mechanically milled material into a dense bulk with a controlled return to some scale of longer-range crystalline order. The following section provides a brief introduction to hot isostatic pressing before describing its use in this work.

4.4.1 Introduction to hot isostatic pressing (HIPing)

Hot isostatic pressing (HIPing) is used in industry to increase density, combine different parts through diffusion bonding, improve mechanical properties and produce products with complex geometries [124]. HIPing enables solid-state sintering in elevated pressures and is therefore comprised of all the solid-state sintering processes discussed earlier in this chapter, and likewise,

Table 4.4: Shortcut route milling experiments.

experiment	*sample*	precursors				*media*	*miller*	program					*atmosphere*	*remarks and results/conclusions*
								cycle mill time	*cycle rest time*	*total mill time*	*rev*	*speed*		
#	*#*	*Nb*	*C*	*NbC*	*NbN*			*(m)*	*(m)*	*(h)*	*Y/N*	*(rpm)*		
1	*1*	•		•		Nb	Fritsch	30	20	15	Y	300	N_2	Initial test of gas valve assembly and attempt to form $NbC_{0.3}N_{0.7}$ using mechanical alloying. Valve assembly worked well. Alloying was unsuccessful – calculated that a minimum of 7 nitrogen atmosphere refills would be needed to supply enough nitrogen to form $NbC_{0.3}N_{0.7}$
2	*2*	•		•		Nb	Fritsch	30	20	5	Y	300	N_2	This experiment was intended to be a shortcut route to nanocrystalline $NbC_{0.3}N_{0.7}$ (the milled product was eventually HIPed). Milling of sample 2 did not consume much nitrogen but samples 3 to 5 did. This was established by the internal pressure of the vial using the turbo pump gauge. Contamination from milling media occurred. XRD showed that $NbC_{0.3}N_{0.7}$ was not formed but that a number of other phases were. In the 15 h sample; Nb_6C_5, Nb_2C and $NbC_{0.7}$. In the 100 h sample; NbN and Nb_2C. Susceptibility data also showed two distinct transitions consistent with multiple superconducting phases.
	3									15				
	4									45				
	5									100				
3	*6*			•	•	Nb	Fritsch	45	0	0.75	N	600	N_2	Experiment designed to mimic Cordoba *et. al.* who alloyed NbC_xN_{1-x} by initiating self-propagating reactions. The recovered mass from this experiment was double the initial mass, which showed that the contamination from the milling media was substantial. XRD also showed a multi-phase product. This route was abandoned.
	7							60		1				
	8							75		1.25				
	9							120		2				
	10							240		4				
4	*11*			•	•	Cu	Spex	30	0	0.5	N	N/A	Ar	Similar to experiment 2 except with different precursor materials and using the Spex miller with copper media. The miller broke down after sample 18 so 19 was never run. Grain sizes of between 10 and 20 nm were achieved but again XRD showed the product to contain multiple phases of Nb_xC_{1-x} and Nb_xN_{1-x}.
	12							45	15	2				
	13							60	30	6				
	14									12				
	15									20				
	16									30				
	17									80				
	18									140				
	19									200				

it employs temperatures that are lower than the melting temperature of the sample being HIPed. However, HIPing utilises elevated temperatures in conjunction with elevated *hydrostatic* pressures to mobilise vacancies and material flow that promotes densification by moving vacancies from neck regions to boundary regions between coalescing grains (see Figure 4.18). This process is enhanced at high pressures. A simple explanation as to why, under elevated applied pressure, a flux of vacancies from neck regions to boundary regions occurs, is described in Figure 4.19 in which three separate surfaces (made from the same material), one concave (Figure 4.19-a), one flat (Figure 4.19-b) and one convex (Figure 4.19-c), are each enclosed in their own sealed, evacuated, container. The difference in the binding energies between the red particle and its vacancy (which serves as an estimate of the vacancy's enthalpy of formation) is less than that between the green particle and its vacancy. The conclusion is that vacancies preferentially form under concave surfaces due to the lower energy demand (see Figure 4.19-d and Figure 4.19-e). For two coalescing grains (see Figure 4.18) the neck regions are concave and therefore serve as a congregation location for vacancies. These neck regions, however, are also close to the grain boundary region. The equation that relates vacancy concentration at a boundary that is subjected to a stress, C_{stressed}, to a vacancy concentration under a stress-free flat surface, C_0, is given by

$$C_{\text{stressed}} = \left(1 + \frac{V_m \sigma_b}{RT}\right) C_0 \tag{4.1}$$

where V_m is the molar volume, σ_b is the effective stress at a boundary due to applied stress, R is the gas constant and T is the temperature [125]. A compressive hydrostatic pressure applied to a group of local grains results in a negative effective stress, σ_b, at their boundaries, which, through equation (4.1), shows that $C_{\text{stressed}} < C_0$. So vacancy concentration at the boundary is smaller than that at a flat surface. The neighbouring, but different, vacancy concentrations at the neck and boundary regions produce a pressure gradient that causes a flux of vacancies to move into the boundary. Conversely, this can also be regarded as a flux of grain boundary material into the neck regions (see Figure 4.18-b). It is this transport of boundary material that fills and builds the neck regions, leading to overall shrinkage and densification. The high pressures utilised in HIPing promote speedy densification over grain growth. This is additionally beneficial in maintaining homogeneity, and in the case of this work, in ensuring that grain growth rate is sufficiently slow to stop a return to grain diameters of micrometer proportions, whilst also ensuring very good grain connectedness.

4.4.2 HIPing NbCN milled samples

NbCN has not been studied extensively in the literature so it is not possible to choose accurately the temperature, pressure and time values necessary to achieve a particular grain size/density. Furthermore, there is no exact knowledge of what the optimum granularity of the sample should be with respect to superconducting properties. We are mindful to reduce the number of control parameters that are varied in order to establish clarity in the deductions made from HIPing

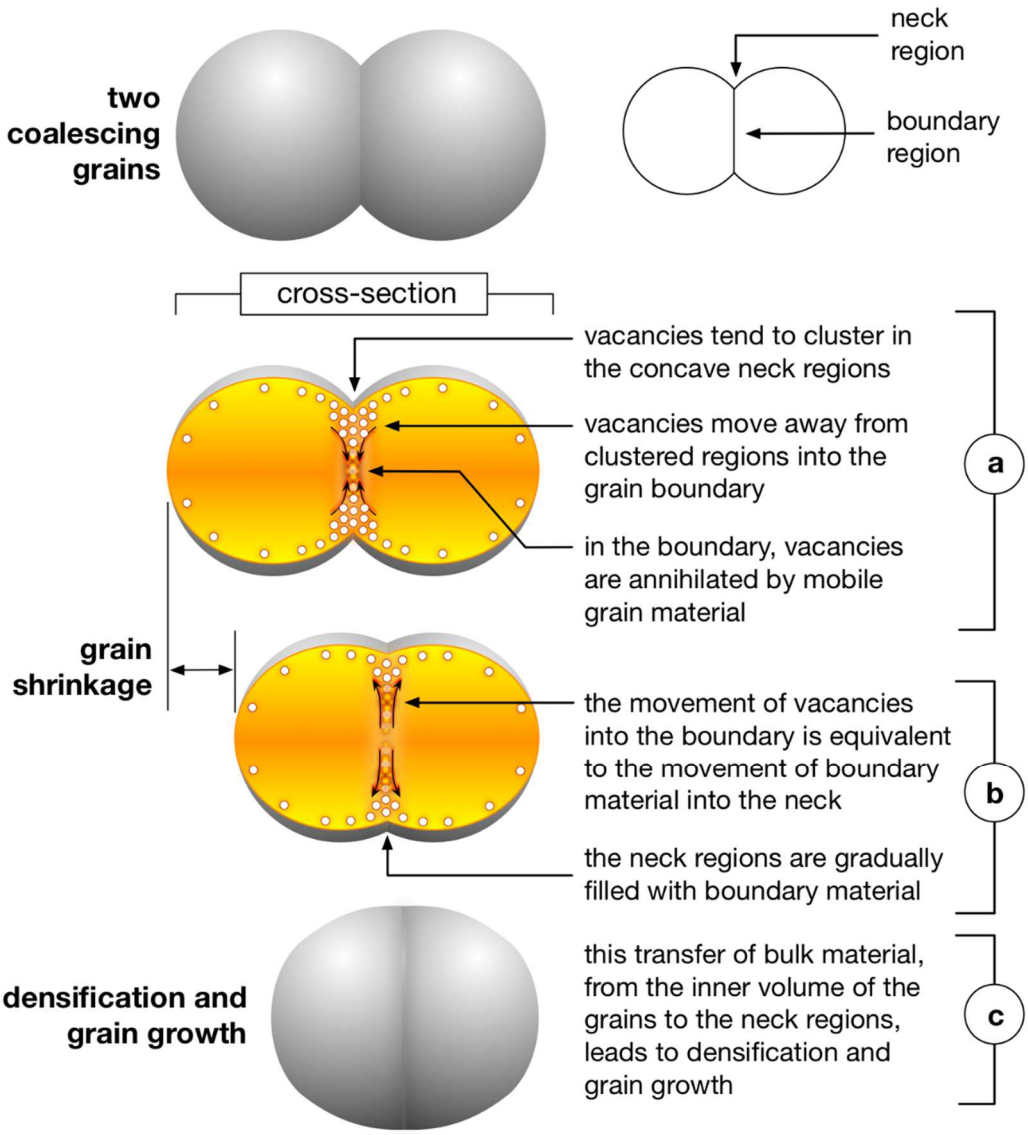

Figure 4.18: The densification through shrinkage and transport of boundary material to neck regions of two coalescing grains subjected to hot isostatic pressing. (a) vacancies preferentially congregate under the concave surfaces of the neck regions and move into the boundary region due to its lower vacancy concentration. Whilst in the boundary region the vacancies are annihilated. (b) the flux of vacancies into the boundary region, and subsequent annihilation, is equivalent to a flux of boundary material into the neck regions. This transport of vacancies/boundary material causes the neck regions to be filled in and for overall shrinkage/densification to occur. (Adapted from [115].)

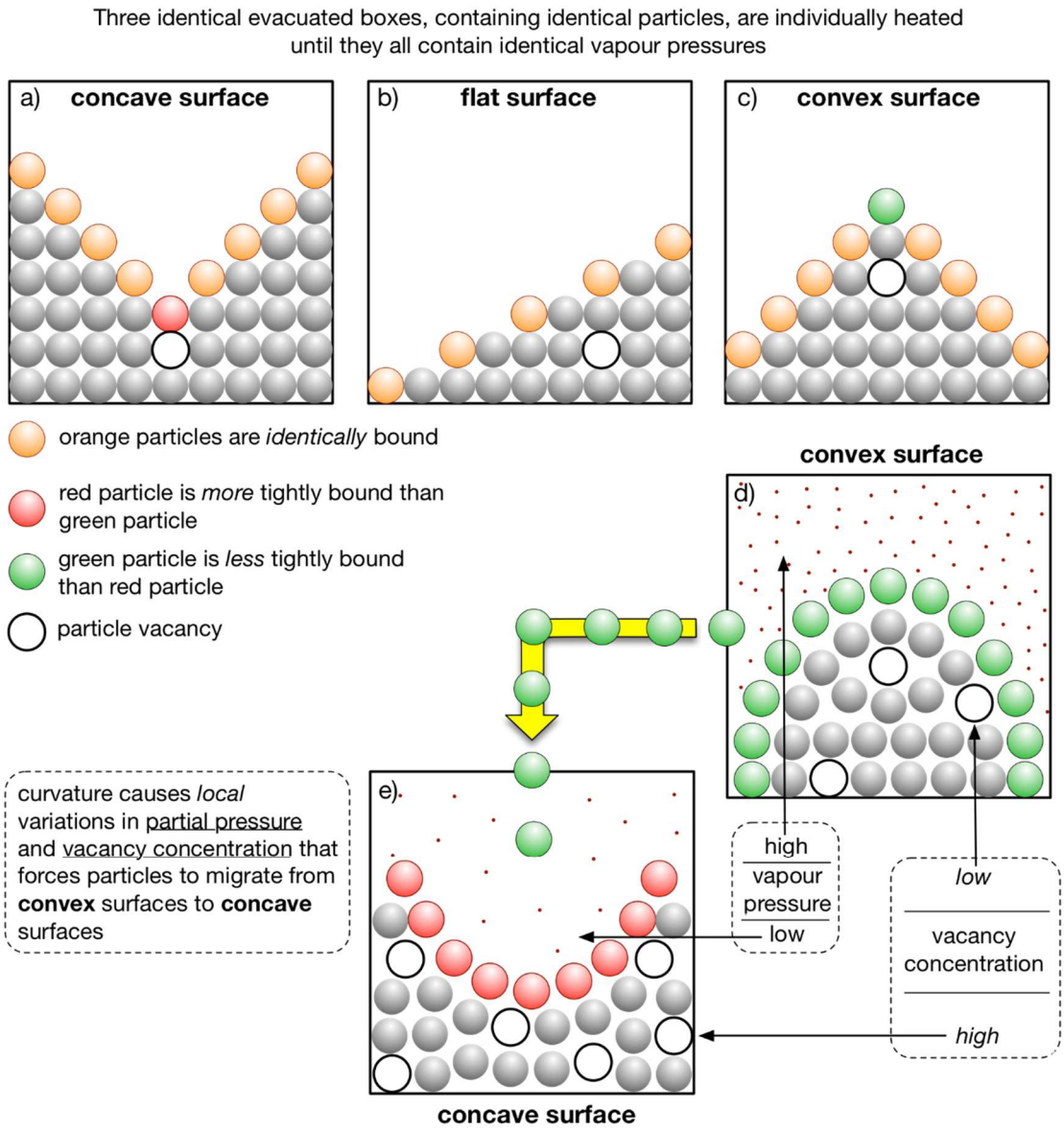

Figure 4.19: Three surfaces each enclosed within a sealed, evacuated, container; a) a concave surface, b) a flat surface, and c) a convex surface. Each container is heated until an equilibrium vapour pressure is obtained within. The red particle (box (a)) is more tightly bound than the green particle (box (c)) and therefore the partial pressure within box (c) is greater than that in box (a) due to the ease with which the green particle can leave its convex surface. These three boxes also show that it is easier for vacancies to form under the concave surface (box (a)) than under the convex surface (box (c)). This is because the difference in the binding energies of the vacancies and their respective surface particles is less under the concave surface (box (a)) than the convex surface (box (c)). Boxes (d) and (e) summarise the discussion given in then text. (Figure adapted from [126].)

experiments. Furthermore, given that lower temperatures and higher pressures lead to densification and limit grain growth, we chose to keep a fixed HIPing pressure of 2000 bar (which is the maximum of the available equipment) for all HIPing runs in this work.

Sample preparation

Each powder sample must be sealed within an evacuated, stainless steel, billet. This ensures that very little gas remains between powder particles. We found this was required to fully densify the samples. Each billet is formed from a stainless steel (316L) tube of 22 mm outside diameter, a ~ 1.0 mm wall thickness, and ~ 250 mm length. One end is pressed flat using a fly press and is then TIG welded (see Stage (1) in Figure 4.20). The powder sample is wrapped in a niobium foil sheet to form a sample packet that is then put into the tube. The niobium foil acts as a contamination barrier between the sample and the inner stainless steel wall. All of this preparation work is conducted within an argon glove box. The tube is temporarily sealed at one end using a

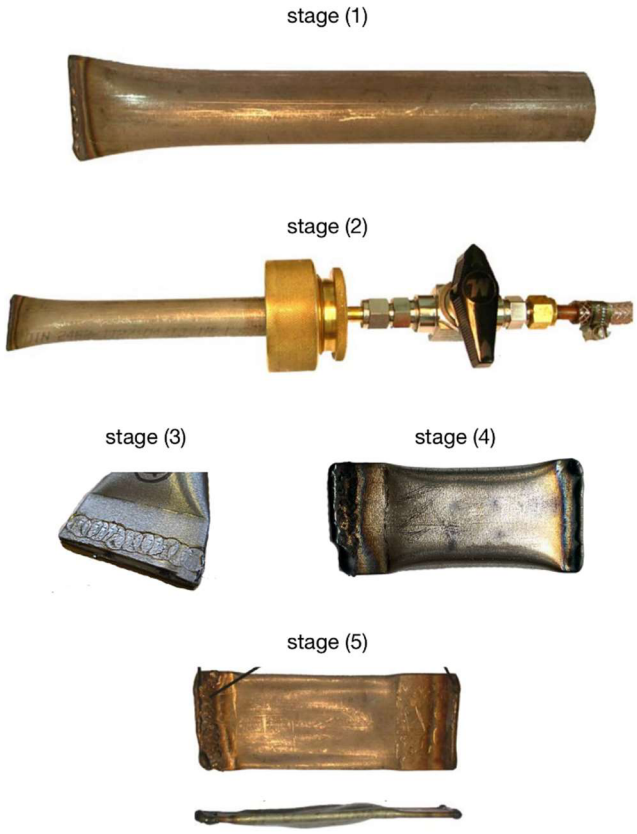

Figure 4.20: A sequence of stages in the HIP billet preparation and HIPing process. Stage (1): a stainless steel tube is flattened and welded at one end. Stage (2): the sample, enclosed within a protective niobium foil wrapper, is put into the tube prior to its open end being sealed with a vacuum valve assembly (this work is conducted in an argon glove box). The tube is then evacuated with a turbo pump to remove the argon. Stage (3): another portion of the tube, just above the sample's location, is flattened with a fly press and is then sealed by spot welding across the flat. The sealed billet is then cut from the remaining tube length. Stage (4): the spot welded end is then TIG welded to reinforce the seal. Stage (5): the billet is then HIPed. This process flattens the billet ready for the sample to be extracted but cutting the billet open.

vacuum valve assembly (see Stage (2) in Figure 4.20). This assembly allows the removal of the tube from the glove box and its subsequent evacuation with a turbo pump to remove the argon gas within. After the tube has been pumped for approximately half an hour, and when the pressure within is of order 10^{-6} mbar, another portion of the tube, just above the sample location, is flattened using the fly press. This flattened area is then sealed by spot welding across the flat (Stage (3) in Figure 4.20). The billet is then cut away from the remaining, unused, length of tube and is TIG welded to reinforce the spot welded seal (Stage (4) in Figure 4.20). The billet is then marked using a letter punch to provide a permanent identification that survives the extreme temperature and pressure of the HIPing process.

HIP runs and failed billets

Each HIP treatment is referred to here as a "run". The HIP chamber can accept six billets for simultaneous treatment. However, if there are any small holes in the welds of a billet through which the internal vacuum can be breached, then the billet will *fail* the HIPing run. This means the sample will not be sufficiently densified and will also be contaminated. All the experimental effort expended in producing and HIPing the sample(s) is wasted. Great care must be taken in the billet preparation process to limit the number of these failed billets. However, it is not uncommon for there to be at least one failure for each batch of six. The quality of the welding (spot and TIG) is paramount to success.

Sample and HIPing details

Eight HIP billets were produced in total. The format of HIP sample identification is explained in Figure 4.21. Billets 1 to 5 contained sample powder that originated from sintered batch 1 material; billets 1 and 2 contained *zero* hour milled powder (sample M_0) and billets 3 to 5 contained *twenty* hour milled powder (sample M_{20}) - see Table 4.5 for details. Billets 6 to 8 contained sample powder that originated from sintered batch 2 material that had been milled for *twenty* hours (also sample M_{20}). Seven of these eight billets were HIPed using five independent HIP runs. Billet 2 was not HIPed. HIP runs 1 to 3 consisted of treatments ranging in temperature from 950 ℃ to 1150 ℃ at a fixed pressure of 2000 bar and a fixed dwell time of 10 minutes. HIP runs 4 and 5 experimented with different dwell times of 120 and 40 minutes respectively.

$$^{20}H^{10}_{1050}$$

The above symbol reads:

HIP billet contains material that was milled for 20 hours and HIPed for 10 minutes at 1050 degrees centigrade

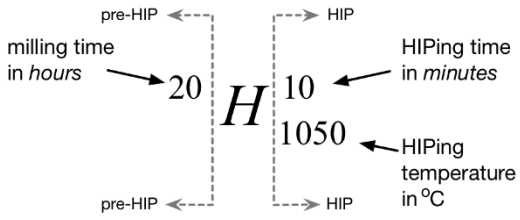

Figure 4.21: HIP sample identification. All numbers that appear before the central "*H*" refer to processes that precede HIPing i.e. milling or fabrication. All numbers that appear after the central "*H*" are direct HIPing parameters.

HIP run 1: Billets 1 and 4 were HIPed at 1050 ℃ for 10 minutes to produce samples ${}^{0}H_{1050}^{10}$ and ${}^{20}H_{1050}^{10}$ respectively. These samples contained *zero* hour milled and *twenty* hour milled material and were selected for simultaneous HIPing to establish how the HIP conditions affected their very different grain sizes.

HIP run 2: Billets 3 and 7 were HIPed at 950 ℃ for 10 minutes to produce samples ${}^{20}H_{950}^{10}$. The reason for HIPing two identical samples was to guard against the chances of one failing.

HIP run 3: Billet 8 was HIPed at 1150 ℃ for 10 minutes to produce sample ${}^{20}H_{1150}^{10}$. This billet failed.

HIP run 4: Billet 6 was HIPed at 1163 ℃ for 120 minutes to produce sample ${}^{20}H_{1163}^{120}$. The set point temperature for this HIP run was actually set to 1150 ℃ to make *time* the only variable. However, problems with the HIP during the temperature/pressure ramp meant the dwell temperature had to be adjusted to 1163 ℃, which was the closest, stable, temperature (to the desired 1150 ℃) that could be achieved.

HIP run 5: Billet 5 was HIPed at 1150 ℃ for 10 minutes to produce sample ${}^{20}H_{1150}^{40}$. This billet failed.

4.4.3 X-ray diffraction

X-ray diffraction data were obtained by measuring each of the HIPed samples using the Siemens D5000 Powder Diffractometer. The data are shown in Figure 4.22. There is a stark visible difference in the XRD patterns of samples ${}^{0}H_{1050}^{10}$ and ${}^{20}H_{1050}^{10}$ of HIP run 1. This is to be expected since sample ${}^{0}H_{1050}^{10}$ is essentially microcrystalline sintered batch material that was not milled. This sample's sharp peaks are indicative of its larger grain size (5980 nm compared to ${}^{20}H_{1050}^{10}$, which was ~ 33 nm). The patterns for the two samples ${}^{20}H_{950}^{10}$ of HIP run 2 are very similar to each other and visibly show some larger peak broadening in comparison to sample ${}^{20}H_{1050}^{10}$ from HIP run 1. This suggests that the lower temperature of HIP run 2 resulted in less grain growth. Another interesting feature is that the two patterns belonging to the two failed HIP runs 3 and 5 are similar to run 4, which suggests similar grain size; though this reveals nothing about these samples' densities or quality of connections between the grains, which is likely to be much inferior due to the HIP billet failure.

Grain diameter and lattice parameter comparison to milled samples

The grain diameters and lattice parameters of the HIPed samples ${}^{0}H_{1050}^{10}$ and ${}^{20}H_{1050}^{10}$ are directly compared to the milled samples M_0 to M_{20} in Figure 4.23. This comparison provides a complete picture of the effects of the processing on the sample material. For instance, HIPing sample M_0

Table 4.5: HIP sample (billet) details and HIP run details.

				material originating from Batch 1					material originating from Batch 2		
				billet 1	*billet 2*	*billet 3*	*billet 4*	*billet 5*	*billet 6*	*billet 7*	*billet 8*
			sample ID	$^{0}H^{10}_{1050}$	^{0}H	$^{20}H^{10}_{950}$	$^{20}H^{10}_{1050}$	$^{20}H^{40}_{1150}$	$^{20}H^{120}_{1163}$	$^{20}H^{10}_{950}$	$^{20}H^{10}_{1150}$
			mass (g)	2.8	2.8	3	3	3	3	3	3
HIP run	*temp* (°C)	*time* (m)	*status*	*HIPing campaign*							
1	*1050*	*10*		*billet 1*	*sample not HIPed*		*billet 4*				
2	*950*	*10*				*billet 3*				*billet 7*	
3	*1150*	*10*	*failed*								*billet 8*
4	*1163*	*120*							*billet 6*		
5	*1150*	*40*	*failed*					*billet 5*			

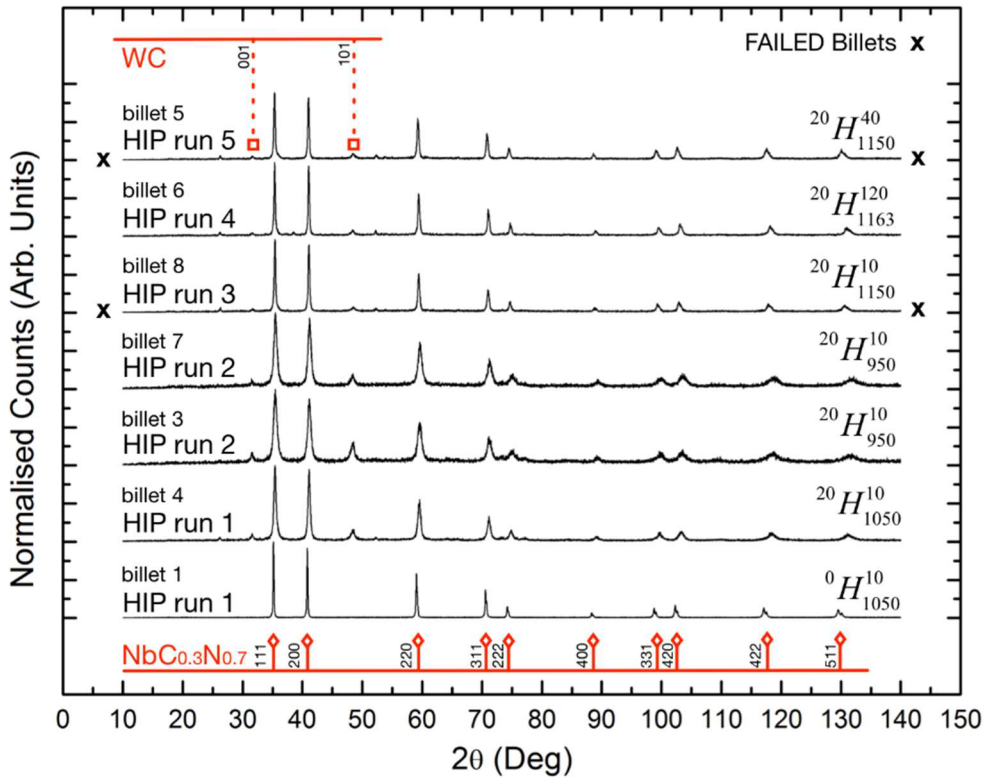

Figure 4.22: XRD data for seven HIPed samples including grain diameter (GD) and lattice parameters (LP) for HIP run 1 samples. The red lines with open diamonds (bottom) indicate the expected peak positions for $NbC_{0.3}N_{0.7}$. The red lines with open squares (top) indicate two of the peak positions of tungsten carbide (indexes 001 and 101) - this is contaminant from the milling media (both data sets obtained from [118]).

has had no effect on its lattice parameter, which is to be expected (see the tabulated data in Figure 4.23). However, HIPing sample M_{20} has resulted in a significant increase to its lattice parameter from ~ 4.39 to 4.40 Å, which is a ~ 27 % recovery to its pre-milled value (sample M_0). This indicates that the HIPing process has allowed a relaxation of the lattice, most likely caused by a reduction in lattice defects due to vacancy annihilation. A comparison of grain sizes tells a similar story. HIPing the microcrystalline, *zero* milled material (sample M_0) has had no effect. However, HIPing the *twenty* hour milled sample, M_{20}, has produced an increase in grain size from ~ 14 to ~ 33 nm.

4.4.4 Differential scanning calorimetry and thermogravimetry

Differential scanning calorimetry (DSC) data and thermogravimetric data (TGA) were collected using the Netzsch 449C/6/G simultaneous thermal analyser (STA). The measurements were performed on HIP run 1 samples, ${}^{0}H_{1050}^{10}$ and ${}^{20}H_{1050}^{10}$ (see Figure 4.25 respectively). These data show similar behaviour to their pre-HIPed counterparts, M_0 and M_{20}, where sample ${}^{0}H_{1050}^{10}$ shows very little difference between its 1st and 2nd runs, which is not the case for sample ${}^{20}H_{1050}^{10}$. Again, the explanation here is outgassing of nitrogen, however, there is now approximately a 130 ℃ increase in temperature before the outgassing from sample ${}^{20}H_{1050}^{10}$ substantially begins to change from its 2nd run data set. This temperature increase is symptomatic of the sample's increased grain size and density.

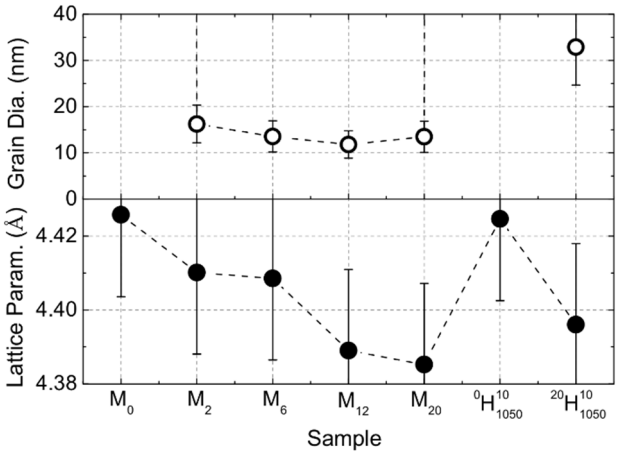

sample	grain size (nm)	Lattice parameter (Å)
M_0	~ 6000	4.426
M_2	16.3	4.410
M_6	13.6	4.409
M_{12}	11.8	4.389
M_{20}	13.5	4.385
${}^{0}H_{1050}^{10}$	~ 6000	4.425
${}^{20}H_{1050}^{10}$	32.9	4.396

Figure 4.23: Comparison between grain size and lattice parameters of milled samples M_0 to M_{20} to HIPed samples ${}^{0}H_{1050}^{10}$ and ${}^{20}H_{1050}^{10}$. The values for each dimension are tabulated on the right. The grain sizes for samples M_0 and ${}^{0}H_{1050}^{10}$ are too large to be plotted in the figure but the tabulated data shows that their grain size is approximately the same.

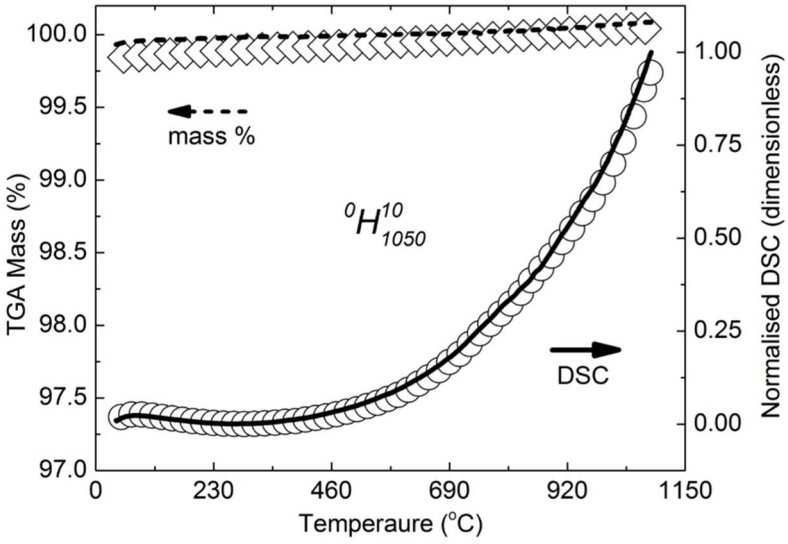

Figure 4.25: Thermogravimetric mass data (TGA) (top of plot – LH axis) and differential scanning calorimetry data (DSC) (RH axis) for the HIPed sample $^{0}H^{10}_{1050}$. The solid and dashed lines show 1st run data and the open diamonds and circles show 2nd run data.

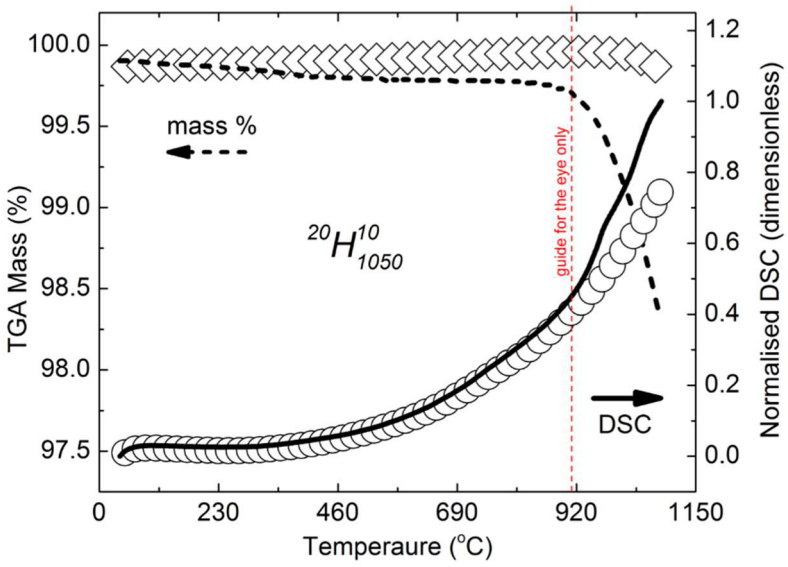

Figure 4.24: Thermogravimetric mass data (TGA) (top of plot – LH axis) and differential scanning calorimetry data (DSC) (RH axis) for the HIPed sample $^{20}H^{10}_{1050}$. The solid and dashed lines show 1st run data and the open diamonds and circles show 2nd run data. The vertical red-dashed line is a guide to the eye and highlights a correlation in both datasets where the 1st run measurements begin to substantially deviate from the trends of the 2nd run measurements.

4.4.5 Concluding comments

A number of material fabrication experiments were conducted to obtain an optimum set of condition parameters (time and temperature, for example) to allow the production by solid-state sintering of ~ 36 g of single phase good quality bulk $NbC_{0.3}N_{0.7}$ (see Figure 4.9) with a superconducting transition temperature of 17.5 K. Small quantities of very high quality material with a transition temperature of 17.7 K were also produced. Batches of the fabricated material were pulverised using mechanical ball milling for up to 20 hours to produce ~ 23.5 g of *nanocrystalline* powder that was used to form eight HIP billets. Seven of these billets were subsequently HIPed using different temperatures and/or times to form *seven* bulk samples. In parallel to this work various measurement and analysis techniques, such as x-ray diffraction, Rietveld refinement and differential scanning calorimetry were employed to characterise the material's physical properties throughout its production and processing. The next chapter augments this physical characterisation with the measurement and analysis of the superconducting properties of some of these microcrystalline and HIPed nanocrystalline samples.

Chapter 5

Characterisation of microcrystalline and nanocrystalline niobium carbonitride

5.1 Introduction

Resistivity, ac-susceptibility, heat capacity and magnetisation measurements were performed on both microcrystalline and nanocrystalline samples of $NbC_{0.3}N_{0.7}$. This suite of measurements was implemented to establish the normal state and the superconducting properties of the samples. The following sections discuss the measurements and the important materials parameters derived, such as, resistivity, transition temperature, upper critical field and critical current density. Unfortunately, not all measurements were completed on all samples because of time and cost constraints, but the choices made were motivated by our intention to understand and improve the effect on the superconducting properties of $NbC_{0.3}N_{0.7}$ by changing the material from microcrystalline to nanocrystalline. The first section describes measurements on the microcrystalline material and the second section is on the nanocrystalline material. Finally, we compare and contrast these two types of materials and discuss our results.

5.2 Microcrystalline material

Four microcrystalline samples were investigated. Three of these samples were S9, S109 and S115 that were fabricated in heat-treatments 5, 28 and 30 respectively (see Table 4.1). We also investigated sample ${}^{0}H_{1050}^{10}$ (that was not milled) whose precursor was obtained from heat-treatment 30 and was subsequently HIPed for ten minutes at 1050 ℃ and 2000 bar. Sample S9 was chosen for investigation because it had the highest T_c. Sample S115 was chosen because it formed part of the batch material used for nanocrystalline fabrication and sample S109 was chosen because it was indicative of the sorts of variation expected in our good material.

5.2.1 Normal state resistivity

Resistivity, ρ_n, as a function of temperature was measured using the Quantum Design Physical Properties Measurement System (PPMS) in resistivity mode. Samples S9, S109 and ${}^{0}H_{1050}^{10}$ were measured and are shown in Figure 5.1. Their resistivities, transition widths and transition onsets are tabulated in Table 5.1. The critical temperature and superconducting in-field properties

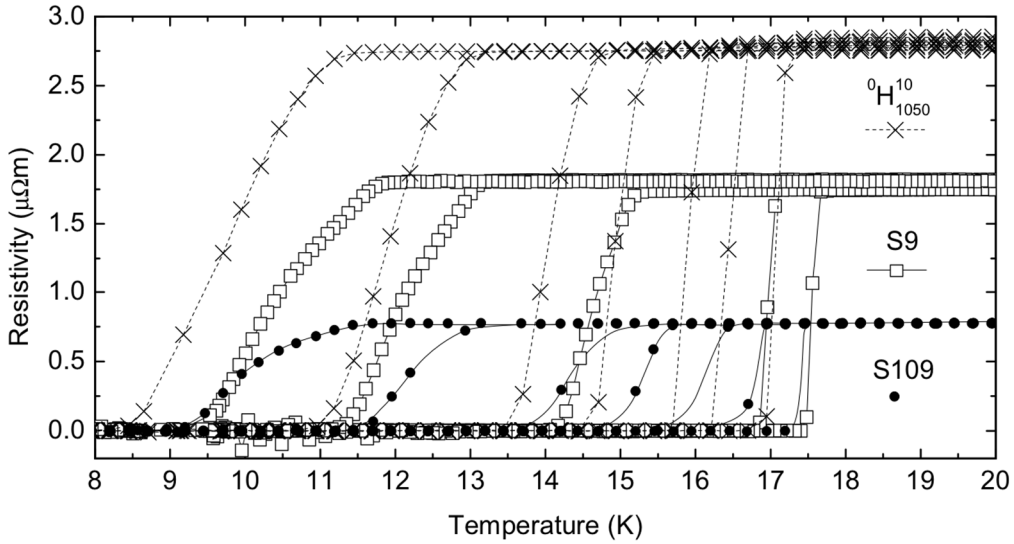

Figure 5.1: Normal state resistivity data of three microcrystalline samples. Samples S9 and S109 (see Table 4.1) are sintered samples and sample $^0H^{10}_{1050}$ is a sintered sample that was HIPed for ten minutes at 1050 ℃ and at 2000 bar. Samples S109 and $^0H^{10}_{1050}$ were measured in applied fields 0, 0.5, 1.0, 2.0, 3.0, 5.5 and 8.0 T. Sample S9 was measured in applied fields, 0, 0.5, 3.0, 6.0 and 8.0 T. The lines are guides to the eye.

are similar for these samples, which suggests that their *intragrain* quality is also similar. We attribute the range in the normal state resistivity of a factor ~ 3 to relatively small differences in the quality of *intergrain* connectedness within each sample. We expect samples S9 and S109 to have similar resistivities due to their very similar heat-treatments and attribute the factor of two difference (Sample S9: $\rho_n = 1.7\ \mu\Omega\mathrm{m}$ and Sample S109: $\rho_n = 0.7\ \mu\Omega\mathrm{m}$) to the differences in the porosities of the pre-heat-treated sample pellets. These pellets were pressed by hand with no means of ensuring a consistent application of pressure across distinct batches [34]. The porosity of precursor materials is a process parameter that affects sintering dynamics. Higher porosities

Table 5.1: Resistivity, ρ_n, transition width, ΔT_C (10 – 90 %), transition temperature, T_C, and upper critical magnetic field, $B_{c2}(0)$, obtained from Figure 5.1. $B_{c2}(0)$ values were obtained by fitting equation (5.5) to the data.

sample	ρ_n ($\mu\Omega\mathrm{m}$)	ΔT_C (B=0) (K)	T_C (onset) (K)	In-field resistivity transition onsets (K)							$B_{c2}(0)$ (T)
				B = 0.5	B = 1.0	B = 2.0	B = 3.0	B = 5.5	B = 6.0	B = 8.0	
$^0H^{10}_{1050}$	2.7	~0.22	17.2	16.7	16.1	15.5	14.7	13.0		11.3	16.7
S9	1.7	~0.11	17.6	17.1			15.2		13.1	11.8	17.4
S109	0.7	~0.22	17.5	16.9	16.5	15.6	15.0	13.1		11.5	16.8

favour atomic driving mechanisms that lead to coarsening instead of densification. A similar situation is evident in the data of the HIPed sample, ${}^{0}H_{1050}^{10}$, which has the highest $\rho_n = 2.7\ \mu\Omega\mathrm{m}$. This sample's precursor was extracted from a coarse grained powder obtained from ground sintered pellets. It is therefore most likely that the relatively low HIPing temperature and dwell time was an insufficient combination of aggressive process parameters, thereby producing a more resistive grain boundary matrix than the much longer (and hotter) sintering conditions applied to samples S9 and S109 that have better grain connectivity.

5.2.2 AC-susceptibility

AC-susceptibility data were obtained from measurements performed with the PPMS in ACMS mode. The PPMS was used to apply a static magnetic field to each sample while the temperature was swept from a few Kelvin above the expected maximum critical transition temperature, T_C, down to 3 K. During the measurements the PPMS superimposed a small oscillating field on top of the applied field to excite the sample's magnetic response. This procedure was repeated for applied fields in the range 0 to 8 T. The data for samples S9, S109, S115 and ${}^{0}H_{1050}^{10}$ are shown in Figure 5.2 and individual plots of the transitions at each applied field are shown in Table 5.3. These data were used to determine the onset of T_C (see Figure 5.4 for how the onset is defined) and the transition width, ΔT_C, between 10 to 90 % and are tabulated in Table 5.2. Samples S9, S109 and S115 all share similar T_C's (17.5 ± 0.1 K) but the HIPed sample, ${}^{0}H_{1050}^{10}$, has a lower T_C of 17.2 K. The transition widths of samples S9, S109 and ${}^{0}H_{1050}^{10}$, from 10 to 90 %, are very similar at ~ 0.48 ± 0.06 but sample S115 has the sharpest transition at ~ 0.21 K. We attribute these variations in T_C to inhomogeneities in Batch 1 material and possibly a slight reduction in T_C due to the HIPing process.

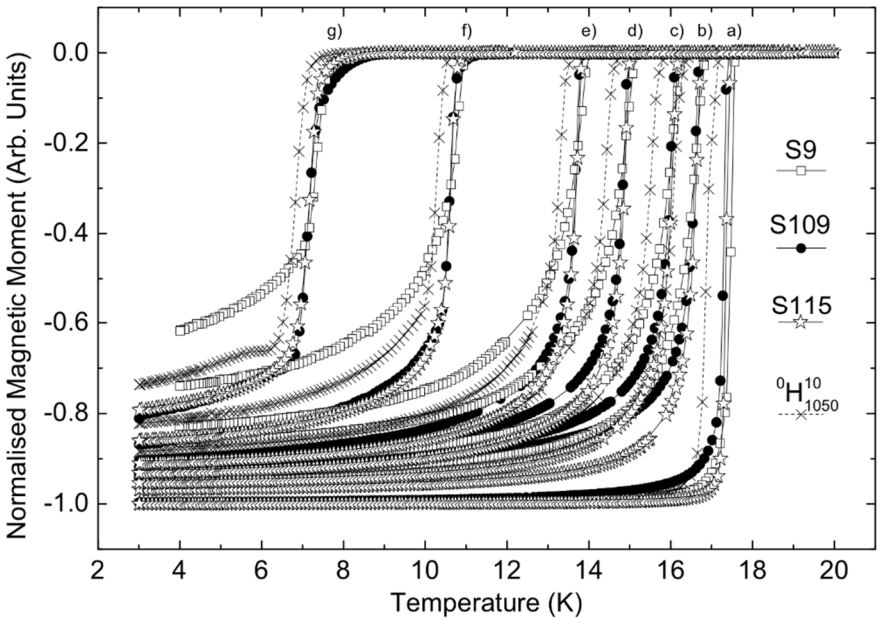

Figure 5.2: AC-susceptibility data of samples S9, S109, S115 and ${}^{0}H_{1050}^{10}$ in applied magnetic fields 0 to 8.0 T. The transitions for each of the fields are shown in plots a) to g) in Figure 5.3. The excitation field was 0.4 mT at 777 Hz.

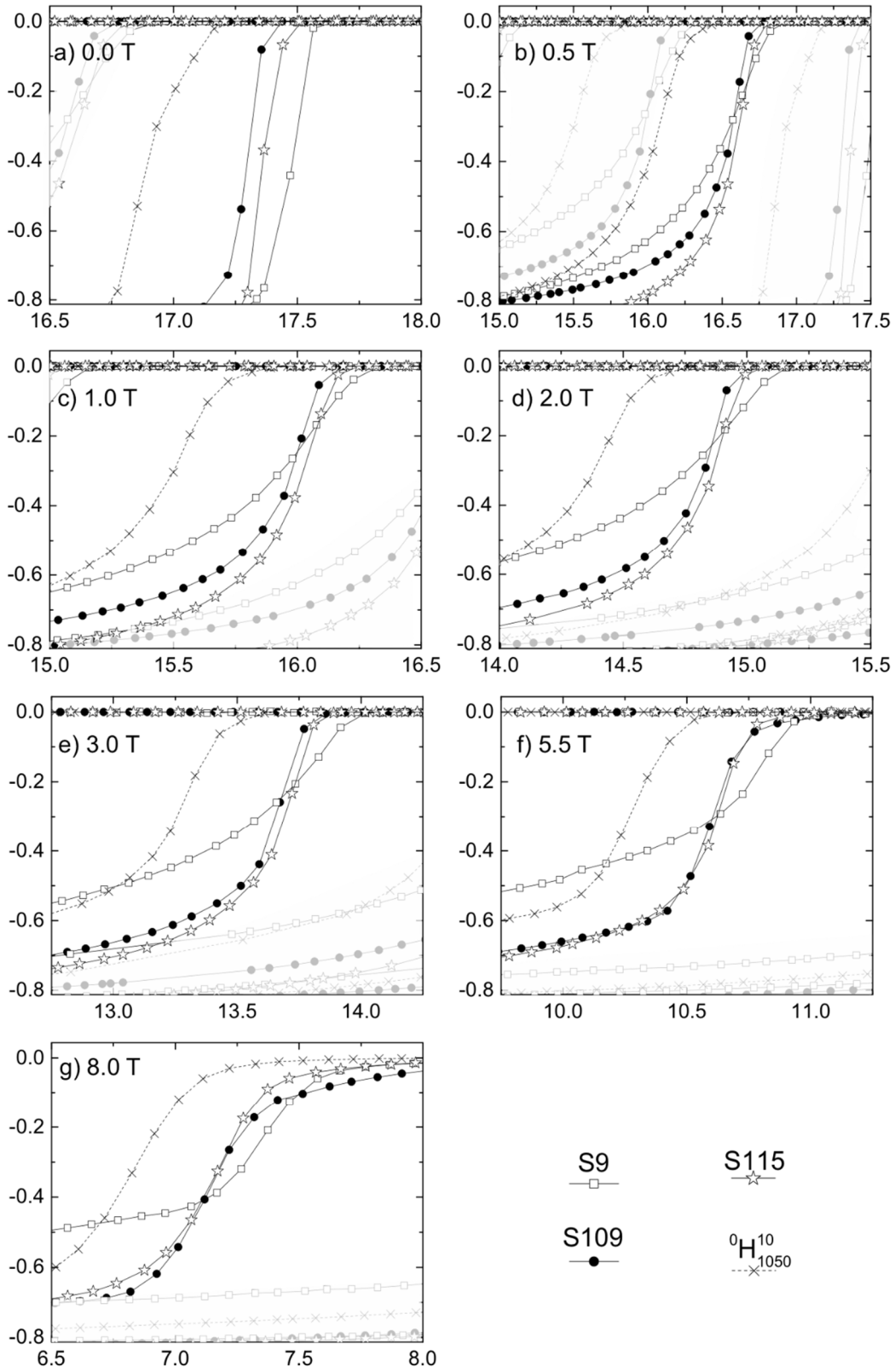

Figure 5.3: Normalised magnetic moment vs temperature for the transitions in applied magnetic fields 0 to 8 T (panels (a) to (g) respectively) of samples S9, S109, S115 and $^{0}H^{10}_{1050}$ from the ac-susceptibility data shown in Figure 5.2.

Table 5.2: Transition temperature, T_C, and transition width, ΔT_C (10 – 90 %) for four samples obtained from ac-susceptibility data.

sample	T_C (onset) (K)	ΔT_C (K)
S9	17.6	~ 0.43
S109	17.4	~ 0.54
S115	17.5	~ 0.21
${}^{0}H_{1050}^{10}$	17.2	~ 0.48

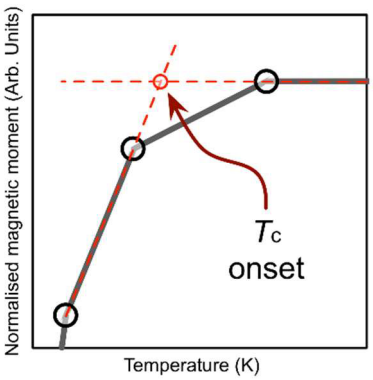

Figure 5.4: Diagram showing how the onset of the superconducting transition was determined.

5.2.3 Heat capacity

Heat capacity data were obtained from measurements performed with the PPMS in heat capacity mode. This first entails preparing the measurement puck by applying a small amount (~ 1.0 mm^3) of N-grease that has a cryogenic working temperature range that includes that of the intended measurement. The puck and grease then have their combined heat capacity measured by the PPMS, which is treated as an addenda dataset. The sample is then mounted onto the puck platform on top of the grease. The grease provides a good thermal contact to the platform and also stops the sample from being easily dislodged during handling. The total heat capacity of the puck, grease and sample are then measured. The addenda dataset is subtracted from the combined (sample and addenda) dataset, providing the heat capacity of the sample alone. Three samples were measured in this way; the sintered samples S9 and S115 and the HIPed sample ${}^{0}H_{1050}^{10}$. These data were analysed in accordance with the well-known equation

$$\frac{C}{T} = \gamma + \beta T^2 \tag{5.1}$$

where C is the heat capacity, γ is the Sommerfeld constant, T is the temperature and β is a constant related to the Debye temperature, θ_D, given by

$$\theta_D = \sqrt[3]{\frac{12}{5\beta}\pi^4 R} \tag{5.2}$$

where R is the gas constant. Debye plots of these data are shown in Figure 5.5 and the data was used to determine the Sommerfeld constants and Debye temperatures of the samples, which are listed in Table 5.3.

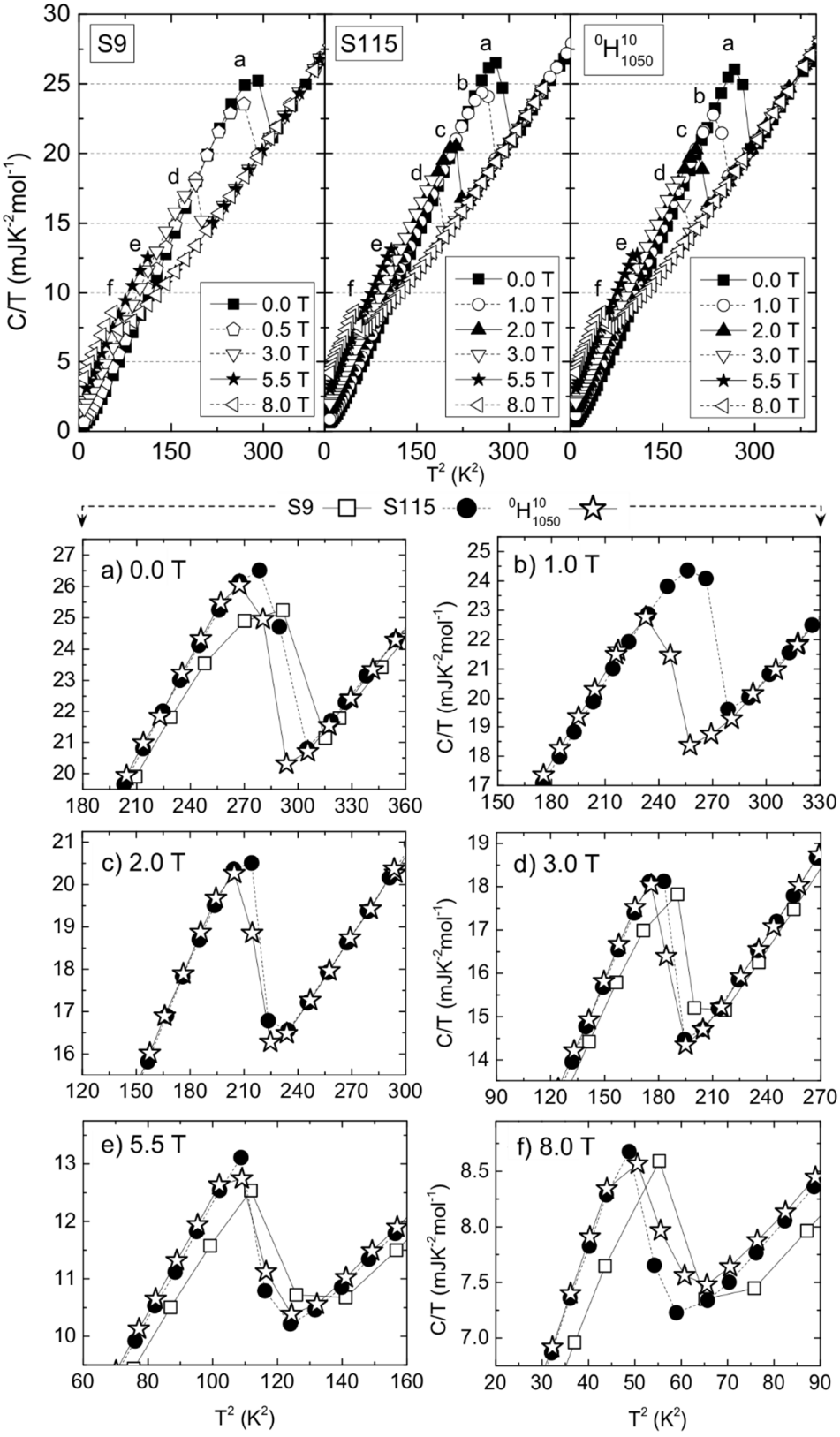

Figure 5.5: Debye plots of the sintered samples S9 and S115 and the HIPed sample $^{0}H^{10}_{1050}$ in applied magnetic fields 0 to 8.0 T. The data for each of the fields 0, 1.0, 2.0, 3.0, 5.5 and 8.0 T are independently shown in plots a) to f) respectively.

Table 5.3: Sommerfeld constant, γ, and Debye temperature, θ_D, obtained from an analysis of heat capacity data taken from three microcrystalline samples. The data for Geballe's sample is included for comparison purposes.

Sample	γ (mJK^{-2}mol^{-1})	θ_D (K)
S9	3.85	345
S115	4.29	362
${}^{0}H_{1050}^{10}$	4.54	372
Geballe [127]	3.26	351

For high field superconductors, it is difficult to obtain accurate values of the parameters γ and β using equation (5.1) because it requires an extrapolation of the normal state data at low temperatures to 0 K from which the intercept and slope correspond to the required values of γ and β. However, because very high magnetic field heat capacity measurements are less readily available in the scientific community, it is difficult to completely suppress the onset of superconductivity all the way to very low temperatures; which is necessary to reduce the extent of the required extrapolation and improve its accuracy. Fortunately, we can use the relationship between heat capacity and entropy to improve the extrapolation [127]. This relationship is expressed by

$$C = T\frac{dS}{dT} \quad \Longrightarrow \quad \frac{C}{T} = \frac{dS}{dT} \tag{5.3}$$

where C is the heat capacity, T the temperature and S the entropy. Equation (5.3) leads to

$$\int_o^T \frac{C}{T}\, dT = \int_0^T \frac{dS}{dT}\, dT = S_T \tag{5.4}$$

which shows that the area under a plot of C/T vs T, over some temperature range, is equal to the entropy, S_T, at the upper bound of that temperature range. This, in conjunction with the fact that, in *zero* field, the entropies of the *normal* and *superconducting* states are equal, can be used to aid the analysis of the heat capacity data. We have used two heat capacity datasets; one in *zero* field and the other in the *highest* field we have available (see Figure 5.6-a). The highest field dataset is used to supress the onset of the superconducting transition as much as possible to facilitate the extrapolation of its normal state curve to 0 K (see Figure 5.6-b). Substitution of the upper limit T for T_c in equation (5.4) provides the entropy at T_c i.e. S_{T_c} (this point is shown in Figure 5.6-b to d), which is the same for both the *zero* field superconducting state and the *normal* state. Then, as depicted in Figure 5.6-c and d, the area under the *normal* curve (area (A)) and that under the *zero* field superconducting curve (area (B)) must be the same. In practice we adjust the extrapolation (consistent with Debye behaviour) until this equality is met as closely as possible.

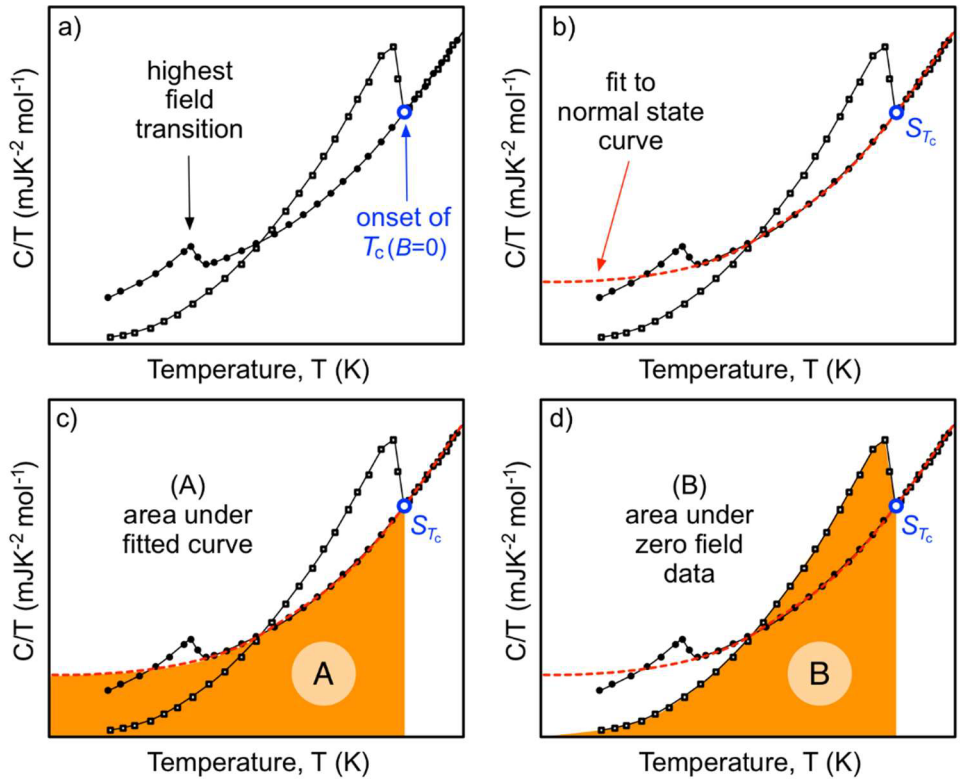

Figure 5.6: Schematic plots of *zero* field and *in-field* heat capacity data in the form C/T vs T; a) shows both datasets and points out the onset of the zero field transition, b) a fit to the normal state curve of the in-field dataset, c) the area (A) under the fitted curve from 0 K up to T_c, d) the area (B) under the zero field curve from 0 K to T_c. Thermodynamic relations show that the areas (A) and (B) are equal. This fact can be used to improve the fit to the in-field dataset until this equality is met. The normal state behaviour of the sample down to 0 K can then be analysed in a Debye plot to obtain the normal state parameters (c.f equation (5.1)).

The extrapolation of the normal state curve (see Figure 5.6-b) can then be plotted on a Debye plot of C/T vs T^2 and a linear fit to its very low temperature behaviour used to obtain γ and β in accordance with equation (5.1).

5.2.4 Upper critical magnetic field

An estimate of the upper critical magnetic field at zero temperature, $B_{c2}(0)$, of microcrystalline $NbC_{0.3}N_{0.7}$ is obtainable from the superconducting transitions in ac-susceptibility, magnetisation and heat capacity measurements performed on the four microcrystalline samples S9, S109, S115 and ${}^{0}H_{1050}^{10}$. The resistivity data were not used in this instance due to them being more representative of the best percolative current paths within a sample rather than representing the sample as a whole. Typically they give values of B_{c2} that are ~ 6 T above the bulk values. They also produce higher T_C's than volumetric measurements, for example. A compilation of the data points obtained from the complimentary measurement techniques is shown in Figure 5.7. The dashed curve in the figure represents the best fit to the data in accordance with [128],

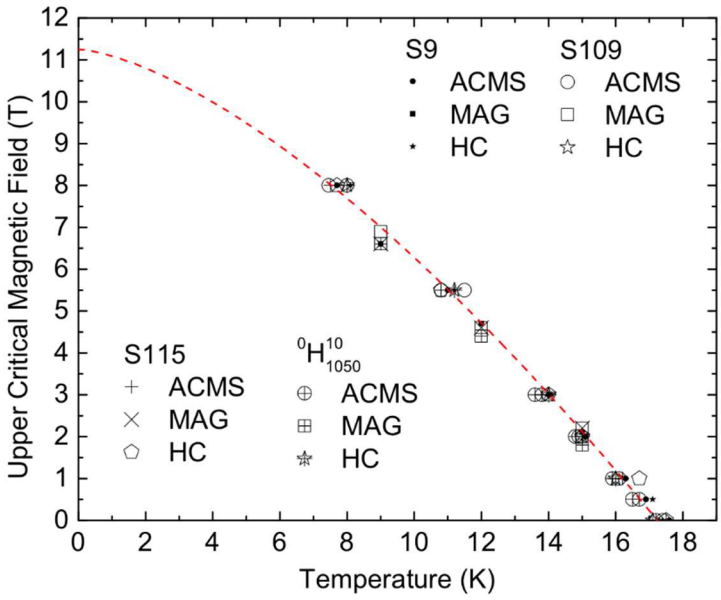

Figure 5.7: Upper critical magnetic field as a function of temperature for $NbC_{0.3}N_{0.7}$ obtained from ac-susceptibility (ACMS), magnetic hysteresis (MAG) and heat capacity (HC) measurements performed on samples S9, S109, S115 and $^0H^{10}_{1050}$. The dashed curve is a best-fit to the complete dataset.

$$B_{C_2}(T) = B_{C_2}(0)\left(1 - \left(\frac{T}{T_C}\right)^{\frac{3}{2}}\right) \qquad (5.5)$$

and the extrapolation to $T = 0$ provides a value of $B_{C_2}(0)$ of 11 ± 1.5 T.

5.2.5 Critical current density

The critical current density, J_C, of the sintered samples S9, S109 and S115 and the HIPed sample $^0H^{10}_{1050}$ were obtained from magnetisation data using Bean's critical state model [28] for slab shaped samples in accordance with equation (2.67). Each of the samples were slab-like in shape and of millimetre dimensions; giving a typical uncertainty in J_C of ~ 10 %. Plots of J_C vs *B* for temperatures 3, 6, 9, 12 and 15 K are shown in Figure 5.8, where individual plots for each temperature are also provided. The values of the critical current density for each sample in an applied magnetic field of 3 T and a temperature of 6 K are listed in Table 5.4. The current density of these samples is very low in comparison to the typical values expected of Nb_3Sn (wire ~ 1.5 x 10^{10} Am^{-2} at 3T and 6 K) [33]. Figure 5.8-b to Figure 5.8-e show that the sintered samples S9, S109 and S115 share very similar J_C's, which is expected given their very similar fabrication methods. However, J_C of the HIPed sample $^0H^{10}_{1050}$, is approximately half that of the sintered samples. This suggests that the connectivity between the grains in the samples sintered at higher temperatures is better than the samples HIPed at low temperatures and is consistent with the resistivity data. We note, however, that in principle it could be argued that HIPing sample $^0H^{10}_{1050}$

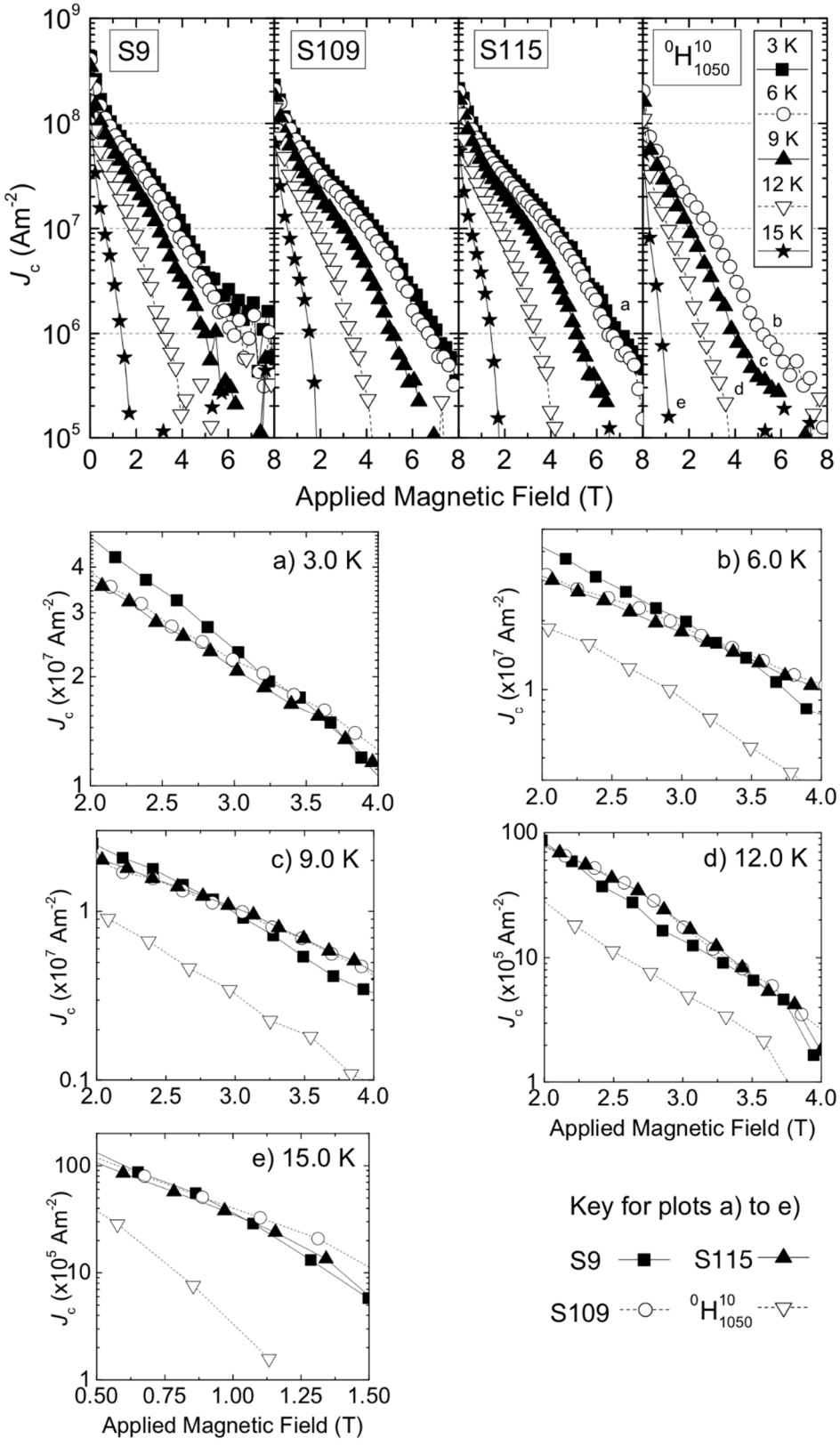

Figure 5.8: Critical current density, J_C, as a function of applied magnetic field for the sintered samples S9, S109 and S115 and the HIPed sample $^{0}H^{10}_{1050}$ at temperatures 3, 6, 9, 12 and 15 K. The data for each of the temperatures are independently shown in plots a) to e). Note: data at 3 K were not obtained for sample $^{0}H^{10}_{1050}$.

Table 5.4: Critical current density, J_C, in applied magnetic field *B*=3 T and at a temperature of *T*=6 K for the microcrystalline samples. (These data points were obtained from Figure 5.8-b.)

sample	$J_C(B = 3\ \mathrm{T},\ T = 6\ \mathrm{K})$ (Am^{-2})
S9	2.0 x 10^7
S109	1.9 x 10^7
S115	1.8 x 10^7
${}^0H_{1050}^{10}$	9.0 x 10^6

has provided an additional annealing of its grains, thus reducing defects that would usually provide additional trapping locations for magnetic flux to reside within. The reduction of these *intragrain* pinning sites would decrease current flow within the volume of the grains and increase the current flow along grain surfaces, which would lead to an overall reduction in the total current that could be carried by the sample. Also, since magnetisation measurements were used to acquire the data from which J_C was calculated, as opposed to actual current transport measurements, this line of reasoning suggests we are seeing the result of an increase in *intra*grain quality (in terms of a reduction in defects) rather than a decrease in *inter*grain connectedness, or more likely, some combination of them both. Nevertheless, in the context of the *nanocrystalline* material considered below, we take the microcrystalline superconducting material that we have used to produce the nanocrystalline material, as high quality, and reasonably homogenous.

5.3 Nanocrystalline material

A similar analysis to that applied to the microcrystalline samples discussed above, was also performed on the five *nanocrystalline* samples produced from HIPed billets 4 to 8 in Table 4.5. These samples were made from two batches of sintered microcrystalline material that was subsequently milled for 20 hours prior to being HIPed. Different HIPing temperatures and/or dwell times were used with a view to achieving optimum sample quality. The following sections analyse the data acquired from ac-susceptibility, heat capacity and dc-magnetisation measurements to determine normal state and critical superconducting properties.

5.3.1 Ac-susceptibility

The magnetic susceptibility of the milled nanocrystalline powder M_{20} from Batch 1 is compared with the microcrystalline sample S115 in Figure 5.9. There is a substantial suppression of the superconducting transition, which is very clearly caused by the milling, from a starting value of ~ 17.5 K down to ~ 5.3 K. Figure 5.10 contains the susceptibility data for the HIPed samples and Table 5.5 contains their transition temperatures and transition widths. Sample ${}^0H_{1050}^{10}$ (which is *microcrystalline*) and the (starting) milled powder sample M_{20} are included in the table for

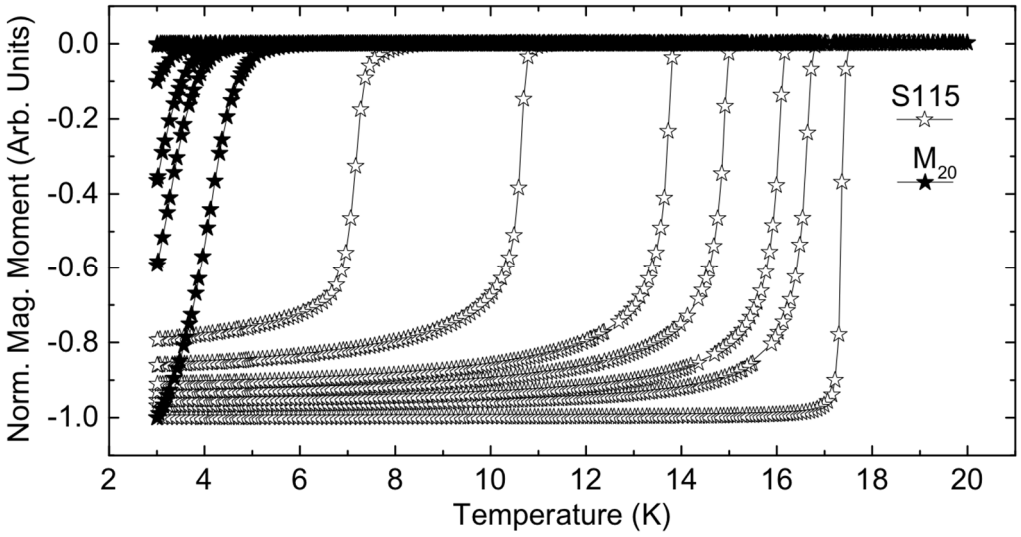

Figure 5.9: AC-susceptibility data of the twenty-hour milled nanocrystalline sample, M_{20}, compared against the zero-hour milled *microcrystalline* sample, M_0, measured in applied magnetic fields 0.0, 0.5, 1.0, 2.0, 3.0, 5.5 and 8.0 T, where increasing field is from right to left. The excitation field was 0.4 mT at 777 Hz.

comparison purposes. The data in Table 5.5 is shown in Figure 5.11 plotted as the upper critical magnetic field *versus* temperature. The curves represent fits to the data using equation (5.5). There is a clear and systematic increase in $B_{c2}(0)$ and a decrease in T_c for the bulk samples HIPed at the hottest temperature (and longest time), ${}^{20}H^{40}_{1150}$, through to the one HIPed at the coolest temperature, ${}^{20}H^{10}_{950}$. We attribute this inverse correlation between HIP temperature and $B_{c2}(0)$ to increased grain growth and less electron scattering. We also note the decrease in $B_{c2}(0)$ due to 100 ℃ increases in HIP temperature (billets 7, 4 and 8 in Figure 5.11) are greater than that due to an increase in HIP dwell time of 30 minutes (billet 5) – though experimentation with other changes in dwell time and HIP temperature would be needed to make a more definitive statement in this respect. Most striking, however, is the increase in $B_{c2}(0)$ of sample ${}^{20}H^{10}_{950}$ (~ 20.6 T) in comparison to the microcrystalline data (~ 11.2 T), which is an ~ 84 % increase with no reason to believe the maximum has yet been reached. Figure 5.12 contains a direct comparison between the HIPed nanocrystalline sample, ${}^{20}H^{10}_{1050}$, (from Figure 5.10-c) to its milled *nanocrystalline* precursor, M_{20}, (from Figure 5.9) and the HIPed *microcrystalline* sample ${}^{0}H^{10}_{1050}$ (from Figure 5.10-a). This figure unambiguously confirms that sample, ${}^{20}H^{10}_{1050}$, (the *nanocrystalline* sample), has better high field properties above 8 T than microcrystalline material.

Beyond the systematic behaviour so far discussed, we can also consider other details in the ac. susceptibility data. Samples ${}^{20}H^{10}_{950}$ and ${}^{20}H^{10}_{1050}$, shown in Figure 5.10-b and c have sharp superconducting transitions and they maintain maximum magnetic screening at all measured fields, which is indicative of good quality, homogeneous, material. The HIP dwell time for these two samples was the same and their HIP dwell temperatures only differed by 100 ℃, and so their similarities are not surprising. Samples shown in Figure 5.10-a (the HIPed microcrystalline sample) and Figure 5.10-d and e, which are both the result of failed HIP treatments (their billets

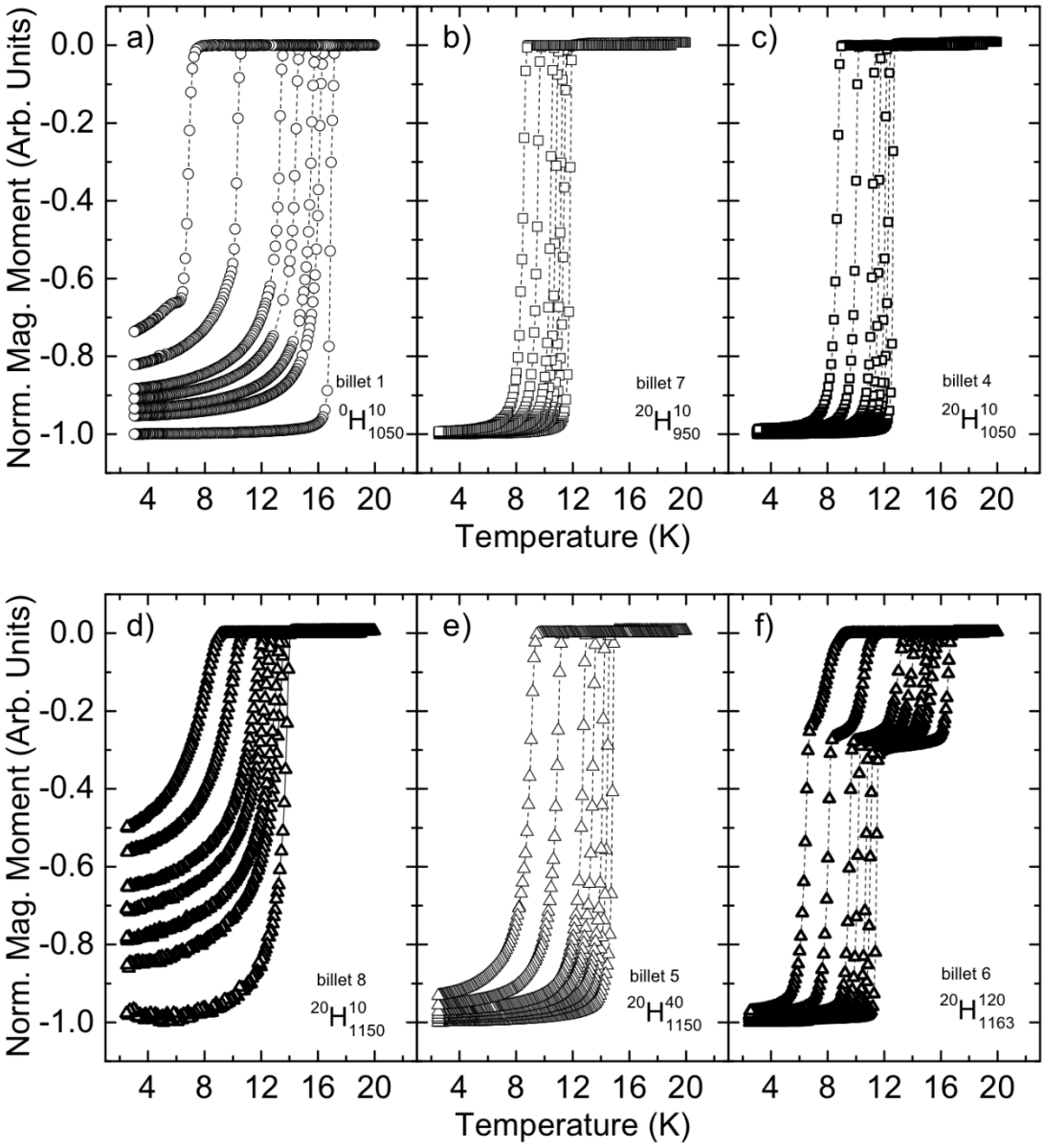

Figure 5.10: AC-susceptibility data of the HIPed samples measured in applied magnetic fields 0.0, 0.5, 1.0, 2.0, 3.0, 5.5 and 8.0 T where the field increases from right to left. a) billet 1 (microcrystalline) sample HIPed at 1050 ℃ for 10 m (this sample is provided for comparison purposes), b) billet 7 sample HIPed at 950 ℃ for 10 min, c) billet 4 sample HIPed at 1050 ℃ for 10 min, d) billet 8 sample HIPed at 1150 ℃ for 10 min, e) billet 5 sample HIPed at 1150 ℃ for 40 min and f) billet 6 sample HIPed at 1163 ℃ for 120 min. The excitation field was 0.4 mT at 777 Hz.

were not gas tight and probably not sufficiently densified), show that in high fields full screening of the samples does not occur. Furthermore, these samples have relatively wide transition widths, which is indicative of wider distributions of varying quality material i.e. inhomogeneity. These results suggest that the grain boundaries do not contact the grains well or that the volume of material that contributes to the superconducting state reduces in high fields and therefore leads to a reduced magnetic moment.

Table 5.5: Transition temperature, T_C, for all measured fields and transition width, ΔT_C (10 – 90 %) for zero-field for the HIPed samples obtained from ac-susceptibility data shown in Figure 5.10. The milled sample, M_{20}, is included for comparison purposes.

sample	figure reference	ΔT_C (B=0) (K)	T_C (onset)	In-field ac. susceptibility transition onsets (K)					
				B = 0.5	B = 1.0	B = 2.0	B = 3.0	B = 5.5	B = 8.0
M_{20}	Figure **5.9**		5.3						
$^{20}H_{950}^{10}$	Figure 5.10-b	~ 0.37	11.9	11.9	11.7	11.0	10.7	9.8	8.7
$^{20}H_{1050}^{10}$	Figure 5.10-c	~ 0.26	12.7	12.4	12.2	11.8	11.3	10.2	8.9
$^{20}H_{1150}^{10}$	Figure 5.10-d	~ 2.8	14.0	13.7	13.4	12.8	12.2	10.7	9.2
$^{20}H_{1150}^{40}$	Figure 5.10-e	~ 0.69	14.9	14.6	14.3	13.6	12.9	11.2	9.4
$^{20}H_{1163}^{120}$	Figure 5.10-f	~ 1.62[a] ~ 0.34[b]	15.7[a] 11.1[b]						
$^{0}H_{1050}^{10}$	Figure 5.10-a		17.2						

a *above shoulder.* b *below shoulder.*

We also note the behaviour of sample $^{20}H_{1163}^{120}$ in Figure 5.10-f in which 'two-phase' behaviour is visible. The standard explanation for these types of dataset is that the sample is comprised of a mixture of good quality grains and poorer quality grain boundary matrix. The group of superconducting transition onsets associated with the high temperature phase can be compared with the *microcrystalline* sample data in Figure 5.10-a. This comparison shows them to be similar (especially at lower applied fields). Likewise, a comparison can be made of the low temperature phase data with the *nanocrystalline* samples in Figure 5.10-b and c. Again, the transition onsets at lower applied fields are similar. A straightforward interpretation would be that the combination of HIPing dwell time, temperature and pressure for sample $^{20}H_{1163}^{120}$ has produced a combination of microcrystalline grains but that a substantial portion of nanocrystalline grains still remain. Had the sample been homogeneous, we would have expected that sample $^{20}H_{1163}^{120}$ would have been much more like the microcrystalline sample $^{0}H_{1050}^{10}$ (Figure 5.10-a) with sharper in-field transitions or like sample $^{20}H_{1150}^{40}$ (Figure 5.10-e) with a slightly higher transition temperature and a greater spread in the onsets of its various in-field transitions. We can also conjecture that the morphology of this sample may be better considered as microcrystalline grains submerged within a matrix of grain boundaries that are in part comprised of nanocrystalline material. One possible explanation is that the vacuum within the HIP billet was not as high as it should have been and not as high as

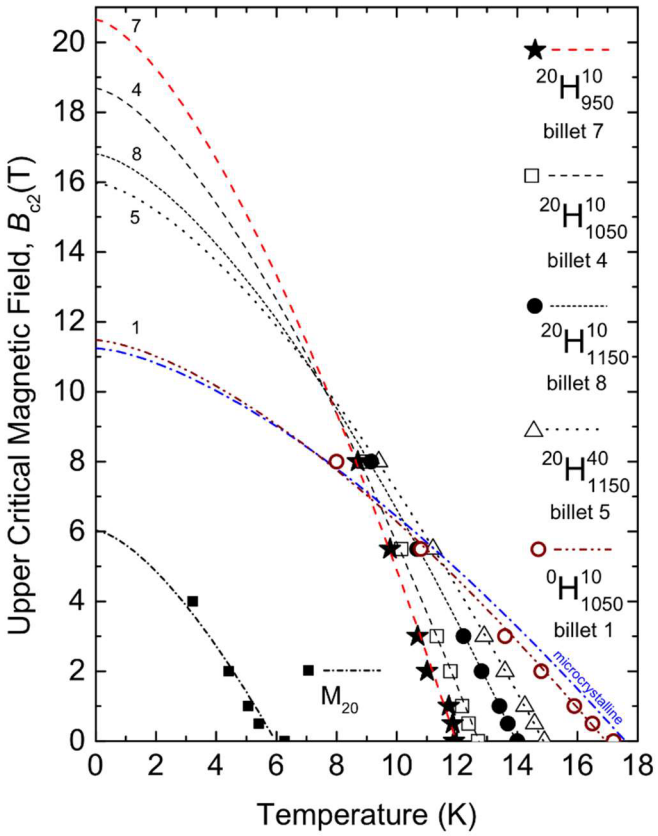

Figure 5.11: Upper critical field as a function of temperature for the nanocrystalline powder M_{20}, the nanocrystalline HIPed samples $^{20}H^{10}_{950}$, $^{20}H^{10}_{1050}$, $^{20}H^{10}_{1150}$ and $^{20}H^{40}_{1150}$, and the HIPed microcrystalline sample $^{0}H^{10}_{1050}$. The dashed curves are best fits to the data (from Figure 5.7) of equation (5.5).

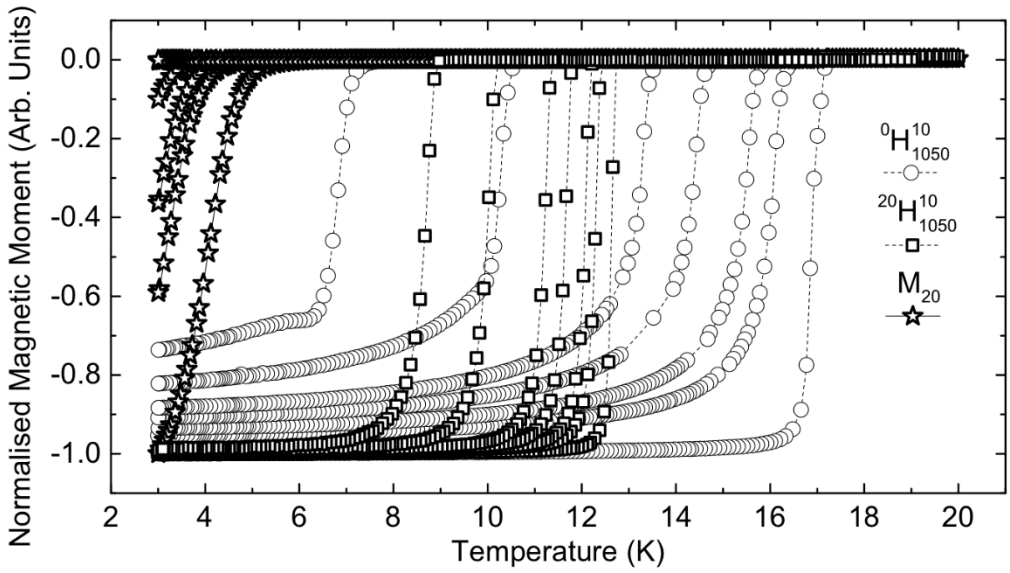

Figure 5.12: A direct comparison of the ac-susceptibility data from the HIPed nanocrystalline sample $^{20}H^{10}_{1050}$ to its nanocrystalline milled precursor, M_{20}, and the HIPed microcrystalline sample $^{0}H^{10}_{1050}$. These measurements were conducted in applied magnetic fields 0.0, 0.5, 1.0, 2.0, 3.0, 5.5 and 8.0 T, where increasing field is from right to left.

the other good samples. A small presence of diffuse gas sealed within the billet might have caused inhomogeneity in the densification by isolating large collections of nanocrystalline grains from smaller pockets of nanocrystalline grains, thereby limiting grain growth within the much smaller pockets. However, the exact cause of the unusual shoulder in the data is difficult to determine without an extended experimental study and currently it is the preparation of this particular sample that remains under suspicion. Clearly, electron microscopy would be an advantageous tool in helping to properly characterise this sample's morphology but at the time a detailed investigation of this sample was not one of the experimental goals and so an explanation for this anomalous two-phase behaviour is still, however, an open question.

5.3.2 Heat capacity

The heat capacity of the nanocrystalline HIPed sample ${}^{20}H^{10}_{1050}$ was measured using the same equipment and techniques used on the microcrystalline samples discussed above. The data are presented in Figure 5.13 in the form of Debye plots. This figure also provides comparisons to the microcrystalline HIPed sample ${}^{0}H^{10}_{1050}$ for each of the measured fields. The Debye temperature and Sommerfeld constant for sample ${}^{20}H^{10}_{1050}$ were not obtained from these data due to the presence of a magnetic component, which is most likely to be cobalt contamination from the milling media (see Contamination Management in section 4.3.1 in Chapter 4). This magnetic component presents itself as a magnetic field dependent vertical shift (visible in the normal state data - see the bottom right-hand inset in Figure 5.13) and also as upturns in the very low temperature superconducting region of the data (see the top left-hand inset in Figure 5.13). This belief is further supported by the fact the unmilled sample, ${}^{0}H^{10}_{1050}$, is free of these additional characteristics in the data. The effects of the magnetic contamination makes it extremely difficult to obtain reliable values of the Debye and Sommerfeld constants, which were intended for comparison against those obtained for the microcrystalline samples. Nevertheless, the heat capacity data for the nanocrystalline sample in Figure 5.13 show very clear bulk superconducting transitions. Furthermore, there is a clear cross-over between panel (a) and panel (f) in the figure, which demonstrates that the large improvement in the upper critical field is an improvement in the *bulk* properties and not simply an improvement in the percolative properties of the sample.

5.3.3 Critical current density

The critical current density, J_C, as a function of applied magnetic field, at various temperatures, for the nanocrystalline HIPed sample ${}^{20}H^{10}_{1050}$ is shown alongside the microcrystalline HIPed sample ${}^{0}H^{10}_{1050}$ in Figure 5.14. These data were collected and analysed using the same Bean's model analysis used for the microcrystalline samples discussed in section 5.2.5 above. At 3 T and at 5.9 K the J_C of the nanocrystalline sample, ${}^{20}H^{10}_{1050}$, is 7.4 x 10^8 A m^{-2}. This is almost two orders of magnitude greater than the J_C of the corresponding HIPed microcrystalline sample, ${}^{0}H^{10}_{1050}$, and is a factor of ~ 40 greater than the microcrystalline precursor sample S115 (see Table 5.4 for microcrystalline J_C values). This realisation of a *fortyfold* increase in J_C highlights the potential for further improvements in the high-field performance of niobium carbonitride.

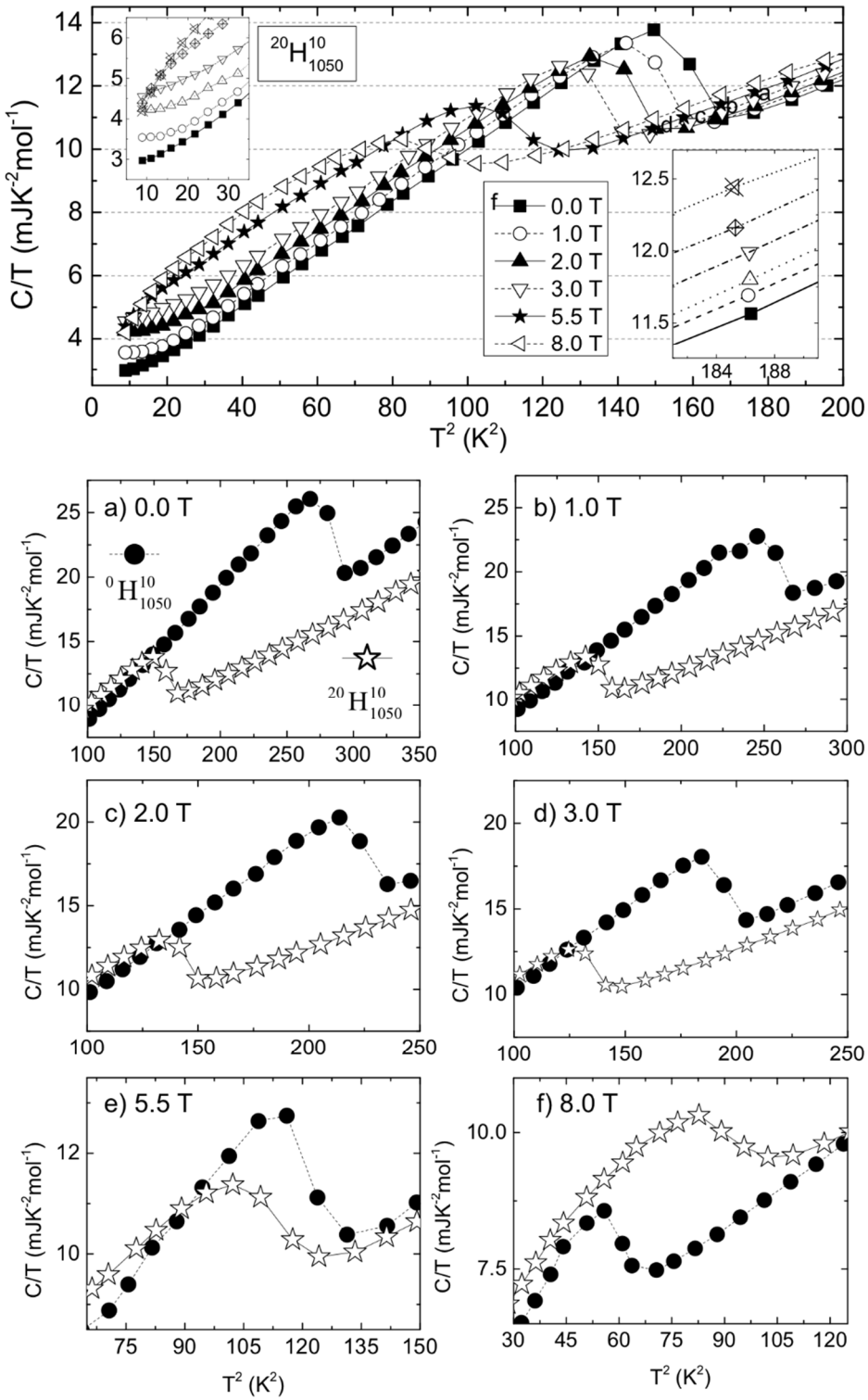

Figure 5.13: Debye plot of the HIPed sample $^{20}H^{10}_{1050}$ (top) in applied magnetic fields 0 to 8.0 T. The top left-hand inset shows the low temperature upturns due to the presence of a magnetic component. The bottom right-hand inset shows the upward shift in the normal state heat capacities (heat capacity increases with field) due to the magnetic component. Plots a) to f) are comparisons between the nanocrystalline sample $^{20}H^{10}_{1050}$ (from the top plot) and the microcrystalline sample $^{0}H^{10}_{1050}$.

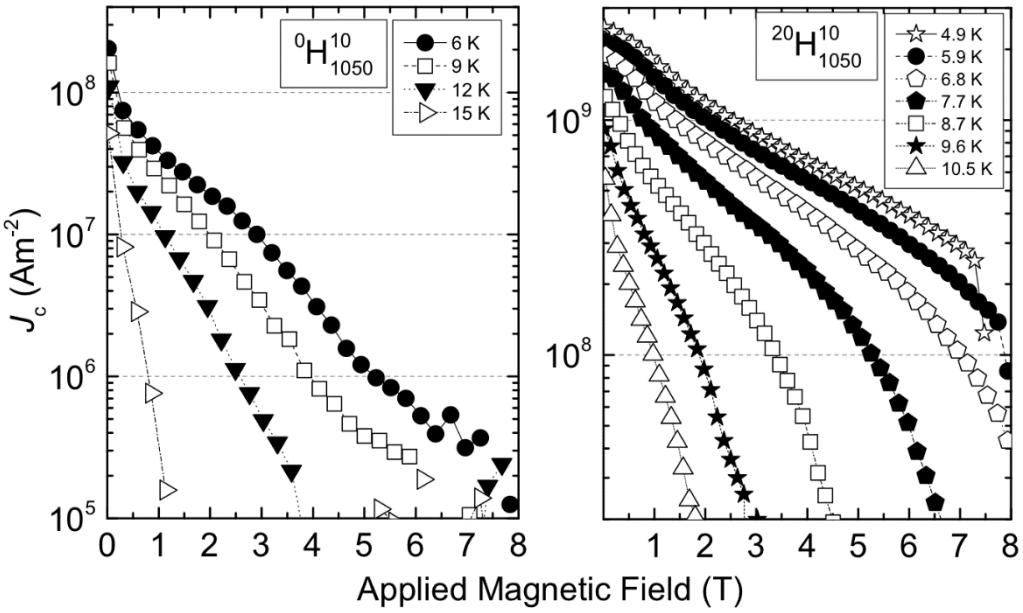

Figure 5.14: Critical current density as a function of applied magnetic field of the nanocrystalline sample, $^{20}H^{10}_{1050}$ (in the temperature range 4.9 to 10.5 K), and the microcrystalline sample, $^{0}H^{10}_{1050}$ (in the temperature range 6 to 15 K).

5.4 Discussion and Concluding Comments

The use of microstructure in the nanocrystalline regime to increase the upper critical magnetic field was pioneered by the group in Durham. It was first reported in a Chevrel phase material [129] and subsequently increases in B_{c2} in Nb [30] and Nb_3Sn [130] were also achieved. The broad experimental observations in those nanocrystalline materials were similar to those reported here for niobium carbonitride i.e. an increase in B_{c2} at the expense of a decrease in T_c. However, in the case of the Chevrel phase materials, although there were large increases in the upper critical field, the irreversibility field and J_c values were only marginally improved. In the cases of Nb and Nb_3Sn, there were significant increases in B_{c2} for Nb up to 3 T and the properties of binary Nb_3Sn were improved to nearly those of ternary material, but the relative improvements were modest. In this work we have found an unprecedented increase in B_{c2} of nearly 10 Tesla. This improvement has been verified using resistivity and susceptibility measurements. Furthermore, this increase has been confirmed as an improvement in bulk properties using heat capacity measurements. Consistent with an improvement in bulk properties, the current density has been increased by nearly two orders of magnitude.

Although an enormous effort has been expended in making these materials, it is clear that we have likely not yet reached the optimum upper critical field and that HIPing at higher temperatures (but for shorter times to keep the grain size low) will probably improve the quality of the grain boundaries, leading to further increases in J_c. A detailed understanding of the underlying science that leads to the improvements in properties we have found is not yet available. The literature provides a plausible explanation that for a homogenous sample, the increases in B_{c2} can be

attributed to increases in resistivity, and that the decreases in T_c are associated with a decrease in the Sommerfeld constant [30]. However, it is clear that as the grain size is reduced to a size comparable to the coherence length of the superconductor, it might not be very accurate to consider the sample as being homogenous, since the distinction in relative dimensions between grains and boundaries is removed. We note that a real hurdle to our theoretical understanding is our limited understanding of grain boundaries, of which we know very little about their electronic properties in complex intermetallic materials, let alone understand how their superconducting properties change on a local scale near them. Nevertheless, despite this lack of understanding, we have found that by making niobium carbonitride *nanocrystalline*, we have produced the most marked improvement in superconducting properties reported to date of any bulk material made nanocrystalline.

Nine samples in total, four *microcrystalline* and five *nanocrystalline*, were analysed using various measurement techniques designed to probe specific normal state and superconducting properties. These properties, namely, resistivity, ρ_n, Debye temperature, θ_D, Sommerfeld constant, γ, transition temperature, T_c, critical current density, J_c, and upper critical magnetic field, B_{c2}, were required to provide a comprehensive knowledge of the samples, with a view to identifying (and understanding) the sample with the most enhanced B_{c2} and thereby establishing the best route by which this optimised material can be fabricated. Our data have shown that a substantial increase in B_{c2} had been achieved in sample ${}^{20}H_{950}^{10}$ ($B_{c2}(0) \approx 20.6$ T: an increase of ~ 84 %), which was accompanied by a modest reduction in T_c so that at the temperature of liquid helium (4.2 K), J_c is a factor *forty* greater than the corresponding microcrystalline sample (measured at 3 T and 6 K). This, in conjunction with the fact that none of the measurement results suggest that an optimum enhancement has been achieved, provides encouragement that it might still be possible to optimise the fabrication process further. A more comprehensive and extended experiment and subsequent analysis is undoubtedly required to fully identify the optimum fabrication route and what maximum enhancements to the material's superconducting properties are possible. However, the current body of work has provided a firm foundation upon which this extended work could be based. This, in conjunction with niobium carbonitride's resilience to irradiation damage (in comparison to the A15's) shows that it has the potential to be an alternative low-temperature material for fusion tokamak applications; though of course, this statement is made in the knowledge that there are a great number of technological/engineering/financial challenges in getting a potential candidate material from the laboratory into a real-world application. With that said, an 84 % increase in upper critical field and a *fortyfold* increase in critical current density, within the same sample, are exciting steps towards what might be achievable.

PART III: The Metrology of Nb_3Sn for ITER

Chapter 6

Metrology of large quantity characterisation of toroidal field Nb_3Sn strands for ITER

6.1 Introduction

In 2011, the Superconductivity Group signed a contract with Fusion for Energy (F4E) to perform *seven* types of characterisation measurement on Nb_3Sn strands as part of the verification and acceptance process. Our aims were:

i) To meet our contractual obligations by making more than 10,000 measurements in three years.
ii) To research and develop the cryogenic and room temperature metrology necessary for large quantity characterisation of Nb_3Sn strands.
iii) To have impact on the success of the ITER tokamak being built in Cadarache, Southern France.

The principle investigator and supervisor for this project (and my thesis) was Professor Damian Hampshire. As with many large projects, however, this was very much a team effort that included several thousand hours of work by dedicated technicians. My main responsibility, on day-to-day basis, was to develop and improve the metrology necessary for making the measurements. In particular, I was the first point of contact for all new results in the laboratory, either because I performed the measurements myself or because I was the line-manager for the technicians instructed by me to make those measurements. I completed all the analysis of the data, both for this thesis and for the formal reporting of the data to F4E. It should also be made clear, that everything written in this chapter does not represent the views or opinions of F4E or the ITER organisation or any actions or decisions that might have been made by those organisations in relation to the content of this chapter. The chapter is written in the context of Durham's role and is limited to only those aspects for which I had direct involvement.

During the contract period there were some 'non-trivial' disagreements with the strand manufacturers about the accuracy of the data generated in Durham. This led to additional verification testing by Durham and other international laboratories including CERN. In *all* cases, the data in Durham were confirmed to within the stated accuracy of our measurements, which led

to scientifically accurate, well-informed and efficient discussions between the manufacturers and F4E about how best to proceed.

This chapter begins by looking at the background to the measurements and the architecture of the strands. It then considers the development of the furnace facilities, heat-treatment preparation and sample mounting, which leads to a discussion about each of the seven measurement types. The developments made to improve the accuracy and practicality of making large quantity measurements are considered. There are some commercial confidentiality issues about presenting all the data but this is made clear where necessary. For each measurement, we describe the final methods and the accuracy achieved by Durham to make high quality, large quantity measurements. All uncertainties or error bars that appear on plots represent one standard deviation.

6.2 Background

A total of 62 tons of copper strand and 95.3 tons of Nb_3Sn strand are being used to manufacture the conductors of the toroidal field (TF) coils for ITER [131]. Two types of Nb_3Sn strand (internal tin and bronze route) were procured by F4E from two different suppliers to minimise the risk of delay to the programme schedule, where delays from one supplier would be rectified by an increased production from the other. In parallel to this supplier production, and to further reduce the risk to the project, it was decided by F4E that the strands would need to satisfy a set of supplier-independent verification tests (see Table 6.1) that would determine their quality and qualify them for inclusion in the conductors. These verification tests were to consist of *seven* types of characterisation measurement: *three* to be performed at cryogenic temperatures - critical current, I_C, (at 4.22 K); hysteresis losses, Q_{hyst}, (at 4.22 K) and residual resistivity ratio, RRR, (at 273 K and at 20 K); the remaining *four* measurements at room temperature - strand twist pitch, T_p, (and direction), strand diameter, d, chromium plating thickness, Cr_{T}, and copper-to-non-copper ratio, CnC.

Table 6.1: Specification parameters for the ITER TF Nb3Sn strands [131].

specification parameter	parameter value
cryogenic measurements	
critical current at 12 T and 4.22 K (10 μVm^{-1})	> 190 A
n-value at 12 T and 4.22 K (between 10 and 100 μVm^{-1})	> 20
hysteresis losses ±3 T at 4.22 K	< 500 mJ/cm^3
residual resistivity ratio at 273 K and 20 K	> 100
room temperature measurements	
strand diameter	0.820 ± 0.005 mm
strand twist pitch	15 ± 2 mm
chromium plating thickness	2 + 0 – 1 μm
Cu to non-Cu ratio	1 ± 0.1

F4E required that Durham heat-treat all the samples earmarked for testing at cryogenic temperatures. While Durham already had the technical expertise and equipment to perform the tests, the large number of samples (~ 10,000 in total) that would be generated during the testing phase (*three* years), and the need to satisfy F4E's delivery schedule, demanded that Durham increase its infrastructure, build a dedicated competent technical team and set in place stringent procedures for handling and tracking large sample quantities. Additionally, it was very important to develop practical and efficient ways of increasing measurement throughput while maintaining high accuracy.

6.3 Strand architecture and brittleness

The cable in conduit conductors (CICCs) that are used in the winding of the TF coils for the ITER magnet system are each comprised of 522 copper strands and 900 Nb_3Sn strands, which are themselves subdivided into two different types, namely, internal tin and bronze route (see Figure 6.1-a) [131]. These two types of Nb_3Sn strand share very similar architectures (see Figure 6.1-b): both employ an outer chromium plating layer that electrically decouples the strands and maintains their independent physical integrity when grouped together; both have a copper layer that occupies approximately half the cross-section and acts as a thermal stabiliser and current shunt during superconductor quenches and both have a tantalum layer that serves as a diffusion barrier to stop mobile tin from reaching the clean copper stabiliser during heat-treatment (the cleanliness of this copper stabiliser is of paramount importance). The main features that actually distinguish each architecture reside under the tantalum barrier. In the case of the internal tin architecture 19 sub-elements are each comprised of a central tin region surrounded by fine niobium filaments. In the case of the bronze route architecture 151 niobium filament bundles are submerged within a bronze matrix.

Nb_3Sn is a brittle material. So, whilst its superconducting characteristics make it a technological workhorse, its brittle nature means that generally a wind-and-react process is used [132]. First, flexible strand is manufactured that contains the separated elemental components niobium and tin (see Figure 6.1-b). This flexible strand can easily be wound into any number of shapes that suit the technological application, with little risk of breakage if handled carefully. Once the desired coil is wound it is then necessary to heat-treat it in accordance with a specific heat-treatment programme to cause the tin component to diffuse into the niobium component, form Nb-Sn and then grow well connected grains of Nb_3Sn with the required superconducting properties.

All the samples earmarked for verification testing were sent to Durham in 44 batches (deliverables) of flexible strand from which three different sample geometries, one for each of the cryogenic measurement types, were prepared and then heat-treated in dedicated high-temperature furnaces.

a)

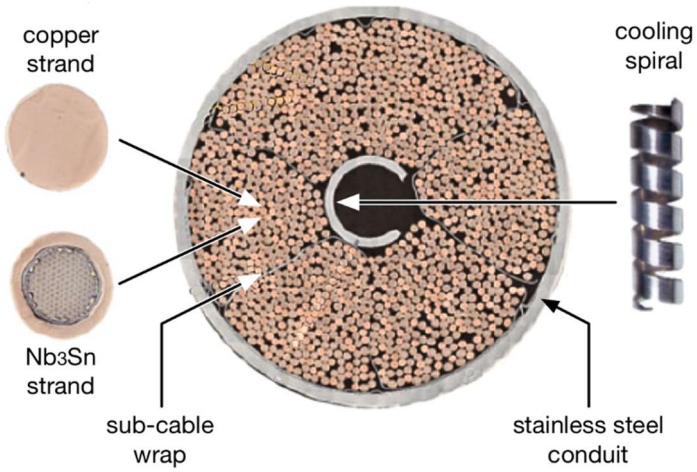

b)

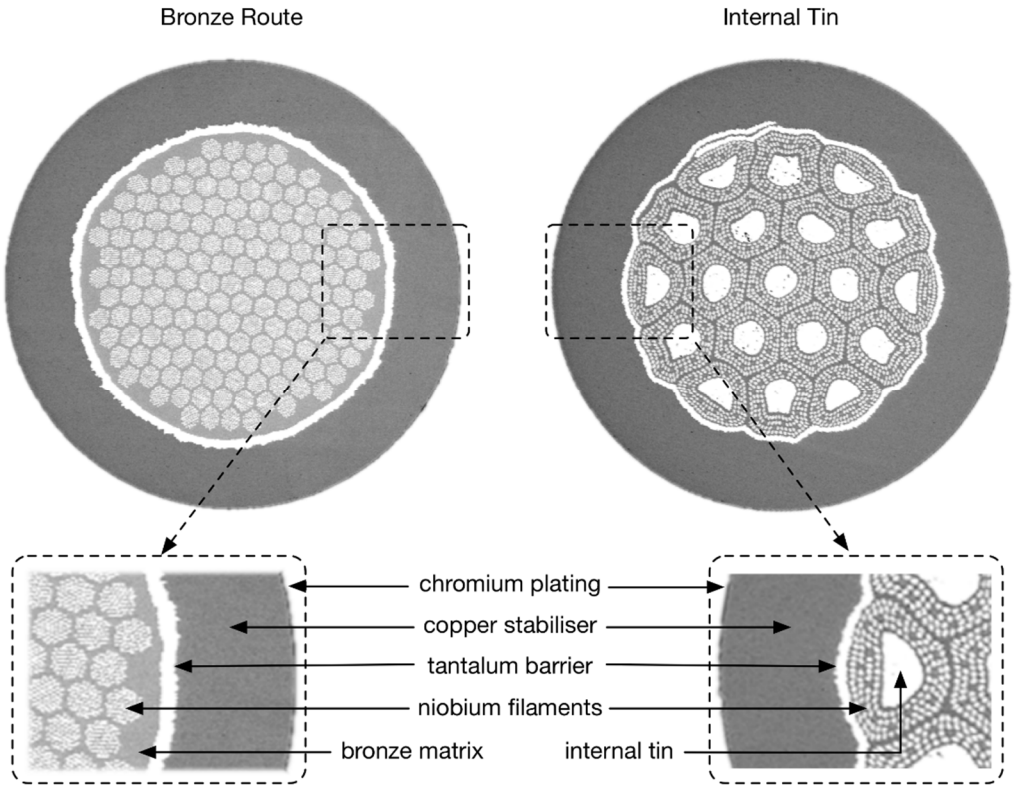

Figure 6.1: a) Cross-section image showing a toroidal field cable in conduit conductor (CICC) within which the Nb_3Sn strands reside (image adapted from [133]. b) Cross-section images (acquired with the scanning electron microscope in Durham) showing the pre-heat-treated architectures of the two types of Nb_3Sn strand being used in the toroidal field CICCs. The main difference between both architectures is the way the tin content is contained. In the case of the bronze route (left-hand image), the tin resides within the bronze matrix, whereas, in the internal tin architecture (right-hand image) it is contained within the central region of the niobium filament bundles.

6.4 Heat-treatment of samples

6.4.1 Sample preparation and mounting

Each of the samples designated for cryogenic measurements had to be individually prepared with the geometries required of their measurement types and then heat-treated in furnaces. Critical current samples and loss samples were heat-treated together, whilst RRR samples - where gas purity was essential - were reacted separately in dedicated furnaces. The research group used stainless steel as an assembly rig material. However, analysis of early heat-treated samples with the scanning electron microscope found that various contaminants, including manganese, sweated out of the steel during heat-treatment. We therefore decided to make all rig parts from the same materials used for the sample barrels - predominantly the titanium alloy recommended by ITER and copper.

Critical current samples

1.7 m lengths of flexible strand were each wound onto individual, engraved (for sample identification purposes), measurement barrels and held in place with screws (see Figure 6.2-a). During heat-treatment the ends of the strand can become tin deficient due to molten tin dripping from the ends. Discussions with F4E established that this tin depletion usually affects no more than 30 mm of strand and that crimping the ends helps to restrict this outward tin flow. Additionally, 30 mm long tails were cut from the ends of each heat-treated strand to remove the possible inclusion of lower quality superconductor entering the measurement process (see Figure 6.2-a1 and a2). Up to thirty wound critical current barrels were then assembled, in ten tiers of three, into a heat-treatment rig that was made from copper and titanium (Ti6Al4V)) (see Figure 6.2-d and e).

Hysteresis loss samples

Coils were formed around 4 mm diameter titanium pins that each contained 50 to 60 turns (see Figure 6.2-c) (after heat-treatment only the central *nine* turns were measured – the extra, unused turns, were included to allow for post heat-treatment handling). The ends of each coil were also crimped to restrict tin depletion. These prepared coils were then mounted onto the critical current rig in a position adjacent to their associated critical current sample barrel (see Figure 6.2-b, c and d).

RRR samples

The research group routinely reacted samples in high purity (six nines) flowing argon gas. However, collaborative experiments conducted with one of the strand manufacturers and CERN showed that the use of close fitting quartz tubes (~ 4 mm OD by ~ 1.5 mm ID by 200 mm long) further increased the visible cleanliness of the samples. 220 mm straight lengths of flexible strand were first prepared by cleaning them with acetone before placing them within quartz tubes. The

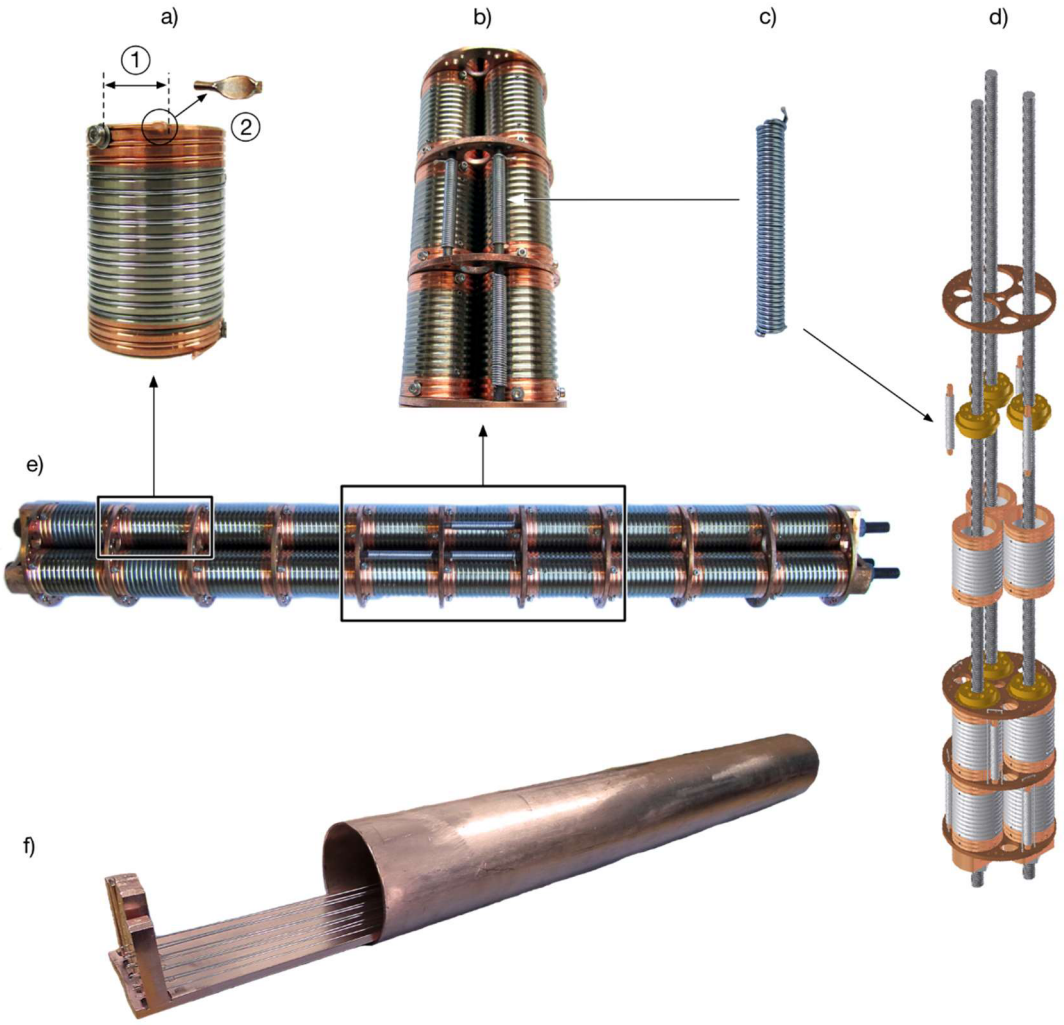

Figure 6.2: Heat-treatment rigs for a) critical current barrels ((1) 30 mm tail left loose at sample ends and (2) sample ends crimped to reduce tin depletion), b) three tiers of three critical current barrels mounted into the heat-treatment rig showing the adjacently mounted hysteresis sample coils c). d) is a diagram showing the assembly of a critical current rig. e) shows a full critical current rig with all ten tiers fully occupied and f) shows a number of RRR samples on a RRR rig being slid into a copper tube (quartz tubes are not shown). The copper tube is used to help equalise the furnace temperature over the sample region and is also used with the critical current sample rig.

tubes were then stacked onto a copper rig, which was then placed within a copper tube (see Figure 6.2-f).

6.4.2 Furnace facilities

Durham set up a suite of ten Elite *three* zone tube furnaces capable of continuous heat-treatments up to 1150 ℃ (see Figure 6.3). Key areas of development were as follows.

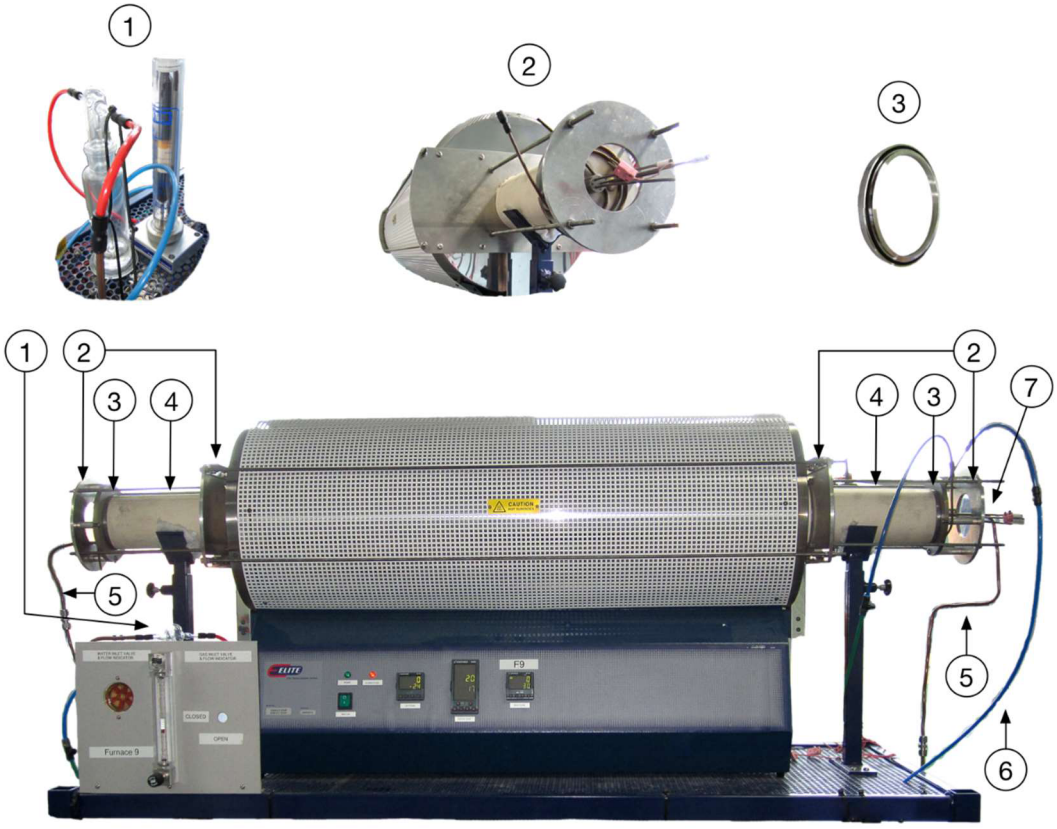

1. Inlet Supelco Superclean gas filter and outlet bubbler
2. Aluminium bracing system for furnace sealing
3. Double O-ring sealing holder (stainless steel)
4. Alumina furnace tube (1.5 m long)
5. Copper piping hard soldered to furnace end plates
6. Flexible water pipe for end plate cooling
7. Independent thermocouples and thermocouple sealing port

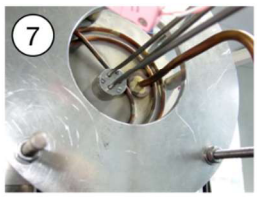

Figure 6.3: Typical high-temperature furnace set up used for Nb_3Sn heat-treatments.

Temperature profiles

Standard practice in the group had been to use a single, centrally placed, thermocouple in a three zone furnace, which was used to monitor the sample temperature throughout the heat-treatment. In these measurements we introduced a copper tube (see Figure 6.2-e) to extend the uniformity of the temperature profile. We also purchased new alumina baffle sets because they were found to substantially affect the homogeneity of the furnace temperature and we increased the number of independently monitored thermocouples from one to three (one for each heating zone). The control thermometry of each of the three zones was carefully balanced to achieve a dwell temperature within ± 2 ℃ of the set point along the central 700 mm sample space region (see Figure 6.3-7). This process was repeated for all temperature plateaus required of each of the two heat-treatment schedules used to react the two types of Nb_3Sn strand (see Figure 6.4). These

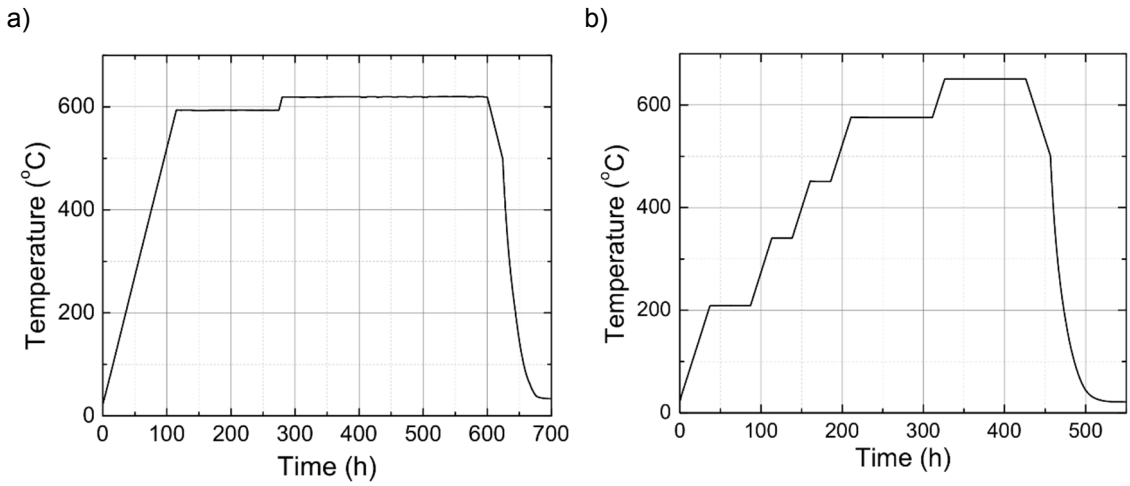

Figure 6.4: Heat-treatment profiles for a) bronze route and b) internal tin strand reactions.

individually tailored temperature programmes were then input into their respective furnace controllers for future use.

Thermocouples

The three thermocouples used to independently check the furnace zone temperatures were of type N (class 1) and were purchased from the furnace manufacturer in batches. The Type N (class 1) thermocouples used by Durham have a manufacturer's tolerance of 2.6 ℃ at 650 ℃. However, when a new batch was received in Durham up to six thermocouples at a time would have their ends placed within a copper block and then put into one of the furnaces. The furnace would be programed to perform a number of temperature dwells for various time periods while data from each thermocouple was recorded. These data were used, not only to confirm that the thermocouples were within the manufacturer's tolerance, but to also establish how well they agreed with one another (see Figure 6.5). Any outliers were not used. This improved the consistency between heating zones and between different furnaces.

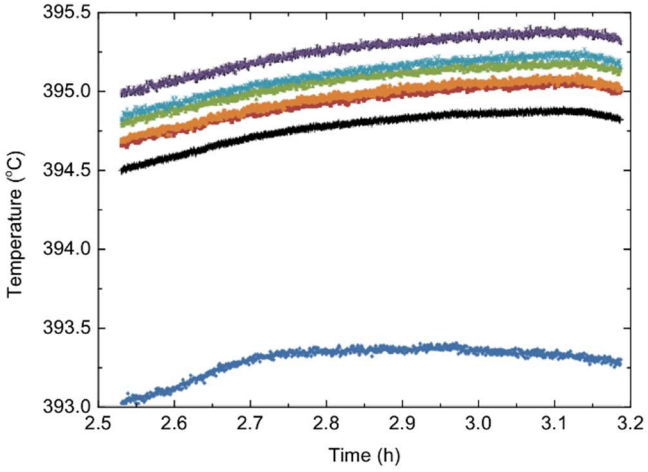

Figure 6.5: Data of six Type N (class 1) thermocouples. The thermocouple that produced the bottom dataset was not used.

Furnace tubes, gas seals and purity

We used two types of furnace tubes/seals: High grade (EA998) alumina tubes with stainless steel double O-ring sealing holders (see Figure 6.3-3) that were developed in-house and held in place with stainless steel end plates that were clamped to the tube ends with aluminium bracing (see Figure 6.3-2). For RRR measurements, where the highest purity environment was required, we used Kanthal (an alloy of iron, chromium and aluminium) tubes. The Kanthal allowed a welded knife-edge sealing flange to be attached to one end of a tube while the remaining end was welded closed with a stainless steel plate. We found that knife-edge seals were extremely robust and reliable. Standard practice in the group for maintaining gas purity was to use four nines gas with an exhaust bubbler to reduce the risk of gas backflow. The risk of backflow was further reduced by fitting one-way gas valves in line with the gas bubblers on all furnaces. Supelco Super Clean gas filters that maintained a minimum argon purity of six nines were also installed into the inlet piping of the RRR furnaces (see Figure 6.3-1).

Gas piping

All the original plastic gas piping to and from the end plates was replaced with 6 mm copper pipe (for increased flexibility over the stainless steel alternative) and was hard soldered to the end plates to increase local ingress protection.

Furnace operation

Furnaces were dedicated to particular types of heat-treatment to stop cross-contamination; three furnaces were only used for high-purity RRR heat-treatments (this included the furnace fitted with the Kanthal tube and knife-edge seal), six furnaces were dedicated to critical current and hysteresis loss heat-treatments and one furnace was used for oxidisation of the titanium critical current barrels. At any particular time one RRR furnace and two critical current furnaces were kept out of use for servicing. The furnaces were also all electrically supported by a back-up generator to protect against power outages.

6.4.3 Furnace loading and operation

Once the loading of a critical current and losses rig or RRR rig was completed, it was slid into a copper tube of a furnace and its open ends were partially blocked with crumpled sheets of zirconium foil that acted as oxygen getters [134]. Once a rig was sited within its respective furnace, and the ends of the sample tube sealed, the furnace would be pumped and flushed with Pureshield argon a minimum of three times before a final (slow) argon flow rate was set. The flow rate was set by adjusting an exhaust valve until (approximately) one bubble per second flowed through the exhaust bubbler. The respective heat-treatment program would then be initiated via the furnace's master controller. During all heat-treatments the three independent thermocouples (located within the sample space) were continuously monitored by National Instruments Signal Express data acquisition software. As well as this real-time data acquisition,

manual temperature checks and adjustments were regularly conducted. Any adjustments made to a furnace were recorded and then used to fine tune its temperature program for use with subsequent heat-treatments.

6.4.4 Errors and uncertainties in heat-treatments

We suggest that the two largest sources of error in these heat-treatments, in the worst case scenario i.e. at the 650 ℃ dwell plateau, are associated with furnace stability (~ ± 0.2 ℃) and the uncertainty in the Type N (class 1) thermocouples. A reasonable estimate to characterise the total uncertainties in the heat-treatments is therefore, ~ ± 2.6 ℃.

6.5 Critical current measurements

Staff in Durham have more than 20 years' experience making critical current measurements on superconductors. The F4E contract specified that critical current measurements were to be performed at 4.22 K and at *three* applied magnetic fields, 12.5 T, 12.0 T and 11.5 T. Durham used a 15 T vertical magnet (homogeneous to 10^{-3} over a 10 mm diameter sphere volume) in conjunction with a Power Ten 2000 A power supply, a Deltec shunt and various nanoamplifiers and Keithley voltmeters connected to a bespoke LabView program for instrument control and data acquisition [135]. During these measurements the current was linearly increased whilst recording the voltages dropped across three voltage taps; a 500 mm tap spanning the central sample region in parallel with two 250 mm taps in series with each other. The critical current criteria was set by F4E at 10 $\mu\mathrm{Vm}^{-1}$ and *n*-value between 10 to 100 $\mu\mathrm{Vm}^{-1}$. The number of samples to be measured, reliably and reproducibly, as part of the F4E contract was very large. This increased the demands made on the methods usually adopted for low quantity measurements. For example, soldering such a large number of samples across electrical joints had to be reanalysed in order to increase sample throughput and remove any possibility of operator dependence. All aspects of the critical current measurements in Durham were therefore carefully considered to see how well they fitted into a high quality, high quantity processing environment. The following sections first consider minor improvements and then discuss the three most beneficial changes that were made, which were a change in the standard ITER barrel design, an improved way to transfer current into a sample, and a complete overhaul of sample mounting methodology. The section ends with an overview of the test result data.

External circuitry

The resistance of the Deltec shunt, used to measure the applied transport current supplied by the Power Ten, was periodically calibrated to an accuracy of two parts in 5000 and the gain of the nanoamplifiers was calibrated to an accuracy of four parts in 5000 using calibrated Keithley instruments capable of measuring voltages to within 0.0038 %. The various equipment uncertainties led to a propagated uncertainty in the measurement of 0.1 %.

Temperature

The atmospheric pressure of the laboratory was monitored on a daily basis to take into account the difference in liquid helium bath temperature from 4.22 K. However, the pressure data for the Durham laboratory, over a period of two years, showed that the most severe consequence to the critical current measurements was a discrepancy in the critical current of less than 0.8 A, which translates as an additional uncertainty in the critical current measurement of ~ 0.3 %. To ensure that the pressure within the magnet Dewar was as close to atmosphere as possible, bubblers were designed and built in-house and installed to replace the mechanical one-way valves (that were prone to "sticking") in the helium gas exhaust ports of the Dewar and measurement probes. This ensured pressure equalisation of the Dewar to the laboratory conditions during helium boil-off.

Magnetic field

The magnetic field profile was checked using a Hall probe that was calibrated against an NMR system in Durham's Chemistry Department.

6.5.1 Change in barrel design

The critical current measurements were performed on coiled samples of Nb_3Sn. This geometry allows for a relatively long length of strand to be measured in a relatively confined volume, which can be accommodated by the kinds of superconducting magnet found in specialist research laboratories like Durham. The sample coil is wound around a dedicated cylinder (or barrel) that performs a number of important roles. For instance, it must support the sample in extremes of temperature from the maximum heat-treatment temperature of 650 ℃ down to that of liquid helium. It must also support the sample against the Lorentz forces that are generated during the measurements and it must support the sample during man-handling. Furthermore, it must be able to deliver the applied transport current to a sufficiently long portion of the sample to allow adequate current transfer into the superconducting filaments. This current transfer region occurs in the copper end rings of a barrel (see Figure 6.6). However, we felt that the physical integrity of the standard barrels used by ITER were insufficiently robust for use through the Durham system. We therefore made two improvements; we changed the way the copper rings were attached to the titanium cylinder and we increased the region over which the sample support groove extended. The copper end rings of the standard ITER design are smooth rings which fit over the ends of the titanium cylinder and are held in place with pins or screws (see Figure 6.6-a). However, we found it was possible to wobble the copper end rings after heat-treatment. The brittleness of heat-treated Nb_3Sn makes it easily susceptible to damage. This increased the onus on careful operator handling, which was felt should be avoided given the large quantity of samples to be handled. The copper rings of the Durham barrel were therefore threaded at one end (see Figure 6.6-d5) allowing them to be screwed directly into the titanium cylinder, which was likewise threaded (see Figure 6.6-c4). This screw thread stopped any relative longitudinal and lateral motion but did not stop rotational motion. Rotation was stopped by also employing two fixing

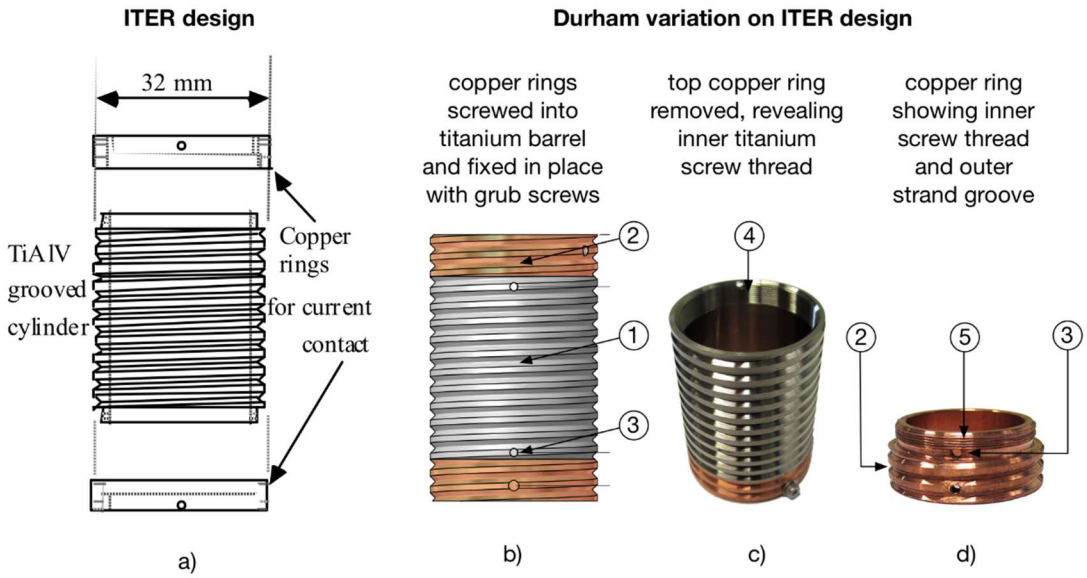

Figure 6.6: Comparison between the standard ITER design critical current barrel and Durham's improvements on the design. a) the standard ITER barrel design showing the separate top and bottom copper current rings and the central titanium cylinder (*page 9 of the F4E Technical Specification Annex B*). Note that only the titanium cylinder is prepared with a groove to support the sample strand. The copper rings are pinned (or supported with screws) onto the titanium cylinder. b) the Durham barrel has copper current rings screwed into the titanium cylinder. Note that the sample strand support groove (1) from the titanium cylinder is extended into the copper rings (2). c) Durham barrel with top copper ring removed showing the internal screw thread (4) for copper ring attachment. d) copper ring showing the screw thread (5) (for attachment to the titanium cylinder) and the outer sample support groove (2).

screws (at ninety degrees to each other) through the sidewall of the titanium cylinder and into the copper end rings (see Figure 6.6-b3 and d3). The second alteration made to the standard ITER design was to extend the sample support groove from the titanium cylinder onto each of the copper end rings (see Figure 6.6-b2 and d2). There were two main reasons for this decision. The first was that without the groove the heat-treated strand could be quite loose in the copper region. This did not present itself as problematic during the measurement because the sample is first soldered to each ring, however, the physical soldering process can result in the sample being moved, possibly causing filament breakage. The second reason was that the copper-to-titanium boundary, between the end rings and the central titanium cylinder, might not be exactly level, maybe due to poor manufacturing. Extending the groove over this boundary, and ensuring that each copper ring is only ever used on the same end of its original cylinder, mitigated this happening.

The consequence of the Durham modifications to the standard ITER barrel design were that the amount of barrel preparation work was increased. After manufacture and inspection, each barrel had to be disassembled, cleaned and its titanium cylinder oxidised (to lubricate its surface to stop the sample sticking during heat-treatment) before being reassembled. The disassembly and

reassembly time was noticeably greater. While increased labour time is an additional burden on any time limited process, it is by far preferable to the alternative in which damaged samples get through the system all the way to measurement. We note that ITER/F4E has effectively adopted the Durham design; the TF pancakes are currently being heat-treated alongside *witness* samples, which are barrel mounted strands that after heat-treatment have their I_c measured to test the quality of the pancake furnace treatments. Durham is providing the world's supply of barrels for the witness samples that are currently being reacted alongside the TF coils and is also performing the measurement of their $I_c's$.

6.5.2 Increasing the data acquisition range of I-V traces

During the early development and testing phase it was soon established that some of the test samples quenched at low E-fields during the transition. These low E-fields were sometimes under 50 μVm^{-1} (though always above 10 μVm^{-1}). Communications with F4E and data supplied by one of the manufacturers confirmed that E-fields below 50 μVm^{-1} were observed by other laboratories. This behaviour was almost exclusive to the internal tin samples. Work conducted by Jewell *et.al.* [136] has showed that the internal tin architecture is substantially more susceptible to crack formation than the bronze route architecture; though no correlated degradation in critical currents was observed. Nevertheless, we considered that cracks within a limited current transfer region, such as the copper end rings of the critical current barrels, might be responsible for premature quenching of samples below 100 μVm^{-1}. Our remedy was to "strap" the barrels. This consisted of soldering short strips of commercially available YBCO tape across the top of four turns of the coiled sample at six to eight locations around each end (see Figure 6.7). Two of the turns resided on a copper end ring and the remaining two on the titanium cylinder. We suggest that the YBCO straps provided lower resistive current paths to an increased number of contact points, bypassing problematic regions that might also be acting as hot zones during the transition causing early thermal runaway. Care was taken when positioning the straps to keep them as far away from the

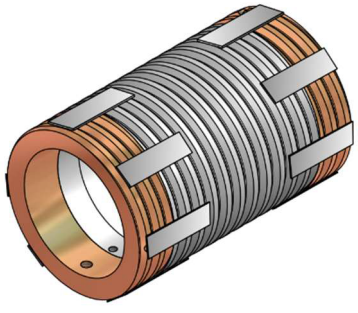

Figure 6.7: Image depicting a "strapped" critical current barrel. Strips of commercially available YBCO tape are soldered at the ends of a sample, crossing from the copper region onto the titanium region. Six to eight straps are applied. These straps increased the number of low resistance current paths into the sample and improve the maximum E-fields that can be measured.

voltage tap region as possible. This solution, in the vast majority of cases, did indeed increase the measured E-fields, not necessarily up to the desired 100 μVm^{-1} (although some were improved to E-fields above 100 μVm^{-1}), but consistently doubling or even tripling the pre-strapped maximum.

6.5.3 Measurement probes

Prior to the F4E contract Durham routinely measured just one sample at a time on a critical current probe. The time and effort involved in only cooling a single sample down to 4.22 K and then warming it back up again was an impractical method to adopt for large quantity measurements. A suite of four critical current measurement probes were therefore designed and built in-house that each had a capacity to simultaneously hold *three* sample barrels (see Figure 6.8-a). Tests were conducted to ensure that the results were independent of sample position by repeating measurements with different position configurations prior to introducing each probe into real-world use. The probes enabled an efficient sample throughput with one technician mounting samples and another performing the measurements. Three probes could be comfortably measured in one day and when needed, this could be increased to four. Durham regularly measured up to 36 samples per week with the potential for this to be increased to 60. The sample mounting assembly at the ends of each probe was designed to accommodate *three* (or less) barrels by physically clamping them together and relying on the pressed copper contact between their clean cross-section interfaces at each of their ends (see Figure 6.8-b). The adequacy of these pressed contacts was tested by performing repeat measurements on samples that had been previously measured in the usual way and were found to perform extremely well over the current range used for Nb_3Sn at high fields. The dramatically reduced preparation time in comparison to soldered joints, with no decrease in measurement quality, made these pressed contacts a much better solution. The cross-sectional area of the copper interface was approximately 350 mm^2 and this area was polished with fine grit Emery paper to increase contact quality. The end of the three barrels was clamped with a copper nut and contact spacer to a central shaft that acted as the negative return path (see Figure 6.8-c, d and e). The end clamp therefore made the electrical connection between the positive terminal (see Figure 6.8-d1 and e) and the negative copper current lead that ran through the centre of the barrel assembly (see Figure 6.8-d and e).

During these measurements there was an international liquid helium ‘crisis’ [137], which Durham had to work around in order to continue satisfying F4E’s delivery requirements. Work conducted by another member of the Durham group, Prapaiwan Sunwong [138], showed that optimal design of current leads could lead to a 30 % reduction in liquid helium consumption during measurements by running the probes hotter. The probes were therefore refitted with new ‘hot’ brass current leads with an approximate reduction in cross-section of 44 %. This change reduced our net helium consumption per sample by ~ 11 %.

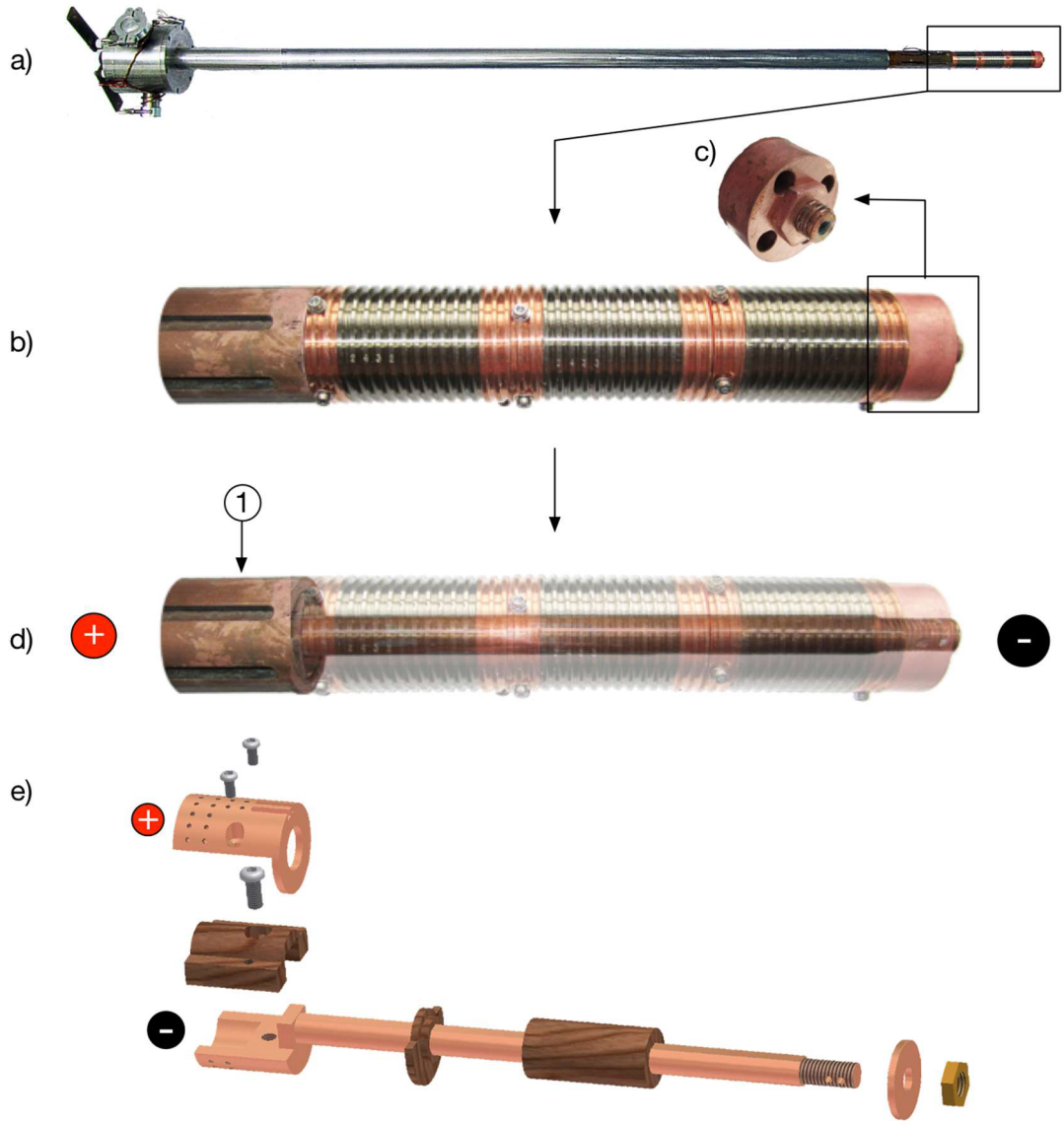

Figure 6.8: Critical current measurement probe. a) Each probe is capable of holding three critical current samples. b) The sample mounting assembly complete with all three barrels. For assembly speed the barrels are clamped together using a copper end nut and contact spacer shown in c). d) The left-hand positive terminal (1) and the central negative current return lead are shown. The positive and negative sides of the electrical circuit are connected by the copper nut and contact spacer shown in c). e) Assembly diagram.

6.5.4 Results, accuracy and interlaboratory comparisons of the I_c data

Durham laboratory uncertainties

Throughout the contract period approximately 1500 critical current measurements were performed in total. Figure 6.9 shows typical data (at 4.2 K and 12.0 T) for both strand architectures and normalised (to the mean) test results for the complete set of samples (not including additional measurements requested by F4E). The calculated instrumental uncertainty in Durham's measurements is ~ 0.1 % and that associated with differences in Durham's daily atmospheric

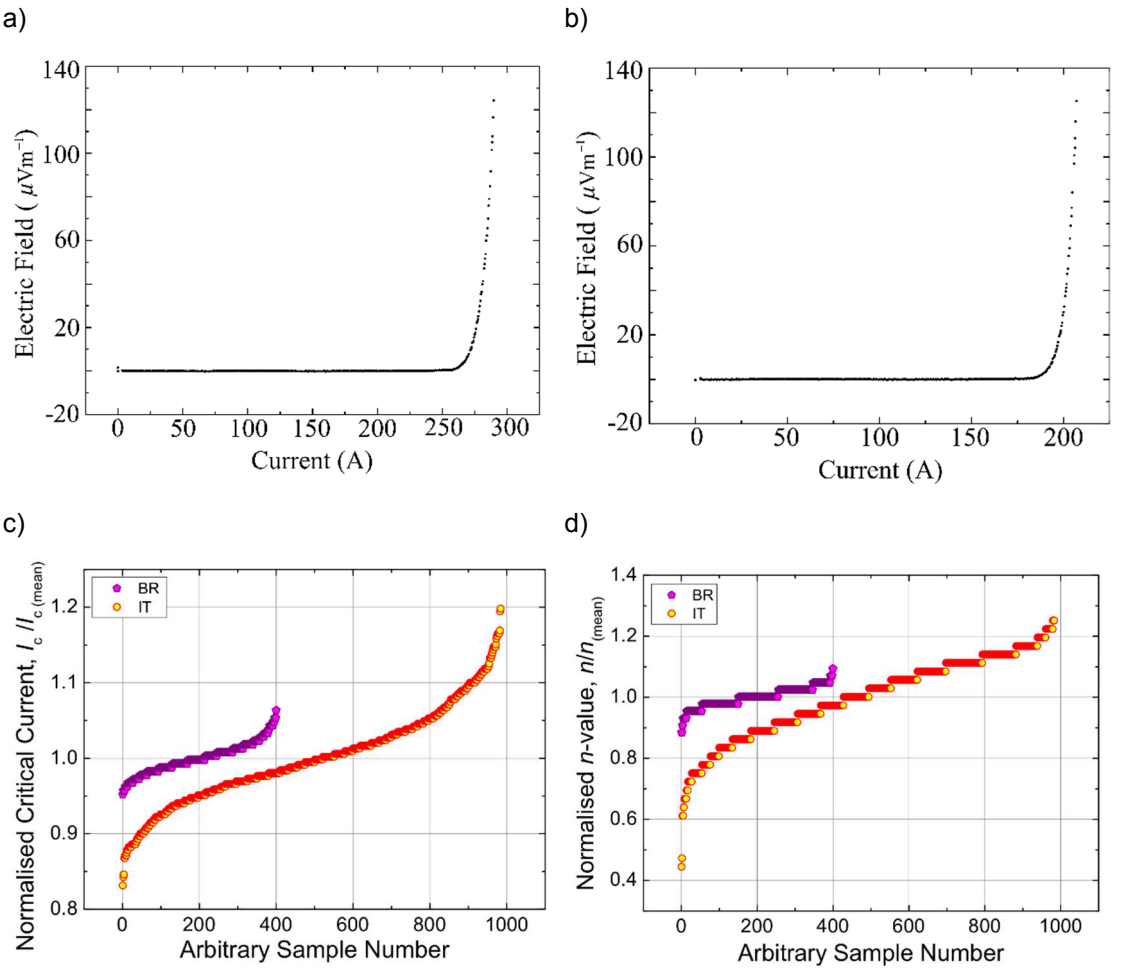

Figure 6.9: a) Typical critical current data for internal tin and b) bronze route architectures. Complete test result data for all samples requested by F4E (except additional measurements); c) critical current and d) *n*-value for both strand architectures; bronze route (BR) and internal tin (IT).

pressure leads to an additional uncertainty in I_c of ~ 0.3 %. We chose to measure fifteen samples twice in Durham and these showed a slight increase in I_c of 0.6 % in the repeat measurement data. Such an increase in I_c after consecutive measurements is not unusual as a result of thermal cycling. For example, Goodrich *et. al*. found increases in I_c of up to 2 % at 12 T occurring in the second thermal cycle of Nb_3Sn samples [139]. It is thought that this is caused by strain relaxation of the filaments. However, we expect the largest uncertainty in I_c to be associated with the uncertainties in the heat-treatment temperature. Figure 6.10 shows the results from a small-scale experiment in which nine samples were heat-treated in a varying temperature profile below the required upper temperature plateau of 650 ℃, and then their $I_c's$ were measured. Using the fit to the data in Figure 6.10, a difference in heat-treatment temperature of 2.6 ℃ leads to a difference in I_c of ~ 2 %. Therefore, the total uncertainty in Durham's measurement of I_c, obtained from the square-root of the sum of the squares of the individual uncertainties, is dominated by the effects of the heat-treatment, and is ~ 2 %.

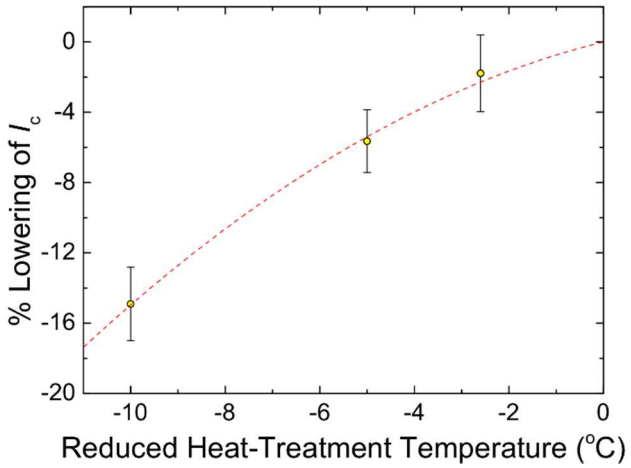

Figure 6.10: Plot of the expected % lowering in the I_c of samples caused by heat-treatment at lower temperatures than the recommended highest plateau of 650 ℃ (internal tin).

Results on ITER samples

Figure 6.11 shows the critical current test results (at 4.2 K and 12.0 T) for both the internal tin (plots a and c) and bronze route (plots b and d) architectures in measurement order. It is clear that the complete dataset for each architecture varies in a non-systematic way that is in part *batch dependent*. We have calculated the standard deviation of the whole dataset and then the standard deviation with respect to an *adjacent moving average* (ama) smoothing procedure. This gives a better estimate of the spread expected of smaller quantity batches. Our approach consisted of taking an average of a set number of data points (25) around each individual point. These averages provided a *locally* representative average.

The adjacent moving average is shown in Figure 6.11 as a solid blue curve and the global mean as a dotted black line. Subtracting the *ama* from each dataset removes the sample/batch specific variations allowing a *localised* spread of the data to be visualised and a more representative standard deviation to be calculated. This *local* standard deviation is shown in Figure 6.11 as dashed red curves. The same analysis was also applied to the *n*-values, which are plotted in Figure 6.12. The global mean critical current value of the internal tin samples, measured by Durham, was 275 A ± 6 % with a *local* one sigma deviation from the *ama* of ± 4 % and that of the bronze route samples was 197 ± 2 % with a deviation from the *ama* of ± 2 %. Corresponding *n*-values were: 36 ± 14 % (with a deviation from the *ama* of ± 8 %) for internal tin and 43 ± 2 % (with a deviation from the *ama* of ± 2 %) for bronze route.

Comparisons with other laboratories

Some data comparisons between Durham, another European laboratory (Lab A) and the manufactures were completed. The manufacturers' measurement results have recently been published by Boutboul *et. al.* in 2014 [140]. The manufacturers' critical current and *n*-values for internal tin and bronze route at 4.2 K and 12.0 T were 281 A ± 5 %, obtained from measurements on over 2500 samples, and 200 A ± 3 %, obtained from measurements on over 580 samples.

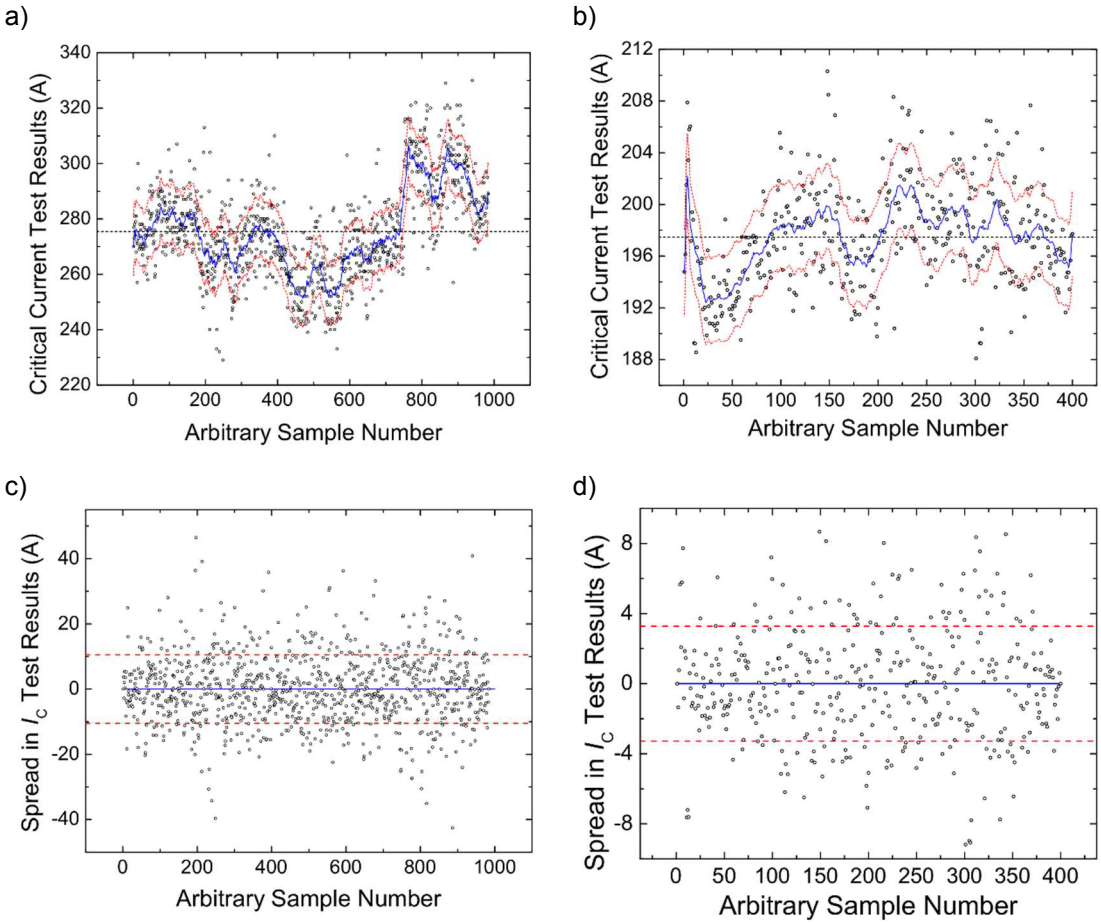

Figure 6.11: Critical current test results for all the samples measured by Durham at 4.22 K and 12.0 T for a) internal tin and b) bronze route strands. The blue curves are adjacent moving average (ama) fits to the data and the black dotted line is the global mean. The red dashed curves represent ± one standard deviation (σ) from the ama. The spread in the data is more clearly shown in plot-c (related to plot-a for internal tin) and plot-d (related to plot-b for bronze route) where the respective ama has been subtracted from its dataset. The spread in the data for the internal tin measurements is ± 11 amps and for the bronze route measurements it is ± 3 amps.

Hence, the manufacturers' data agree well with Durham data - within 2 % of the mean for both architectures and a similar standard deviation for both architectures. In smaller quantity sample comparisons with Lab A, where independent heat-treatments were conducted, Lab A measured lower values of I_c (~ 6 %) and *n*-values (~ 8 %) than Durham (see Figure 6.13). Subsequent repeat experiments on other small quantity cross-check samples were also performed (with no changes made to our measurement procedure). These showed agreement with mean values to within 0.4 % for I_c and 2.5 % for *n*-value.

There is very good agreement between Durham and the manufacturers (within 2 %). We therefore suggest that these measurement results are indeed representative of the characteristics of the samples themselves, and that any inclusive variations due to handling, differences in heat-treatments or measurement inaccuracies do not hinder the formation of broad conclusions about

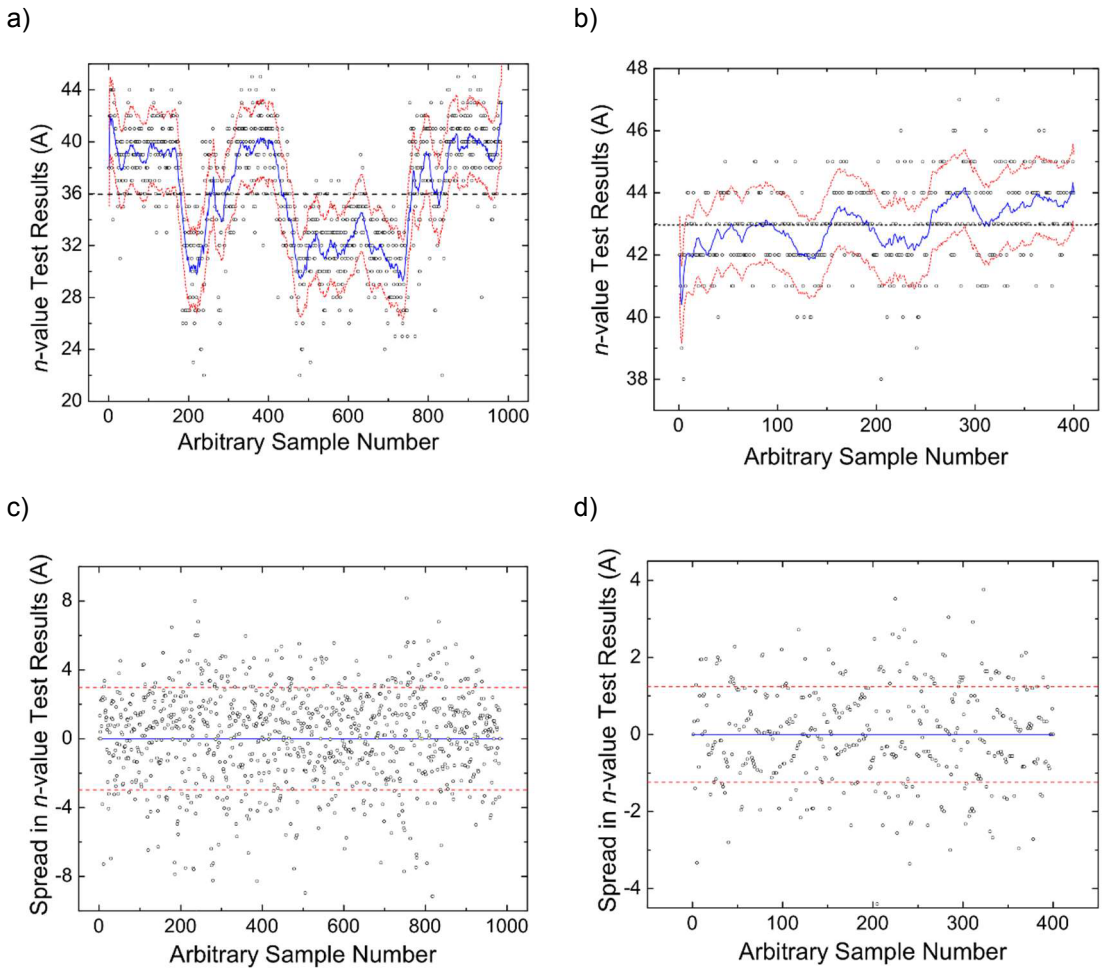

Figure 6.12: *n*-value test results for all the samples measured by Durham for a) internal tin and b) bronze route strands. The blue curves are adjacent moving average (ama) fits to the data and the red dashed curves represent ± one standard deviation from the ama. The spread in the data is more clearly shown in plot-c (related to plot-a for internal tin) and plot-d (related to plot-b for bronze route) where the respective ama has been subtracted from its dataset. The spread in the data for the internal tin measurements is ± 3 and for the bronze route measurements it is ± 1.

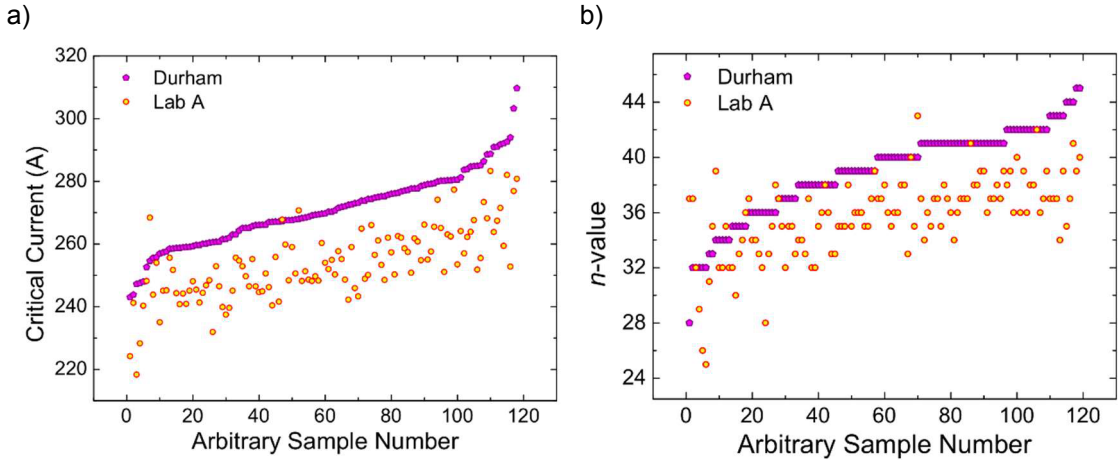

Figure 6.13: Comparison of the critical currents (a) and n-values (b) of a set of internal tin strands independently heat-treated and measured by Durham and Lab A.

the samples as a whole. For instance, in the case of the internal tin strands Figure 6.9-c shows that the critical current of a small fraction of samples is ~ 17 % below the mean i.e. ~ 47 A. This is not an artefact of sample handling, heat-treatment or measurement. Of course, the average internal tin I_c is so far above the acceptance criteria that even these extreme samples do not present cause for concern. To our knowledge the dataset produced by Durham is the first time such a large dataset has been produced by an independent non-commercial laboratory.

6.6 Hysteresis loss measurements

The hysteresis loss measurements were performed on coils of Nb_3Sn containing *nine* turns each using a standard commercial magnetometer - the QD PPMS in dc-extraction mode [141, 142]. In order to avoid any end-effects associated with tin loss, the hysteresis loss sample coil of *nine* turns was cut from the centre of its heat-treated coil, which typically contained fifty to sixty turns. The mass of the sample was then measured using a Mettler Toledo balance capable of measuring up to 81.0 g to within ±0.005 mg. The sample mounting consisted of holding the sample coil at the end of a 6 mm (outside diameter) sample straw with small amounts of Kapton tape blocking the open end. The outside diameter of each sample coil was designed to fit snuggly within the straw but sometimes two diametrically opposite 10 mm slits would be cut (within the sample location) to ensure no additional stress was needed when sliding the sample into the straw. One turn of Kapton tape would then be wound around the circumference of the cut region to hold the sample in place. The other end of the straw was then cut to the length required of the PPMS. The calibration of the magnetometer was periodically checked by measuring a 3.1 mm diameter by 3.9 mm long cylindrical standard sample of palladium with a well-known susceptibility. The measurement procedure consisted of setting the PPMS temperature to 4.22 K and then measuring the magnetic moment of the sample in a swept field between ± 3 T. Up to four samples per day were measured. The losses per unit strand volume were calculated from the integral of the magnetic moment vs applied field divided by the post-heat-treated sample volume. It was not practical to calculate the volume of each individual sample from direct dimensional measurements, so the volume was obtained from the mass of the sample and an *average* post-heat-treated sample density. The following sections begin by discussing how these densities were determined, before moving on to discuss some results from small-scale experiments that investigated the relationship between sample losses and furnace cleanliness, sample elongation, number of turns and insulation of turns and a round-robin experiment with other laboratories.

6.6.1 Change in sample density pre-to-post heat-treatment

During heat-treatment elemental niobium and tin are converted into Nb_3Sn and large voids (including Kirkendale voids) are produced. These internal structural changes mean that we cannot expect that the pre and post heat-treatment densities of the strands are the same. In order to determine any change in density that might occur we set up two experiments; one designed to detect changes in length and the other to determine changes in diameter. The length change experiment consisted of holding twelve strands in rectangular grooves milled out of a copper base

plate (see Figure 6.14-a). The strands were fixed at one end with a copper clamp and left loose at the other end while being gently held within the grooves with Nb_3Sn links bolted into the copper base plate at either side of the samples. Four lines were scored across the base plate and the strands, at arbitrary locations near their loose ends (see Figure 6.14-a (1) to (4)). The set up was then heat-treated in accordance with the internal tin schedule. After heat-treatment close-up photographs of the score lines were taken and Photoshop was used to measure the displacements (see *d* in Figure 6.14-c) between the score lines on the strands and those in the original locations on the copper base plate. The average elongation was found to be -0.3 % ± 0.1 % i.e. a *negative* elongation, or *contraction*, seemed to have occurred. However, this *apparent* contraction is compensated for by the strands bowing slightly at various locations along their lengths during the heat-treatment. Evidence of this bowing was visible upon close inspection of the side profile of the experimental set up after heat-treatment. Our conclusion is that to within the accuracy of the experiment (~ 0.1 %) there was no change in length.

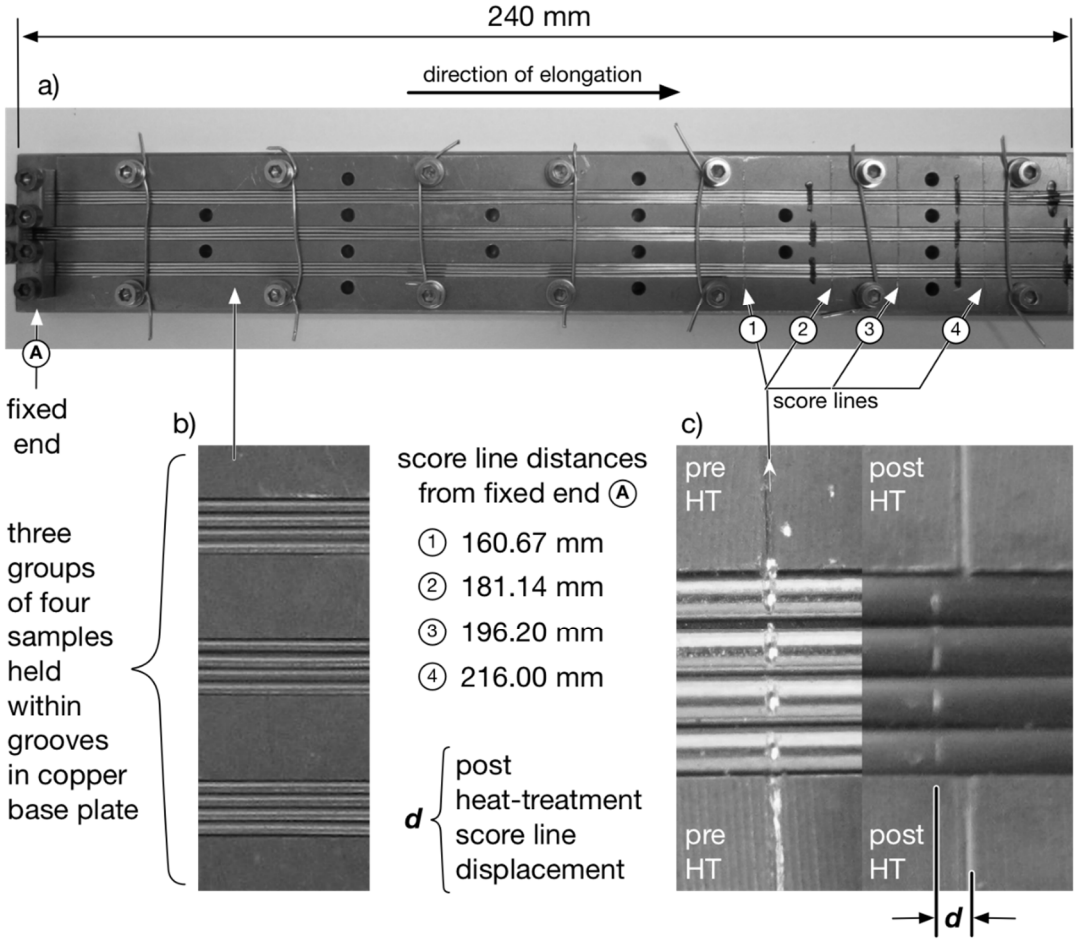

Figure 6.14: Experimental set up to find any length change that might occur in Nb_3Sn strands during heat-treatment; a) a 240 mm long copper platform with three rectangular grooves within which b) twelve samples were loosely held in place with Nb_3Sn links. c) Lines were scored through the copper platform and strand sample surfaces before heat-treatment (HT) at arbitrary locations (1) to (4). Only one end of the samples was clamped in place with a copper block (A). After heat-treatment the displacements between the sample scorelines and their original positions, d, were measured to establish an average elongation.

The experimental procedure for measuring the change of diameter consisted of performing diameter measurements at multiple circumferential locations and at different positions along 600 mm lengths of strand (from both architectures) to obtain a representative average diameter of each strand. The lengths and masses of each sample were also measured before separately heat-treating each strand architecture using its specific temperature programme. After heat-treatment the diameters of the strands were re-measured. Figure 6.15 shows the *pre* and *post* heat-treatment diameters. For the internal tin strands there was a 1.3 % ± 0.2 % increase in strand diameter after heat-treatment and for the bronze route the increase was just 0.4 % ± 0.1 %. These data, in conjunction with the pre-heat-treated sample dimensions and masses, were used to calculate the post-heat-treated densities, which were 8.71 ± 0.05 g/cm^3 for the internal tin strands and 9.15 ± 0.04 g/cm^3 for the bronze route strands.

6.6.2 The effect of furnace gas purity on losses

An experiment to investigate the effect of gas purity (or furnace cleanliness) on hysteresis losses was performed. The methodology consisted of heat-treating two sets of sample coils (twelve per set) taken from three separate batches of internal tin strands. One set of twelve samples was heat-treated in the usual way i.e. in one of the low-purity critical current furnaces, alongside critical current samples, and the other set was heat-treated on its own within one of the high-purity RRR furnaces using a RRR heat-treatment rig to stop the introduction of contamination. The heat-treated samples were then measured in the usual way using the PPMS. The data is shown in Figure 6.16 and Table 6.2. An overview of the results is shown in Figure 6.16-a where it can be seen that approximately half the sample set shows very little change between both furnace conditions while the remaining half of the samples heat-treated in the high-purity furnace show a distinct *decrease* in losses. Figure 6.16-b provides more detail from which it is clear that changes in losses are batch dependent and that on average there is at most a relatively small (~ 4 %) reduction in the losses of the high-purity furnace, and more probably, no effect given the variation in losses across the samples. It is known that the inclusion of titanium around the filament bundles during manufacture leads to a decrease in hysteresis losses after heat-treatment by increasing

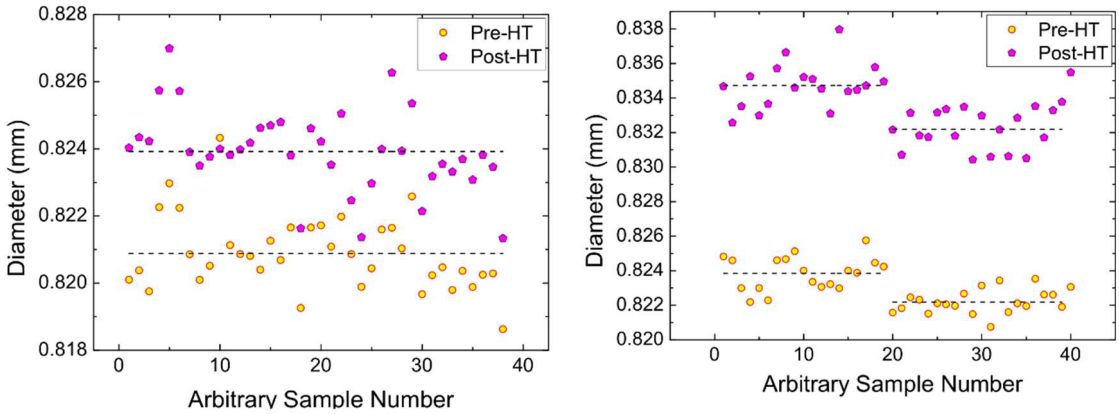

Figure 6.15: Change in pre to post heat-treatment strand diameter for bronze route (LEFT) and internal tin (RIGHT). The measurements were made using the Scantron dual axis laser micrometer. The uncertainty in the data is ± 1 μm.

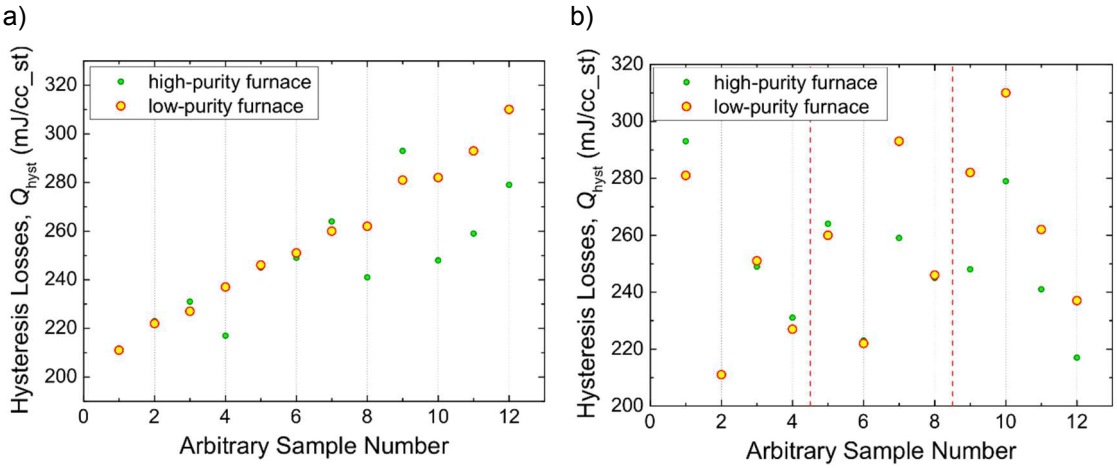

Figure 6.16: Difference in hysteresis losses between internal tin coils heat-treated in the standard way (red encircled yellow symbols) i.e. in one of the I_c furnaces alongside I_c samples, and in a high-purity RRR furnace on their own (green symbols). The left-hand plot shows the data ordered from low to high. The right-hand plot shows all 24 samples grouped in their original batches.

Table 6.2: Data from Figure 6.16 listing batch and full sample set averages and standard deviations for the hysteresis losses of samples heat-treated in a high-purity furnace compared to a standard I_c furnace. There is a reduction in losses by ~ 4% for those samples heat-treated in a high-purity environment.

batch	arbitrary sample number	losses (mJ/cc_st)		% increase from low-purity furnace		av. losses (*std dev*)	
		Low-purity furnace	high-purity furnace	per sample	per batch	Low-purity furnace	high-purity furnace
1	*1*	281	293	4.3	1.5	243 *(30)*	246 *(35)*
	2	211	211	0.1			
	3	251	249	-0.7			
	4	227	231	1.9			
2	*5*	260	264	1.5	-2.9	255 *(30)*	248 *(18)*
	6	222	223	0.6			
	7	293	259	-11.5			
	8	246	245	-0.4			
3	*9*	282	248	-12.2	-9.7	273 *(31)*	246 *(25)*
	10	310	279	-10.0			
	11	262	241	-7.9			
	12	237	217	-8.3			
all samples					-3.9	257 *(30)*	247 *(25)*

the upper critical magnetic field and reducing the critical current density [143] but it is difficult to see how any substantial contaminants could diffuse into the filaments via a route that traversed the outer chromium plating, then the copper stabiliser, followed by the tantalum barrier. We conclude that furnace cleanliness does not significantly affect loss measurements.

6.6.3 Experimental results on sample length and insulation

We investigated whether there was any dependence of hysteresis loss on the number of turns in a sample coil used to make the measurement. Standard measurements were performed on a sample with thirteen turns (this number of turns produced a sample with a length of 11.9 mm, which was within the maximum sample length (12 mm) specified for the PPMS dc-magnetisation option). Five successive magnetisation measurements were performed on the same sample with one whole turn cut away prior to each measurement, down to nine turns. Figure 6.17-a shows that the magnitude of the losses changed by ~ 3 %. We suggest the variation in results shows the effects of the finite lengths in our magnetometer. The magnetometer manufacturer recommends samples no longer than 12 mm. Observation of the geometry of the secondary pick-up coils suggests we can expect a variation in signal over a 12 mm sample to be different from that of the 3.9 mm palladium sample by approximately 2 %.

a)

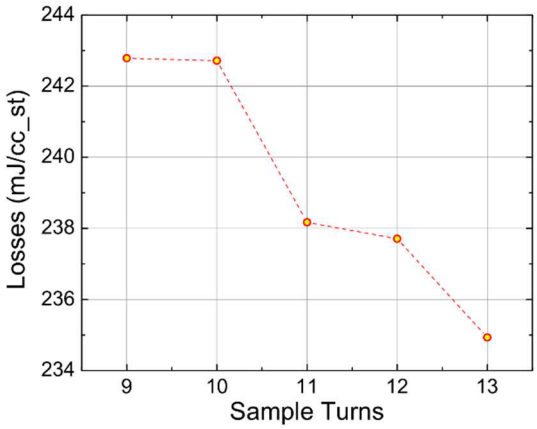

b)

c)

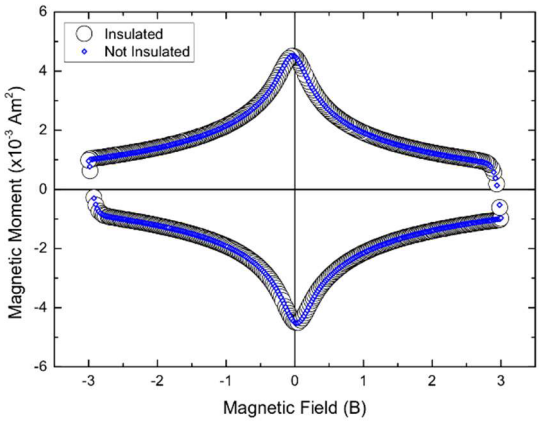

Figure 6.17: a) Hysteresis losses as a function of number of turns in a sample coil, b) photo showing a sample with each turn insulated from its adjacent turn using cigarette paper and c) a comparison of the two data sets of the uninsulated and insulated sample magnetisation data.

A small experiment was conducted to test if the losses of a tightly wound sample coil, whose turns were touching, were different from one whose turns were insulated from one another. The logic here was that touching turns might provide conductive current paths through which additional current loops might flow and change the coupling losses. A photo of the sample with its turns insulated is shown in Figure 6.17-b and the measurement data are shown in Figure 6.17-c. Both non-insulated and insulated sample measurement results were to within 0.2 % of each other. While this is above the calculated uncertainty of repeat measurements (~ 0.03 %) the likelihood of achieving this level of accuracy is regarded as *negligible* if the sample has been man-handled between measurements. We therefore regard the 0.2 % difference between non-insulated and insulated turns to be well within the experimental accuracy and so no change in hysteresis losses was measured.

6.6.4 Results, accuracy and interlaboratory comparisons of the hysteresis loss data

Durham laboratory uncertainties

Over the contract period approximately 700 hysteresis loss measurements were performed in total. Figure 6.18-a shows a typical dataset and Figure 6.18-b shows the normalised (to the mean) test results for the complete set of samples for both strand architectures (not including additional measurements requested by F4E). There are three aspects to the measurement (and calculation) of hysteresis losses that introduce uncertainties. These are: the accuracy (and stability) of the set point temperature, which we estimate is ~ 2 mK i.e. an uncertainty of 0.05 %; the effect of field sweep rate, which is kept low (4 mT/s) and produces an uncertainty of ~ 0.2 %; the effect of the difference in sample sizes between the palladium standard used for calibration of the PPMS and the sample coils, which we estimate to be ~ 2 %, and also the uncertainty in the value of the calculated sample volume, which is 0.6 %. These individual uncertainties are dominated by the difference in the palladium/sample sizes and therefore the overall uncertainty in the hysteresis loss results is ~ 2 %.

Results on ITER samples

Figure 6.18-c and Figure 6.18-d show the hysteresis loss test results for each architecture measured by Durham, in measurement order. The mean *global* losses are: internal tin, 271 mJ/cc_st ± 14 % and bronze route, 58 mJ/cc_st ± 21 %. If the batch influence is removed (see Figure 6.18-e and f) the deviation from the *ama* for internal tin is ± 9 % and that for the bronze route is ± 12 %. Since the magnetisation of a sample and its critical current are related quantities (Bean's model), to some extent, one would expect the standard deviation of the hysteresis loss datasets to be similar to those of the critical current measurement results. However, the deviation from the *ama* for the internal tin critical current was 4 %, whereas the same value for the hysteresis losses was 9 %. Likewise, for the bronze route the deviation from the *ama* for the critical current was 2 %, whereas for the hysteresis losses it was 12 %. Furthermore, the data points at the

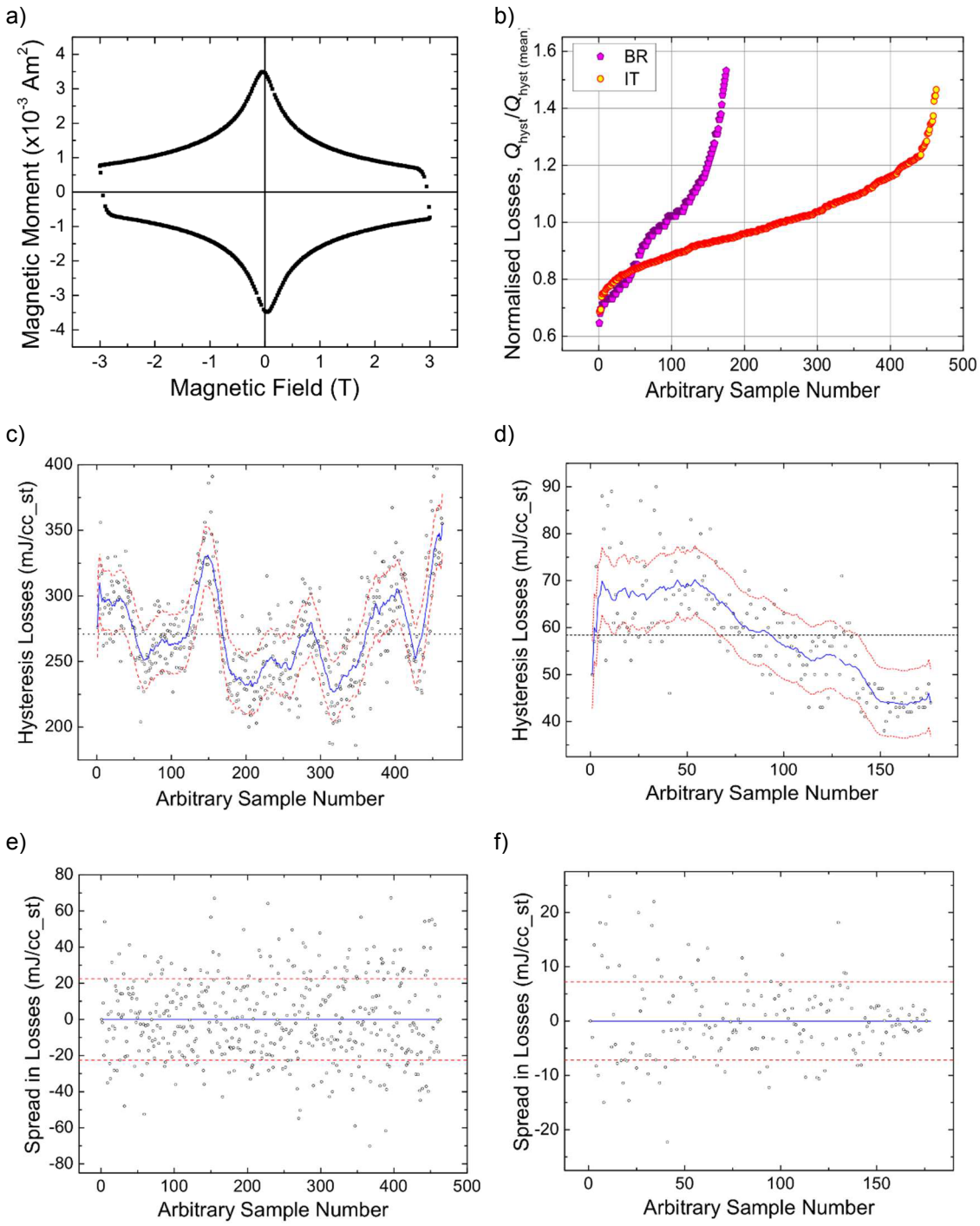

Figure 6.18: a) Typical hysteresis loss data and b) hysteresis losses of all samples measured, normalised to the mean for both strand architectures. Hysteresis loss test results for all the samples measured by Durham at 4.22 K and ± 3.0 T are shown in c) for internal tin and d) for bronze route strands. The blue curves are adjacent moving average (ama) fits to the data and the black dotted line is the global mean. The red dashed curves represent ± one standard deviation from the ama. The spread in the data is more clearly shown in plots e) and f) for internal tin and bronze route, respectively, where the ama has been subtracted from the datasets. The mean losses are: internal tin, 271 ± 23 mJ/cc_st and bronze route, 58 ± 7 mJ/cc_st.

extremes of the ordered critical current data (see Figure 6.9-c) are up to 20 % from the mean, whereas those of the loss dataset are more than twice this value away from their mean. A similar, but much more pronounced situation exists with the bronze route samples. A comparison of Figure 6.11-b and Figure 6.18-d goes some way to highlight the differences. Of course, the losses associated with a composite material are more complicated than a bulk superconductor due to additional contributions from induced eddy currents within the matrix and between filaments through the matrix but these additional contributions are frequency dependent and so at the very slow sweep rate used (4 mT/s) the superconducting hysteresis should be the most dominant contributor. So, the dissimilarity between critical current and hysteresis losses here could be a consequence of morphology. There is a wide distribution of grain sizes, compositions and connectedness within Nb_3Sn strands that are the product of the heat-treatment [144], which is designed to optimise the material for applications. It is therefore likely that the wider distribution in hysteresis losses is due to contributions from grains with compositions and grain connectedness that play a very limited role (if any role) in the transportation of current that do, however, contribute to the losses.

There is a distinct chronologically reducing trend in the bronze route data shown in Figure 6.18-d, which could have in principle been a symptom of changing heat-treatment or measurement quality, for example. However, the trend is absent from the corresponding internal tin data shown in Figure 6.18-c. The chronology of each architecture's heat-treatment and measurement, as well as the furnace and measurement equipment used, was the same, and therefore any problems that would lead to such a trend in the bronze route dataset should also be present in the internal tin dataset to some extent, which is clearly not the case. This deduction is supported by the various benchmarking and cross-check experiments to be discussed below. It is therefore reasonable to suspect that the trend is intrinsic to the samples themselves. Taking into account the fact that the loss values for all the bronze route, and indeed the internal tin, strands were all substantially within the acceptance criteria of 500 mJ/cc_st, these trends have remained purely an academic issue, which we attribute to changes made to the manufacturing process.

Comparisons with other laboratories

Some small quantity measurement comparisons were organised between Durham and other laboratories where each lab heat-treated and measured their own samples. The data of one such comparison is provided in Figure 6.19-a where the difference between the averages was ~ 11 %. The general agreement between Durham and other laboratories was, in general, similarly low when all participating laboratories heat-treated their own samples. Figure 6.19-b shows a data comparison of a larger set of samples heat-treated and measured independently by Lab B and Durham for which the agreement was 17 %. Figure 6.19-c, however, shows a comparison of a subset of the same samples for which Lab A also participated by heat-treating and measuring their own samples. The agreement for this smaller set of samples between Durham and Lab A was 6 % while that between Lab B and Lab A was 12 %. In parallel to these comparisons, we also sent some samples that had been heat-treated and measured by Durham to Cambridge

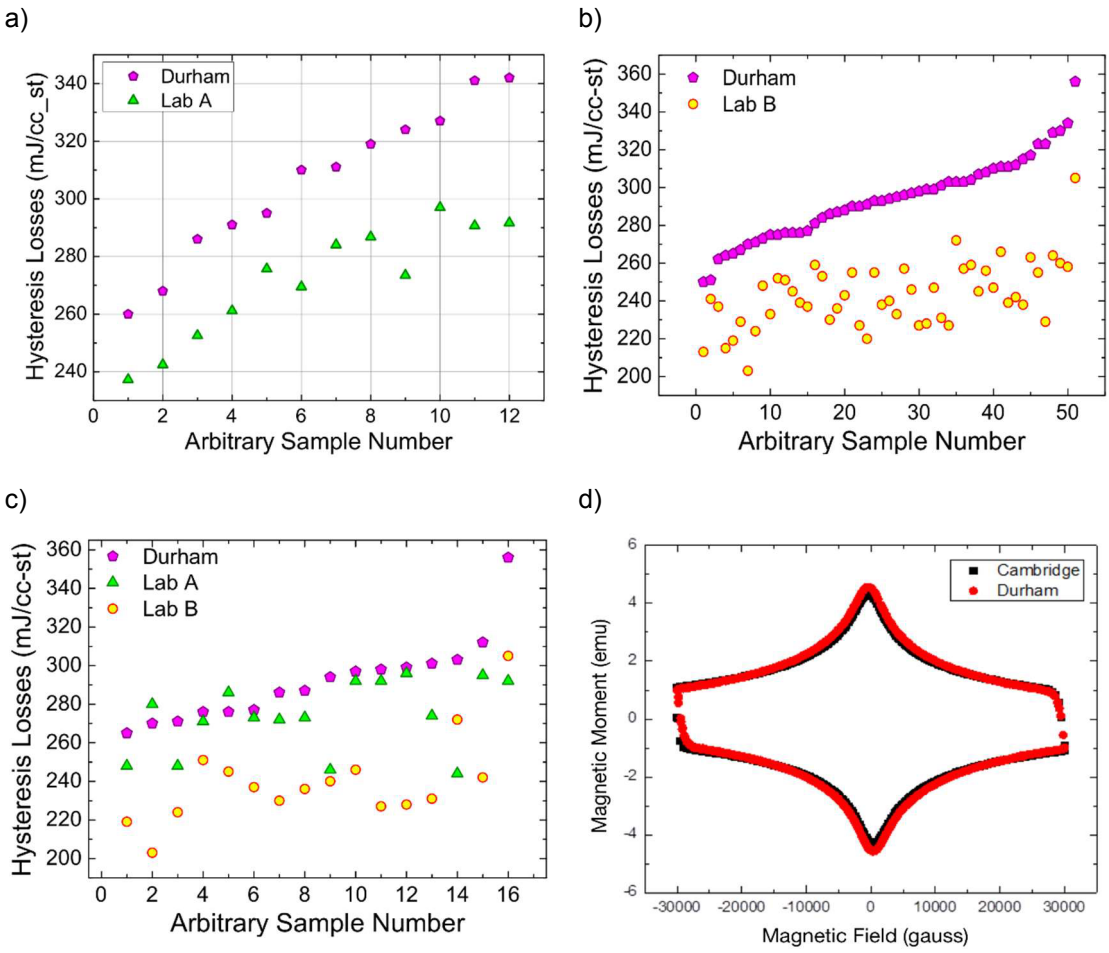

Figure 6.19: Comparison of hysteresis losses of: a) twelve pairs of samples (each pair cut from the same strand) ordered from low to high. One sample from each pair was independently prepared, heat-treated and measured by Durham while the second was likewise treated and measured by Lab A; b) Larger sample set comparison between Durham and Lab B; c) A comparison between Durham, Lab A and Lab B on a subset of samples from b); d) Comparison of losses data from the same sample independently measured by Durham and Cambridge Universities.

University for measurement in their PPMS (see Figure 6.19-d). The agreement here was within 1.8 %. A further two experiments in which one batch of ten samples was prepared and heat-treated by Durham and another set of ten samples, from the same batch, were prepared and heat-treated by Lab B was performed. Both sets of heat-treated samples were then sequentially measured by Durham and NIST. The agreement in the measurement results for each sample batch was 3 % and 4 % respectively. The origin of the much greater variability between the various laboratories is not yet well understood but a number of factors, including heat-treatment quality, sample inhomogeneity, calculation of sample length, sample handling and measurement method must all play a role to some extent.

6.7 Residual resistivity ratio

The residual resistivity ratio for each sample was obtained from four-terminal resistance measurements performed at 273 K and at 20 K using Durham's RRR probes that were specifically designed and built in-house (see Figure 6.20-a). Each probe had the capacity to simultaneously measure *ten* short samples (~ 20 mm long) that were connected together in groups of five (see Figure 6.20-b and c) with copper wire, forming a ladder. These copper ladders provided support to the samples while they were being mounted on to the sample probe and were also used as

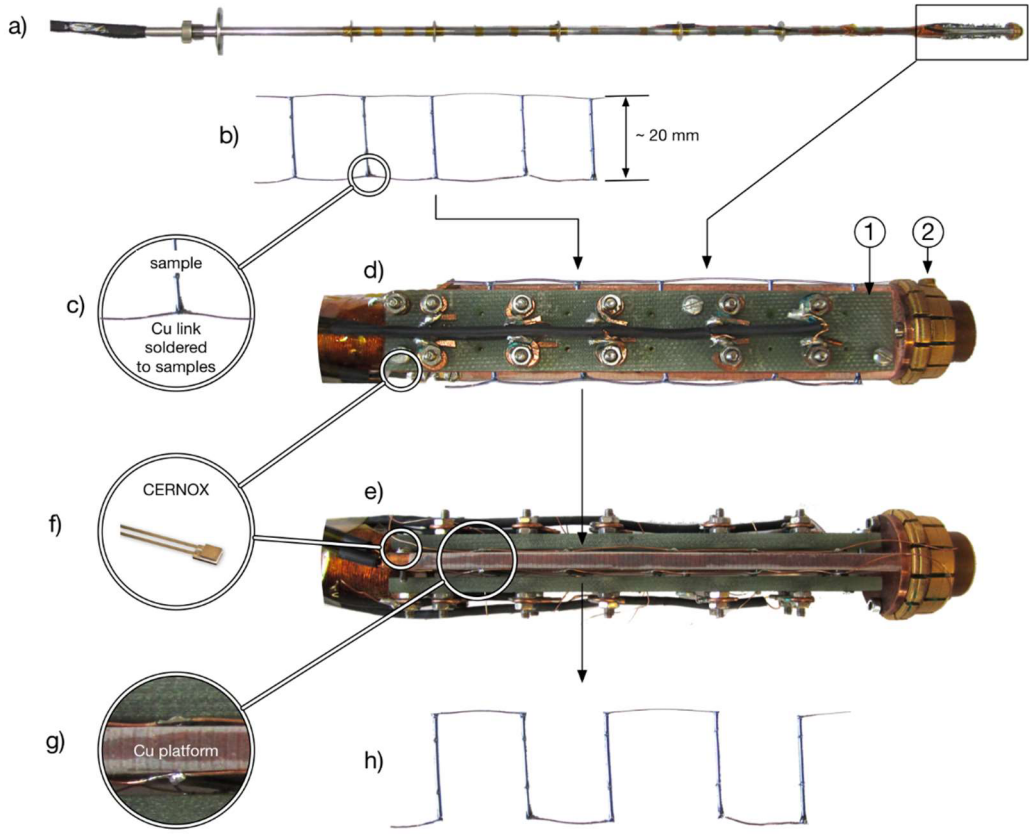

Figure 6.20: Residual resistivity ratio measurement probe. a) Each probe is capable of holding ten short samples connected together in two ladders of five samples each, as shown in b). c) The samples are soldered to copper wire (current leads) at their ends. d) Each sample ladder is mounted to opposite sides of the copper sample platform and voltage taps (not shown) from each sample are threaded through holes in the G10 terminal plates (1) before being soldered to copper probe lead terminals. e) Side view of the sample mounting assembly showing the sample ladders being held against the central copper platform with the G10 terminal plates (1). f) The temperature of the copper platform is monitored by a calibrated CERNOX thermometer. g) Image showing a close up of the copper platform and the ends of two mounted samples. h) After the samples have been mounted, alternate sections of the sample current leads are cut away to form a series current path through each of the samples. One end of a current lead from each sample ladder are connected so all ten samples are in series.

current leads. Each ladder of five samples was mounted onto one side of the central copper sample platform of a probe (see Figure 6.20-d and e) and was held in place with G10 terminal plates (see Figure 6.20-d1). The central copper platform was thermally connected to a standard (blank) PPMS measurement puck (see Figure 6.20-d2). The voltage taps from each sample were connected to their respective terminals on one of the G10 plates, which provided a good electrical connection to the measurement leads. The temperature of the central copper platform was monitored using a calibrated CERNOX thermometer (see Figure 6.20-f) and the terminal plates ensured that each sample was held in good thermal contact with the copper platform (see Figure 6.20-g), which was also electrically isolated from the samples using cigarette paper. Once the samples were connected to the probe, alternate sections of the supporting ladder were cut away to form a series current loop through each sample (see Figure 6.20-h). The ends of the loop were also connected to their respective terminals on the G10 plates, completing the electrical circuit. The fitted measurement probe was then inserted into the PPMS until its puck mated with the socket at the bottom of the sample chamber. The contact between its socket and the probe puck provided a good thermal contact to the central copper platform and to the samples. The PPMS thermometry was used as a secondary means of temperature monitoring and for temperature control. All data were acquired by a bespoke LabView program connected to Keithley voltmeters and nanoamplifiers. Measurement consistency was ensured by giving up one of the sample positions to a “standard” sample of NbTi with a RRR of 105. Further consistency checks were periodically performed by making multiple measurements on a set of samples in different positional configurations. A suite of six RRR probes allowed a constant measurement throughput of two to three probes per day, giving a potential measurement capacity of 135 sample measurements per week (excluding standard samples). The measurement methodology is discussed below. The results of a small experiment to determine the effect on RRR of heat-treating samples alongside critical current barrels is also presented. Due to the commercial sensitivity of RRR test results we have restricted the scope of all plots and discussions to one of comparison by normalised data.

6.7.1 Data acquisition

The PPMS temperature was set to 273 K and sufficient time allowed for the temperature to stabilise. Once the measurement sequence was initiated a Keithley current source delivered 200 currents, stepped in polarity reversed pairs (to cancel thermal voltages), in the range 0 to 100 mA to all ten samples. This sequence was repeated at 20 K and the data were saved to a comma delimited text file for analysis. The resistance of each sample, at each temperature, was then obtained by fitting a least-squares best fit line to the voltage vs current data (see Figure 6.21). The RRR was simply the ratio of these two resistances. The uncertainty in the RRR results is estimated to be below 1.0 %.

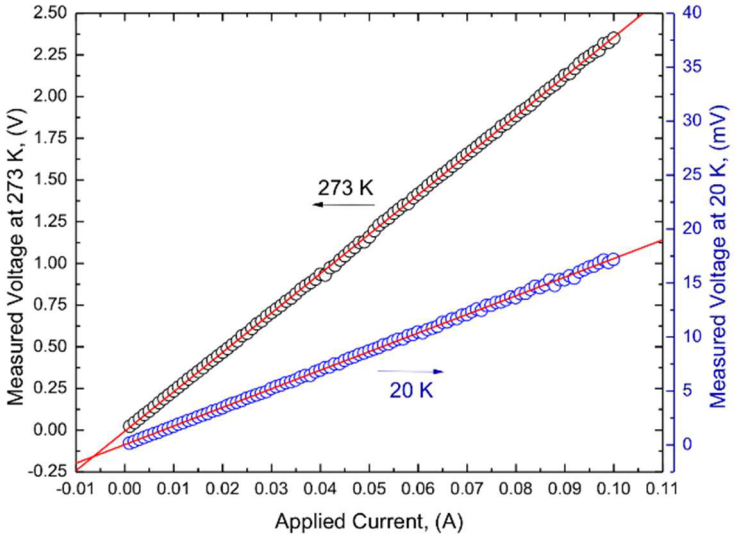

Figure 6.21: Typical voltage vs current data at 273 K and 20 K used to obtain the residual resistivity ratio of the Nb_3Sn samples.

6.7.2 Furnace cleanliness and RRR

A small experiment to investigate the effect of furnace cleanliness on residual resistivity ratio was performed. The methodology consisted of heat-treating two sets of samples (twelve per set) derived from three separate batches of internal tin strands. (These samples were obtained from adjacent lengths of the same samples used for the hysteresis loss experiment discussed above.) One set of twelve samples was heat-treated in one of the high-purity (six nines) RRR furnaces and the other set was heat-treated in one of the lower purity (four nines) critical current furnaces, alongside critical current samples. The heat-treated samples were then measured in the same way as described above. The normalised (to the mean) results are contained within Figure 6.22 and Table 6.3. An overview of the results is clearly visible in the plot of the ordered data in Figure 6.22-b where the RRR of all the samples heat-treated in the lower purity furnace can be seen to be lower than their respective high-purity counterparts. Table 6.3 provides more detail and shows that across all samples there was an average reduction in RRR of ~ 48 %. This decrease is accompanied by a reduction in the standard deviation, which is to be expected since lower RRRs are closer to a convergent minimum that should restrict variability. The reduction in RRR is, of course, an expected result. It is common knowledge that the RRR, being a measure of material purity, is highly dependent on furnace cleanliness. However, this small experiment goes some way to quantify the magnitude of the reduction associated with heat-treatments directly related to samples that are designed to fulfil the ITER acceptance criteria, which is a RRR of 100 or above. In this regard, samples 7 and 10 were purposely selected because they were both below the acceptance criteria. However, their reductions are not too dissimilar from the average, which shows they do not seem to be any more sensitive to decreased purity than any of the other samples. This observation is supported in Figure 6.22-c where the high-purity furnace RRR results are compared against their percentage drop in RRR due to the lower purity heat-treatment. The conclusion of this experiment is that a halving (on average) in RRR can be expected with a decrease in reaction purity of more than two nines.

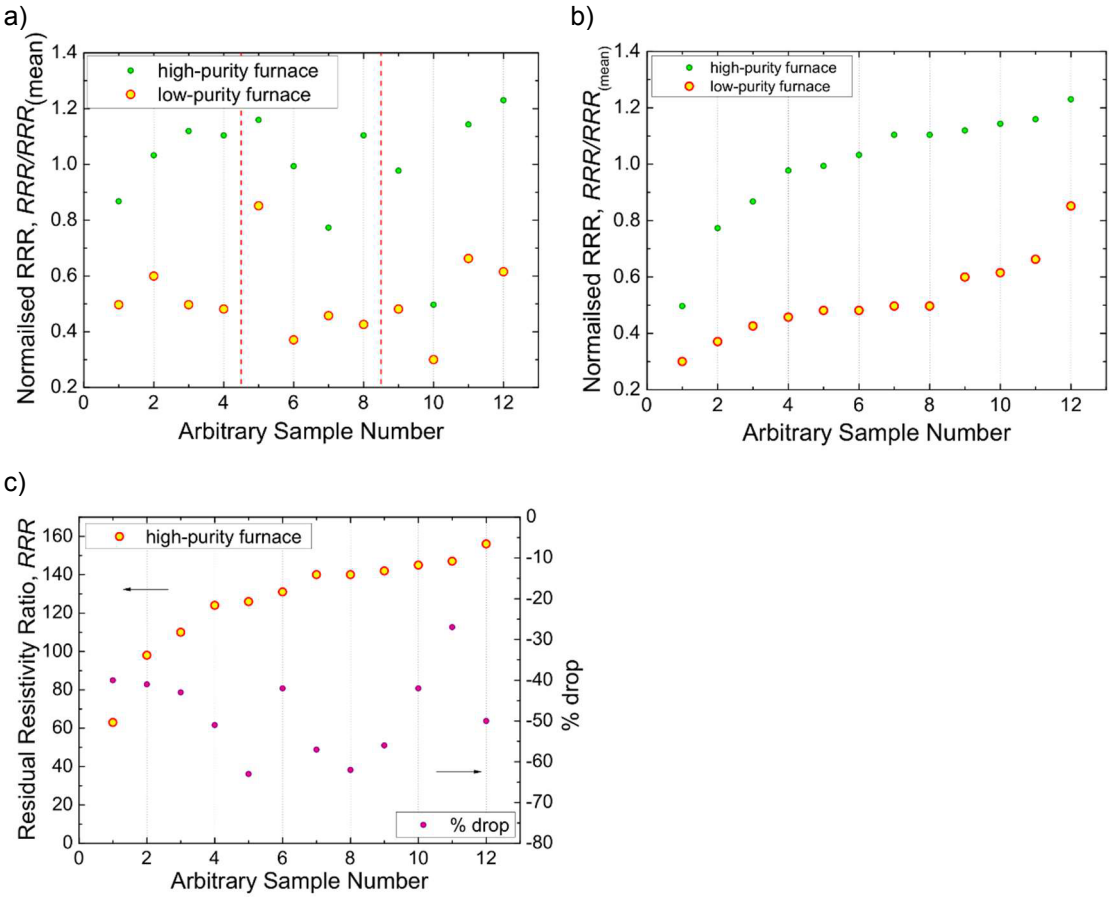

Figure 6.22: a) comparison of the RRR of internal tin samples heat-treated in the standard way (green symbols) i.e. in a high-purity furnace, and of the RRR of adjacent lengths of the same samples heat-treated in one of the lower-purity furnaces, alongside I_c samples (red encircled yellow symbols). This plot shows all 24 samples grouped in their original batches. b) Shows the same data ordered from low to high. c) Shows the high-purity furnace RRR results compared against the percentage drop in RRR of the same samples heat-treated in the low-purity furnace. This plot highlights that the percentage drop in RRR is independent of the high-purity RRR value.

6.7.3 Results, accuracy and interlaboratory comparisons of the RRR data

Durham laboratory uncertainties

Over the contract period over 2200 RRR measurements were performed in total.

Figure **6.23** shows the normalised (to the mean) test results for the complete set of samples for both strand architectures (not including additional measurements requested by F4E). The main factors that contribute to the measurement uncertainty are temperature set point accuracy (and stability), uniformity of temperature along the sample platform (see Figure 6.20-e and g) and instrumental errors. The uncertainty in the temperature set point of the PPMS at 273 K is 0.04 % and at 20 K it is 0.4 %. The effect of deviations in temperature from the set point to the resistivity of the copper at 273 K is ~ 0.4 % per Kelvin and that at 20 K is ~ 2.8 % per K. (These approximations were obtained from fits to data contained in [145].) Taking our temperature uncertainties into account,

Table 6.3: Data from Figure 6.22 listing batch and full sample set averages and standard deviations for the normalised RRR of samples heat-treated in a high-purity furnace (in the usual way) compared to a lower-purity furnace. The data suggest that there is a reduction in RRR of ~ 48% for those samples heat-treated in the lower-purity furnace.

batch	arbitrary sample number	*normalised RRR*		% reduction from *RRR* furnace		av. normalised *RRR* (*std dev*)	
		high-purity furnace	Low-purity furnace	per sample	per batch	high-purity furnace	Low-purity furnace
1	*1*	0.87	0.50	-43	-50	1.03 *(0.10)*	0.52 *(0.05)*
	2	1.03	0.60	-42			
	3	1.12	0.50	-56			
	4	1.10	0.48	-56			
2	*5*	1.16	0.85	-27	-48	1.01 *(0.15)*	0.53 *(0.19)*
	6	0.99	0.37	-63			
	7	0.77	0.46	-41			
	8	1.10	0.43	-61			
3	*9*	0.98	0.48	-51	-47	0.96 *(0.28)*	0.51 *(0.14)*
	10	0.50	0.30	-40			
	11	1.14	0.66	-42			
	12	1.23	0.61	-50			
all samples					-48	1.00 *(0.20)*	0.52 *(0.14)*

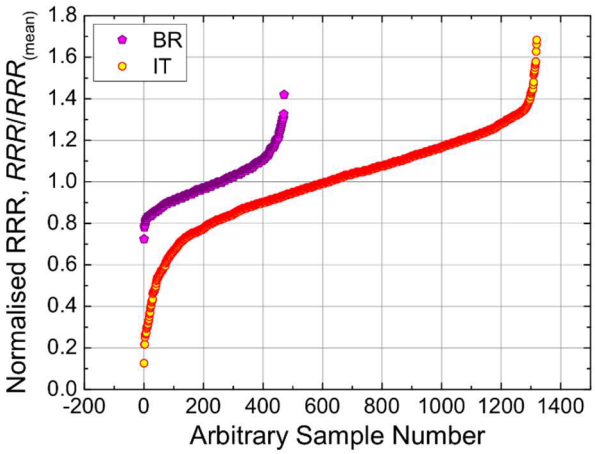

Figure 6.23: Residual resistivity ratio normalised to the mean for both strand architectures for all samples measured under the F4E contract (excluding additional measurements requested).

this leads to an uncertainty in the RRR, due to uncertainties in the set point temperature, of ~ 0.2 %. The uncertainty due to temperature gradients along the sample platform could have been obtained by performing direct temperature measurements at, at least, the two extreme ends of the platform (with a linear temperature gradient assumed). However, we felt that an alternative method would, not only capture the uncertainty associated with this temperature profile, but would also capture the instrumental uncertainty. This method consisted of performing multiple sequential measurements on a set of ten NbTi samples in different positions (and different sides) on a sample platform. The uncertainty in performing these measurements was 0.5 %. However, this includes any uncertainty in the set point temperatures (0.2 % - from above) and so 0.5 % is the total uncertainty in performing the RRR measurements using our equipment.

Results on ITER samples

Figure 6.24-a and Figure 6.24-b show the normalised (to the mean) RRR test results for each architecture measured by Durham, in measurement order. For the internal tin strands the global spread in the data was ± 23 % and that of the bronze route strands was ± 11 %. If the batch influence is removed (see Figure 6.24-c and d) then the deviation from the *ama* for the internal tin samples is ± 17 % and that for the bronze route samples is ± 9 %.

Comparisons with other laboratories

Data comparisons between Durham and a number of other laboratories were conducted at various occasions throughout the contract period. These checks were usually initiated by contradictions between Durham's test results and those of a manufacturer and included, not only testing Durham's measurement accuracy, but also Durham's heat-treatment quality. In all tests Durham's results were supported by the third party data. Figure 6.25 shows a comparison between three datasets of two batches of 45 adjacent samples. One batch was heat-treated and measured by Durham and the other batch was heat-treated by CERN and then subsequently measured by Durham and Lab A. The test results of both Durham and Lab A agreed to within 2.5 %. The average RRR of the set of samples heat-treated in Durham was 5 % higher than those heat-treated at CERN, which could be regarded as confirmation of Durham's heat-treatment gas purity. Additionally, a blind cross check between Durham, CERN and two independent laboratories, Lab A and Lab B was performed. This consisted of ten samples being heat-treated by CERN and then measured by Durham and Lab A. The measurement results were then compared against the same samples previously heat-treated and measured independently by Durham and Lab B. There was a 1 % agreement between the measurements performed by Durham and Lab A on CERN heat-treated samples. The average RRR of the samples heat-treated by Durham was 7 % higher than those heat-treated by CERN and the RRR of Lab B's heat-treated (and measured) samples was a further 8 % higher. The quality of the heat-treatments and measurements, however, is not the only major factor that determines the degree of agreement between different laboratories. Durham measured relatively small sample lengths (~ 20 mm), whereas some other laboratories measured lengths that could be up to five times as

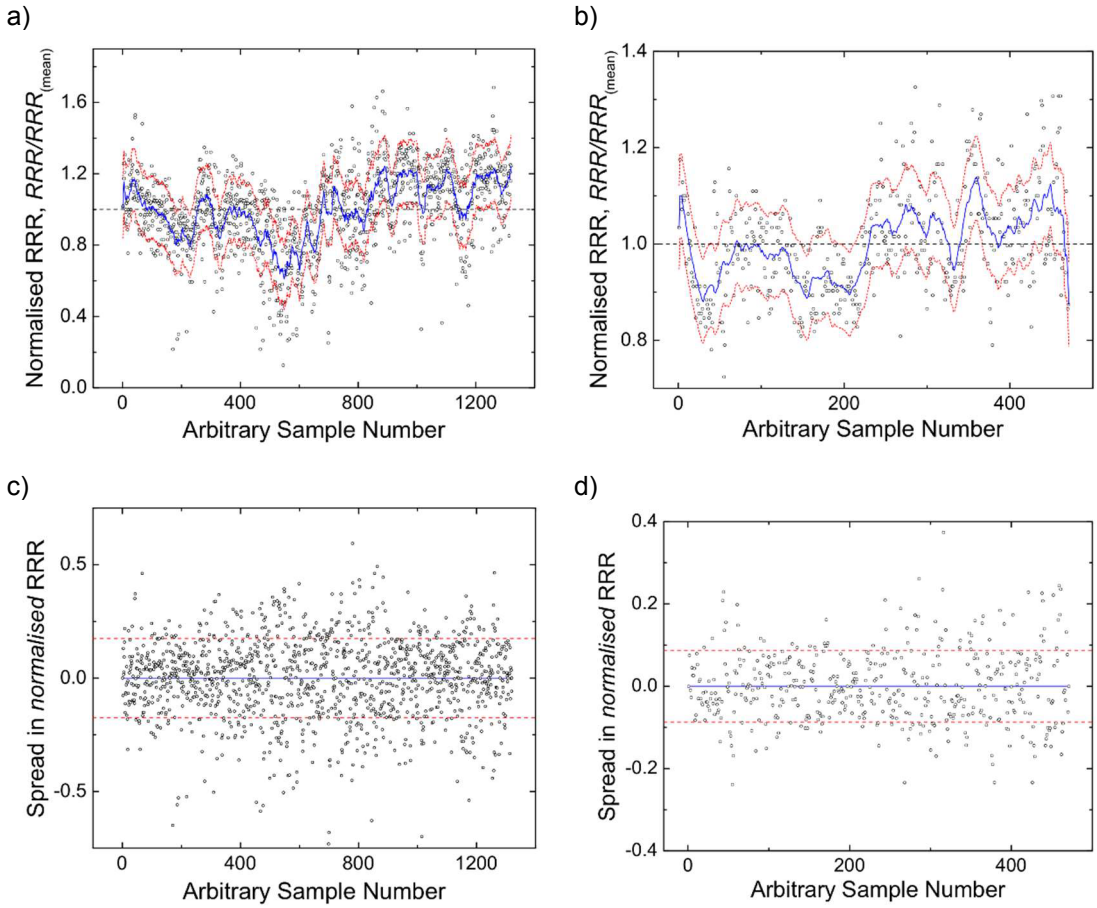

Figure 6.24: RRR test results (normalised to the mean) for all the samples measured by Durham for a) internal tin and b) bronze route strands. The blue curves are adjacent moving average (ama) fits to the data and the red dashed curves represent ± one standard deviation from the ama. The spread in the data is more clearly shown in plot-c (related to plot-a for internal tin) and plot-d (related to plot-b for bronze route) where the respective ama has been subtracted from its dataset. The spread in the data for the internal tin measurements is ± 25 and for the bronze route measurements it is ± 9.

long. This means that inhomogeneity in the strands, due to the manufacturing process, could have a more pronounced effect on Durham's measurement results than those laboratories who measure significantly longer samples. Of course, this depends on the length scale of the inhomogeneity. A test to check the homogeneity of two different strands was conducted by Lab B in unison with Durham. Two 1 km strand lengths were each cut into 44 pieces. Two sample batches (from each strand) were then produced by consecutively separating the 44 pieces so that each batch contained 22 samples that were originally adjacent to one another. Lab B and Durham then each heat-treated and measured one batch from each strand. For sample batch a) Lab B's average was 53 % higher than Durham's and Durham's spread was 19 % higher. For sample batch b) Lab B's average was 31 % higher than Durham's and Durham's spread was 1 % lower. The differences in the spread of each laboratory's dataset could have been partially explained by the difference in the sample lengths used to perform the measurements, where Lab B measured lengths that were *four* to *five* times the length of Durham's. Also, there are profound disagreements in the average RRR's measured by both laboratories (53 % and 31 %

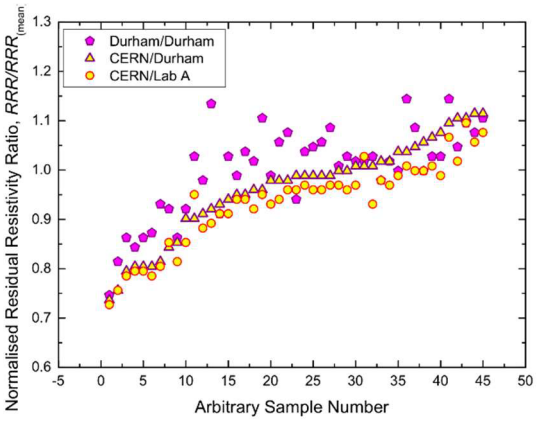

Figure 6.25: A comparison of the residual resistivity ratio (normalised to the Durham mean) of two batches of 45 adjacent samples. One batch was heat-treated and measured by Durham and the other batch was heat-treated by CERN and then subsequently measured by Durham and Lab A.

respectively). This disagreement prompted valuable discussions between Durham and Lab B that revealed their heat-treatments were performed in flowing *nitrogen*, as opposed to *argon*. Durham has been instructed by F4E to use argon for all heat-treatments since this inert gas was to be used in heat-treating the TF coils for the ITER tokamak. Interestingly, further tests by Lab B showed that the use of nitrogen consistently produced significantly higher RRR values – possibly because nitrogen binds to electronic scattering sites. When argon was used, the agreement between Durham and Lab B improved substantially. Aside from these additional complicating factors, the experiments showed that the inhomogeneity of the strands could lead to large discrepancies in the RRR of samples obtained from non-adjacent locations.

6.8 Room temperature measurements

Four different measurements were performed at room temperature on flexible, non-heat-treated, strands. The characteristics to be measured were strand diameter, chromium plating thickness, twist pitch (and direction) and the ratio between the amount of copper and the amount of non-copper used in each architecture. The following sections consider these measurements in three parts – first we discuss the measurements and how Durham performed them, we then provide information as to how the quality of the data was maintained, including round-robin measurements and calibrations. Finally we provide overviews of the large datasets measured and discuss the error bars associated with each measurement.

6.8.1 Diameter measurements

1000 mm lengths of sample strand were cleaned with acetone to remove any surface grease/dirt before being individually placed into the Scantron dual-axis laser micrometer. Dual-axis measurements were then made at ten angles around the circumference of each sample and at

four separate locations along their lengths and the data saved in a comma delimited text file from which the average diameter was calculated.

Durham laboratory uncertainties

The laser micrometer is capable of performing measurements on wire diameters in the range 0.03 to 3.0 mm with a resolution of 0.01 μm and according to the manufacturer's specification has a repeatability of 0.08 μm. There are in principle three dominant contributing sources to the uncertainties in performing the diameter measurements. They are: the inhomogeneity in the diameter at different positions along a strand; the difference in the ovality (and orientation of ovality) at different locations; and the uncertainty associated with the operator not ensuring the strands are situated correctly within the measurement equipment. We suggest that the influence of the latter is substantially reduced through proper training and regular checks that the strands are straight and seated correctly. We conclude that these sources of error are below the sensitivity of our instrument, the calibration of which was periodically checked by measuring four precision gauges purchased from Yorkshire Precision Gauges with diameters in the range 0.800 mm to 0.830 mm (each with a tolerance of + 0.001 mm – see Figure 6.26). The Gauges were made from stainless steel and stored within an argon glove box when not in use. These gauges were the closest we had to standards and none of our calibration checks showed that the accuracy of the equipment had changed. Therefore, the uncertainty of the diameter measurements was 1 µm.

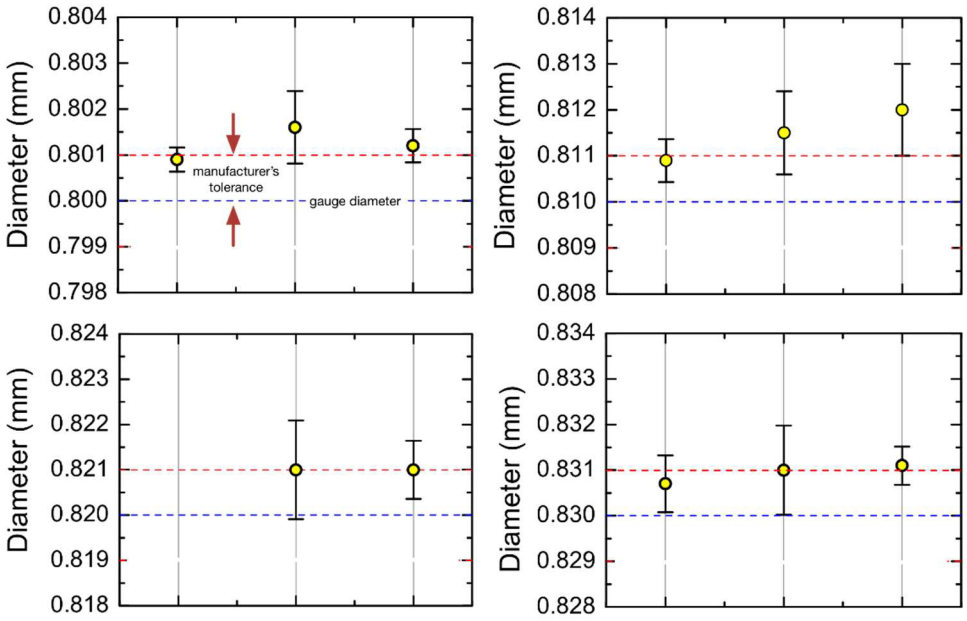

Figure 6.26: Annual calibration checks of the Scantron Dual Axis Laser Micrometer using four precision gauges with diameters 0.800, 0.810, 0.820 and 0.830 mm (blue dashed lines). The manufacturer's tolerance on the gauges was + 0.001 mm (red dashed line). The 0.820 mm gauge was not measured in the first year due to it not being as readily available from the manufacturer.

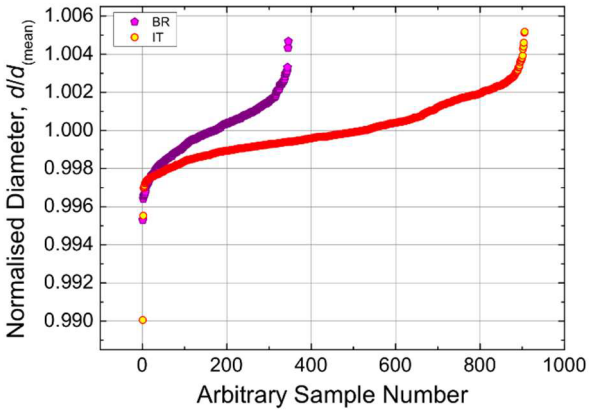

Figure 6.27: Diameter normalised to the mean for both strand architectures.

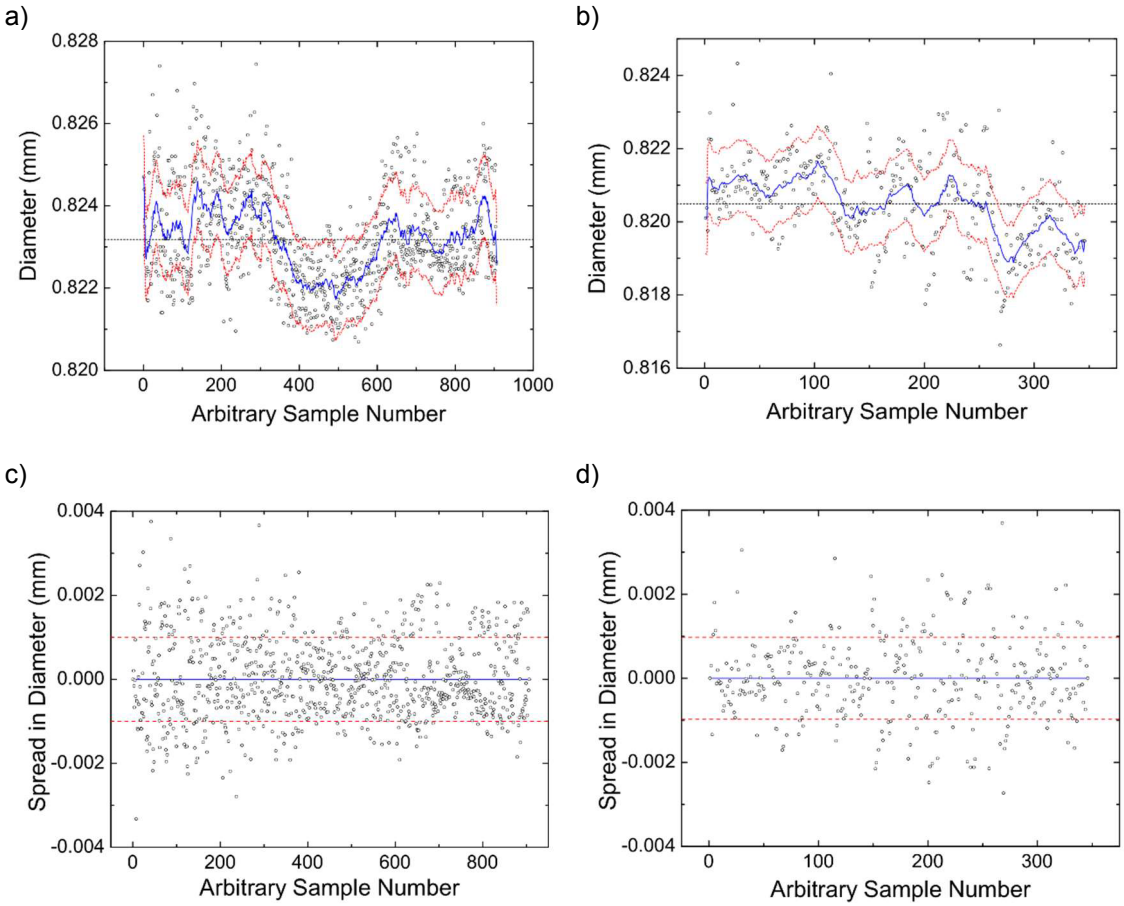

Figure 6.28: Diameter test results for the samples measured by Durham for a) internal tin and b) bronze route strands. The blue curves are adjacent moving average (ama) fits to the data and the red dashed curves represent ± one standard deviation from the ama. The spread in the data is more clearly shown in plot-c (related to plot-a for internal tin) and plot-d (related to plot-b for bronze route) where the respective ama has been subtracted from its dataset. The spread in the data for both strand architectures is ± 0.001 mm.

Results on ITER samples

Over the contract period ~ 1400 diameter measurements were performed. Figure 6.27 shows the normalised (to the mean) test results for the complete set of samples for both strand architectures (not including additional measurements requested by F4E). Figure 6.28 shows the diameter test results for each architecture measured by Durham, in measurement order. For the internal tin strands the global mean diameter for the complete dataset is 0.823 mm ± 0.1 % and for the bronze route strands it is 0.820 mm ± 0.1 %. If the batch influence is removed (see Figure 6.28-c and d) then the variation in the diameters remains unchanged at ± 0.1 % for both architectures.

Comparisons with other laboratories

As well as equipment calibration checks some additional (small quantity) cross-check measurements were performed between Durham and Lab A that showed agreement to within 0.2 % (see Figure 6.29). Each laboratory measured their own set of twelve samples obtained from twelve different strands i.e. two adjacent samples from each strand were separated to form two sets of twelve correlated samples. The agreement between both laboratories was very good.

6.8.2 Chromium plating thickness measurements

Initially Durham used the SEM facility to measure the chromium plating thickness at six locations around the circumference of each wire separated by 60 degrees. An average of these data were then taken. However, this method was machine and labour intensive and required each sample to be electroplated with copper to help stop smudging of the thin chromium plating caused by the polishing process, which also had to be completed to a very high standard, and also compounded the time issue. We therefore adopted a different method that could be completed in a more efficient way. This entailed cleaning 1000 mm long samples with acetone to remove any surface grease/dirt. Their masses were then measured four times and an average taken. The chromium plating was then removed by etching with dilute hydrochloric acid and another four mass

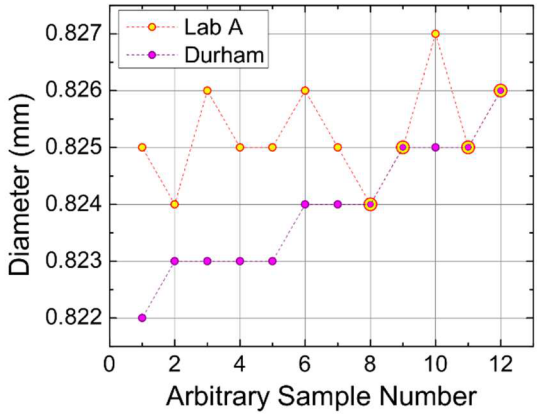

Figure 6.29: Cross-check diameter measurements between Durham and Lab A. Both laboratory's measurements agreed to within 0.2 %.

measurements taken to obtain an average. The diameter data and the change in mass data were then used to calculate the average chromium plating thickness of each sample in accordance with the following formula,

$$Cr_T = \frac{1}{2}\left[D_0 - \sqrt{D_0^2 - \frac{4V_{Cr}}{\pi L}}\right] \tag{6.1}$$

where D_0 is the average diameter (with chromium), V_{Cr} is the volume of the chromium and L is the strand length. The chromium volume was obtained by dividing the difference in the mass measurements by the density of chromium.

The quality of the measurement procedure was checked by repeating the process on different sample lengths of each strand architecture to make sure that a linear relationship between chromium mass and sample length existed and that a 1000 mm length was a sufficient choice. The data for this check are presented in Figure 6.30.

Durham laboratory uncertainties

There are *four* sources of measurement uncertainty that contribute to the total uncertainty in the chromium plating thickness. These uncertainties originate from measuring a sample's diameter (~ 0.1 %), length (~ 0.05 %) and mass (~ 0.002 %) – all quantities required of equation (6.1) – as well as the uncertainty in the standard value of the density of chromium (0.07 %). The most dominant uncertainty is therefore that associated with the diameter measurement. The propagation of these values through equation (6.1) leads to a total uncertainty in the chromium plating thickness of ~ 0.2 %.

Results on ITER samples

Over the contract period ~ 1400 chromium plating thickness measurements were performed. Figure 6.31 shows the normalised (to the mean) test results for the complete set of samples for both strand architectures (not including additional measurements requested by F4E). Figure 6.32

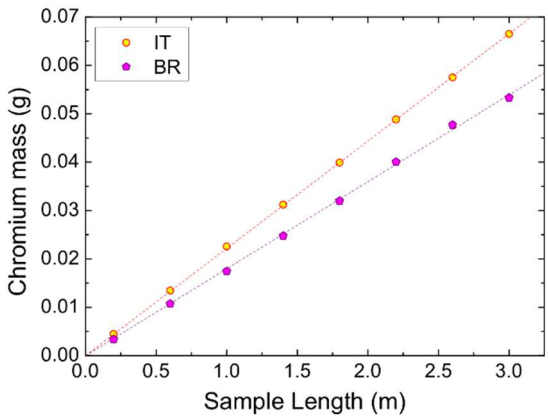

Figure 6.30: Quality check of the chromium plating thickness measurements that confirmed an expected linear relationship between chromium mass and sample length.

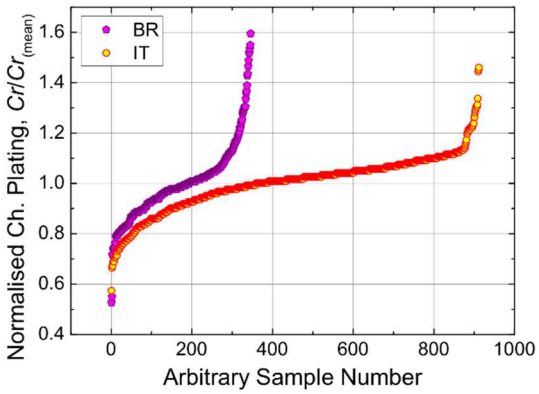

Figure 6.31: Chromium plating thickness normalised to the mean for both strand architectures.

shows the chromium plating test results for each architecture measured by Durham, in measurement order. For the internal tin strands the mean plating thickness for the complete

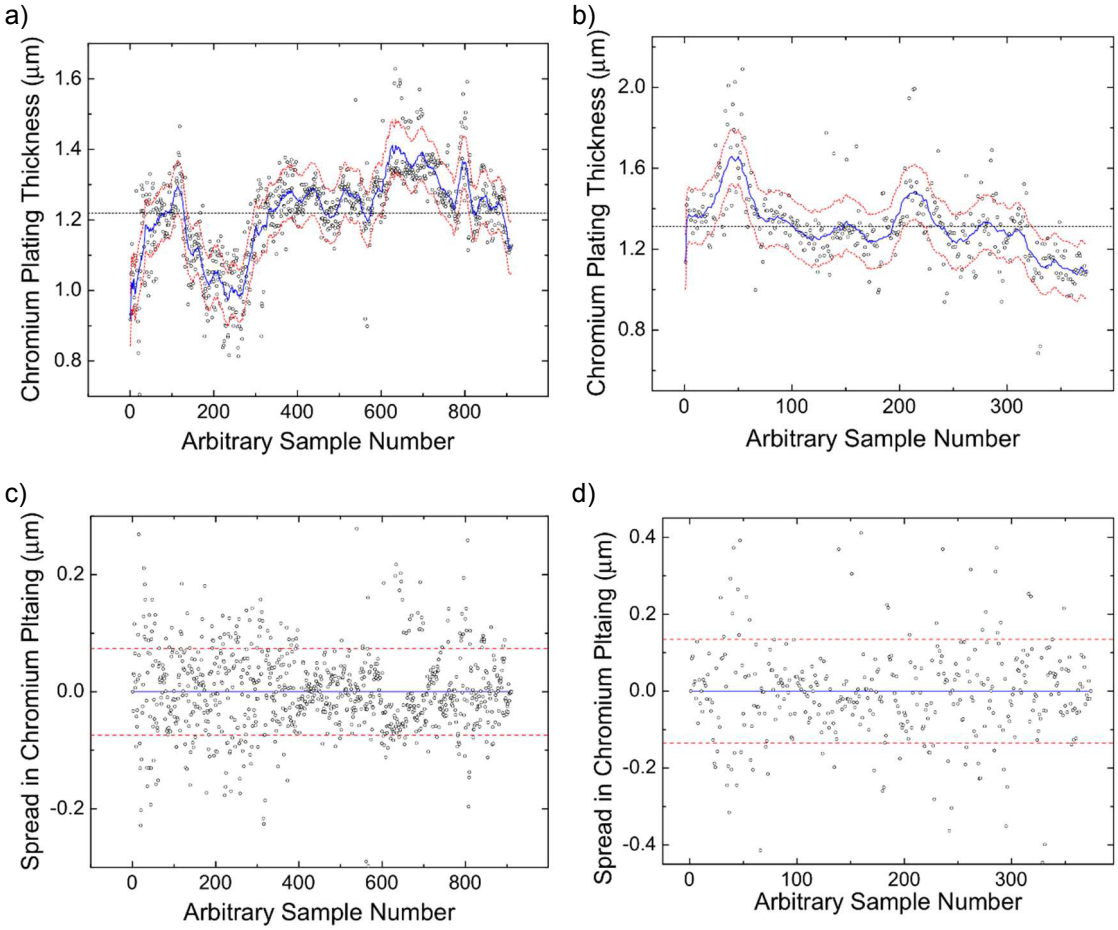

Figure 6.32: Chromium plating thickness test results for the samples measured by Durham for a) internal tin and b) bronze route strands. The blue curves are adjacent moving average (ama) fits to the data and the red dashed curves represent ± one standard deviation from the ama. The spread in the data is more clearly shown in plot-c (related to plot-a for internal tin) and plot-d (related to plot-b for bronze route) where the respective ama has been subtracted from its dataset. The spread in the data for both strand architectures is ± 0.1 µm.

dataset is 1.2 μm ± 8 % and for the bronze route strands it is 1.3 μm ± 8 %. If the batch influence is removed (see Figure 6.32-c and d) the deviation from the *ama* is ± 6 % for the internal tin architecture and for the bronze route architecture it is ± 8 %.

Comparisons with other laboratories

Some small quantity comparisons between Durham and Lab A were also conducted (see Figure 6.33). The agreement was 8 %. It is known, however, that the chromium thickness is not uniform over a strand's length and so some variability in comparisons is to be expected; although the exact contribution from this variability to this small-scale comparison is not known. Lab A's data are however, systematically higher than Durham's, which could be symptomatic of different measurement methodologies between both labs (Durham do not know how Lab A performed their measurements).

6.8.3 Twist pitch measurements

There are number of ways in which an estimate of strand twist pitch can be determined. For example, a sample can be etched to reveal its filament bundles and then untwisted. Dividing the exposed length by the number of twists provides an estimate of its twist pitch. Alternatively, a sample can be sliced longitudinally to reveal the periodic twist pattern from which the twist pitch can be measured. A method that relied on the striations that are visible on the surface of the tantalum barrier (see Figure 6.34-a) was adopted by Durham. The central ~ 30 mm of a ~ 100 mm long sample has its chromium plating mechanically removed with Emery paper and then its copper stabiliser etched away in dilute nitric acid to reveal the underlying tantalum barrier. The twist pitch of the niobium bundles under the barrier is clearly visible as striations on the barrier's surface (see Figure 6.34-a). The etched region of a sample is then placed on top of a rule so that the sample, and the gradations on the rule, are clearly visible through the eyepiece of an optical microscope. The striations (and gradations) are then photographed through the eyepiece of the microscope using a fourteen megapixel digital camera. The photographs were analysed in Adobe

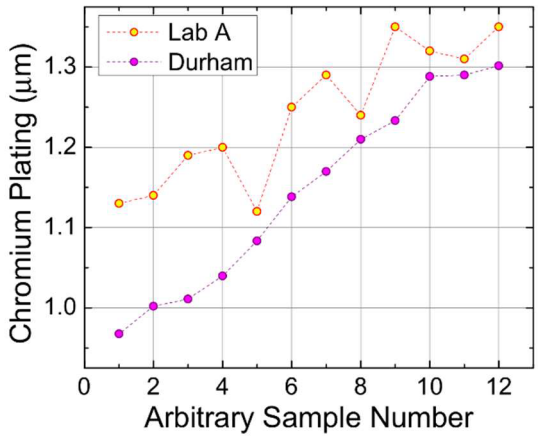

Figure 6.33: Chromium plating cross-check measurements between Durham and Lab A in which there was an 8 % agreement in the average.

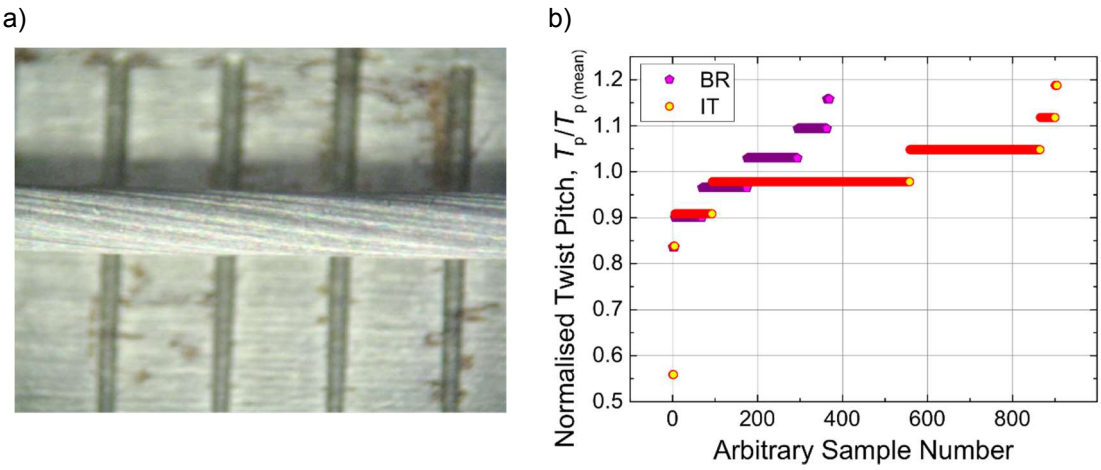

Figure 6.34: a) Twist pitch visible in the striations on the tantalum barrier and b) twist pitch normalised to the mean for both strand architectures.

Photoshop by measuring the diameter, d, of the etched strand and the angle, θ, the striations make to the horizontal (through the central axis of the strand), at a minimum of three independent locations along its length. An average of these measurements was calculated and used to determine the twist pitch, T_P, in accordance with the following equation.

$$T_P = \frac{180d\cos\theta}{\theta} \tag{6.2}$$

The direction of the twist pitch was also recorded.

Durham laboratory uncertainties

This measurement is reasonably simple to perform and because of the tolerance of the acceptance criteria, which only required an estimate of the twist pitch to within 13 % we did not work to improve the uncertainty on this straightforward measurement. We estimate the uncertainty in our twist pitch measurement/calculation to be ~ 8 %; predominantly from the uncertainty in measuring the angle (~ 10 %). Nevertheless, as can be seen in Figure 6.34-b, this accuracy was sufficient to identify strand that must have been twisted twice during manufacture resulting in half the specified twist pitch. These strands were subsequently rejected from use in the TF coils.

Results on ITER samples

Over the contract period ~ 1400 twist pitch measurements were performed. Figure 6.34-b shows the normalised (to the mean) test results for the complete set of samples for both strand architectures (not including additional measurements requested by F4E). Figure 6.35 shows the twist pitch test results for each architecture measured by Durham, in measurement order. For the internal tin strands the global mean twist pitch for the complete dataset is 14 mm ± 5 % and that of the bronze route strands is 16 mm ± 7 %. If the batch influence is removed (see Figure 6.35-c and d) then the deviation from the *ama* for both architectures is ± 5 %.

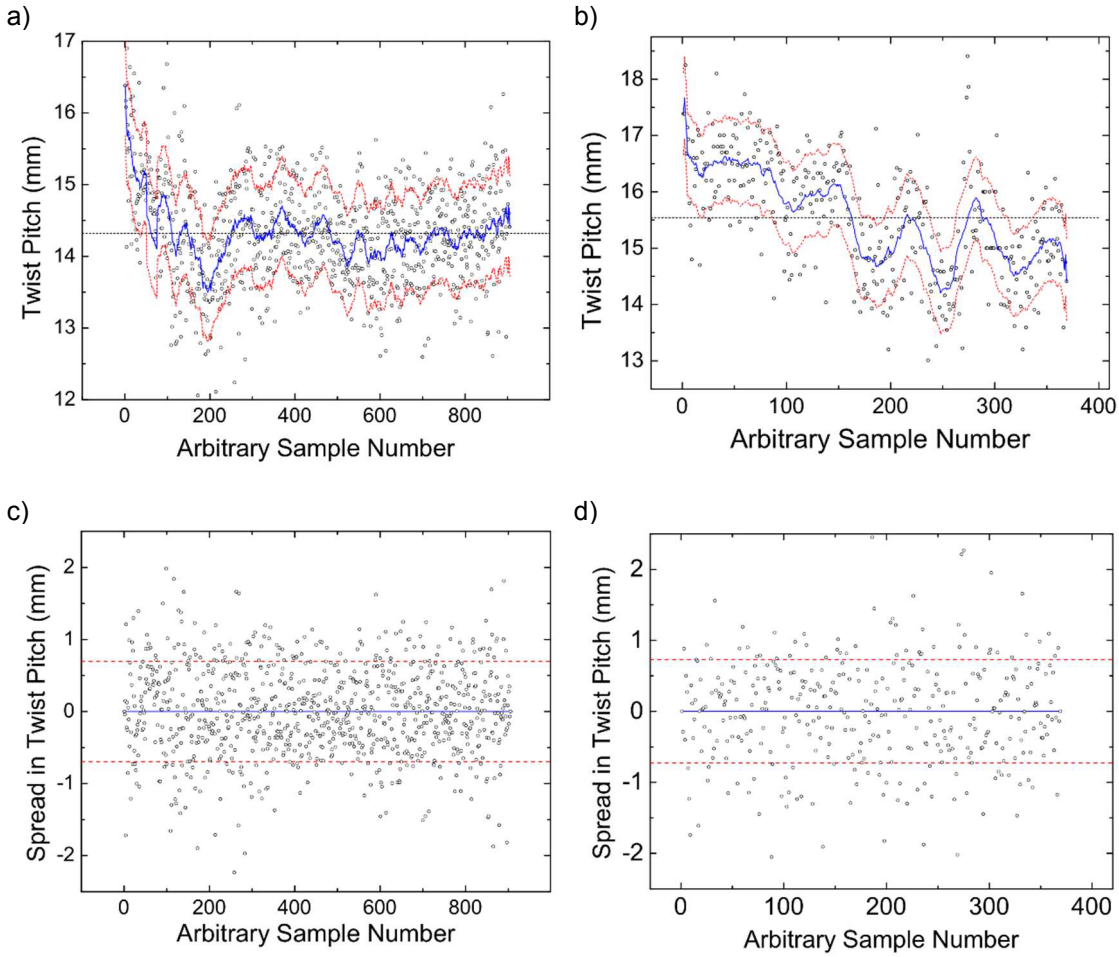

Figure 6.35: Twist pitch test results for all the samples measured by Durham for a) internal tin and b) bronze route strands. The blue curves are adjacent moving average (ama) fits to the data and the red dashed curves represent ± one standard deviation from the ama. The spread in the data is more clearly shown in plot-c (related to plot-a for internal tin) and plot-d (related to plot-b for bronze route) where the respective ama has been subtracted from its dataset. The local spread in the data for both strand architectures is ± 0.7 mm.

Comparisons with other laboratories

No inter-laboratory cross-check measurements were performed - other than the original benchmarking measurements that were required of all parties within the contract bidding process to establish their ability to perform the measurement.

6.8.4 Copper to non-copper ratio measurements

The copper to non-copper ratio was measured by first acquiring cross-section images of the samples using the Hitachi SU-70 FEG SEM in the Durham Microscopy Unit, which provides magnifications from x20 up to x300,000. The usual practice is to mount a single sample, or maybe two, within a Bakelite puck, but this was not a practical way to deal with the large number of samples to be measured as part of this contract. We therefore mounted up to 36 samples (the maximum feasible number that could be fitted within a standard sized puck) into a Bakelite puck

in which 36 holes had been drilled. One sample was fixed in each hole with an epoxy resin prior to polishing (see Figure 6.36-a). The polishing process consisted of a staged grinding routine in which polishing disks of increasingly finer grit would flatten the sample surfaces and reduce abrasion marks. The process would then continue with even finer grit diamond pastes, substituted for the grinding discs, until the required polishing level was achieved. The cross-section images (see Figure 6.36-b) were then analysed in Adobe Photoshop to measure the cross-sectional areas occupied by the copper region (see Figure 6.36-c) and the non-copper region (see Figure 6.36-d) from which a value of the copper to non-copper ratio was easily calculated.

Durham laboratory uncertainties

The electron microscopes in Durham are part of a £3M investment made by the University in around 2010. The SEM we use is a world-class piece of equipment with superb reliability and calibration, and so, any error associated with its use is negligible. Additionally, assuming the errors are reasonably uniform over each image and taking into account that the copper to non-copper ratio of these strands is around one, the ratio should not be noticeably affected by the machine uncertainty. We must therefore look to operator polishing as the next likely source of error. However, any significant errors introduced by polishing, such as the production of an

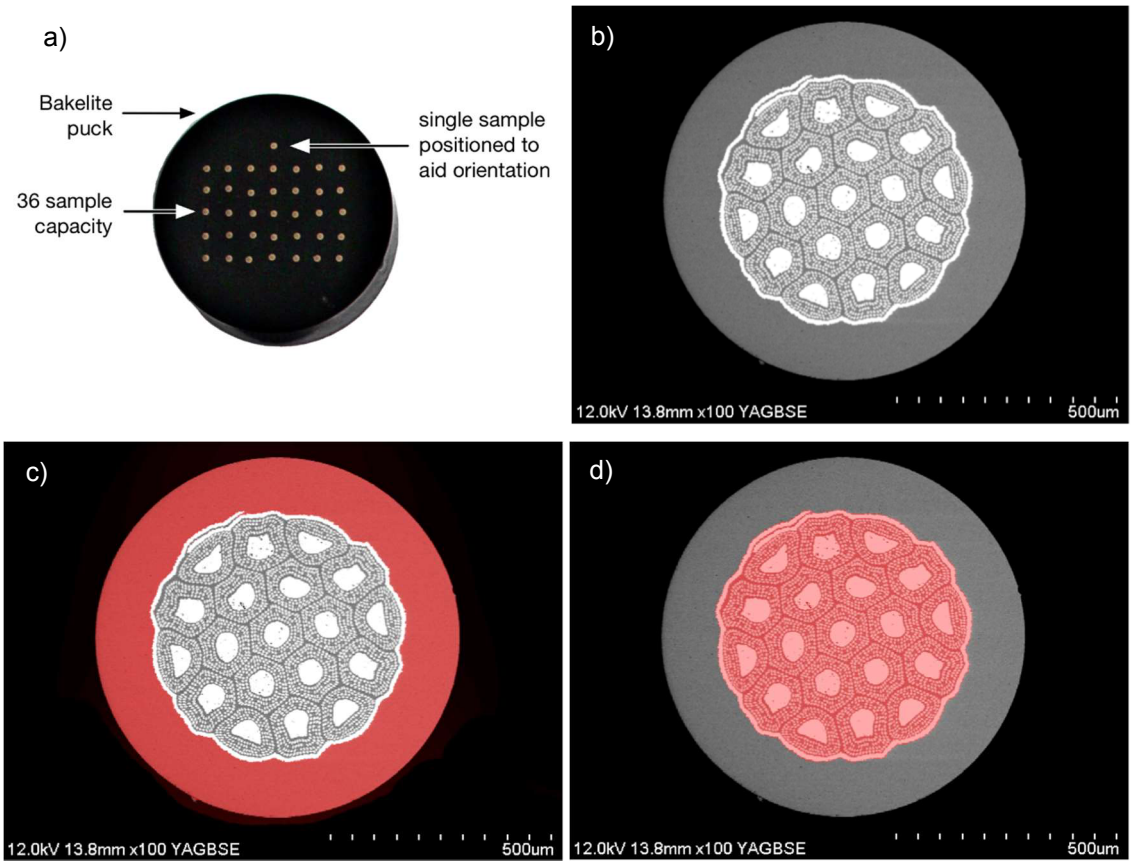

Figure 6.36: Copper to non-copper ratio; a) mounting puck (Bakelite) used to image the cross-sections of up to 36 samples with the SU-70 FEG SEM, b) example image, c) copper region highlighted, d) non-copper region highlighted.

angled surface, should be visibly detectable through uncharacteristic ellipsoidal cross-sectional areas - these were not detected. Image processing errors associated with the identification of the copper and non-copper areas in Photoshop have also been considered. Our conclusion is that the errors in these measurements are very small and certainly below 1 %, which is far smaller than that needed for the ITER measurements.

Results on ITER samples

Over the contract period ~ 1400 copper to non-copper ratio measurements were performed. Figure 6.37 shows the normalised (to the mean) test results for the complete set of samples for both strand architectures (not including additional measurements requested by F4E). Figure 6.38 shows the copper to non-copper ratio test results for each architecture measured by Durham, in measurement order. For the internal tin strands the global mean copper to non-copper ratio for the complete dataset is 1.00 ± 6 % and for the bronze route it is 0.93 ± 2 %. If the batch influence is removed (see Figure 6.38-c and d) then the deviation from the *ama* for the internal tin strands is ± 6 % and that of the bronze route strands is ± 2 %.

Comparisons with other laboratories

Some small quantity comparisons between Durham and Lab A showed agreement to within 1.0 % (see
Figure **6.39**). Each laboratory measured their own set of twelve samples, where both sets were produced from 24 adjacent samples cut from twelve strands.

6.9 Concluding comments

At the beginning of this chapter we stated three aims that we sought to achieve. The first was to satisfy our contractual obligations, which we achieved by meeting every agreed delivery deadline and by providing high quality data upon which valued quality assessments could be made. The second aim was to develop the cryogenic and room temperature metrology for very large sample quantities. We achieved this by developing new ways to maintain sample throughput without undermining measurement quality, for example, in using press-fit contacts between critical current barrels rather than soldered joints. We also conducted a large number of repeat measurements

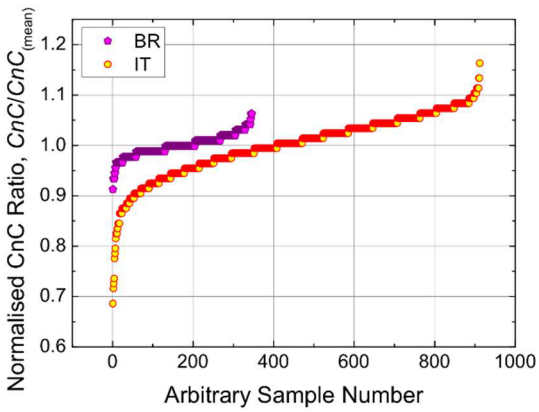

Figure 6.37: Copper-to-non-copper ratio normalised to the mean for both strand architectures

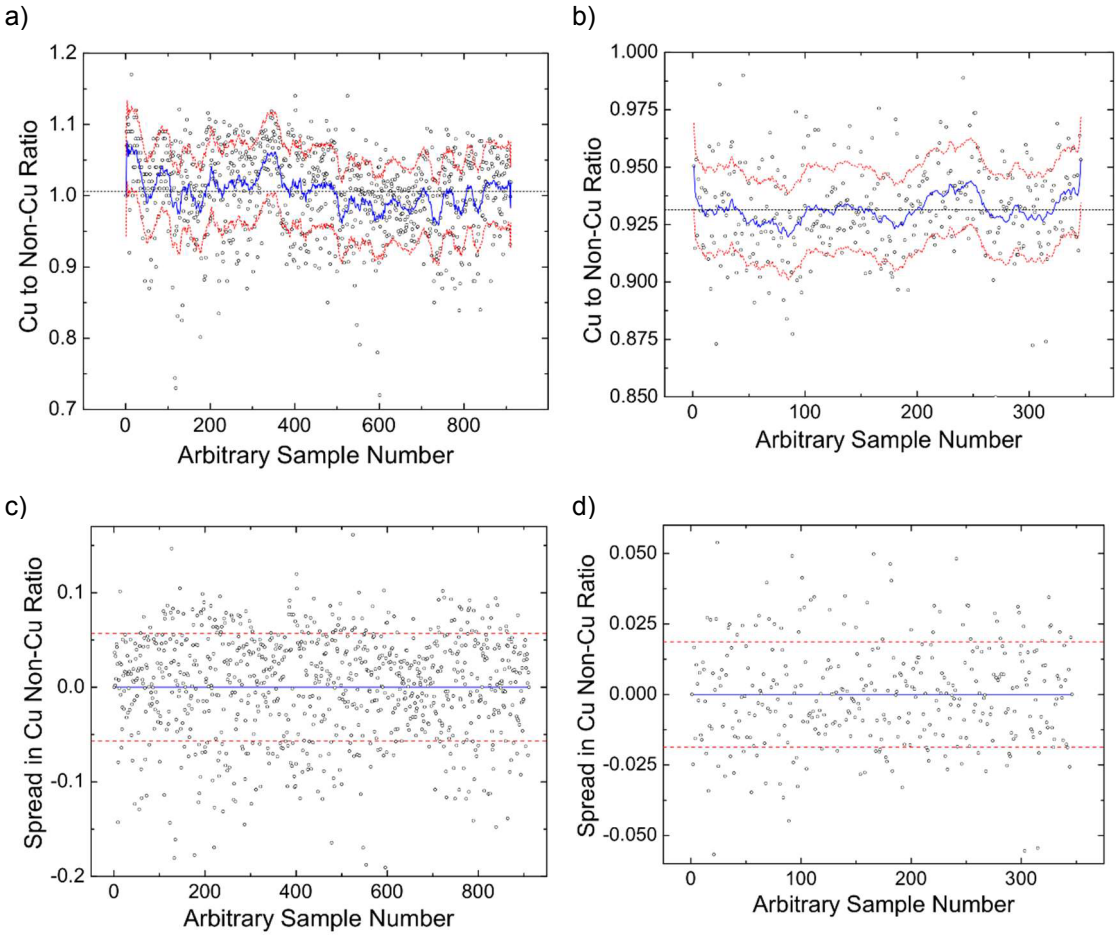

Figure 6.38: Copper to non-copper ratio test results for the samples measured by Durham for a) internal tin and b) bronze route strands. The blue curves are adjacent moving average (ama) fits to the data and the red dashed curves represent ± one standard deviation from the ama. The spread in the data is more clearly shown in plot-c (related to plot-a for internal tin) and plot-d (related to plot-b for bronze route) where the respective ama has been subtracted from its dataset. The spread in the data for the internal tin measurements is ± 0.06 and for the bronze route it is ± 0.02.

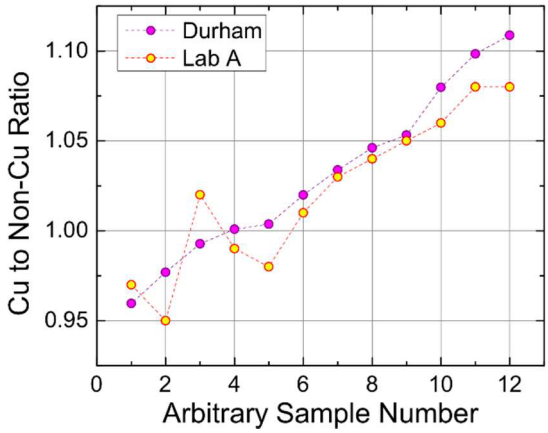

Figure 6.39: Copper-to-non-copper cross-check measurements between Durham and Lab A in which there was a 1 % agreement in the average.

in different test configurations to improve and test our measurement methodologies. Lastly, we aimed to have an impact on the success of the ITER project itself. This is a tall demand to satisfy but by performing accurate measurements, not only on an extremely large quantity of samples, in a fairly short period of time, but also on a great number of additional measurements requested by F4E, we believe this aim has also been satisfied. The scrutiny that Durham's processes and measurements were subjected to throughout the contract period was, of course, perfectly reasonable and correct, but on every occasion fault could not be found with Durham's results. This meant that Durham's role helped to filter out substandard materials and in this respect, although we were but a minute cog in a very complicated timepiece, our impact was largely down to the accuracy, reliability and timeliness of our data.

During the contract period we established successful and reliable methods for handling, heat-treating and measuring large sample quantities. For the critical current measurements we improved data acquisition by strapping the samples with YBCO tape to increase E-fields during the transition that allowed more accurate measurements of *n*-value to be determined. We also established the degree to which a sample's critical current would be effected by temperature deviations from the specified upper heat-treatment plateau, and included this analysis in our estimate of the total uncertainty in the test results. For the hysteresis loss measurements we measured the change in volume of the strands during heat-treatment and used these data to determine the post heat-treatment densities that were used in the calculation of the losses per unit strand volume, thus providing improved accuracy. We also established that the purity of the gas used in the heat-treatments did not significantly affect losses and that the number of turns in a sample and electrically insulating turns, had little (if any) effect on measurement accuracy. Conversely, we found that heat-treating RRR samples in an environment with a gas purity less than four-nines halved the expected RRR values; adding further credence to the importance of environmental cleanliness on RRR and providing a ball-park guide as to the severity of deviations away from best practice. The degree to which we subjected the cryogenic measurements to additional experiments signifies their greater complexity over the room temperature measurements, which were reasonably straight forward to perform and were far less susceptible to operator/process influences. However, no less diligence was expended in conducting them and all reasonable calibration (and consistency) checks were performed.

For commercial reasons we have not *explicitly* quantified the number of samples that did not meet the ITER acceptance criteria but it is reasonable to say that by far the most difficult verification test to satisfy was RRR and the least difficult was hysteresis losses. The requirement for very clean copper stabiliser naturally presents great technological problems in composite strands where the method needed to process the superconducting volume, namely, heat-treatment, can be detrimental to stabiliser purity. Any small breaks in the tantalum barrier or the chromium plating, for instance, can severely reduce RRR and lead to significant inhomogeneities. Overall, however, the strands from both manufacturers performed very well and this is in spite of the hefty demands made on their production facilities given the shear amount of Nb_3Sn required for ITER.

We would like to end this chapter by pointing out that metrology is never a done deal… it's only done, done, and done again with better accuracy and finer precision.

Chapter 7

Concluding comments and future work

The work discussed in this thesis has been concerned with the fabrication and processing of nanocrystalline niobium carbonitride and the metrology of a large number of Nb_3Sn samples for ITER; two different subjects that might only seem connected by their shared relationship to superconductivity. However, the interest and motivation that has driven each kind of work has been the same. We are fundamentally interested in applying a combination of technology and methodology, based on intelligence, expertise, experience and perseverance to superconductors and superconductivity in any way that might benefit its application within society, no matter how small that benefit might be.

Will nanocrystalline niobium carbonitride with an upper critical field of ~ 21 T benefit society? On its own, most likely not, but this, in conjunction with the observed increase in critical current density, serves to show the potential for real benefits that might be achieved with more work. In the future we would like to substantially augment the nanocrystalline work discussed in the thesis by performing, on all the samples so far produced, a full suite of resistivity, heat capacity and magnetisation measurements to more fully complete the nanocrystalline characterisation. We would also like to measure the very best samples in higher applied magnetic fields than are currently available to us in Durham by visiting a national/international facility with the necessary equipment. A full analysis of this data would lead to a better understanding of the relationship between the samples' morphologies and their characteristic parameters, such as, Sommerfeld constant and Debye temperature and their superconducting critical values. This comprehensive data set should therefore aid the selection of a set of process parameters that would enable a more directed experiment, designed to seek out the optimum upper critical field and critical current density and to test our understanding of the relevant parameters. This increased understanding would greatly facilitate widening the scope of Taylor's model to those materials that don't have a peak in their density of states, centred at the Fermi energy. At the very least it would enable a refinement of the model and would increase the model's applicability, which in itself might lead to an increased ability to predict those materials that might benefit the most from being made nanocrystalline; either generating an accelerated route to superior materials for real-world applications such as ITER or enabling routes to a greater understanding of the underlying physics.

The methods that we have used to produce nanocrystalline material, namely, mechanical ball milling and HIPing, are a good tried and tested means of material processing. However, they are also brutish ways of manipulating material. They do not provide the means by which grain boundaries themselves could be delicately engineered, for example. This kind of engineering would be of benefit, not only (or necessarily) to increase or control flux pinning, but also to optimise *inter*granular current paths. It might be possible to augment milling and HIPing with other technologies that facilitate finer control over grain boundaries. For example, it might be possible to HIP a milled material while simultaneously agitating it with ultrasonic waves to reduce *inter*granular pores that would lead to more compacted samples. The frequency of the ultrasonic waves could be adjusted to target the much smaller, amorphous, material that resides within the grain boundaries, causing it to be more evenly distributed; possibly leading to a reduction in average grain separation and cleaner grain boundaries without excessively reducing pinning sites. Of course, the milling and HIPing parameters would need to be adjusted to facilitate this more targeted form of grain boundary engineering. It might even be that the ultrasonic treatment is conducted during an initial low temperature, low pressure, HIPing session that prepares a partially compacted sample that is subsequently HIPed independently of the ultrasonic stage, at much higher pressures and temperatures. Fortunately, we have found that niobium carbonitride is sensitive to milling and HIPing and therefore it also serves as an ideal candidate for testing the viability of using ultrasound in this way to further improve material quality.

The other major part of this thesis has been the metrology of the Nb_3Sn samples for ITER. This has provided us with the opportunity to conduct over 100 heat-treatments and 10,000 measurements. This level of experience is a specialist commodity that has so far largely remained confined within the walls of those commercial organisations in which complete openness can be a detrimental altruistic quality. To our knowledge this is the first time that such a large data set has been generated by a non-commercial, scientific institution for one specific type of material important to contemporary applications. The sharing of information, techniques and data is the basis upon which the scientific method is moulded. We have to compete in ideas and the successes that those ideas generate, without relying on the benefits that confidentiality affords. Unlike business, which has no choice but to concern itself with issues of self-interest, academia must only concern itself with working within the generous bounds of the scientific way so that everyone benefits from its successes. In this respect we would also like to, not only share what we have learnt about performing accurate measurements on very large sample quantities, but also to extend some of the small-scale experiments discussed in this thesis to inform the wider community about some of the very important characteristics of the workhorse superconductor Nb_3Sn in wire form. For example, the RRR of the copper stabiliser used in superconducting strands is an extremely important characteristic. An understanding of the effect on RRR, not only from contamination (as has been discussed in this work) but also as a function of temperature and applied magnetic field, for strands with different RRR values, might further aid the setting of suitable specification parameters for engineering applications in the future. In light of this we

would like to publish a comprehensive, important and influential paper that defines, in one publication, a benchmark methodology for handling, processing and performing the kinds of measurement we have performed. The kinds of measurement that are in fact not specific to any one particular type of superconductor but are more widely applicable to superconductors in general.

Materials fabrication, processing and measurement are all distinct facets related by the way in which they can be used to compliment nature's provision for life. As scientists, tasked with the fortunate goal of understanding nature's underlying mechanisms, we justify our scrutiny of nature's ways by sharing our findings.

References

[1] "International Energy Agency - United Kingdom: Electricity and Heat for 2012," http://www.iea.org/statistics/statisticssearch/report/?year=2012&country=UK&product=ElectricityandHeat, 2015.

[2] C. P. Poole, H. A. Farach, and R. J. Creswick, "Ginzburg-Landau Theory," in *Superconductivity*. San Diego, California: Academic Press Inc, 2007, pp. 155.

[3] V. L. Ginzburg and L. D. Landau, "On the Theory of Superconductivity," *Zhurnal Eksperimentalnoj i Teoreticheskoj Fiziki*, vol. 20, pp. 1064-1082, 1950.

[4] P. J. Ford and G. A. Saunders, "Understanding Superconductivity," in *The Rise of the Superconductors*. Florida: CRC Press, 2004, pp. 29.

[5] J. Matricon and G. Waysand, "East is East, and West is West," in *The Cold Wars - A History of Superconductivity*. New Brunswick, New Jersey: Rutgers University Press, 2003, pp. 130.

[6] C. P. Poole, H. A. Farach, and R. J. Creswick, "Order Parameter," in *Superconductivity*. San Diego, California: Academic Press Inc, 2007, pp. 144.

[7] D. R. Tilley and J. Tilley, "Ginzburg-Landau Theory," in *Superfluidity and Superconductivity*, 3rd ed. Bristol: IOP publishing Ltd., 1990, pp. 296-302.

[8] M. Tinkham, "The Ginzburg-Landau Differential Equations," in *Introduction to Superconductivity*, 2nd ed. New York: Dover Publications, 1996, pp. 117.

[9] C. P. Poole, H. A. Farach, and R. J. Creswick, "Zero-Field Case Near Superconductor Boundary," in *Superconductivity*. San Diego, California: Academic Press Inc, 2007, pp. 149.

[10] P. Ford and G. A. Saunders, "What Causes Superconductivity?," in *The Rise of the Superconductors*. Florida: CRC Press, 2004, pp. 91-92.

[11] M. Tinkham, "Magnetic Properties of Classic Type II Superconductors," in *Introduction to Superconductivity*, 2nd ed. New York: Dover Publications, 1996, pp. 149-154.

[12] D. R. Tilley and J. Tilley, "Second-order critical fields," in *Superfluidity and Superconductivity*, 3rd ed. Bristol: IOP publishing Ltd., 1990, pp. 305.

[13] C. P. Poole, H. A. Farach, and R. J. Creswick, "Fluxoid Quantization," in *Superconductivity*. San Diego, California: Academic Press Inc, 2007, pp. 149-150.

[14] D. R. Tilley and J. Tilley, "Abrikosov vortex lattice," in *Superfluidity and Superconductivity*, 3rd ed. Bristol: IOP publishing Ltd., 1990, pp. 312-318.

[15] G. Burns, "Superconducting Properties," in *High-temperature Superconductivity*: Academic Press Limited, 1992, pp. 156-157.

[16] J. Bardeen, L. N. Cooper, and J. R. Schrieffer, "Theory of Superconductivity," *Physical Review*, vol. 108, pp. 1175-1204, 1957.

[17] M. Tinkham, "The Energy Gap and the BCS Theory," in *Introduction to Superconductivity*. New York: Dover Publications, 1996, pp. 9.

[18] J. Matricon and G. Waysand, "East is East, and West is West," in *The Cold Wars - A History of Superconductivity*. New Brunswick, New Jersey: Rutgers University Press, 2003, pp. 129.

[19] E. Maxwell, "Isotope effect in the superconductivity of mercury," *Physical Review*, vol. 78, pp. 477, 1950.

[20] D. R. Tilley and J. Tilley, "Microscopic Theory of Superconductivity," in *Superfluidity and Superconductivity*. Bristol: IOP Publishing Ltd, 1990, pp. 119-122.

[21] M. Tinkham, "The BCS Theory," in *Introduction to Superconductivity*. New York: Dover Publications, 1996, pp. 64.

[22] C. P. Poole, H. A. Farach, and R. J. Creswick, "BCS Theory," in *Superconductivity*. New York: Dover Publications, 2007, pp. 189-190.

[23] J. G. Bednorz and K. A. Müller, "Possible high T_C superconductivity in the Ba-La-Cu-O system," *Zeitschrift für Physik B*, vol. 64, pp. 189-193, 1986.

[24] M. K. Wu, J. R. Ashburn, C. J. Torng, P. H. Hor, R. L. Meng, L. Gao, Z. J. Huang, Y. Q. Wang, and C. W. Chu, "Superconductivity at 93 K in a new mixed-phase Y-Ba-Cu-O compound system at ambient pressure," *Physical Review Letters*, vol. 58, pp. 908-910, 1987.

[25] P. Dai, B. C. Chakoumakos, G. F. Sun, K. W. Wong, Y. Xin, and D. F. Lu, "Synthesis and neutron powder diffraction study of the superconductor $HgBa_2Ca_2Cu_3O_{8+\delta}$ by Tl substitution," *Physica C*, vol. 243, pp. 201-206, 1995.

[26] "http://www.magnet.fsu.edu/education/tutorials/magnetacademy/superconductivity101/page6.html," in *The Iceman Succumbeth: High-Temperature Superconductivity*. Florida, 2014, pp. National High Magnetic Field Laboratory.
[27] T. P. Sheahen, "Theory of HTSCs," in *Introduction to High-Temerature Superconductors*. New York: Plenum Press, 1994, pp. 228.
[28] C. P. Bean, "Magnetization of high-field superconductors," *Reviews of Modern Physics*, vol. 36, pp. 31-39, 1964.
[29] "http://www.magnet.fsu.edu/." Florida, 2014, pp. National High Magentic Field Laboratory.
[30] D. M. J. Taylor, M. Al-Jawad, and D. P. Hampshire, "A new paradigm for fabricating bulk high-field superconductors," *Superconductor Science & Technology*, vol. 21, pp. 125006, 2008.
[31] T. Wang, T. Plackowski, and A. Junod, "Specific heat in the superconducting and normal state (2-300 K, 0 - 16 T) and magnetic susceptibility of the 38 K superconductor MgB2: evidence for a multicomponent gap," *Physica C*, vol. 355, pp. 179-193, 2001.
[32] C. P. Poole, H. A. Farach, and R. J. Creswick, "Internal and Critical Fields," in *Superconductivity*. San Diego, California: Academic Press Inc, 2007, pp. 338-344.
[33] M. N. Wilson, *Superconducting Magnets*: Oxford University Press, 1986.
[34] M. J. Raine and D. P. Hampshire, "Characterization of the Low Temperature Superconductor Niobium Carbonitride," *IEEE Transactions on Applied Superconductivity*, vol. 21, pp. 3138-3141, 2011.
[35] A. L. Giorgi, B. T. Matthias, A. L. Bowman, E. K. Storms, and E. G. Szklarz, "Effect of Composition on Superconducting Transition Temperature of Tantalum Carbide and Niobium Carbide," *Physical Review*, vol. 125, pp. 837-&, 1962.
[36] L. E. Toth, "Superconducting Properties," in *Refractory Materials: A Series of Monographs*: Academic Press Inc. (London) Ltd, 1971, pp. 240.
[37] C. P. Poole, H. A. Farach, and R. J. Creswick, "Vortex Anisotropies," in *Superconductivity*. San Diego, California: Academic Press, 2007, pp. 359-362.
[38] C. C. Tsuei and J. R. Kirtley, "d-wave pairing symmetry in cuprate superconductors," *Physica C*, vol. 341-348, pp. 1625-1628, 2000.
[39] J. M. Tarascon, W. R. McKinnon, P. Barboux, D. M. Hwang, B. G. Bagley, L. H. Greene, G. W. Hull, Y. LePage, N. Stoffel, and M. Giroud, "Preparation, structure, and properties of the superconducting compound series $Bi_2Sr_2Ca_{n-1}Cu_nO_y$ with n=1, 2, and 3," *Physical Review B*, vol. 38, pp. 8885-8892, 1988.
[40] I. Matsubara, H. Tanigawa, T. Ogura, H. Yamashita, and M. Kinoshita, "Upper critical field and anisotropy of the high-Tc BSCCO phase," *Physical Review B*, vol. 45, pp. 7414-7417, 1992.
[41] C. Politis and H. L. Luo, "Superconductivity in Tl-Ca-Ba-Cu-O compounds," *Modern Physics Letters B*, vol. 2, pp. 793-798, 1988.
[42] W. Buckel and R. Kleiner, *Superconductivity : fundamentals and applications*: Weinheim ; New York : Wiley-VCH, 2004.
[43] "Address Before a Joint Session of the Congress Following the Soviet-United States Summit Meeting in Geneva," in *The Public Papers of President Ronald W. Reagan.*: Ronald Reagan Presidential Library.
[44] "ITER, the way to new energy. www.iter.org," accessed 2015.
[45] "Reaching 150,000,000 °C," *https://www.iter.org/sci/plasmaheating*, 2015.
[46] "ITER, the way to new energy. https://www.iter.org/sci/fusionfuels," accessed 2015.
[47] "Radionuclide half-life measurements," *http://www.nist.gov/pml/data/halflife-html.cfm*, 2015.
[48] "45 Tesla, 32 mm Bore Hybrid Magnet," *https://nationalmaglab.org/user-facilities/dc-field/instruments-dcfield/resistive-magnets/45-tesla*, 2015.
[49] "Resistive Magnets," *https://nationalmaglab.org/user-facilities/dc-field/instruments-dcfield/resistive-magnets/45-tesla*, 2015.
[50] "iter newsline," *http://www.iter.org/newsline/122/182*, 2015.
[51] C. Sborchia, Y. Fu, R. Gallix, C. Jong, J. Knaster, and N. Mitchell, "Design and specifications of the ITER TF coils," *Ieee Transactions on Applied Superconductivity*, vol. 18, pp. 463-466, 2008.
[52] A. Ulbricht, J. L. Duchateau, W. H. Fietz, D. Ciazynski, H. Fillunger, S. Fink, R. Heller, R. Maix, S. Nicollet, S. Raff, M. Ricci, E. Salpietro, G. Zahn, R. Zanino, M. Bagnasco, D. Besette, E. Bobrov, T. Bonicelli, P. Bruzzone, M. S. Darweschsad, P. Decool, N. Dolgetta, A. della Corte, A. Formisano, A. Grunhagen, P. Hertout, W. Herz, M. Huguet, F. Hurd, Y.

Ilyin, P. Komarek, P. Libeyre, V. Marchese, C. Marinucci, A. Martinez, R. Martone, N. Martovetsky, P. Michael, N. Mitchell, A. Nijhuis, G. Nother, Y. Nunoya, M. Polak, A. Portone, L. S. Richard, M. Spadoni, M. Susser, S. Turtu, A. Vostner, Y. Takahashi, F. Wuchner, and L. Zani, "The ITER toroidal field model coil project," *Fusion Engineering and Design*, vol. 73, pp. 189-327, 2005.

[53] J. L. Duchateau, P. Komarek, and B. Turck, "The History of Fusion Magnet Development," in *100 Years of Superconductivity*. Florida: CRC Press, 2012, pp. 760.

[54] "iter newsline. https://www.iter.org/newsline/-/1951," accessed 2015.

[55] L. E. Toth, "General Properties, Preparation, and Characterization," in *Refractory Materials: A Series of Monographs*: Academic Press Inc. (London) Ltd, 1971, pp. 6-7.

[56] M. Hansen and K. Anderko, "N-Nb Nitrogen-Niobium," in *Constitution of Binary Alloys*, 2nd ed: Genium Publishing Corporation, 1998, pp. 983-984.

[57] J. H. Ma, Y. H. Du, and Y. T. Qian, "Low-temperature synthesis of nanocrystalline niobium nitride via a benzene-thermal route," *Journal of Alloys and Compounds*, vol. 389, pp. 296-298, 2005.

[58] M. P. Mathur, D. W. Deis, and J. R. Gavaler, "Lower Critical-Field Measurements in NbN Bulk and Thin-Films," *Journal of Applied Physics*, vol. 43, pp. 3158-&, 1972.

[59] K. Senapati, N. K. Pandey, R. Nagar, and R. C. Budhani, "Normal-state transport and vortex dynamics in thin films of two structural polymorphs of superconducting NbN," *Physical Review B*, vol. 74, 2006.

[60] D. Dewhughes and R. Jones, "The Effect of Neutron-Irradiation Upon the Superconducting Critical-Temperature of Some Transition-Metal Carbides, Nitrides, and Carbonitrides," *Applied Physics Letters*, vol. 36, pp. 856-859, 1980.

[61] L. Shi, Y. L. Gu, L. Y. Chen, Z. H. Yang, J. H. Ma, and Y. T. Qian, "Synthesis and characterization of superconducting NbC nanotubes," *Letters to the Editor / Carbon*, vol. 43, pp. 211-213, 2005.

[62] V. daSilva, M. Schmal, and S. T. Oyama, "Niobium carbide synthesis from niobium oxide: Study of the synthesis conditions, kinetics, and solid-state transformation mechanism," *Journal of Solid State Chemistry*, vol. 123, pp. 168-182, 1996.

[63] M. Miki, T. Yamasaki, and Y. Ogino, "Preparation of Nanocrystalline NbN and (Nb, Al)N Powders by Mechanical Alloying under Nitrogen Atmosphere," *Materials Transactions, JIM*, vol. 33, pp. 839-844, 1992.

[64] B. T. Massalski, *Binary Alloy Phase Diagrams*. Ohio: American Society for Metals, 1986.

[65] G. Brauer and J. Jander, "Die Nitride Des Niobs," *Zeitschrift fur Anorganische*, vol. 270, pp. 160-178, 1952.

[66] H. Rogener, "Zur Supraleitung Des Niobnitrids - (Mitteilungen Zur Supraleitung-Iii, Erlangen)," *Zeitschrift für Physik*, vol. 132, pp. 446-467, 1952.

[67] G. Brauer, J. Jander, and H. Rogener, "Zur Struktur Und Zusammensetzung Von Niob-Stickstoffverbindungen," *Zeitschrift fur Physik*, vol. 134, pp. 432-434, 1953.

[68] C. Y. Ang and C. Wert, "Some Properties of Columbium Containing Nitrogen," *Transactions of the American Institute of Mining and Metallurgical Engineers*, vol. 197, pp. 1032-1036, 1953.

[69] E. A. Gulbransen and K. F. Andrew, "Kinetics of the Reactions of Columbium and Tantalum with O-2, N-2 and H-2," *Transactions of the American Institute of Mining and Metallurgical Engineers*, vol. 188, pp. 586-599, 1950.

[70] Mattheis.Lf, "Electronic Band-Structure of Niobium Nitride," *Physical Review B*, vol. 5, pp. 315-&, 1972.

[71] J. F. Smith, O. N. Carlson, and R. R. Deavillez, "The Niobium Carbon System," *Journal of Nuclear Materials*, vol. 148, pp. 1-16, 1987.

[72] A. Nigro, G. Nobile, V. Palmieri, G. Rubino, and R. Vaglio, "Superconducting and Normal State Properties of Niobium-Nitride Thin-Films," *Physical Review*, vol. 38, pp. 483-485, 1988.

[73] L. E. Toth, "General Properties, Preparation, and Characterization," in *Refractory Materials: A Series of Monographs*: Academic Press Inc. (London) Ltd, 1971, pp. 188.

[74] J. W. Ekin, *Experimental Techniques for Low-Temperature Measurements*. New York: Oxford University Press, 2007.

[75] K. Schwarz, "Electronic-Structure of NbC and NbN," *J. Phys. C: Solid State Phys*, vol. 10, pp. 195-210, 1977.

[76] V. Buscaglia, F. Caracciolo, M. Ferretti, M. Minguzzi, and R. Musenich, "Effect of pressure on the composition and superconducting T_c value of NbN prepared by combustion synthesis," vol. 266, pp. 201-206, 1998.

[77] N. Pessall, C. K. Jones, H. A. Johansen, and J. K. Hulm, "Critical Supercurrents in Niobium Carbonitrides," *Applied Physics Letters*, vol. 7, pp. 38-&, 1965.
[78] T. Watari, Y. Takakura, M. Murakami, and A. Kato, "Preparation and Superconductivity of NbN Powder by a Vapor-Phase Reaction," *Journal of Materials Science*, vol. 19, pp. 2915-2920, 1984.
[79] Y. G. Li and L. Gao, "Synthesis and characterization of nanocrystalline niobium nitride powders," vol. 86, pp. 1205-1207, 2003.
[80] R. M. Powell, W. J. Skocpol, and M. Tinkham, "Preparation and Superconducting Properties of Ultrafine Powders and Sintered Compacts of NbC and NbN," *Journal of Applied Physics*, vol. 48, pp. 788-794, 1977.
[81] E. K. Storms and N. H. Krikorian, "The Variation of Lattice Parameter with Carbon Content of Niobium Carbide," *Journal of Physical Chemistry*, vol. 63, pp. 1747-1749, 1959.
[82] E. K. Storms, "The Niobium-Niobium Carbide System," in *The Refractory Carbides*. New York and London: Academic Press, 1967, pp. 61-81.
[83] E. K. Storms, N. H. Krikorian, and C. P. Kempter, "Niobium Monocarbide," *Anal Chem*, vol. 32, pp. 1722-1722, 1960.
[84] T. Tsuchida and Y. Azuma, "Synthesis of niobium carbide and nitride in air from mechanically activated Nb-C powder mixtures," *J. Mater. Chem.*, vol. 7, pp. 2265-2268, 1997.
[85] S. T. Oyama, J. C. Schlatter, J. E. Metcalfe, and J. M. Lambert, "Preparation and Characterization of Early Transition-Metal Carbides and Nitrides," *Ind. Eng. Chem. Res.*, vol. 27, pp. 1639-1648, 1988.
[86] M. W. Williams, K. M. Ralls, and M. R. Pickus, "Superconductivity of Cubic Niobium Carbo-Nitrides," *J. Phys. Chem. Solids*, vol. 28, pp. 333-&, 1967.
[87] H. S. Kim, G. Bugli, and G. Djega-Mariadassou, "Preparation and characterization of niobium carbide and carbonitride," *Journal of Solid State Chemistry*, vol. 142, pp. 100-107, 1999.
[88] R. Frerichs and C. J. Kircher, "Properties of Superconducting Niobium Films Made by Asymmetric Ac Sputtering," *Journal of Applied Physics*, vol. 34, pp. 3541-&, 1963.
[89] K. S. Keskar, Yamashit.T, and Y. Onodera, "Superconducting Transition Temperatures of Rf Sputtered Nbn Films," *Japanese Journal of Applied Physics*, vol. 10, pp. 370-&, 1971.
[90] R. Frerichs, "Superconductive Films Made by Protected Sputtering of Tantalum or Niobium," *Journal of Applied Physics*, vol. 33, pp. 1898-&, 1962.
[91] J. R. Gavaler, J. K. Hulm, M. A. Janocko, and C. K. Jones, "Preparation and Superconducting Properties of Thin Films of Transition Metal Interstitial Compounds," *The Journal of vacuum science and technology*, vol. 6, pp. 177, 1968.
[92] D. Gavrilov, O. Vinogradov, and W. J. D. Shaw, "Computer simulation of mechanical alloying in a shaker ball mill," presented at Proceedings of the Tenth International Conference on Composite Materials, Whistler, British Columbia, Canada, 1995.
[93] E. J. Cukauskas, W. L. Carter, and S. B. Qadri, "Superconducting and Structure Properties of Niobium Nitride Prepared by Rf Magnetron Sputtering," *Journal of Applied Physics*, vol. 57, pp. 2538-2542, 1985.
[94] D. D. Bacon, A. T. English, S. Nakahara, F. G. Peters, H. Schreiber, W. R. Sinclair, and R. B. Vandover, "Properties of NbN Thin-Films Deposited on Ambient-Temperature Substrates," *Journal of Applied Physics*, vol. 54, pp. 6509-6516, 1983.
[95] J. R. Gavaler, M. A. Janocko, and C. K. Jones, "Superconducting Properties of Niobium Carbonitride Thin Films," *Applied Physics Letters*, vol. 19, pp. 305-&, 1971.
[96] H. J. Spitzer, "Superconducting Properties and Structure of Reactively Sputtered Niobium Carbide Thin-Films," *Journal of Vacuum Technology*, vol. 10, pp. 20-21, 1973.
[97] H. Morita, K. Watanabe, K. Noto, and H. Fujimori, "Production of a Long Superconducting NbN Wire by the Sputtering Method," *Japanese Journal of Applied Physics*, vol. 26, pp. 953-954, 1987.
[98] U. Patel, S. Avci, Z. L. Xiao, S. H. Yu, Y. Ito, R. Divan, L. E. Ocola, C. Zheng, H. Claus, J. Hiller, U. Welp, D. J. Miller, and W. K. Kwok, "Synthesis and superconducting properties of niobium nitride nanowires and nanoribbons," *Applied Physics Letters*, vol. 91, pp. 162508-1 - 162508-3, 2007.
[99] G. E. Pike, A. W. Mullendore, J. E. Schirber, and J. Napier, "Superconducting Properties of Thin-Film Niobium Carbonitrides on Carbon-Fibers," *IEEE Transactions on Magnetics*, vol. MA11, pp. 185-188, 1975.
[100] J. M. Cordoba, M. J. Sayagues, M. D. Alcala, and F. J. Gotor, "Monophasic nanostructured powders of niobium, tantalum, and hafnium carbonitrides synthesized by

a mechanically induced self-propagating reaction," *Journal of the American Ceramic Society*, vol. 90, pp. 381-387, 2007.
[101] D. W. Deis, J. R. Gavaler, J. K. Hulm, and C. K. Jones, "High Field Properties of Pure Niobium Nitride Thin Films," *Journal of Applied Physics*, vol. 40, pp. 2153-&, 1969.
[102] J. R. Gavaler, M. A. Janocko, Patterso.A, and C. K. Jones, "Very High Critical Current and Field Characteristics of Niobium Nitride Thin Films," *Journal of Applied Physics*, vol. 42, pp. 54-&, 1971.
[103] Z. Wang, A. Kawakami, Y. Uzawa, and B. Komiyama, "Superconducting properties and crystal structures of single-crystal niobium nitride thin films deposited at ambient substrate temperature," *Journal of Applied Physics*, vol. 79, pp. 7837-7842, 1996.
[104] G. Horn and E. Saur, "Preparation and Superconductive Properties of Niobium Nitride and Niobium Nitride with Admixtures of Titanium Zirconium and Tantalum," *Zeitschrift fur Physik*, vol. 210, pp. 70-&, 1968.
[105] B. Komiyama, Z. Wang, and M. Tonouchi, "Penetration depth measurements of single-crystal NbN films at millimeter-wave region," *Applied Physics Letters*, vol. 68, pp. 562-563, 1996.
[106] V. N. Troitskiy, I. A. Domashnev, E. N. Kurkin, O. M. Grebtsova, V. I. Berestenko, I. L. Balikhin, and S. V. Gurov, "Synthesis and characteristics of ultra-fine superconducting powders in the Nb-N, Nb-N-C, Nb-Ti-N-C systems," *Journal of Nanoparticle Research*, vol. 5, pp. 521-528, 2003.
[107] L. Shi, Y. L. Gu, L. Y. Chen, Z. H. Yang, J. H. Ma, and Y. T. Qian, "Synthesis and characterization of superconducting nanocrystalline niobium nitride," *Journal of Nanoscience and Nanotechnology*, vol. 5, pp. 296-299, 2005.
[108] C. P. Poole, H. A. Farach, and R. J. Creswick, "Internal and Critical Fields," in *Superconductivity*. San Diego, California: Academic Press Inc, 2007, pp. 343-344.
[109] B. T. Matthias, "Transition Temperatures of Superconductors," *Physical Review*, vol. 92, pp. 874-876, 1953.
[110] J. S. Moodera, T. L. Francavilla, and S. A. Wolf, "Upper Critical-Field Measurement and Penetration Depth Determination for Superconducting NbCN Films," *IEEE Transactions on Magnetics*, vol. 23, pp. 1003-1006, 1987.
[111] M. Suzuki, T. Anayama, K. Watanabe, N. Toyota, N. Kobayashi, K. Noto, and Y. Muto, "Critical Current-Density in Superconducting Nb_3Ge and NbN Films at Fields up to 30-T," *Japanese Journal of Applied Physics Part 2-Letters*, vol. 24, pp. L767-L769, 1985.
[112] "http://www.magnet.fsu.edu/magnettechnology/research/asc/plots.html," 2013.
[113] J. W. Ekin, J. R. Gavaler, and J. Gregg, "Effect of Strain on the Critical Current and Critical-Field of B1-Structure NbN Superconductors," *Applied Physics Letters*, vol. 41, pp. 996-998, 1982.
[114] M. Barsoum, *Fundamentals of Ceramics*: McGraw-Hill Inc., US, 1996.
[115] M. Barsoum, "Chapter 10: Sintering and Grain Growth (Fig. 10.9)," in *Fundamentals of Ceramics: The McGraw-Hill series in marterials science & engineering*: McGraw-Hill Inc., US, 1996, pp. p344.
[116] C. D. Service, in *https://cds.dl.ac.uk/*, 2009.
[117] TOPAS-Academic, "http://www.topas-academic.net/," 2014.
[118] "Powder Cell," http://www.ccp14.ac.uk/tutorial/powdcell/, 2014.
[119] C. Suryanarayana, "Mechanical Alloying and Milling," *Progress in Materials Science*, vol. 46, pp. 1-184, 2001.
[120] SPEX, "Features & Specification," in *http://www.spexsampleprep.com/equipment-and-accessories/equipment_product.aspx?typeid=6*, 2014.
[121] SPEX-SamplePrep, "8004 - Tungsten Carbide Grinding Vial Set," in *http://www.spexsampleprep.com/equipment-and-accessories/accessory_product.aspx?partnumber=8004&equipcat=3&typeid=6*
[122] A. A. Ammann, "Inductively coupled plasma mass spectrometry (ICP MS): a versatile tool," *Journal of Mass Spectrometry*, vol. 42, pp. 419-427, 2007.
[123] R. B. Schwarz and R. R. Petrich, "Calorimetry study of the synthesis of amorphous Ni-Ti alloys by mechanical alloying," *Journal of the Less Common Metals*, vol. 140, pp. 171, 1988.
[124] Hot_Isostatic_Pressing, "http://www.hipping.co.uk/HotIsostaticPressing," TTI Group, 2014.
[125] M. Barsoum, "Chapter 10: Sintering and Grain Growth (Hot pressing and hot isostatic pressing)," in *Fundamentals of Ceramics: The McGraw-Hill series in marterials science & engineering*: McGraw-Hill Inc., US, 1996, pp. p378.

[126] M. Barsoum, "Chapter 10: Sintering and Grain Growth (Fig. 10.8)," in *Fundamentals of Ceramics: The McGraw-Hill series in marterials science & engineering*: McGraw-Hill Inc., US, 1996, pp. p342.

[127] T. Geballe, B. T. Matthias, J. P. Remeika, A. M. Clogston, V. B. Compton, J. P. Maita, and H. J. Williams, "High Temperature SP-Band Superconductors," *Physics (New York)*, vol. 2, pp. 293-310, 1966.

[128] N. R. Werthamer, E. Helfand, and P. C. Hohenberg, "Temperature and Purity Dependence of the Superconducting Critical Field, H_{C2}. III. Electron Spin and Spin-Orbit Effects.," *Physical Review*, vol. 147, pp. 295-302, 1966.

[129] H. J. Niu and D. P. Hampshire, "Disordered Nanocrystalline Superconducting $PbMo_6S_8$ with Very Large Upper Critical Field," *Physical Review Letters*, vol. 91, pp. 027002, 2003.

[130] L. D. Cooley, Y. F. Hu, and A. R. Moodenbaugh, "Enhancement of the upper critical field of Nb_3Sn utilizing disorder introduced by ball milling the elements," *Applied Physics Letters*, vol. 88, pp. 142506, 2006.

[131] M. Sborchia, E. Barbero Soto, R. Batista, B. Bellesia, A. Bonito Oliva, E. Boter Rebollo, T. Boutboul, B. E, J. Caballero, M. Comelis, J. Fanthome, R. Harrison, M. Losasso, A. Portone, H. Rajainmaki, P. Readman, and P. Valente, "Overview of ITER Magnet System and European Contribution," *IEEE/NPSS 24th Symposium on Fusion Engineering*, pp. S03D-l, 2011.

[132] H. Muller and T. Schneider, "Heat treatment of Nb_3Sn conductors," *Cryogenics*, vol. 48, pp. 323-330, 2008.

[133] A. Devred, I. Backbier, D. Bessette, G. Bevillard, M. Gardner, C. Jong, F. Lillaz, N. Mitchell, G. Romano, and A. Vostner, "Challenges and status of ITER conductor production," *Superconductor Science & Technology*, vol. 27, pp. 39, 2014.

[134] A. Dobi, D. S. Leonard, C. Hall, L. J. Kaufman, T. Langford, S. Slutsky, and Y. R. Yen, "Study of a zirconium getter for purification of xenon gas," *Nuclear Instruments and Methods in Physics Research Section A: Accelerators, Spectrometers, Detectors and Associated Equipment*, vol. 620, pp. 594-598.

[135] S. A. Keys and D. P. Hampshire, "Characterisation of the transport critical current density for conductor applications," in *Handbook of Superconducting Materials*, vol. 2, D. Cardwell and D. Ginley, Eds. Bristol: IOP Publishing, 2003, pp. 1297-1322.

[136] M. C. Jewell, "The effect of strand architecture on the fracture propensity on niobium-tin composite wires," in *Department of Materials Science*. Wisconsin: University of Wisconsin, 2008.

[137] W. J. Nuttall, R. H. Clarke, and B. A. Glowacki, "Stop Squandering Helium," *Nature*, vol. 485, pp. 573, 2012.

[138] P. Sunwong, J. S. Higgins, and D. P. Hampshire, "Probes for investigating the effect of magnetic field, field orientation, temperature and strain on the critical current density of anisotropic high-temperature superconducting tapes in a split-pair 15 T horizontal magnet," *The Review of scientific instruments*, vol. 85, pp. 065111, 2014.

[139] L. F. Goodrich, L. T. Medina, and T. C. Stauffer, "Repeatability of critical-current measurements on Nb_3Sn and Nb-Ti wires," *IEEE Transactions on Applied Superconductivity*, vol. 7, pp. 1508-1511, 1997.

[140] T. Boutboul, P. Readman, E. Viladiu, M. Losasso, J. Caballero, J. Abou-Yehia, and R. Batista, "Status of the Procurement of the European Superconductors for the ITER Magnets," *IEEE Transactions on Applied Superconductivity*, vol. 24, pp. 4, 2014.

[141] S. Foner, "Vibrating Sample magnetometer," *Review of Scientific Instruments*, vol. 27, pp. 548, 1956.

[142] Quantum Design, "Magnetometry." San Diego: Quantum Design http://www.qdusa.com/sitedocs/productBrochures/mag3-07.pdf.

[143] E. Gregory, M. Tomsic, M. D. Sumption, X. Peng, X. Wu, E. W. Collings, and B. A. Zeitlin, "The introduction of titanium into internal-tin Nb_3Sn by a variety of procedures," *Ieee Transactions on Applied Superconductivity*, vol. 15, pp. 3478-3481, 2005.

[144] D. Uglietti, V. Abacherli, M. Cantoni, and R. Flukiger, "Grain Growth, Morphology, and Composition Profiles in Industrial Nb3Sn Wires," *IEEE TRANSACTIONS ON APPLIED SUPERCONDUCTIVITY*, vol. 17, pp. 2615, 2007.

[145] J. W. Ekin, "Experimental Techniques for Low-Temperature Measurements." New York: Oxford University Press, 2007, pp. 575.